Brigham Young University
BYU ScholarsArchive

Theses and Dissertations

2019-04-01

Multi-Instrument Surface Characterization of Display Glass

Cody Vic Cushman

Brigham Young University

Follow this and additional works at: https://scholarsarchive.byu.edu/etd

Multi-Instrument Surface Characterization of Display Glass

Cody Vic Cushman

A dissertation submitted to the faculty of
Brigham Young University
in partial fulfillment for the requirements for the degree of

Doctor of Philosophy

Matthew Richard Linford, Chair
Daniel E. Austin
Robert C. Davis
Barry M. Lunt
Adam T. Woolley

Department of Chemistry and Biochemistry

Brigham Young University

ABSTRACT

Multi-Instrument Surface Characterization of Display Glass

Cody Vic Cushman
Department of Chemistry and Biochemistry, BYU
Doctor of Philosophy

Flat panel displays (FPDs) are microfabricated devices that are often fabricated on specialized glass substrates known as display glass. The surface chemistry of the outer few nanometers of display glass can have an important influence on FPD performance and yield. Dsiplay glass surface characterization is difficult because (i) display glass surface composition varies significantly from its bulk composition; (ii) high-surface area forms of glass, such as fibers and powders, may not have the same surface composition as melt-formed planar surfaces, and (iii) the surface composition of display glass may be altered through exposure to chemical treatments commonly used during flat panel display production, including acids, bases, etchants, detergents, and plasmas.

We have performed a detailed surface composition of Eagle XG®, a widely used commercial display glass substrate, using a range of surface analytical techniques including time-of-flight secondary ion mass spectrometry (ToF-SIMS), angle-resolved X-ray photoelectron spectroscopy (AR-XPS) and low energy ion scattering (LEIS). The information from these techniques has given us a detailed understanding of the elemental surface composition and surface hydroxylation of Eagle XG® at length scales ranging from ca. 10 nm from the surface to the outermost atomic layer. These analyses reveal that the surface composition of Eagle XG® varies significantly from its bulk composition, having generally lower concentrations of Al, B, Mg, Ca, and Sr, and higher concentrations of Si. Treatment with an industrial alkaline detergent results in significant recovery of aluminum concentration at the Eagle XG® surface, while treatment with hydrochloric and hydrofluoric acid result in further depletion of Al, B, Mg, Ca, and Sr at the sample surface.We used ToF-SIMS to quantify surface hydroxyls at the sample surface of this material. The $SiOH^+/Si^+$ peak area ratio was a useful metric of surface hydroxylation. We studied the effects of adventitious surface contamination on the measurements by analyzing samples dosed with perdeuterated triacontane, a model alkane, prior to analysis. Thick triacontane overlayers suppressed the $SiOH^+$ signal, indicating that this approach gives inaccurately low estimates of surface hydroxylation for samples with high degrees of surface contamination, and accurate measurements are only possible for very-clean surfaces. The number of of hydroxyls on Eagle XG® surfaces varied as the surfaces were exposed to different chemical treatments. HF- and HCl- treated surfaces had the highest degree of hydroxylation, while detergent-treated surfaces had the lowest.

Keywords: ToF-SIMS, XPS, LEIS, flat panel display, display glass, surface hydroxyl, multivatiate curve resolution

ACKNOWLEDGMENTS

My lab mates are an impressive and caring group of people. The opportunity to work with excellent scientists from Iran, China, India, and various corners of the United States has been an enlarging experience for me, a guy from a small town in Idaho who had seen little of the world prior to graduate school. I admire how openly they live their religions and adhere to their values. Their faith and optimism, well, it can't help but rub off a little. I'd like to follow their example by thanking my God for the many blessings he has given me through graduate school.

I'd like to thank my brothers, who are strange like I am, my parents, who have sacrificed a lot to help me get here. My wife, Amber Cushman, deserves special credit for her support, both moral and financial through 5 years of graduate school.

The work herein builds on the scientific advances of many who came before me. I hope my small contribution to glass surface science is a worthy addition to their excellent work.

TABLE OF CONTENTS

LIST OF ABBREVIATIONS

AES	Auger electron spectroscopy
ALD	Atomic layer deposition
AP	Atmospheric pressure
AR-XPS	Angle-resolved X-ray photoelectron spectroscopy
BEMA	Bruggeman effective medium approximation
BO	Bridging oxygens
CHA	Concentric hemispherical analyzer
CIO	Classical interdiffusion
DTA	Double toroidal analyzer
ESA	Electrostatic analyzers
FPD	Flat panel display
FTIR	Fourier transform infrared spectroscopy
HLW	High level waste
HSA	Hemispherical analyzer
IDP	Interfacial dissolution precipitation
ISG	International simple glass
ISMA	Informed sample model approach
ISS	Ion scattering spectroscopy
LEIS	Low energy ion scattering
LF	Lorentzian finite
LLS	Linear least squares
MCR	Multivariate curve resolution
MSE	
NBO	Non-bridging oxygen
PC	Principal component
PCA	Principal components analysis
PFA	Perfluorinated alkane

PRI   Passivating reactive interface

RBS   Rutherford back scattering

RSF   Relative sensitivity factor

SIMS   Secondary ion mass spectrometry

SOFC   Solid oxide fuel cell

T-L   Tauc-Lorentz

TEM   Transmission electron microscopy

TMAH   Tetramethylammonium hydroxide

ToF-SIMS   Time-of-flight secondary ion mass spectrometry

UV-VIS   Ultraviolet/visible spectroscopy

LIST OF FIGURES

LIST OF TABLES

CHAPTER 1: Introduction

1.1 The Focus of This Work

This work focuses on the surface characterization of glass substrates for flat panel displays (FPDs). In this application, glass is the substrate for microfabricated circuit elements that form pixels in these FPDs. FPDs are prevalent in electronic devices like smartphones, laptops, televisions, etc. The substrate material in FPDs fulfills two essential roles. First, it is a window. In most applications, FPDs generate color by passing white light through a color filter. This light passes through multiple layers of glass before reaching the users' eyes. Second, glass must be a microfabrication substrate.[1] Therefore, much of the value of display glass is as a surface for technical coatings. The vast majority of FPDs are fabricated on silicate glass substrates, while only a small fraction utilize other materials like organic polymers.

Glass's bulk material properties explain its prevalence as a display substrate; silicate glasses have excellent optical transparency, thermal stability, strength, and chemical durability.[2-4] However, display glass's surface properties are increasingly important. To produce defect-free display panels, display glass surfaces must be free from particulates large enough to cause circuit defects (ca. 300 nm as of 2016).[2,4] They must also be free from any contamination that can impede thin-film adhesion to the glass surface or poison the materials that are later deposited on the glass.[1-2,4] Current industry trends increase the demands placed on FPD substrates. At the time of writing, a brief internet search revealed commercially-available televisions with diagonal screen dimensions of 86 inches (2.2 meters), giving ca. 2.3 m^2 of screen area. These may be fabricated in batches on sheets of glass up to 2.8 x 3.2 m^2.[1,5] In contrast, the largest commonly used silicon

wafers are only 0.3 m in diameter, and the individual dies fabricated on these wafers are typically a few cm^2. VLSI devices fabricated on silicon typically have much smaller critical dimensions than FPDs. However, FPD critical dimensions in hand-held devices continue to decrease as pixel counts increase. This decrease makes FPDs ever more sensitive to contamination and particulate related failures during device fabrication.[2, 4]

The demands placed on display glass surfaces drive a need to understand how they interact with their environments, change with exposure to wet-chemical treatments common on FPD production lines, and how to tune display glass surface chemistry for each processing step. These are also important questions for glass surfaces in general. This is a multi-disciplinary problem. Some researchers investigate specific phenomena, e.g., static buildup and discharge on glass surfaces, while others try to understand glass surfaces at the theoretical level through computational modeling.[6-9]

This work focuses on the surface characterization of Corning Eagle XG®, a widely-used display substrate. The goals are to provide comprehensive surface compositional analysis of this sample system and explore methodologies and best practices for performing this type of characterization. Detailed compositional information is essential to understand the link between glass surface composition and surface-mediated processes. We characterized the surface of Eagle XG® using X-ray photoelectron spectroscopy (XPS), time-of-flight secondary ion mass spectrometry (ToF-SIMS), and low energy ion scattering (LEIS). By combining information from these techniques, we gain insight into glass surface composition from a depth of 10 nm to the outermost layer. In addition, we analyzed surface hydroxyls on display glass substrates using ToF-SIMS. Hydroxyls are among the most-important reactive functional groups at silicate glass surfaces, but few studies have proposed methodologies to measure them on low-surface area multi-

component silicate glass substrates.[10-15] Instead, most studies focus on samples with higher surface areas and simpler compositions, e.g. silica nanopowders.[16-24] Accordingly, our hydroxyl measurements on Eagle XG® using ToF-SIMS represent an important contribution to glass surface science. The importance of surface hydroxyls and the challenges associated with measuring them will be discussed in greater detail below.

We have also analyzed the optical properties of Eagle XG® using spectroscopic ellipsometry. While glass optical constants are bulk material properties, optical thin film measurements for films deposited on these substrates require a detailed knowledge of substrate optical constants. Accordingly, these studies are included as appendices to this dissertation.

Display substrates are the focus of this work because there is a current industrial need to understand them. However, better knowledge of multicomponent glass surfaces helps address a wide range of manufacturing challenges and possibly enables new glass functionalities.[25-27] This work is beneficial for any application where coatings are applied to glass surfaces to enhance their functionality and value. The findings presented here may also be useful for the surface analysis of oxide materials and coatings in general. Therefore, while we have chosen display glass as a model system, this work has value beyond addressing the needs of a single industry or providing a compositional analysis of a single material.

1.2 Approach

Our goal is to provide the compositional knowledge necessary for understanding the link between glass surface composition and the surface processes that impact display fabrication. Accordingly, this study focuses on the composition at the outermost atomic layer, which can

directly affect thin-film adhesion, contamination, and surface reactivity.[28] In particular, we focused on the elemental composition and number of surface hydroxyls, which largely determine glass surface reactivity.[11-13, 16-21, 29-31] We selected the analytical techniques based on their surface sensitivity. Angle-resolved XPS provides quantitative elemental information from ca. 10 – 2 nm. ToF-SIMS provides both elemental and molecular compositional information about a sample. ToF-SIMS's information depth depends on numerous factors, but is typically cited between 2 nm and a few atomic layers.[32-35] ToF-SIMS is generally considered more surface sensitive than AR-XPS. LEIS analyzes the elemental composition of the outermost layer.[28, 36-37]

A multi-instrument approach provides several advantages compared to relying on a single technique.[38-39] The techniques used here each have unique characteristics, advantages, and drawbacks. They have different depths of analysis. They provide different types of information; XPS and LEIS give elemental information, while SIMS gives both elemental and molecular information. The disadvantages of each technique are mitigated by combining information from the other techniques. For example, LEIS is the most surface sensitive probe used in this study, but has poor detection limits for boron and poor resolution between aluminum and silicon. These issues are resolved in part by comparing the LEIS data to XPS and ToF-SIMS results. ToF-SIMS has the best detection limits of the techniques used here, but static SIMS is seldom used quantitatively due to potential strong matrix effects. Comparison to XPS and LEIS data helps determine whether a matrix effect is present. Angle-resolved XPS is not as surface sensitive as LEIS or ToF-SIMS, but quantitation in XPS is the most straightforward. Also, angle-resolved XPS is capable of gathering depth-resolved information without sputtering. This ability makes XPS valuable for detecting near-surface compositional gradients, which are scrambled during the equilibration period in a sputter depth profile analysis.[34, 40]By combining information from these

techniques, we obtained a deeper understanding about the compositional profile of Eagle XG® at its outer 10 nanometers and how this composition changes in response to production-line wet-chemical treatments. An understanding of elemental composition is also an essential part of our efforts to quantify surface hydroxyls.

This work is as much about developing analytical protocols as it is understanding display glass surfaces. Some of the analyses and conclusions herein are made possible through recent advances in instrumentation. In particular, the LEIS analysis presented here relied on recent advances in LEIS instrumentation that improved sensitivity and resolution.[28, 36, 41-44] We also addressed significant challenges in data analysis and interpretation. We used chemometric techniques including principal components analysis (PCA) and multivariate curve resolution (MCR) to simplify data reduction interpretation of ToF-SIMS spectra. We tackled the difficult challenge of resolving overlapping contributions from aluminum and silicon in our LEIS analysis. Surface hydroxyl measurements by ToF-SIMS required the most method development of all the work presented here. We adapted an existing approach used to measure hydroxyls on fused silica surfaces and applied it to multicomponent glasses.[11-13] This work required exploration of instrumental parameters, statistical analysis of variability between a high number of replicates, and experimental and computational studies on the influence of adventitious hydrocarbon surface contamination on these measurements.

1.3 Background Information

This section explains the need for the analyses performed in this work, and the challenges inherent in analyzing glass surfaces. It begins with a discussion of the technological importance of

glass and the basics of its structure and composition. It then reviews current knowledge of glass surfaces and commonly used analytical techniques. Finally, it discusses the theory of the analytical techniques we used in this dissertation.

1.3.1 The Technological Importance of Glass and Amorphous Materials

Glass is historically and technologically important. Naturally occurring glass is abundant in nature, with some specimens dated to 65 million B.C.[25, 45] These ancient glasses demonstrate the long-term stability and chemical durability of the material. Glass played an important role in human history, being widely used to make stone-age tools starting ca. 75,000 years ago.[45-46] Man-made glass artifacts produced by casting date to before 1500 B.C.[46] Syrians possibly invented glassblowing ca. 650 B.C., and the Romans produced flat glass sheets by 200 A.D. through a process of blowing glass cylinders, cutting the cylinders lengthwise, and annealing and flattening the resulting segments.[45]

Glass compositions and forming technology continued to develop as glass played an increasingly important role in practical, technological, and artistic applications. Glass is inexpensive and ubiquitous in our era due to modern advances in glass compositions and glass-forming technology.[45] Soda-lime float glass is an important construction material, forming nearly the entire exterior walls of some buildings. It is also an essential component of practically all automobiles.[47] Glass fiber optics are essential in modern communications, and glass fibers are commonly used to reinforce polymer composites.[48-49] Glass enables many important discoveries in modern synthetic chemistry because chemically durable and thermally stable glassware with elaborate geometries are essential to synthesize and purify substances.[50] Glass is an integral part

of optical devices that influence astronomy, spectroscopy, microscopy, photonics, and microfabrication.[47, 51-52] In addition, glass has a long history in electronics and computing. Glass vacuum tubes enabled the development of computers, radio, television, electronic amplifiers, etc.[53-55] Many modern consumer electronics include FPDs, most of which are fabricated on glass.[1-2, 4-5] In previous technological generations, electronic displays mainly communicated information to the device operator. However, FPDs are now often the main input device for many consumer electronics.

The prevalence of glass in modern civilization is partly due to its unique material properties. Although the definition of a glass varies depending on source and context, glass will be defined here as an amorphous solid showing a glass transition.[45] The structure of glass is often described as a frozen liquid.[45, 56] Zachariasen described glass by his widely-accepted continuous random network theory, where glass has an extended 3D network that lacks symmetry and periodicity.[57] In other words, glass structures are described in terms of a few repeating molecular subunits, but the connectivity of these subunits is random throughout the network. This results in a distribution of local chemical environments, with possible distortions in bond angles and bond lengths. This is different from single-crystal and polycrystalline materials (e.g., silicon wafers and most metals, respectively). These materials are described in terms of repeating subunits with the same stoichiometry and structure. Accordingly, these structures have short- and long-range order and relatively fixed bond angles and lengths throughout the structure. The contrast between these two types of structures is shown in Figure 1.1. Figure 1.1a shows a crystalline material with stoichiometry of C_2A_3 where A is a cation and A is an anion. Figure 1.1b shows a material of the same stoichiometry but with a glassy structure.

Glass subunits are categorized into three types: network formers, network modifiers, and intermediate species.[45, 51] Network formers bond to each other to create a polymeric network. Silica tetrahedra are the most important network former in silicate glasses. Network formers connect to one another via bridging oxygens (BOs), and in the case of SiO_4^{4-} subunits, up to four BOs are possible. Boron also acts as a network former and exists in trigonal or tetrahedral subunits depending on glass composition. Network formers in glass are often referred to using Q^n notation, where the superscripted number indicates the number of BOs associated with the network forming species. Modifier ions reduce the connectivity of glass networks by forming non-bridging oxygens (NBOs), as shown in Figure 1.2. Here, negatively charged non-bridging oxygens are charge-compensated by the nearby presence of a Na^+ ions. Network modifiers reduce network connectivity, decrease glass melt viscosity, improve workability, and promote glass-forming. Intermediate species like Al either act as a network former or a network modifier depending on glass composition.[45]

Processing temperature is a key factor in glass production costs.[47] Accordingly, modifiers are essential in producing highly-formable and inexpensive glasses. For example, fused silica consists entirely of Q^4 silicon species, and requires high processing temperatures. On the other hand, soda-lime glass contains Na^+ and Ca^{2+} modifier ions, which result in non-bridging oxygens in the silicate network. This leads to reduced network connectivity, which results in lower processing temperatures and better formability.

Glass's random structure influences its material properties. As a consequence, glass is often more compositionally flexible than crystalline materials.[47] The ability to form glass over wide compositional ranges means it can be tuned to achieve application-specific physical properties.[1, 47] In optical applications, it is often tuned to achieve a desired refractive index.[58] Its compositional

flexibility and chemical durability are essential for its application in nuclear waste storage.[59] Radionucilides can be added to glass formers in large percentages without phase-separation. Glass's high chemical durability slows the release of these radionuclides into the environment.[59]

Silicate glasses are the most widely used class of glass in the modern world.[26] However, other glass compositions also have technological relevance. Chalcogenide consists of the chalcogen elements S, Se, and Te combined with metal ions. These glasses are important in IR optics, lasing, and phase-change memory devices.[60-61] Bioglasses used in dental and bone implants consist of phosphate and silicate-phosphate glasses.[62] Metallic glasses, alloys with an amorphous structure displaying a glass transition, have many of the properties of silicate glasses, e.g., high compressive strength, low Young's modulus, and high wear resistance. They are used in high-strength surgical implants, aerospace and defense applications, and ultrasharp surgical tools.[63-64] Numerous organic glasses also exist. Polymethylmethacrylate can form glasses. This material is known by many trade names, including plexiglass and lucite, and is widely used. Organic glasses generally have much lower forming temperatures and glass transitions than inorganic glasses and are used as model systems for studying glass structure and relaxation. While we acknowledge the importance of these glasses, we will only discuss silicate glasses in this work.[65]

1.3.2 Display Glass and Flat Panel Display Fabrication

Flat panel displays are microfabricated devices and most are fabricated on specially engineered glass known as display glass.[1-4] The FPD fabrication process imposes stringent demands on display glass.[1, 3-4] The glass must have precise geometry, including a high degree of flatness and uniform thickness. It must have excellent surface finish and optical properties. It must

be dimensionally stable during exposure to high processing temperatures. It must be rigid and strong, but many modern display designs also require a high degree of flexibility. It must be chemically durable with respect to the harsh chemistries it will encounter during FPD fabrication, and must not interfere with the circuitry fabricated on it, either chemically or electronically. Alkali ions are mobile in glass at high temperatures and may migrate under electrical fields. They have the potential to diffuse into display glass circuit elements and degrade their performance. As a result, most display glass compositions are alkali-free borosilicates.[1, 3] Alkali-containing glasses are also used, but require additional steps to control alkali migration. These steps include acid leaching to remove alkali ions from the glass surface, or depositing barrier layers to limit alkali diffusion.

Several processes are used for display glass fabrication including the microfloat, slot-draw, and fusion draw processes.[1, 3] Fusion-drawn glass currently accounts for ca. 50% of total display glass production.[2] Eagle XG®, the model system used in our studies, is formed by the fusion draw process. The fusion draw process produces glass with low surface roughness and excellent dimensional uniformity without the need for surface grinding or polishing.[1] A schematic representation of the fusion draw process is shown in Figure 1.3. Here, molten glass is poured into a trough known as an isopipe. The isopipe is filled to overflowing, and molten glass flows down both sides of the isopipe. These two sheets of molten glass meet at the root of the isopipe and fuse to form a single sheet. Rollers near the edge of the sheet draw the glass to the desired thickness and length, after which the sheet is cut from the draw and stored. Notably, the surfaces of the finished glass never come into contact with forming mandrels of any kind during this process and only a small area near the edges of the sheet make contact with rollers.[1] This is the main reason the fusion draw process produces a high-quality surface finish. A 2010 article states that generation

10 fusion drawn sheets can be as thin as 700 um and as large as 3.2 x 2.8 meters.[1] This is an impressive feat, given the surface finish and dimensional uniformity requirements for this material. Thinner fusion drawn glasses are also available.

Fusion draw process requirements govern the range of compositions that are formed by this process. The fusion draw process requires glass viscosities in the range of 10^4-10^5 Pa.s.[1] In contrast, viscosities of ca. 1000 Pa.s are typical in the float process.[1] Display glass compositions with high glass transitions temperatures are preferred to achieve dimensional stability during high temperature processing steps of FPD production. Accordingly, Eagle XG® is a an alkali-earth modified boroaluminosilicate. Its main oxides are SiO_2, B_2O_3, Al_2O_3, CaO, MgO, and SrO. Small amounts of tin are also added to the glass as a fining agent, i.e., to inhibit the formation of bubbles that in the glass melt, which can act as optical defects.[1]

There are various device architectures for FPDs. Currently, the most common type of flat panel display is the active matrix (AM) thin-film transistor (TFT) liquid crystal display (LCD), commonly referred to as active matrix liquid crystal displays (AMLCDs).[5] A schematic representation of an AMLCD is shown in Figure 1.4. There are four main components to the device: a backlight unit (BLU), TFT backplane, color filter, and liquid crystal between the TFT backplane and the color filter. Polarized light from the BLU provides illumination for the display. Each pixel on the display is divided into red, green, and blue subpixels by passing this light through the color filter layer. The light then passes through a second polarizer at the surface of the display, which acts as a light filter. The liquid crystal (LC) adjusts the polarization state of the light entering from the BLU, which determines light transmission through the second polarizer. Adjusting the voltages applied by the TFT backplane alters the orientation of the liquid crystal. Placing the polarization orientation of the liquid crystal in the the correct orientation allows maximum light

transmission and maximum brightness at a given subpixel. Placing the polarization orientation of the liquid crystal at 90 degrees to this position causes the light to be blocked by the second polarizer, resulting in near-zero light transmission through a subpixel. Accordingly, the red, green, and blue light intensities at each pixel on the display can be tuned by adjusting voltages at specific subpixel addresses on the TFT backplane. Other display types, like active matrix organic light emitting diode displays (AMOLED) are gaining increased market share. In these devices, red, green, and blue organic light emitting diodes provide the light for the display, and their intensity is controlled by a TFT backplane that governs current to each subpixel.[5]

Both AMOLEDs and AMLCDS are microfabricated devices produced through photolithography, thin film deposition, and etching processes. They have simpler device architecture than most modern VLSI devices, and are often produced in 6 or fewer lithography steps.[55] However, FPD fabrication poses its own unique challenges, especially considering the size of glass panels used. Many of these challenges relate to the surface composition of the display glass. Particulate-related failures currently account for 80% of FPD production line failures.[2, 4, 55] Display glass must be manufactured, stored, and shipped long distances without accumulating significant particulate contamination in order to be useful as a substrate material. Organic contamination on display glass surfaces can inhibit thin-film adhesion and degrade the optical quality of deposited films. It is important to understand what conditions give optimal thin film adhesion to glass surfaces. Unwanted static discharge can damage FPD circuitry.[2, 6, 66] The surface composition of display glass influences its static charge accumulation and dissipation properties.[6, 66] Understanding the complex nature of glass surfaces is key to addressing many FPD production-line challenges.

1.3.3 Glass Surface Properties and Glass Surface Analysis

Glass has historically been used for its bulk material properties. While bulk glass material research continues to flourish, glass is increasingly used for its surface properties. Glass surfaces influence the manufacturing yield of many products.[27] The value and function of glass goods are often improved by adding functional coatings to their surfaces. Coatings to improve glass strength, improve optical properties, enhance chemical durability, and improve aesthetic appeal are routinely applied[67]. These coatings can be producing an altered layer in the glass itself through leaching, etching, or ion bombardment.[67] They can also be added to the surface by dip coating, chemical vapor deposition, and physical vapor deposition.[67] For example, low-emissivity coatings on insulated glass units increase the energy efficiency of buildings.[68-69] Self-cleaning coatings for windows are also available.[69-70] Coverslip glasses on smartphones are typically used as touch screens. These may include anti-friction coatings to improve their feel, optical coatings to reduce glare, and antimicrobial coatings to improve device hygiene.[2, 71] Complex coatings improve the glass/polymer interface strength of glass fibers used in composite materials.[29-30, 48] Glass surfaces are also used as substrates for microfabricated devices.[72] As such, the quality of the glass/coating interface directly affects device lifetime and yield., Wire-grid polarizers for visible light used in projectors and other optical devices are multi-layer devices often fabricated on glass wafers.[73]Perhaps the most ubiquitous example of glass as a microfabrication surface is its widespread use as a FPD substrate.[1-4]

Because of the importance of glass surfaces, decades' worth of studies focus on this topic.[29-30, 74-79] Glass surfaces are important to advancing glass science but are an under-represented research area.[26] Glass surfaces remain poorly understood compared to bulk glass composition and structure. Part of the reason for this knowledge gap is techniques that comprehensively

characterize bulk glass structure and composition are less applicable to surfaces. Techniques for bulk glass characterization include fourier transform infrared (FTIR) spectroscopy, Raman spectroscopy, and magic-angle spinning nuclear magnetic resonance (MAS-NMR), X-ray fluorescence (XRF), and X-ray diffraction (XRD), among others.[46, 80] While ion beam and X-ray techniques provide near-surface compositional information, they cannot probe glass network connectivity as well as these bulk techniques.

Glass surfaces pose unique analytical challenges. Silicate glasses are insulators, and sample charging hinders analysis with x-ray photoelectron spectroscopy, e-beam, and ion beam techniques.[74] Sample charging also causes charge-induced migration of some glass species, which perturbs the surface composition.[74] Knock-on effects also distort glass composition during sputter-depth profiling. Advances in instrumentation and methodology have addressed some of these issues.[74, 81]

Much of the interest and challenge in glass surface analysis is due to glass's lability. Glass surfaces typically vary from their bulk composition.[27, 67, 74, 77] Altered surface compositions are the norm, and surface compositions identical to bulk compositions occur only rarely. Production-line conditions alter surfaces during glass manufacturing. These alterations are especially evident in the float process, during which several environmental factors perturb glass surface composition. The glass comes into direct contact with water-cooled steel rollers, resulting in surface defects and water induced damage. A sulfur-dioxide atmosphere used during the float glass process creates a lubricious coating on the 'air' side of float glass melts. This coating reduces friction between the melt and the steel rollers used to draw it. Also, refractory materials from the glass furnace may fall on the glass, resulting in surface inclusions.[45] One side of the glass melt is in contact with the molten tin float bath. As a consequence, a tin-enriched layer up to several μm deep forms on this

side of the glass.[45, 82-85] Multiple studies observed significant differences in the reactivity and optical properties of the 'air' and 'tin' sides of float glass.[82-83, 86-87]

Species may preferentially segregate toward glass surfaces during melting and forming to minimize surface free energy. For example, antimony oxide preferentially accumulates at the surface of some alkaline-earth aluminoborosilicate glasses.[88] It follows that some species may also segregate away from the surface. This is the case for the tin-side of float glass, where a tin-enriched layer often occurs several microns below the glass surface, especially for iron-rich glasses. This effect is thought to be the result of differing redox conditions between the glass surface and its interior.[84-85]

Glass's thermal history influences its surface composition.[79, 89] An ion scattering spectroscopy study in which a binary alkali-silicate glass was heated *in situ* demonstrated these effects.[89] (Ion scattering spectroscopy is an alternate name for LEIS). In this study, a sodium silicate glass fracture surface was heated in situ and its elemental composition was measured by ion scattering spectroscopy. At room temperature, the glass composition was stable. Measurements at elevated temperatures below the glass transition temperature (T_g), however, showed decreased modifier concentration indicative of sodium evaporation from the surface. Measurements taken above T_g showed modifier concentration similar to the bulk concentration, suggesting sodium diffusion from the bulk of the glass toward the surface.[89] The formation of the tin-enriched layer below the surface of some float glasses also depends on the thermal history of glass. Higher temperatures favor diffusion of hydrogen through the glass melt, which affects the degree of tin enrichment and the depth of the layer.[85]

Aqueous solutions, acids, etchants, and atmospheric contaminants readily alter glass surfaces.[76-77] Hench and Clark described five basic types of silicate glass surfaces, shown

schematically in Figure 1.5.[77] In type I surfaces, a thin hydrated layer less than five nanometers thick forms on the glass surfaces without any dissolution of the silicate network or leaching of modifier ions. For type II surfaces, leaching of modifier ions results in a silica-rich surface layer that inhibits further corrosion of the underlying glass. This type of surface requires a glass with a low modifier concentration and high network connectivity. Type III surfaces occur in aluminosilicate and phosphosilicate glasses. Alumina-silicate and/or calcium-phosphate layers form on top of silica rich layers, resulting in glass with excellent chemical durability. These layers form through modifier leaching or precipitate from solution. Type IV glass surfaces have silica-rich layers, but the layer is porous and does not inhibit diffusion into and out of the underlying glass. As a result, it does not significantly inhibit glass corrosion. Leaching of modifier-rich glasses creates type IV surfaces. Type V surfaces result from congruent network dissolution. These surfaces have a composition approximately equal to the bulk composition. This type of surface may occur under controlled etching conditions, e.g., with HF or highly alkaline solutions.[77]

Local fluctuations in solution phase chemistry further complicate glass surface alteration. Local glass structure or environmental factors limit the diffusion between the glass and solution phase. For example, glass powders altered solution often suffer from local concentration cell effects.[76-77] As a result, these powders typically have different surface compositions than similarly treated planar shards. Deep scratches in glass surfaces also cause variations in solution-phase chemistry and will etch and corrode differently from smooth portions of the surface.[76-77]

Studies on nuclear glass waste storage have expanded knowledge of solution phase glass corrosion. Nuclear waste storage glass sequesters radionuclides from the environment over geological time spans by incorporating them into a corrosion-resistant glass network. This glass is known as known as high-level waste (HLW) glass.[59, 90-93] Archeological and geological glasses

provide evidence for the long-term chemical durability of glass, suggesting that it is a suitable vehicle for nuclear waste storage.[94-96] However, HLW glass will likely be in contact with groundwater during its radioactive lifetime. Therefore, it is important to understand the extent of radionuclide release into the environment via glass corrosion. This concern has prompted a wide range of experimental and computational studies. To promote collaboration between nations, standard glass compositions were introduced, including international simple glass (ISG).[90] ISG contains the same main oxides as French nuclear storage glass.[90]

HLW glass corrosion studies have divided glass corrosion into four kinetic regimes which are shown in Figure 1.6:(i) initial dissolution, (ii)rate drop, (iii) residual dissolution, and (iv) resumption of initial dissolution.[92] During initial dissolution, low starting concentrations of rate limiting species are in solution. Additionally, glass corrosion layers are not thick enough to limit diffusion between the glass and solution phase. These two factors create a very high initial corrosion rate. Ion exchange and hydrolysis are the main modes of glass corrosion during this phase. During the rate drop phase, accumulation of corrosion products in solution and the growth of a transport-limiting altered layer slows glass corrosion. Under static conditions, these processes eventually result in a low residual dissolution rate. However, corrosion abruptly resumes under certain conditions. For example, precipitation of zeolite phases from alumina-rich solutions results in reduced silica concentration in solution, which lead to an increased glass corrosion rate.[92]

Solution-phase glass alteration is complex and involves multiple processes. Glass composition, solution temperature, pH, internal and applied stresses to the glass, concentration of glass corrosion products in solution, and any additional solution phase species all influence glass corrosion mechanisms.[37, 76-77] Numerous studies have presented evidence for various modes of

glass corrosion. It is generally accepted that no single model can explain glass corrosion under every set of conditions.[97]

The classical interdiffusion (CID) model has been an important theory for explaining glass surface alteration for several decades.[98-99] CID describes glass alteration by two processes: (i) hydrogen interdiffusion and leaching of modifier species and (ii) dissolution of the silicate network. Interdiffusion dominates at low pH, resulting in type II, III, and IV surfaces. Network dissolution, in contrast, is rapid at pH values >10, resulting in more congruent network dissolution and type V surfaces.[77] However, interdiffusion occurs over a wide pH range, and the final surface composition depends on the relative rates of interdiffusion and network dissolution.[77] Early interdiffusion models focused only on extraction of the alkali elements and posited a concentration-dependent diffusion rate for these species.[98] Further refinements to these models added charge compensation consideration for the presence of alkaline earth modifier ions and alumina tetrahedra, which were not previously considered to participate in ion exchange.[77, 99] More recent work showed that alkali earth modifier ions participated in ion exchange with hydronium ions, albeit at a reduced rate compared to alkali earth ions.[97] CID often dominates during the early stages of glass corrosion. It was once thought that CID was relatively unimportant in later stages of glass corrosion. However, recent work revealed that CID continues even under conditions of silica saturation in the solution phase.[100] Given the CID model's importance for early-stage glass corrosion, it is probably the most important corrosion model for understanding the wet chemical treatments used in this work.

Recent studies have posited the interfacial-dissolution-precipitation model (IDP), that congruent dissolution of the silicate network may occur simultaneously with the growth of an altered layer formed by products precipitated from solution.[101] Precipitation occurs after a thin-

film of interfacial water becomes super-saturated with layer precursors. The interfacial water is assumed to have different solvating properties and higher concentrations of glass corrosion products than the bulk solution phase. These characteristics facilitate altered layer deposition at the dissolution interface. The IDP mode of glass corrosion works under near-neutral pH conditions and with solution phase silica concentrations well below saturation levels. We note, however, that the solutions used in the presented studies are for the most part either highly acidic or highly alkaline.

The chemical affinity model of glass corrosion describes glass corrosion in terms of differences in chemical potential between the solution phase and the bulk glass.[100] Such an approach greatly improves our understanding of long-term glass corrosion behavior under static corrosion conditions. It potentially falls short, though, for understanding short-term glass alteration in solutions with low concentrations of glass alteration products.

The formation of a gel layer during the initial phases of glass corrosion limits reactant transport to the unaltered glass surface in the passivating reactive interface (PRI) model.[102] This passivating layer governs corrosion kinetics. The passivating gel layer is thought to form via classical interdiffusion. However, recent work shows that the passivating layer may also contain elements from solution. These findings suggest that precipitation from the solution phase can play a role in forming the PRI.[102]

Altered glass surfaces are the norm rather than the exception. Therefore, understanding glass surface mediated processes requires direct measurement of those surfaces. For this reason, rather than using powdered samples, we focused our efforts on low-surface area planar samples and exposed them to chemical treatments representative of FPD production lines.

1.4 Glass Surface Composition Affects Surface Mediated Processes

Glass surface properties and processes depend on surface composition, including wetting, adhesion, contamination, and electrostatic charge buildup and discharge. These processes and properties are important for thin film deposition and device fabrication on oxide surfaces, and are especially important for FPD fabrication.[2, 5-6]

Surface hydroxyls play a governing role in the chemistry of glass and oxide materials.[11-13, 86, 103-104] Silanols are the most important class of hydroxyl on silicate glass surfaces. Other hydroxyls including boronols, aluminols, and hydroxyls associated with alkali-earth and modifier species may also be present. Silanols may be vicinal, geminal, or isolated.[16-17, 21] Silanols can be described as H-bonding silanols or non-interacting silanols. Isolated silanols may be isolated or geminal as shown in Figure 1.7.[16-17] On amorphous silica surfaces, approximately 60% of isolated silanols are geminal and 40% are isolated. H-bonding most often occurs for silanols in vicinal configurations.

Silanols have been studied on high-surface area amorphous silica powders using a range of techniques including infrared spectroscopy, temperature programmed desorption mass spectrometry (TPD-MS), thermogravimetric analysis, etc.[16-17, 21, 24, 105]. An infrared spectrum from a study by Hair and coworkers is shown in Figure 1.8. Here, amorphous silica powder surfaces have been thermally treated and/or chemically treated to produce surfaces with only isolated silanols, only H-bonded silanols, or to completely remove all surface hydroxyls. Bands corresponding to interacting and non-interacting silanols can be seen. Non-interacting silanols give a sharp band at 3747 cm^{-1}, while a broad band from ca 3700 to 3400 cm-^{1} corresponds to H-bonded silanols. The samples were heated *in vacuo* to remove physisorbed water prior to analysis. Correspondingly, there is no band for physisorbed water at ca. 3450 cm^{-1} in any of the spectra. The

diffuse nature of the interacting silanol band indicates a range of H-bonding environments exists on amorphous silica surfaces. Computational studies confirm this finding.[106]

Zhuravlev and coworkers published a widely accepted model of surface hydroxyls on silica surfaces based on measurements of over 100 amorphous silica powders using vibrational spectroscopy, temperature programmed desorption mass spectrometry, deuterium isotope exchange experiments, and thermogravimetric analysis.[21] They reported a least-squares average of 4.6 OH/nm^2 on a fully hydroxylated silica surface. This value agrees with early modeling studies based on cristobalite silica surfaces. TPD-MS experiments show several different dehydroxylation regimes. At temperatures below 200 °C, physisorbed water desorbs from the sample surface, but silanols do not condense to form bridging oxygens. At temperatures between 200 °C and 400 °C, vicinal silanols condense to form bridging oxygens, leaving a surface with mostly isolated silanols. These changes are reversible upon re-exposure to water. Treatment at higher temperatures further dehydroxylates the surface through a process of proton migration. The changes are increasingly non-reversible as heat-treatment temperature increases.[21] Other studies proposed that strained siloxane bonds form during heat-treatment between 200 °C and 400 °C, but exposure to higher temperature allows the surface to remodel, relieving strain in the siloxane bonds and reducing their reactivity.[11-12] Amorphous silica surfaces treated at 1100 °C are completely dehydroxylated.[21] These surface have only bridging siloxane bonds and are moderately hydrophobic. Rehydroxylation for these surfaces is an activated process and can take years at room temperatures. However, hydrothermal treatment, i.e., boiling the powder in deionized water, can rapidly restore it to a fully-hydroxylated state.[21] Various chemical treatments can also hydroxylate silica surfaces, including strong acids/oxidizers like HCl or piranha solution, or etching with hydrofluoric acid or strong bases.[11]

High surface-area silica nanopowders are the most common sample system for studying surface hydroxyls. However, additional challenges arise when measuring surface hydroxyls on low-surface area samples.[10, 13] The introduction to Chapter 4 includes a more detailed literature review on this topic.

Surface hydroxyls are often the target of surface modification reactions.[107-108] Organic moieties are frequently reacted with glass surfaces to modify their surface properties.[29-30, 48] These surface modifications are essential in tailoring glass interfaces for thin film adhesion. Organic surface modification reactions are also used in several applications, including anti-corrosion coatings, anti-scratch and antiwear coatings, anti-friction coatings, antimicrobial coatings, and chemical sensing devices.[71-72, 109-110] A range of reactive functions can be used to modify oxide surfaces, including silanes, phosphonates, carboxylates, catechols, alkenes, alkynes, amines, thiols, hydroxamic acids, and borates.[111] Silanes are typically used for SiO_2 surfaces. Silanes and carboxylates are frequently used to tailor reactive interfaces on multicomponent glasses.[111] Phosphonates form relatively weak bonds to SiO_2 surfaces but strong bonds to alumina and several other metal oxides.[111]

Besides being the target of surface modification reactions, surface hydroxyls govern a number of other processes on glass surfaces. They are important adsorptive and reactive sites. Non-interacting silanols are the most effective adsorptive and reactive sites for most organic molecules. They are particularly strong adsorptive sites for molecules with lone pairs. H-bonded silanols only weakly adsorb most organic molecules.[17] OH containing compounds like water and methanol, however, adsorb on H-bonded silanols. Water, in particular, adsorbs strongly and preferentially to H-bonded silanols.[17]

As important adsorptive sites, surface hydroxyls mediate the physisorption and chemisorption of water. Computational and spectroscopic studies have demonstrated that water H-bonds in different orientations to interacting and non-interacting silanols, with adsorption preferentially occuring on H-bonded silanols.[106, 112] The strength and orientation of the H-bonds relative to the sample surface influences their effectiveness as adsorptive sites.[106] Water first physisorbs to H-bonded silanols, and then the physisorbed water acts as an adsorptive site for additional water.[112] The physisorption of water is also important in forming surface hydroxyls. Rehydroxylation of silica surfaces occurs autocatalytically. In the first step, water physisorbs at surface hydroxyl sites. In the second step, that water reacts with neighboring siloxane bonds to form additional hydroxyls. Accordingly, rehydroxylation occurs by islanded growth.[21]

Water physisorbed on glass and oxide surfaces alters their physical properties. This physisorbed water is an important adsorptive and reactive site in and of itself. It is important for charge transport on oxide surfaces, such that charge build-up and discharge is a function of surface hydroxylation and relative humidity.[6, 66] A thin layer of physisorbed water can also act as a solvent, promoting corrosion for some glass compositions.[113] Notably, some glass artifacts readily corrode as network modifiers dissolve in physisorbed water on the glass surface, resulting in a high-pH solution that can hydrolyze bonds in the silicate network.[114-115] Physisorbed water on glass surfaces can absorb atmospheric gasses, including CO_2, SO_2, and NO_2. These gasses can alter the pH of the water layer on the glass surface and affect the composition of the weathering layer that forms.[115] Physisorbed water can also participate in surface modification reactions. In some cases, the presence of physisorbed water catalyzes surface modification reactions, while in others, it acts as an interfering species.[107-108, 116]

As a key adsorptive site, surface hydroxyls play an important role in surface contamination and thin film adhesion. Highly-hydroxylated surfaces usually promote thin film adhesion. Paradoxically, hydroxylated surfaces also contaminate quickly, and this adventitious surface contamination impedes thin film adhesion. In a series of studies on multi-component glasses, sputtered metal-oxide films, and sputtered metal-doped silica films, Takeda and coworkers found that the most hydroxylated surfaces contaminated the most severely over a period of 14 days, as indicated by increased water contact angles.[86, 103-104]

Hydroxyls are important in electrostatic charge accumulation and discharge. Hydroxyls are important charging sites on glass surfaces, especially when in contact with aqueous solutions.[117] Hydroxyls are thought to play a role in contact electrification.[6] Surface contamination and particulates promote electrostatic faults in microfabricated circuits.[2, 4, 66] However, thin, adsorbed layers of hydrocarbon on glass surfaces can also reduce contact electrification.[6]

The reactivity and hydroxylation behavior of multicomponent surfaces is significantly more complex and less-understood than for silica surfaces. Takeda's studies suggest that adding only a few atom percent of a metal dopant to a silica surface can radically increase its surface hydroxyl density.[104] More electropositive dopant metals (e.g., zirconium) promoted hydroxylation more effectively than relatively electronegative dopants (e.g. aluminum).[103-104] Likewise, he showed that the number of hydroxyls at multicomponent glass surfaces varied according to glass composition. The number of surface hydroxyls generally scaled with the quantity of silicon at the sample surface. A notable exception to this trend was the tin-rich side of float glass, which had the most hydroxyls of any sample in the study, in spite of its relatively low silica concentration.[86] Multicomponent glass surfaces are likely to have multiple types of hydroxyls, including aluminols, boronols, and in the case of float glass, Sn-OH moieties.[86, 118-119] Boronols have been shown to

play an important role in adsorption on multicomponent glass surfaces and have different adsorptive behavior depending on the identity of modifier ions in the glass.[119] In addition, boronols may interact with and alter the reactivity of neighboring silanols. Hair and coworkers demonstrated that the addition of boron to silicon surfaces altered the reaction rate between silanols and chlorosilanes.[16] While these other hydroxyls are known to play a role in glass surface reactivity, they are not as well-studied as silanols. Few studies exist for these hydroxyls in relatively simple model systems, and it is difficult to address their potentially complex interactions on multicomponent surfaces.[16, 79, 119]

In addition to surface hydroxyls, multicomponent glasses include reactive functions that are not present in simple oxide materials. In particular, non-bridging oxygens and modifier ions influence multicomponent glass reactivity. Two notable studies examined bonding of carboxylic acids on silica surfaces and sodium borosilicate glass surfaces. Carboxyl functions are often used to link sizing agents to glass fiber surfaces.[29-30] These studies showed that carboxylic acids bind to silica surfaces through silyl-ester linkages. There was no evidence of silyl-ester bonds on the sodium borosilicate surface. Rather, the carboxylic acids bonded preferentially to sodium ions by forming sodium carboxylates. Interestingly, no silyl-ester bonds could be observed on the multicomponent glass surfaces even when they were leached with acid to remove sodium from the surface prior to treatment with carboxylic acids. Aged sodium borosilicate surfaces displayed additional complexity. Carbonate corrosion products often form on multicomponent glass surfaces with exposure to atmospheric water vapor. These carbonates react with the acetic acid probe molecules to produce water and CO_2, such that no covalent bond was formed between the acetic acid and the glass surface. Accordingly, corrosion products at the glass fiber surfaces can impede surface modification reactions.[29-30]

1.5 Surface Analytical Techniques for Glass

There are many approaches for performing surface analysis on glass. The technique used depends on the form-factor of the glass available and the desired information. We have already made special mention of secondary ion mass spectrometry, x-ray photoelectron spectroscopy, low energy ion scattering, and spectroscopic ellipsometry. Given their direct importance to this work, we will provide a detailed discussion of each of these techniques. Other approaches for characterizing glass surfaces will also be briefly reviewed.

1.5.1 Secondary Ion Mass Spectrometry of Glass Surfaces

Secondary ion mass spectrometry provides both molecular and elemental information about glass surfaces. SIMS depth profiles appear often in glass analysis, showing the distribution of species in altered layers in corroded glass.[120] These have been especially important in HLW glass corrosion studies, studies on the conservation of glass art and artifacts, and in elucidating the underlying mechanisms of glass corrosion.[101, 115, 120] Most static SIMS studies on glass focus on adsorbates on glass surfaces but few focus on the glass itself. One study proposes an approach using XPS and SIMS data to measure chain length in zinc-phosphate glass.[121] Importantly for this work, SIMS has been proposed as a technique for quantifying surface hydroxyls on oxide materials, and SIMS depth profiling is also used for quantifying bulk water- and hydrous-species concentrations in minerals and oxide materials.[10-13, 118, 122-126] These efforts are discussed in more detail in the introduction to Chapter 4.

1.5.2 SIMS Theory and Instrumentation

Secondary ion mass spectrometry (SIMS) probes a sample surface with a beam of primary ions with energies typically on the order of 10-30 keV. In a few cases, neutrals are used instead of ions. Common primary ion beams include O^+, Cs^+, Ga^+, Bi^+, Bi_3^+, and Bi_5^+.[34, 40, 127] More recently, a range of SIMS cluster sources including C_{60}^+ and argon clusters have improved SIMS ion yields and enabled low damage depth profiles for some material.[40] When primary ions impact the sample, they initiate a collision cascade or thermal spike that sputters material from the sample surface.[34, 40] A fraction of these particles are ionized and can be analyzed by mass spectrometry. SIMS can either be performed at low ion doses, i.e., in static mode, or at high doses, i.e., in dynamic mode. Static SIMS is typically performed at an ion dose below 1×10^{13} ions/cm^2. At these low doses, there is a low probability that any ion will strike a spot on the surface that has previously been altered by ion impact. As a result, each ion strike analyzes a pristine surface unaltered by sputter damage.[34] Static SIMS can provide detailed elemental and molecular information about a sample surface. In contrast, dynamic SIMS operates at a high ion dose, resulting in erosion of the sample surface. By continuing eroding and analyzing the surface, dynamic SIMS can provide a compositional depth profile of a sample's near-surface region. The high ion dose in dynamic SIMS results in an altered layer at the sputter-etch front arising from ion beam damage, preferential sputtering, and knock-on and charge-induced species migration, among other effects.[40] This sputter-altered layer can extend *ca.* 20 nm into a material, and an equilibration period is needed for this altered layer to reach a steady-state composition before quantitative information can be obtained from it.[40] The sample damage inherent to dynamic SIMS has traditionally limited its use

to obtaining elemental compositional information.[34, 40] However, molecular information can also be obtained due to recent advances in cluster ion sources.[40]

The most common types of mass spectrometers used in SIMS are quadrupole, sector, and time-of-flight mass spectrometers.[34, 127] In principle, each of these instruments can be used for static or dynamic SIMS. Each of these geometries has unique advantages, with sector and quadrupole instruments being especially well-suited to high sensitivity and/or high depth resolution depth profiling experiments.[127] Time-of-flight instruments offer parallel detection of all ions of a given polarity and can provide excellent resolution, ca. m/Δm of 10,000 in some cases. These features make them especially well-suited for static-SIMS analysis.[33-34]

Only ToF instruments are used in this study and will be the focus of the remainder of this discussion. Figure 1.9 shows a schematic representation of common instrument geometry found in ToF-SIMS instruments. The analysis cycle starts with a short pulse of the primary ion beam, typically at oblique incidence to the sample surface, during which secondary ions sputtered from the sample surface are extracted at normal incidence into a time-of-flight mass analyzer. Extraction voltages in the range of 2-3 keV are typical for the instrumentation used in this study. Ion optics for focusing the primary beam, centering it through apertures, and rastering it across the target are essential components of most ion sources. Additional raster and focusing optics are included in the ToF analyzer for focusing the secondary ions and directing them toward the detector.

The relationship between mass and time-of-flight for a given species is easily derived from the equation for kinetic energy, $E_k = \frac{1}{2} mv^2$, where $\underline{E_k}$ is kinetic energy, m is mass, and v is velocity.[34] Here, the ion's charge, q, and the extraction voltage used to accelerate ions into the ToF analyzer, U, govern the kinetic energy of ions in ToF-SIMS. The ions' velocities can be calculated from their kinetic energy. The time required for an ion to traverse the flight tube in a ToF analyzer

is given by $t = d/v$, where d is the length of the flight path and v is the velocity of the ion. Combining the equations for time and kinetic energy and solving them for mass, we have Equation (1.1):

(1.1) $m = \frac{2qUt^2}{d^2}$

The mass of ions can be calculated by measuring their time-of-flight. In practice, the kinetic energy of ions can be influenced by sample charging, and the distance of the flight path through the analyzer may vary depending on reflector voltage settings, as discussed in further detail below.[34] Consequently, the mass scale in ToF-SIMS spectra is usually calibrated by identifying several peaks. Peaks from adventitious hydrocarbons are often present on samples and can be helpful in this process. *A priori* knowledge of a sample's elemental composition may be a further aid, as SIMS is a relatively hard-ionization mass spectrometry and produces strong atomic signals in addition to molecular fragments.[40, 127]

ToF analyzers measure mass under the idealized assumption that all ions enter the analyzer at the same time (T_0) and have the same kinetic energy (E_0), which is mostly governed by the extraction voltage. T_0 is assumed to be the time at which a pulse of primary ions strikes the sample surface. In practice, distributions in T_0 (ΔT_0) result from the finite width of the primary ion pulse and from a finite distribution of secondary ion sputter and ionization times after the collision cascade process has been initiated. Ions may also sputter from the surface with different initial kinetic energies.[34] Sample charging may influence the ions' kinetic energy.[34] Sample roughness can also impact mass resolution.[34] These factors result in a distribution of initial energies (ΔE_0). In turn, ΔT_0 and ΔE_0 determine the mass resolution of ToF-SIMS instruments.

Primary ion beam pulse width is a contributor to ΔT_0, and it influences instrument mass resolution. Some ion beams include bunchers to generate ion pulses with high currents and narrow temporal widths. For applications requiring high mass resolution, buncher elements apply an

electrical field along the longitudinal axis of the ion pulse to compress the ions, resulting in narrow temporal distributions of primary ion impact at the sample surface.[34] Bunchers can reduce primary ion pulse widths dramatically. Pulses that are tens of nanoseconds wide can be reduced to a few picoseconds.[34] This narrow pulse width is key to obtaining high mass resolution in ToF-SIMS. However, narrow primary ion pulse-width comes at the expense of spatial resolution.[34] Lateral resolution for liquid metal ion gun (LMIG) primary ion sources in high-current bunched mode is ca. 7 μm, while lateral resolutions of < 70 nm are possible in un-bunched mode.[34, 40]

Distributions in kinetic energy of the sputtered secondary ions are an important contributor to ΔE_0. Not all species follow the same kinetic energy distribution. Elemental species can have energies as high as 100 eV. Molecular ions and small clusters follow lower kinetic energy distributions, typically ranging from 0-20 eV.[34, 127] These energies are relatively small compared to the extraction energies used in ToF-SIMS. However, they result in a distribution of flight times for a given species and correspondingly degraded mass resolution.

Reflectors in ToF analyzers improve mass resolution in two ways. First, they effectively double the length of the flight tube, which enhances the difference in flight time between species of different masses. Second, they provide a variable flight path to compensate for ΔE_0.[34] A schematic representation of a reflector ToF analyzer is shown in Figure 1.10, with hypothetical flight paths for ions of different energy represented by different colored lines. Ions with low kinetic energy only penetrate a short distance into the reflector element, resulting in a shorter overall flight path, while ions with higher kinetic energy penetrate further into the reflector, having a longer overall flight path. Varying their flight length to compensate for differences in velocity focuses their arrival time at the detector, improving mass resolution. The reflector has an additional important function, which is to set the analyzer acceptance energy, i.e., the maximum initial energy

an ion can have before it is no longer focused onto the detector.[34] The importance of analyzer acceptance energy and its potential impact on quantitation of SIMS data is discussed in more detail in the context of the surface hydroxyl measurements performed in Chapter 4.

1.5.3 SIMS Surface Sensitivity

SIMS is among the most surface-sensitive analytical techniques, having better surface sensitivity than XPS and Auger electron spectroscopy (AES) but lower surface sensitivity than LEIS. Most sputtered species in SIMS originate from the outer monolayer.[33, 127] Values given for SIMS surface sensitivity vary widely depending on source, and computational studies have shown that the actual depth depends on a number of factors. Sample composition, primary ion species, energy, and angle of incidence all influence SIMS surface sensitivity.[33-35, 130] Finally, the maximum depth from which an ion can originate depends on its kinetic energy, with higher-energy ions originating from a greater sample depth.[131]

1.5.4 Quantitation in SIMS

A common misconception is that SIMS is not quantitative due to matrix effects. Provided that a suitable reference material is available, SIMS can provide both precise and accurate quantitation, and experiments have demonstrated long-term stability in instrument response.[34, 127] Dynamic SIMS is used quantitatively more often than static SIMS, given that reference materials based on known bulk compositions can be used.[127] Alternatively, reference materials can be created by ion implantation, where a known ion dose is implanted to known depth within a matrix

of interest.[127] Finding suitable reference materials for quantitative static SIMS is more challenging because composition at the extreme outer surface of a sample can vary in unpredictable ways from the bulk composition and because adventitious contaminants present at the surface can have an unanticipated impact on ion yield. Accordingly, it is difficult to ascertain that a chosen reference material is truly representative of the sample matrix at the extreme surface of a sample. For the cases where we have attempted quantitation of the static SIMS results presented herein, we have used glass fracture surfaces as our reference materials, under the assumption that they closely reflect glass bulk composition. There is precedent for using glass fracture surfaces to establish SIM relative sensitivity factors in dynamic SIMS.[132-134] Fracture surfaces represent an idealized glass surface, are also used to establish elemental sensitivity factors for XPS and auger electron spectroscopy (AES) studies of glass surfaces.[14-15, 135]

The matrix effect in SIMS arises from the complexity of the SIMS ionization process. The following processes may participate in SIMS ionization:[127]

1. Electron Impact

2. Atom Impact

3. Surface Ionization

4. Charge Transfer

5. Thermal Ionization

Species in SIMS are in intimate contact with one another prior to ionization and may react with each other in unpredictable ways. Matrix species and even adventitious hydrocarbon contaminants can impact ion yields, such that signal may not vary linearly with concentration for a given species. Matrix effects can result in either suppression or enhancement of selected signals. Suppression can result when an ion reacts with matrix constituents to form a neutral species.[118] Signal enhancement

can result if matrix species act as a proton donor for a species of interest.[40] Adventitious hydrocarbon attenuates signal from the underlying sample.[131] However, the effect is kinetic-energy dependent, such that not all signals are affected to the same degree. Ions sputtered with high kinetic energy i.e., elements and small clusters, are less attenuated than ions with low kinetic energy, i.e., large clusters and molecular ions. Therefore, adventitious hydrocarbon contamination may skew quantitative results.[131]

In some cases, matrix effects are used advantageously. Oxygen at the sample surface promotes the formation of positive ions. Consequently, O_2^+ beams have become the ion source of choice for performing positive ion SIMS depth profiles.[127] However, under most circumstances, matrix effects remain detrimental to SIMS quantitation. There is currently no theoretical model of SIMS ionization that can fully account for matrix effects.[34, 127] Therefore, any reference material used in SIMS must closely match the matrix composition of the samples of interest.[34, 127] In the absence of a good reference material, SIMS data is best interpreted semi-quantitatively.

1.5.5 Data Reduction Tools for ToF-SIMS

ToF-SIMS spectra may contain thousands of peaks.[136-137] The data are even more complex in SIMS images where each pixel contains an entire mass spectrum.[136-138] Therefore, SIMS data reduction can pose a significant challenge. In spite of the spectral complexity, a skilled analyst can provide insight into sample composition by a manual analysis of the peaks.[136] A growing range of data analysis tools are now routinely used to consider the data from a multivariate perspective. These include principal components analysis (PCA) and multivariate curve resolution (MCR), among others.[136, 139-140] PCA plots the data on a set of eigenvectors that optimally capture the

variance in the data. In the parlance of PCA, these eigenvectors are known as principal components (PCs). The eigenvectors consist of a linear combination of the original variables. The projections of the original variables on to the PCs are known as loadings. The samples are then plotted in this optimized coordinate system. The sample's projections onto each of the eigenvectors are known as their scores.[141] More detail about the algorithms used for PCA can be found in a recent review article.[142]

The major advantage of using PCA is that it can dramatically reduce the dimensionality of a data set. This makes it much easier to consider the relative similarity or difference between samples and to identify outliers in a data set. For example, the SIMS data sets in this work contain over 1,000,000 data points each, and in the extreme case, the full-rank data could be plotted as a data point in 1,000,000 degree hyperspace. More practically, if we consider the data in terms of the number of peaks present, or even if we use a reduced set of selected peaks, a SIMS data set may still have hundreds of dimensions to consider. However, it is unlikely that all of these peak intensities vary independently. Rather, they are likely to vary in some correlated fashion. These correlations are naturally discovered when the data is plotted in PC space, and data sets with a high number of variables can often be plotted in simple 2- or 3-dimensional plots after PCA. This simplifies data interpretation, making it easy to identify outliers, visualize which samples are similar to one another, understand the spectral vectors along which samples vary, and identify subtle spectral variations between samples.[136]

One disadvantage of PCA is that PCs must be orthogonal to one another. This is a necessary component of the algorithm. However, most chemical variance in a spectrum is not truly orthogonal. For example, hexane and pentane give very similar IR spectra even though they are different compounds, and it would be inappropriate to perform PCA on spectra from a mixture of

pentane and hexane and ascribe one of the PCs to pentane and another to hexane. In most instances, it is best to think of the PCs, scores, and loadings as useful mathematical abstractions. They can be helpful for determining if a given sample is rich in certain spectral components, but PCs may not correspond to unique chemical compounds.

We have largely used PCA as a preliminary analysis in our work. It is a useful tool for determining the minimum dimensionality of a data set and understanding trends in the data prior to performing follow-up analysis either by manual peak integration or with other algorithms including multivariate curve resolution.

Multivariate curve resolution (MCR) is similar to PCA in that it plots the data on a small number of spectral vectors that are derived by an algorithm. Unlike PCA, these spectral vectors are not required to be orthogonal to one another. Thus, it is a less-constrained form of data fitting than PCA. The spectral vectors are derived via a process of alternating least squares (ALS), as described in more detail in the introduction to chapter 2. The resulting vectors often closely resemble real spectra.[143] MCR and other ALS algorithms have successfully derived the spectra of pure components in chemical mixtures in many instances.[144-145] MCR requires the user to specify the number of spectral components to derive, and preliminary analysis with PCA can provide a useful starting guess. [144]

1.6 XPS Analysis of Glass Surfaces

XPS is widely used for glass analysis, especially in analyzing altered layers on glass and in analyzing adsorbates on glass surfaces.[14-15, 29-30, 86, 103-104] XPS analysis has demonstrated different bonding chemistries between adsorbates and fused silica, pristine multicomponent glass

surfaces, and weathered multicomponent glass surfaces.[29-30] Recent efforts used elemental information from XPS to estimate the number of bridging oxygens, non-bridging oxygens, and surface silanols at multicomponent glass surfaces. Surface hydroxyls on glass and silica have also been analyzed using a chemical derivatization/XPS approach, where the hydroxyls are tagged through reaction with a fluorosilane, amine, or other appropriate molecules, and the total quantity of reactive groups is estimated through XPS analysis.[86, 103-104]

1.6.1 X-ray Photoelectron Spectroscopy Theory and Data Analysis

XPS is among the most widely used surface analytical techniques due to its surface sensitivity, minimal sample preparation requirements, and straightforward quantitation.[146] XPS is based on the photoelectric effect. In XPS, a material is bombarded with X-rays. When X-rays interact with atoms at the sample surface, they can dislodge core-level electrons. An appropriate analyzer measures the the kinetic energy of the photoelectrons, and the core-level binding energy of the electron is calculated according to Equation (1.2),

(1.2) $\quad E_{Photon} = E_{kinetic} + E_{binding} + E_{work}$,

where $E_{kinetic}$ is the measured kinetic energy of the photoelectron, E_{photon} is the energy of the photon used to excite the photoelectric transition, $E_{binding}$ is the core-level binding energy, and E_{work} is the work function of the instrument. Note that work function term only applies for conducting samples, given that their work function will align with the work function of the instrument when the two are in electrical contact. For electrically isolated samples, peak positions in XPS will shift depending on the voltage at the sample surface. This can be accounted for by adjusting the entire

energy scale based on a reference peak. Adventitious carbon is present on most samples and can be used for this purpose.

The binding energies of core electrons are characteristic of their elements of origin. Generally, core electron binding energies scale with the nuclear charge Z of their corresponding atoms. They also increase with the decreasing principal quantum number n.[146] Elements in the sample are identified by comparing photoelectron peaks in XPS spectra to tabulated or calculated photoelectron binding energies. The peak areas of photoelectron transitions for a given element are proportional to its concentration at the sample surface.

Minor shifts in core level binding energies in XPS also provide information about the elements' chemical environment.[146-147] The partial-charge formalism often used in introductory chemistry can explain this effect. The electron density of an atom emitting a photoelectron is influenced by the electron-donating or -withdrawing properties of nearby atoms. The effect is most pronounced for atoms directly bonded to the atom of interest and much weaker for second-nearest neighbors. Electron-donating neighboring atoms will increase the electron density for the atom of interest, reducing coulombic attraction between the atom and the escaping photoelectron. The resulting photoelectron peak will appear at a lower binding energy than for an atom of the same species with no partial charge. The effect is reversed for an atom bonded to electron-withdrawing neighbors, which results in a partial positive charge on the atom of interest, increased coulombic attraction between the photoelectron and its parent atom, and a photoelectron peak appearing at higher binding energy compared to an atom with no partial charge. This effect is easily visualized in the high-resolution XPS spectrum of the Si 2p photoelectron transition for silicon oxide on silicon shown in Figure 1.11. The photoelectron peak for silicon oxide appears at higher binding energy than the peak for silicon in its unoxidized state.

Peak widths in XPS depend on instrumental resolution and on several sample-dependent parameters.[146] Instrument resolution depends on the line width of the X-ray emissions used to excite photoelectron transitions and the energy resolution of the analyzer used to measure photoelectron energy. The intrinsic photoelectron line width is influenced by factors causing a distribution of energies in the initial core-level binding energies and distributions in energies of the final core-hole states. In general, crystalline samples, where atoms throughout the sample are in well-defined chemical environments give relatively narrow Lorentzian photoelectron transitions. Atoms in amorphous materials, where a distribution of bond angles, lengths, and chemical environments result in a broader, more Gaussian photoelectron transition. For example, In Figure 1.11, the width of the oxide peak is wider than for unoxidized silicon.

The Si 2p peak in Figure 1.11 for unoxidized silicon is resolved into a doublet with a 2:1 peak area ratio. This is due to spin orbit splitting, where core-level electron energies are influenced by magnetic effects stemming from interactions between the electron spin of the electron and the motion of the electron around the atom's nucleus. Two degenerate core-level states result for all transitions with a value greater than 0 for the quantum number l.[146] The peak area ratio for the peaks in doublet depends on the number of electrons in each of these degenerate states, with a 2:1 ratio for p-transitions, a 3:2 ratio for d-transitions, and a 4:3 ratio for f-transitions. The energy separation between the doublets generally increases with Z.[146]

XPS is a surface sensitive probe.The surface sensitivity of XPS is a result of electrons having a relatively short inelastic mean-free path (λ) through materials.[146] For laboratory scale XPS instruments operating with Al or Mg anodes as X-ray sources, typical λ on the order of 2-3 nanometers are typical. Lower kinetic energy photoelectrons have shorter mean free paths than the higher energy ones. λ is also a function of sample composition. The depth of analysis of XPS

instruments is usually cited as 3λ, but this fails to communicate some of the underlying complexity. Electron attenuation through a material can be expressed in terms of Beer's law, Equation (1.3),

$$(1.3) \quad I = I^0 e^{-d/\lambda cos\theta}$$

where I is photoelectron intensity after attenutation and I^0 is the unattenuated photoelectron intensity of a layer of atoms at depth d is the depth within the sample measured normal to the sample surface.[149] Photoelectron intensity attenuates exponentially as a function of pathlength through a material. Approximately 63% of total photoelectron intensity originates within 1λ of the sample surface, approximately 86% originates with 2λ, and approximately 95% originates within 3λ.[146] Because lambda is a function of photoelectron energy, not all electrons have the same surface sensitivity. In addition, quantitative results for XPS may be influenced by differential attenuation of photoelectrons with different kinetic energies.[146] Corrections exist to account for differential signal attenuation by adventitious hydrocarbon overlayers.[150] These corrections are nearly negligible for samples with <15 at. % of carbon.[150] However, they become significant if the hydrocarbon overlayer is thick or there is large energy difference between the photoelectron transitions used for quantitation.[150]

XPS is inherently quantitative. Photoelectron intensity is proportional to elemental concentration. Most commonly, concentrations are expressed in terms of atom percentage. Each photoelectron transition has a unique photoemission cross-section, and relative sensitivity factors are required. These are often provided by instrument manufacturers based on analysis of appropriate reference materials. Alternatively, they can also be calculated based on theoretical considerations, as from Schofield's tables. In addition, sensitivity factors include corrective terms to account for the transmission function of photoelectron energy analyzers and may include terms to account for differences in mean-free path of photoelectrons through materials as a function of

their kinetic energy. Once sensitivity factors have been established, the atom percentage for a given species can be expressed according to Equation (1.4),

(1.4) $C_a = (I_a/F_a)/(I_a/F_a + i_b/F_b + I_c/F_c ...) \; x \; 100$

where C_a is the atom percentage of the species of interest, I is the photoelectron transition intensity, F is the sensitivity factor, and the subscripts a, b, c… denote species present in the sample. Here, all elements in the sample must be accounted for. Otherwise, the quantitation only provides relative ratios of the species included in the calculation.[146]

The manufacturer-provided sensitivity factors often provide relative quantitation accurate to within 10%.[146] Greater accuracy is possible if reference materials are used to derive sample-specific sensitivity factors. Glass fracture surfaces are the preferred reference material for glass surface analysis. Accurate sensitivity factors can be derived by obtaining XPS spectra from glass fracture surfaces and assuming that their composition is equivalent to the known bulk composition of the glass, as verified2 by a suitable referee technique like X-ray fluorescence or inductively-coupled plasma mass spectrometry.[14-15]

1.6.2 XPS Instrumentation

In lab scale instruments, like the one represented schematically in Figure 1.12, X-rays are generated by shooting an electron beam at a metal anode, most commonly Mg or Al for non-monochromated X-ray beams and Al for monochromated X-ray beams. Quartz crystals are commonly used to generate monochromated beams for Al k_{alpha}, Ag l_{alpha} X-rays because the lattice spacing between quartz $I0\bar{1}0$ planes corresponds to integer numbers of wavelengths for these X-rays at ca. 78.25° angles of incidence. Monochromated beams simplify XPS analysis by

eliminating multiple peaks that result from multiple exciting X-ray wavelengths. In addition, monochromators are a focusing element, providing bright and relatively small X-ray spots.[146]

XPS instruments commonly use electrostatic concentric hemispherical spherical analyzers (CHA), as shown in Figure 1.12. These analyzers act as an energy filter, allowing only photoelectrons of a specified kinetic energy, i.e., pass energy, to reach the detector. The pass energy is determined by the ratio of voltages between the outer and inner electrodes in the HSA. HSA energy resolution is a function of pass energy. Accordingly, HSAs are most often operated at fixed pass energies, and the range of photoelectron energies is scanned by adjusting voltages to retarding fields prior to the analyzer.[146]

1.7 Low Energy Ion Scattering for Glass Surfaces

Low Energy Ion Scattering (LEIS), also known as ion scattering spectroscopy (ISS), is a less prevalent technique than either XPS or SIMS. However, a few notable studies have used this technique to analyze glass.[89, 151-153] One important study demonstrated that amorphous silica surfaces are oxygen-terminated.[151] In contrast, sodium preferentially terminates the surface of sodium silicate glasses, presumably to minimize surface free energy by shielding negatively charged oxygens.[151] Another study used LEIS to analyze the surface composition of sodium silicate glasses as a function of temperature.[89] At elevated temperatures below the glass transition, modifier ions evaporated from the surface, leaving a sodium poor/silica rich surface. At temperatures approaching Tg, sodium ions migrated from the bulk to the surface, giving a composition equivalent to bulk fracture surfaces analyzed at room temperature.[89] These studies are discussed in more detail in Chapter 3.

1.7.1 Low Energy Ion Scattering Theory and Instrumentation

LEIS probes sample surfaces with a beam of low-energy ions with energies typically from 1-10 keV.[28] These atoms backscatter after colliding with atoms at the sample surface. The energies of the backscattered ions are measured using an appropriate analyzer, e.g., CHA or double-toroidal analyzer (DTA). The energies of the backscattered ions depend on their initial energy, their angle of incidence, and the mass of the elements from which they backscatter. The governing equation of LEIS Equation (1.5):[28]

$$(1.5) \quad E_S = k \cdot E_P = \left(\frac{\cos\Theta + \sqrt{\left(\frac{M_S}{M_P}\right)^2 - \sin^2\Theta}}{1 + \frac{M_S}{M_P}} \right)^2 \cdot E_P, \ \frac{M_S}{M_P} \geq |\sin\Theta|.$$

Here, E_s is the energy of the backscattered ion, E_p is the energy of the primary ion, Θ is the angle of backscattering, M_s the mass of the analyte surface species, and M_p is the mass of the particle. Accordingly, LEIS identifies elements by their mass. Resolution in LEIS depends on several factors, including the mass of the species analyzed, the mass of the probing ion, the angle through which backscattering occurs, and the angular acceptance ($\Delta\Theta$) of the analyzer. Wide analyzer angular acceptances give good sensitivity but poor mass resolution, while low angular acceptances give high mass resolution and low sensitivity.

LEIS is the most surface-sensitive analytical technique used in this study. In principle, LEIS can be performed with any ion source, but noble gas ions are preferred because they have a high neutralization cross-section. Only noble gas ions backscattered from the outermost atomic layer have a short enough interaction time with the sample to avoid neutralization.[28] Accordingly,

LEIS analysis performed with noble gas ions analyzes the elemental composition of the outermost atomic layer of the sample.

Quantitation in LEIS is straightforward. Peak areas in LEIS scale linearly with the surface coverage of elements.[28] Quantitation requires the use of reference materials. In the case of oxide materials, it is often assumed that the peak area of the metal species scales linearly with their corresponding oxide. A sample that has 10% SiO_2 surface coverage gives 10% of the silicon peak area as a pure SiO_2 reference material. Response is dependent on the primary ion beam energy and identity, so it is imperative that reference materials be analyzed under the same conditions as the unknown samples. LEIS is relatively insensitive to sample roughness, such that pressed powder pellets can often be used as reference materials.

The double-toroidal analyzer, (DTA) represented schematically in Figure 1.13, is an important advance in LEIS instrumentation.[36, 42-44] This analyzer collects ions through nearly a 360 degree azimuthal angle while maintaining a low $\Delta\Theta$. This analyzer provides improved mass resolution and ca. 3 orders of magnitude improvement in sensitivity over LEIS instruments using CHAs.[28] Commercially available instrumentation using this analyzer has only recently become available. This advance in LEIS instrumentation has enabled some of the conclusions in this dissertation, providing the mass resolution necessary to separate resolve and quantify Al and Si at the outermost atomic layer of our samples.

We have authored a review article giving a practical introduction to this technique, which provides more discussion of theory and applications of LEIS analysis.[41] It is included as an appendix to this dissertation. An even more in-depth discussion of LEIS theory can be found in Brongersma's 2007 review article.[28]

1.8 Other Techniques for Glass Surface Analysis

A range of other techniques are used for glass surface analysis. Rather than attempt a comprehensive review, we will mention some of the studies that have been influential to this work.

Infrared spectroscopy is used extensively in glass analysis, though most IR studies probe bulk glass structure. Transmission IR spectroscopy is not inherently surface sensitive. However, it can provide valuable surface insight to samples with a high-surface-area form factor. In particular, infrared studies of high-surface area fused silica powders have been influential in establishing the chemistry of surface silanols.[16-17, 23-24, 105] More recently, attenuated total reflection infrared spectroscopy (ATR-IR) has been used to analyze near-surface hydrous species in soda-lime float glasses.[154]

Surface hydroxyls have been studied extensively by computational modeling.[7-9, 106] These modeling studies have considered SiO_2 model surfaces and simple multicomponent glass surfaces. They have shown that H-bonded and non-interacting silanols interact differently with physisorbed water. They have also identified important surface sites for surface hydroxyl formation. These include strained siloxane bonds, which are most likely to occur in rings consisting of two or three silica tetrahedra.

Chemical derivatization is an important surface analysis strategy. Reactive groups at sample surfaces (usually hydroxyls in the case of glass) are tagged using a derivatizing agent.[155] The quantity of derivatizing agent reacted is then measured using a suitable technique, e.g., fluorescence spectroscopy or XPS. This can enable the detection of normally undetectable functional groups.[155] For example, oxygen in surface silanols has only a very minor chemical shift

in XPS compared to bridging oxygens. By reacting surface hydroxyls with fluorosilanes and quantifying detected fluorine, the quantity of surface silanols can be measured. Numerous studies have used this approach to provide important insights into glass surface chemistry.[13, 86] However, there are important limitations to chemical derivatization. The derivatizing agent may not be reactive towards all functional groups of interest. In particular, isolated silanols may react more readily with silanes than H-bonded silanols.[17] Steric hindrance may also prevent reaction with some sites of interest, resulting in undercounting.[16] The sample surface must be carefully prepared to remove all interfering contaminants, and all unreacted derivatizing agents must be removed from the sample surface prior to quantitation. Derivatization studies have played an important role in verifying that ToF-SIMS can be used to quantify surface hydroxyls.[13] Derivatization/XPS measurements have also established that multicomponent glasses and fused silica have significantly different surface reactivities.[29-30]

More recently, sum frequency generation (SFG) and evanescent wave cavity ringdown spectroscopy have been used to study the interaction of water and other adsorbates with surface hydroxyls.[112, 156-157] These studies have shown that atmospheric water adsorbs on glass surfaces in islands.[112] They have also provided insight into the spatial distribution of adsorption sites on glass surfaces.

1.9 Conclusion

The functionality and value of glass goods are often improved through surface modification and thin-film deposition. For this reason there is a need to better understand glass surface composition and reactivity. In particular, FPDs are microfabricated devices manufactured on the surface of specially engineered glass. Understanding how display glass surface composition

45

evolves with exposure to production line chemical treatments is key to addressing FPD manufacturing challenges, including particulate adhesion, surface charging, and thin film adhesion.

Amorphous silica and multicomponent glasses have significantly different surface reactivities and corrosion mechanisms. Surface hydroxyls are the most important reactive function on these surfaces, but multicomponent glass contains additional potential reactive sites. These reactive sites include modifier ions, weathering products, non-bridging oxygens, aluminols, and boronols. These additional surface sites alter the reactivity of silanols on the glass surface.

Glass corrosion and surface alteration are complex processes. Several different mechanisms have been posited for solution phase glass corrosion, and several types of glass surfaces have been documented on the literature. Previous work established that glass surface composition is a function of its thermal history and exposure to atmospheric water vapor, atmospheric contaminants, and wet chemical treatments. Powdered and fracture surfaces vary significantly from melt-formed surfaces. Therefore, understanding display glass surfaces requires analytical methodologies capable of analyzing low-surface area planar samples. In this study, we explore the chemistry of display glass surfaces exposed to common FPD fabrication chemical treatments using ToF-SIMS, XPS, and LEIS.

1.10 Figures
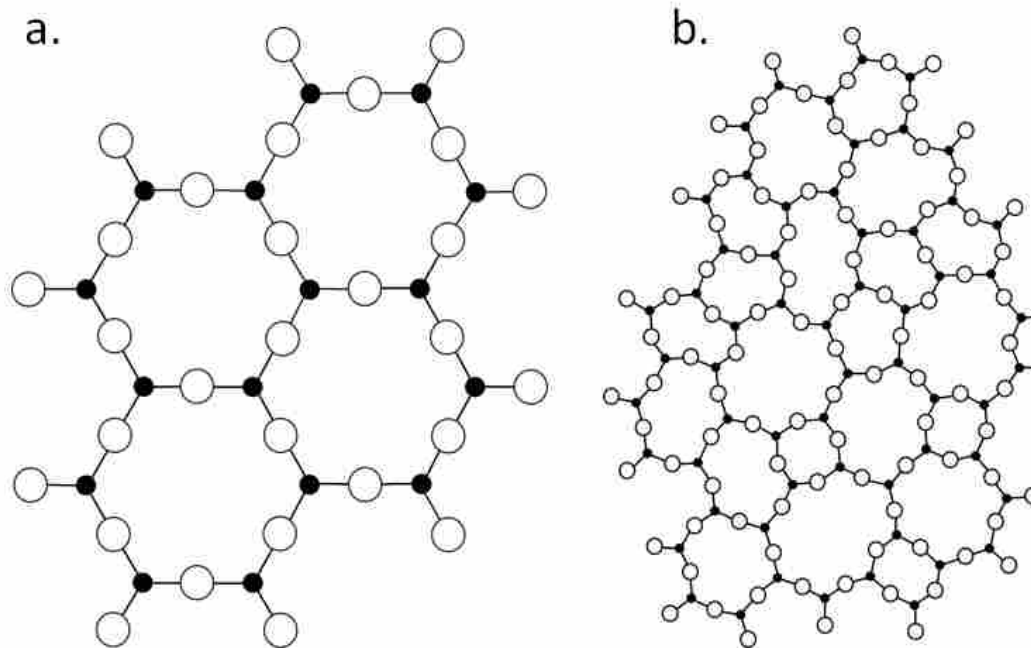
Figure 1.1 (a) A continuous crystalline network with stoichiometry of C_2A_3 where C is a cation and A is an anion. (b) A continuous random network with the same stoichiometry. Adapted with permission from Zachariasen, W. H. The atomic arrangement in glass. *Journal of the American Chemical Society* **1932,** *54* (10), 3841-3851.[57]
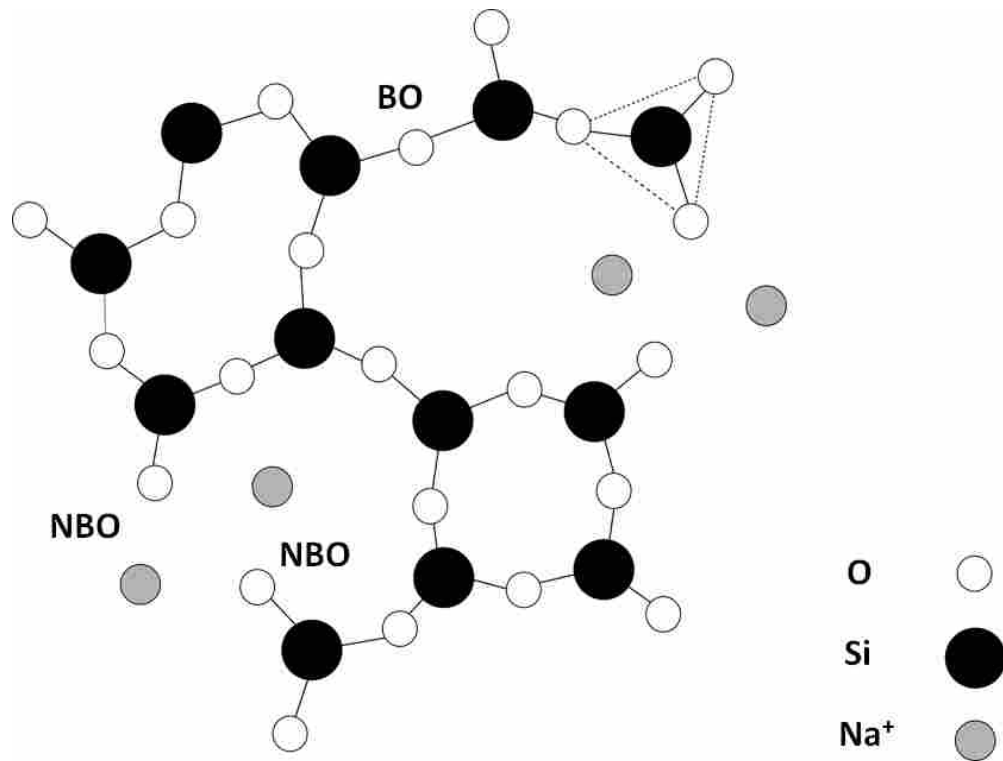
Figure 1.2. Schematic representation of a sodium silicate glass. Note that one oxygen in each silicon tetrahedron is omitted for clarity. Adapted with permission from Le Bourhis, E., *Glass: mechanics and technology*. John Wiley & Sons: **2014.**[45]

Molten glass overflows isopipe

Melt side 1

Melt side 2

Melts from both
sides of isopipe fuse
at root to form a
single sheet

Rollers at edge
Draw sheet to thickness
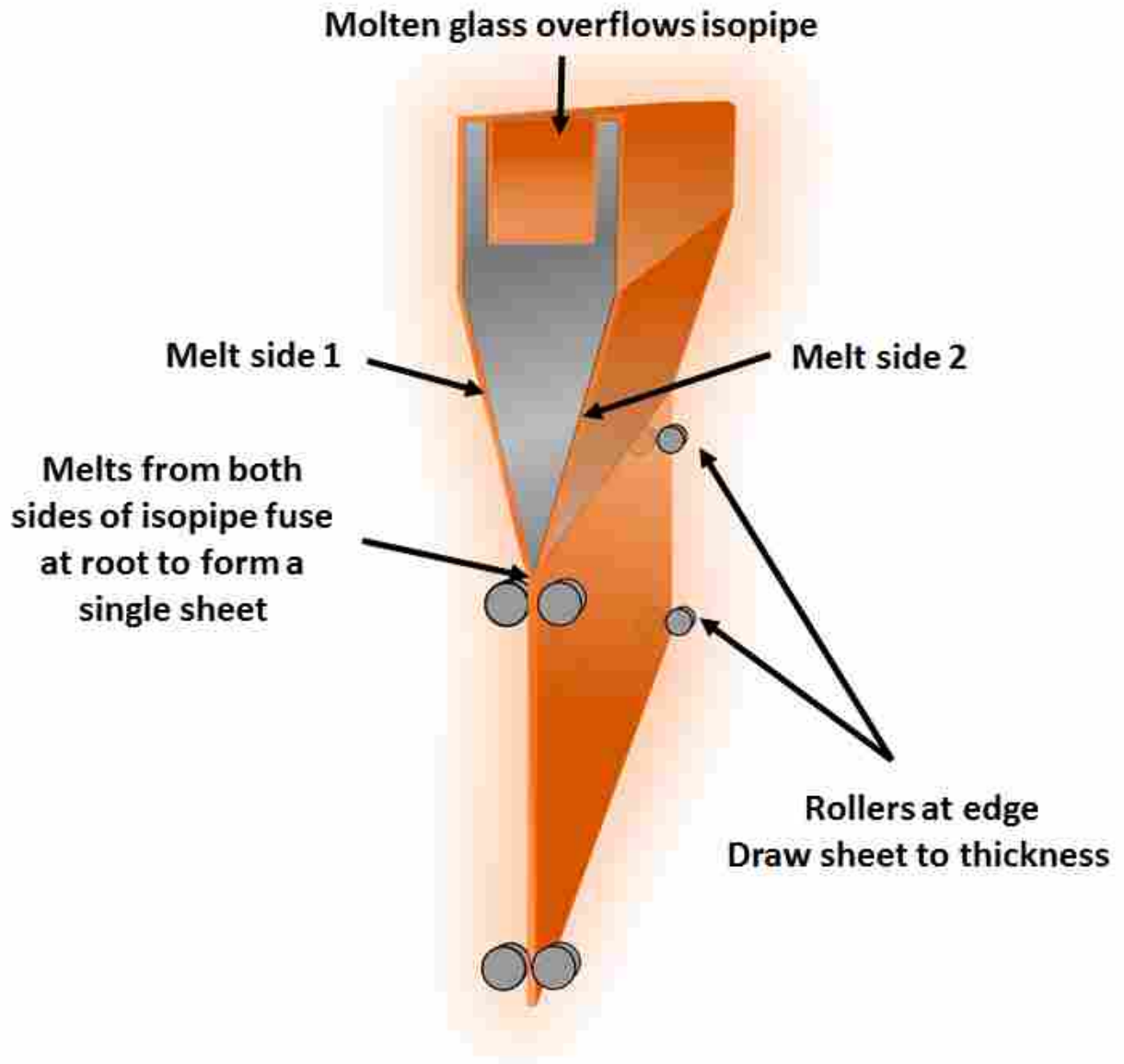
Figure 1.3. Schematic representation of the fusion draw process.
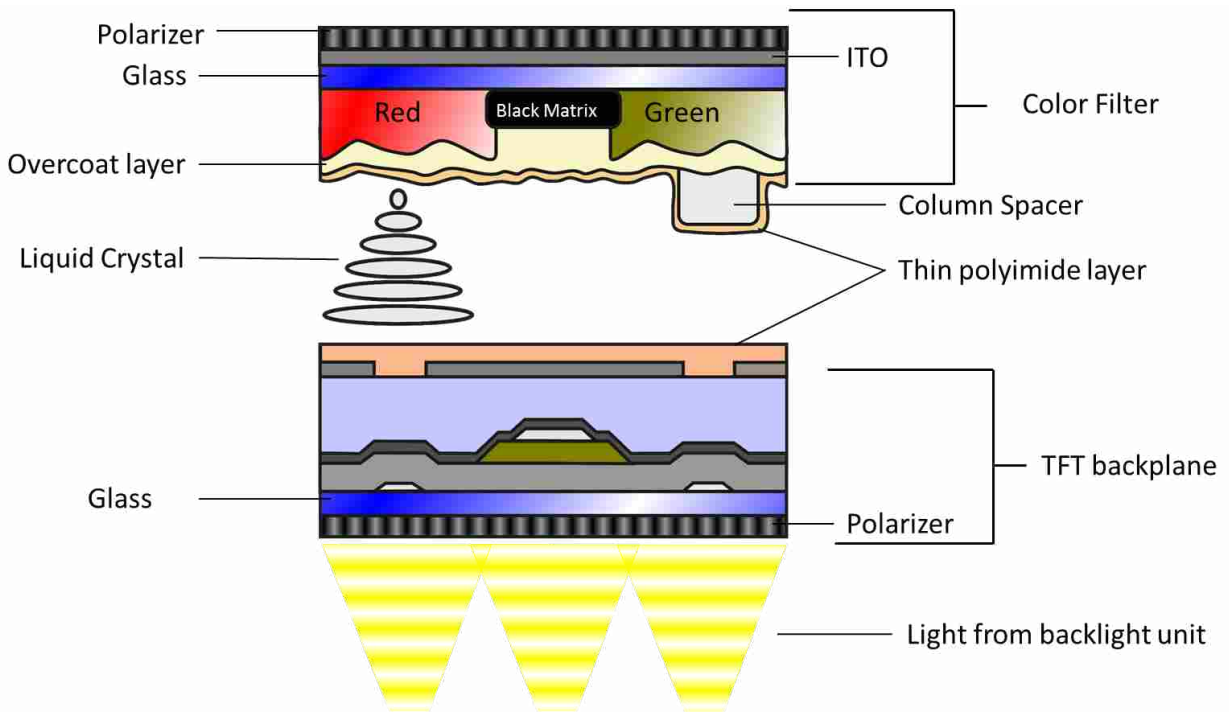
Figure 1.4. Schematic representation of an active matrix liquid crystal display (AMLCD). Adapted with permission from Souk, J.; Morozumi, S.; Luo, F.-C.; Bita, I., *Flat Panel Display Manufacturing*. John Wiley & Sons: **2018.**[5]
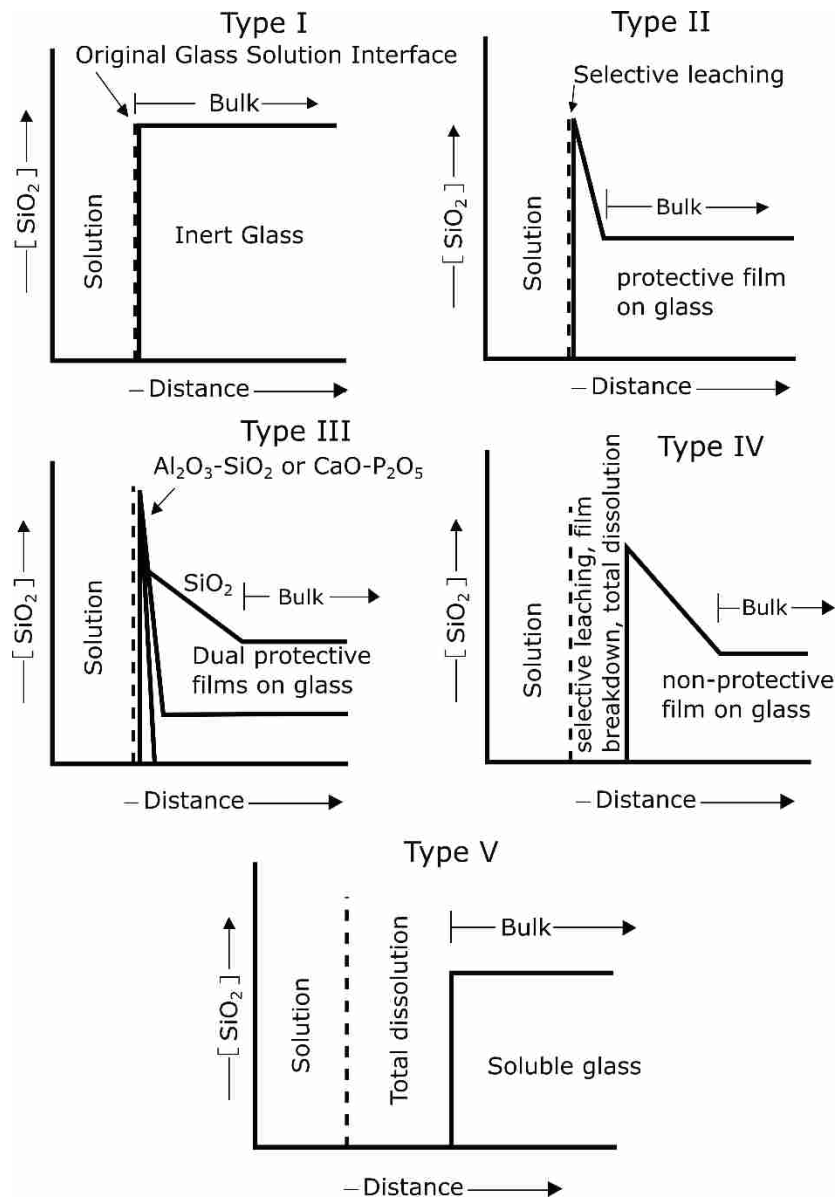
Figure 1.5. The five types of solution-altered glass surfaces. Adpted with permission from Hench, L.; Clark, D. E. Physical chemistry of glass surfaces. *Journal of Non-Crystalline Solids* **1978**, *28* (1), 83-105.[77]
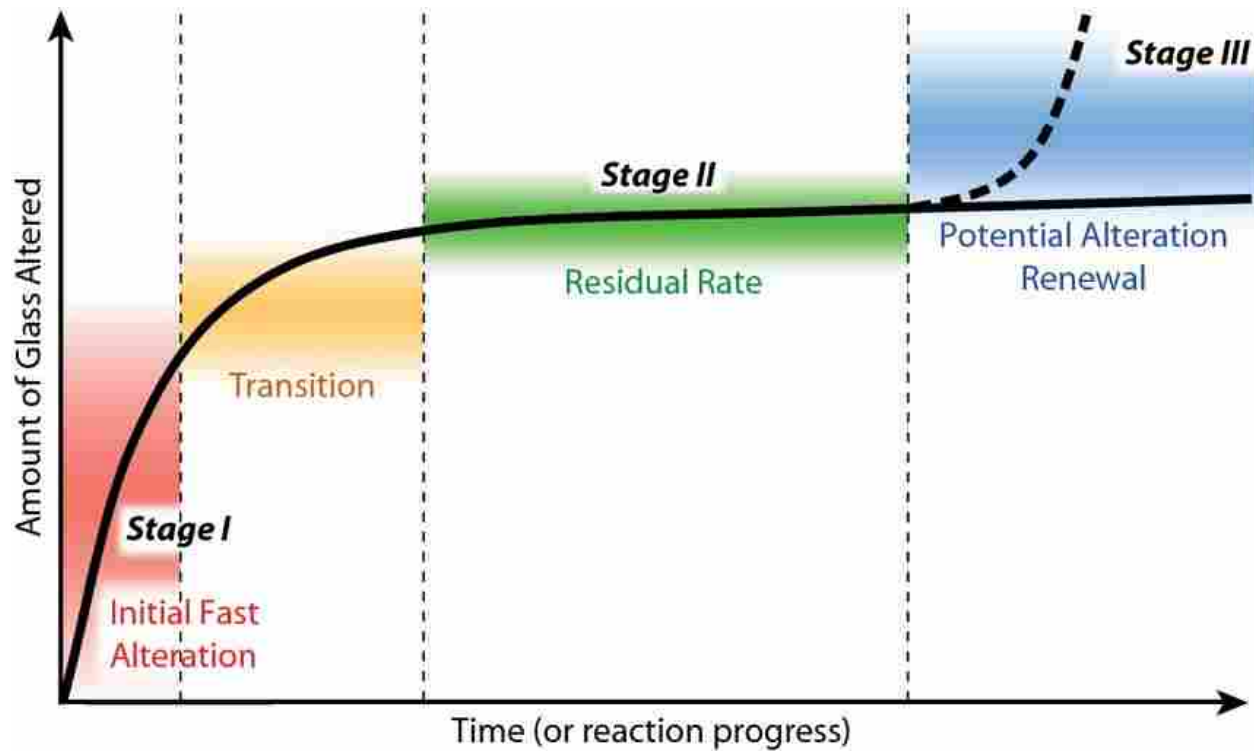
Figure 1.6. Kinetic phases of glass corrosion. Used with permission from Vienna, J. D.; Ryan, J. V.; Gin, S.; Inagaki, Y. Current understanding and remaining challenges in modeling long-term degradation of borosilicate nuclear waste glasses. *International Journal of Applied Glass Science* **2013,** *4* (4), 283-294.[92]
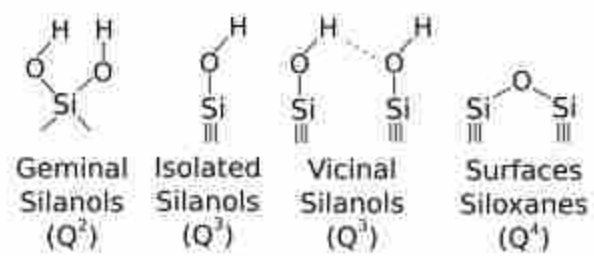
Figure 1.7. Types of silanols present on glass surfaces.
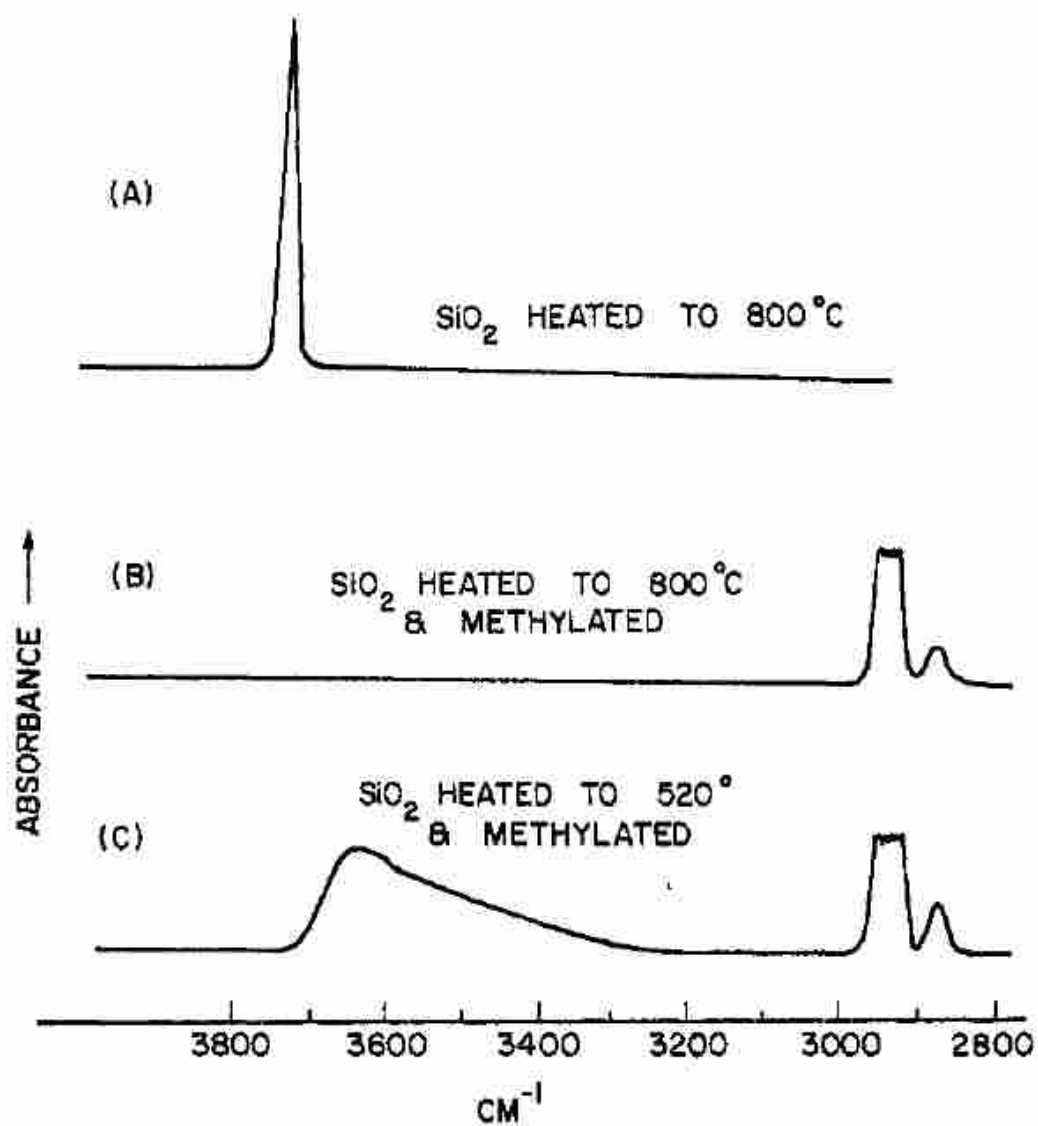
Figure 1.8. Infrared spectra of amorphous silica powder surfaces. (A) Surface heated to 800 °C to contain only free OH groups. (B) Surface heated to 800 °C and reacted with trimethylchlorosilane to produce surfaces with no OH groups. (C) Silica heated to 520 °C and reacted with trimethylchlorosilane. Surface contains H-bonded OH groups and methyl groups, but no free OH groups. Used with permission from Hair, M. L.; Hertl, W. Adsorption on hydroxylated silica surfaces. *The Journal of Physical Chemistry* **1969**, *73* (12), 4269-4276.[17]
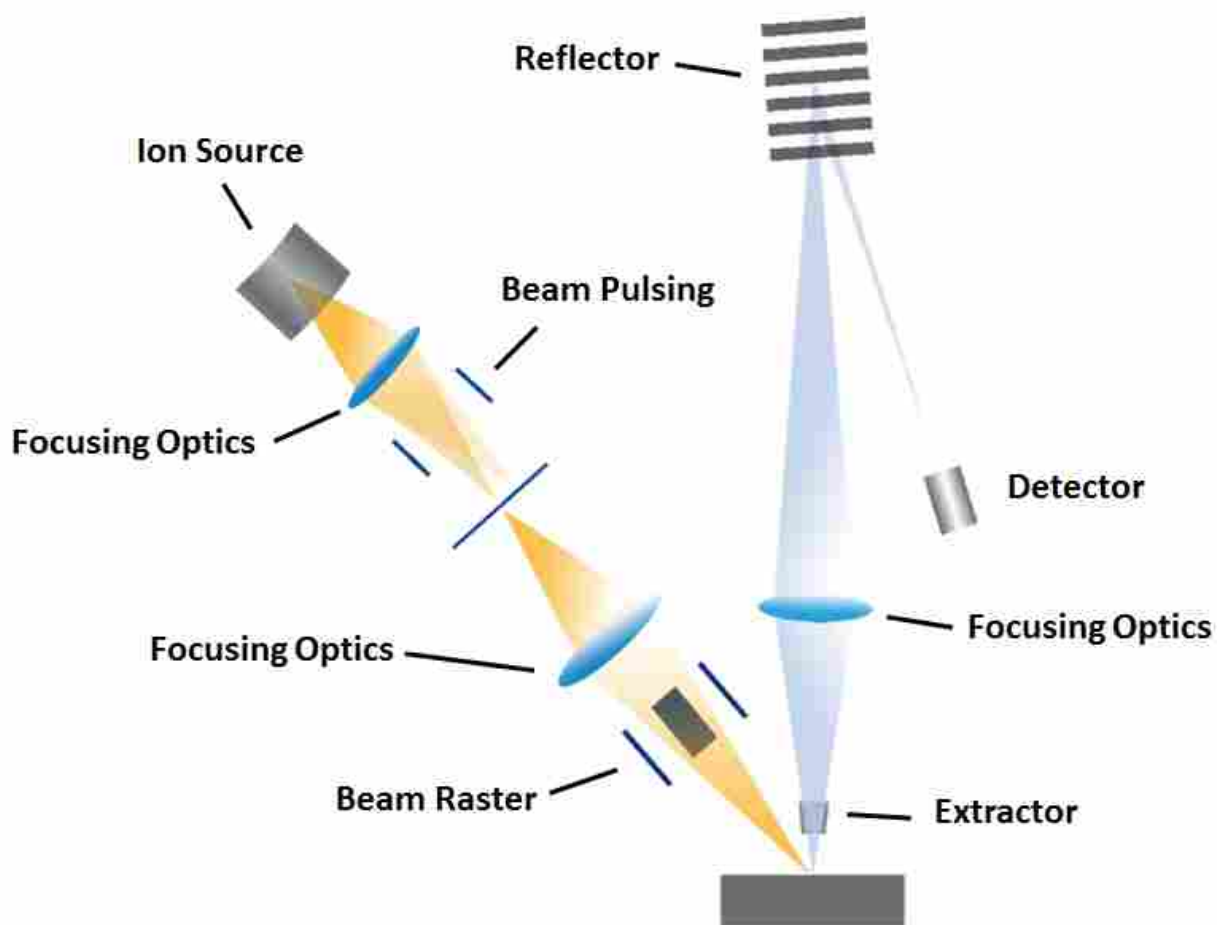
Figure 1.9. Schematic representation of a ToF-SIM instrument. Used with permission from Cushman, C. V.; Brüner, P.; Zakel, J.; Major, G.; Lunt, B. M.; Grehl, T.; Smith, N. J.; Linford, M. R. A Pictorial View of LEIS and ToF-SIMS Instrumentation. **February, 2016.**[128]
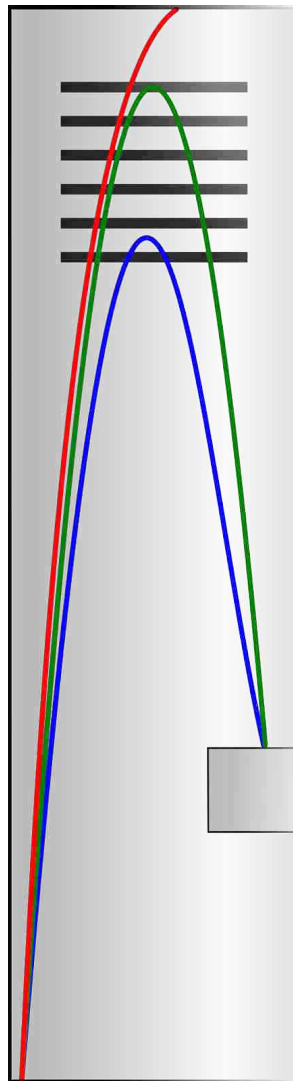
Figure 1.10. Schematic representation of a time-of-flight analyzer. Ion trajectories for ions with different kinetic energies are shown in different colors. Blue represents ions with a low kinetic energy which travel only a short distance into the reflector. Green represent ions with moderate amount of kinetic energy which travel a greater distance into the reflector. Red represents ions with sufficient energy to penetrate the reflector entirely. These do not reach the detector, and are not counted. Used with permission from Cushman, C. V.; Fisher, L. S.; Zakel, J.; Linford, M. R. Sample Charging in ToF-SIMS: How it Affects the Data that are Collected and How to Reduce it. *Vacuum Technology & Coating* **March, 2018.**[129]
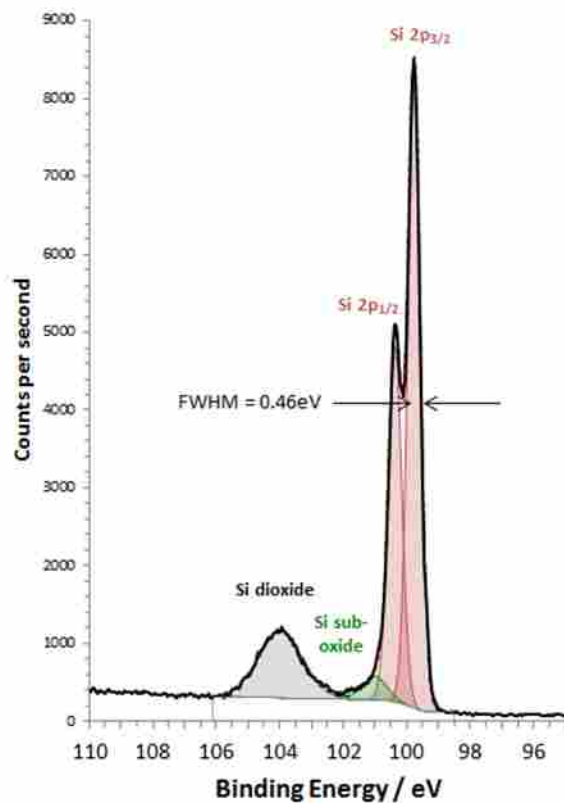
Figure 1.11. High resolution XPS spectrum of Si 2p envelope. Used with permission from Cushman, C. V.; Chatterjee, S.; Major, G. H.; Smith, N. J.; Roberts, A.; Linford, M. R. Trends in Advanced XPS Instrumentation. I. Overview of the Technique, Automation, High Sensitivity, Snapshot Spectroscopy, Gas Cluster Ion Beams, and Multiple Analytical Techniques on the Instrument. *Vacuum Technology & Coating* **November, 2016,** 20-28.[148]
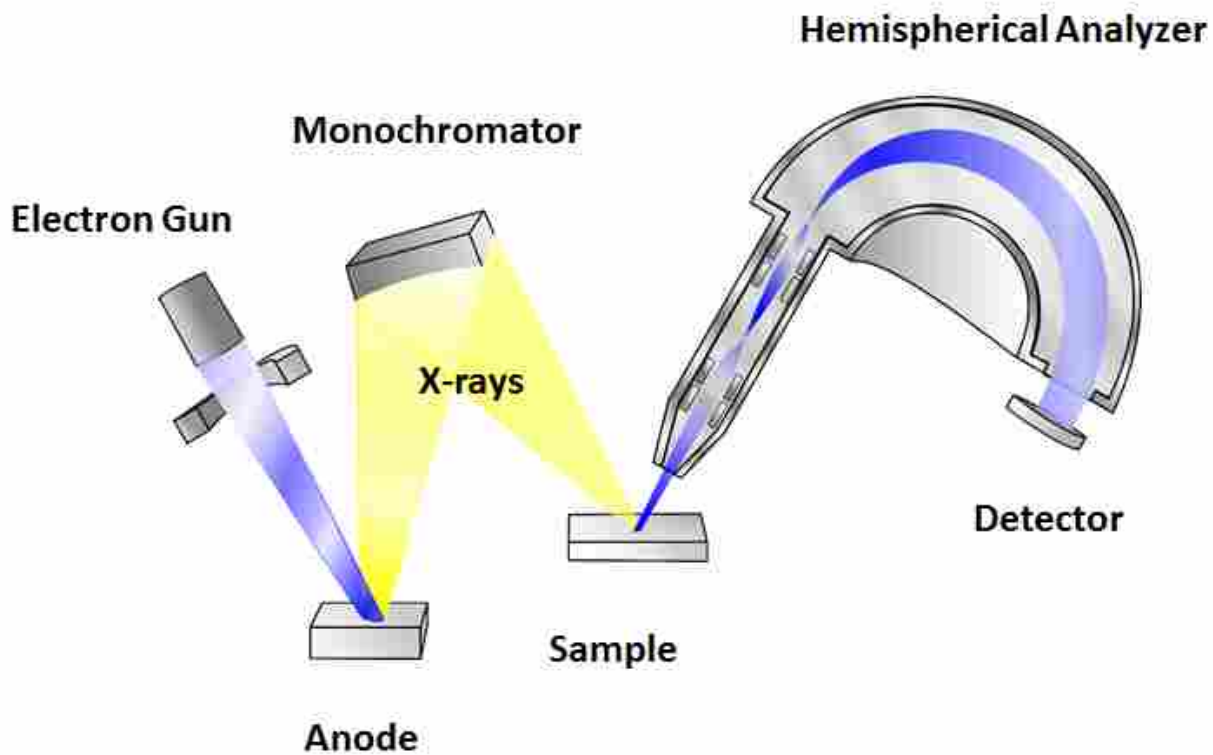
Figure 1.12. Schematic representation of laboratory-scale XPS instrument with parts labeled. Used with permission from Cushman, C. V.; Chatterjee, S.; Major, G. H.; Smith, N. J.; Roberts, A.; Linford, M. R. Trends in Advanced XPS Instrumentation. I. Overview of the Technique, Automation, High Sensitivity, Snapshot Spectroscopy, Gas Cluster Ion Beams, and Multiple Analytical Techniques on the Instrument. *Vacuum Technology & Coating* **November, 2016,** 20-28.[148]
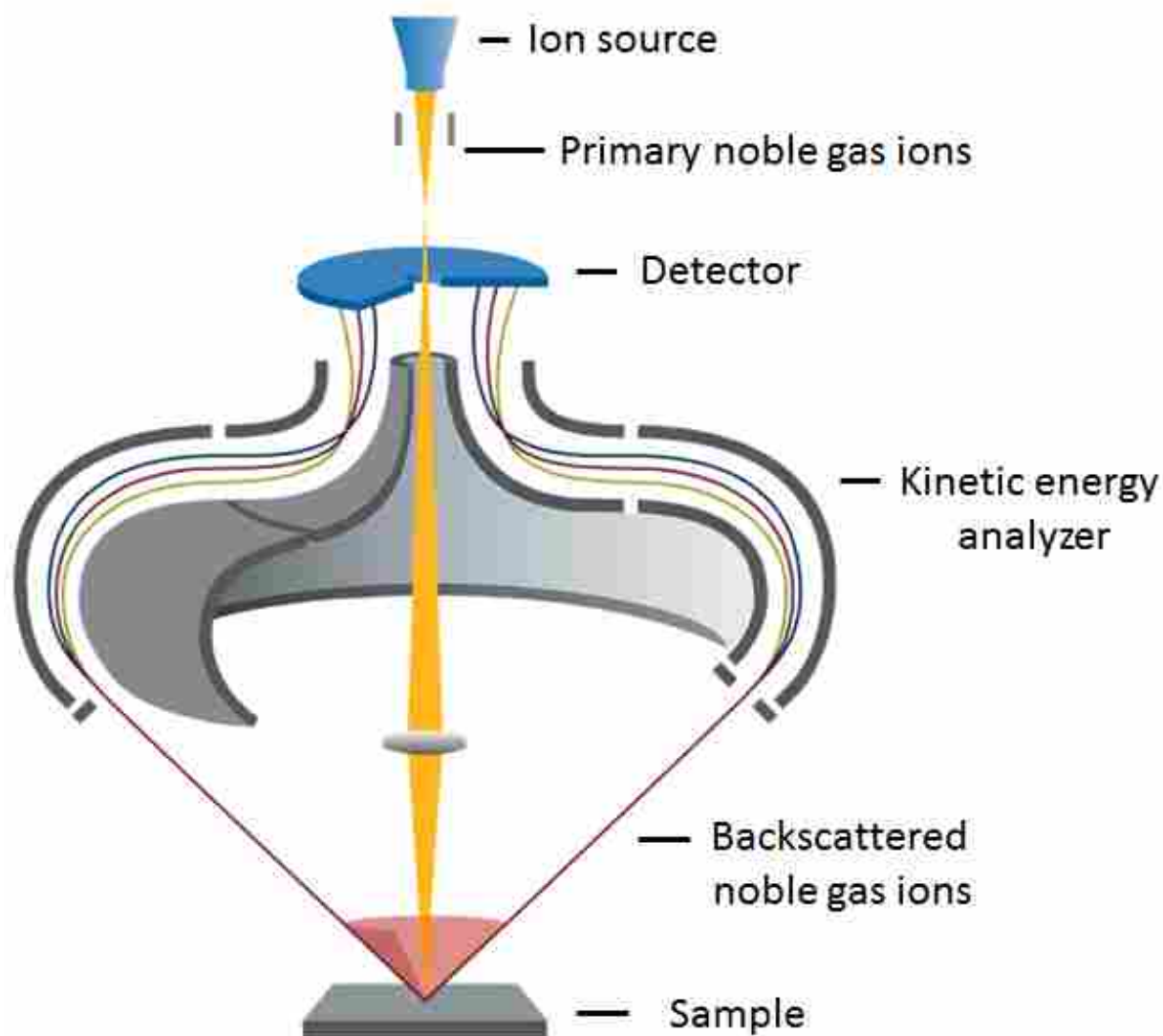
Figure 1.13. Schematic representation of a LEIS instrument equipped with a double-toroidal analyzer. Used with permission from Cushman, C. V.; Brüner, P.; Zakel, J.; Major, G. H.; Lunt, B. M.; Smith, N. J.; Grehl, T.; Linford, M. R. Low energy ion scattering (LEIS). A practical introduction to its theory, instrumentation, and applications. *Analytical Methods* **2016,** *8* (17), 3419-3439.[41]

1.11 References

1.   Ellison, A.; Cornejo, I. A. Glass Substrates for Liquid Crystal Displays. *International Journal of Applied Glass Science* **2010,** *1* (1), 87-103.

2.   Choi, Y. S.; Yun, J. U.; Park, S. E. Flat Panel Display Glass: Current Status and Future. *Journal of Non-Crystalline Solids* **2016,** *431*, 2-7.

3.   Kloss, T.; Lautenschläger, G.; Schneider, K. Advances in the Process of Floating Borosilicate Glasses and some Recent Applications for Specialty Borosilicate Float Gslasses. *Glass technology* **2000,** *41* (6), 177-181.

4.   Hamilton, L. L. Display Innovations Through Glass. *Japanese Journal of Applied Physics* **2016,** *55*, 03CA01.

5.   Souk, J.; Morozumi, S.; Luo, F.-C.; Bita, I., *Flat Panel Display Manufacturing*. John Wiley & Sons: 2018.

6.   Agnello, G.; Hamilton, J.; Manley, R.; Streltsova, E.; LaCourse, W.; Cormack, A. Investigation of Contact-Induced Charging Kinetics on Variably Modified Glass Surfaces. *Applied Surface Science* **2015,** *356*, 1189-1199.

7.   Leed, E. A.; Sofo, J. O.; Pantano, C. G. Electronic structure calculations of physisorption and chemisorption on oxide glass surfaces. *Physical Review B* **2005,** *72* (15), 155427.

8.   Mahadevan, T. S.; Du, J. Evaluating Water Reactivity at Silica Surfaces Using Reactive Potentials. *The Journal of Physical Chemistry C* **2018,** *122* (18), 9875-9885.

9.   Lockwood, G. K.; Garofalini, S. H. Bridging oxygen as a site for proton adsorption on the vitreous silica surface. *The Journal of chemical physics* **2009,** *131* (7), 074703.

10.   Wood, B.; Lamb, R.; Raston, C. Static SIMS study of hydroxylation of low-surface-area silica. *Surface and interface analysis* **1995,** *23* (10), 680-688.

11.   D'Souza, A. S.; Pantano, C. G. Mechanisms for silanol formation on amorphous silica fracture surfaces. *Journal of the American Ceramic Society* **1999,** *82* (5), 1289-1293.

12.   D'Souza, A. S.; Pantano, C. G. Hydroxylation and dehydroxylation behavior of silica glass fracture surfaces. *Journal of the American Ceramic Society* **2002,** *85* (6), 1499-1504.

13.   D'Souza, A. S.; Pantano, C. G.; Kallury, K. M. Determination of the surface silanol concentration of amorphous silica surfaces using static secondary ion mass spectroscopy. *Journal of Vacuum Science & Technology A: Vacuum, Surfaces, and Films* **1997,** *15* (3), 526-531.

14.   Banerjee, J.; Bojan, V.; Pantano, C. G.; Kim, S. H. Effect of heat treatment on the surface chemical structure of glass: Oxygen speciation from in situ XPS analysis. *Journal of the American Ceramic Society* **2018,** *101* (2), 644-656.

15.   Banerjee, J.; Kim, S. H.; Pantano, C. G. Elemental areal density calculation and oxygen speciation for flat glass surfaces using x-ray photoelectron spectroscopy. *Journal of Non-Crystalline Solids* **2016,** *450*, 185-193.

16.   Hair, M. L. Hydroxyl groups on silica surface. *Journal of Non-Crystalline Solids* **1975,** *19*, 299-309.

17.   Hair, M. L.; Hertl, W. Adsorption on hydroxylated silica surfaces. *The Journal of Physical Chemistry* **1969,** *73* (12), 4269-4276.

18.   Potapov, V.; Zhuravlev, L. Temperature dependence of the concentration of silanol groups in silica precipitated from a hydrothermal solution. *Glass Physics and Chemistry* **2005,** *31* (5), 661-670.

19.   Zhuravlev, L. Concentration of hydroxyl groups on the surface of amorphous silicas. *Langmuir* **1987,** *3* (3), 316-318.

20.   Zhuravlev, L. Surface characterization of amorphous silica—a review of work from the former USSR. *Colloids and Surfaces A: physicochemical and engineering aspects* **1993,** *74* (1), 71-90.

21.   Zhuravlev, L. The surface chemistry of amorphous silica. Zhuravlev model. *Colloids and Surfaces A: Physicochemical and Engineering Aspects* **2000,** *173* (1), 1-38.

22.   Anderson Jr, J.; Wickersheim, K. Near infrared characterization of water and hydroxyl groups on silica surfaces. *Surface Science* **1964,** *2*, 252-260.

23.   McDonald, R. S. Surface functionality of amorphous silica by infrared spectroscopy. *The Journal of Physical Chemistry* **1958,** *62* (10), 1168-1178.

24.   Gallas, J.-P.; Goupil, J.-M.; Vimont, A.; Lavalley, J.-C.; Gil, B.; Gilson, J.-P.; Miserque, O. Quantification of water and silanol species on various silicas by coupling IR spectroscopy and in-situ thermogravimetry. *Langmuir* **2009,** *25* (10), 5825-5834.

25.   Mauro, J. C. Grand challenges in glass science. *Frontiers in Materials* **2014,** *1*, 20.

26.   Mauro, J. C.; Philip, C. S.; Vaughn, D. J.; Pambianchi, M. S. Glass science in the United States: current status and future directions. *International Journal of Applied Glass Science* **2014,** *5* (1), 2-15.

27.   Pantano, C. G. In *What do we know about glass surfaces?*, 61st Conference on Glass Problems: A Collection of Papers Presented at the 61st Conference on Glass Problems, John Wiley & Sons: 2009; p 137.

28.   Brongersma, H. H.; Draxler, M.; de Ridder, M.; Bauer, P. Surface composition analysis by low-energy ion scattering. *Surface Science Reports* **2007,** *62* (3), 63-109.

29.   Stapleton, J. J.; Suchy, D. L.; Banerjee, J.; Mueller, K. T.; Pantano, C. G. Adsorption reactions of carboxylic acid functional groups on sodium aluminoborosilicate glass fiber surfaces. *ACS applied materials & interfaces* **2010,** *2* (11), 3303-3309.

30.   Rivera, L. O.; Bakaev, V. A.; Banerjee, J.; Mueller, K. T.; Pantano, C. G. Characterization and reactivity of sodium aluminoborosilicate glass fiber surfaces. *Applied Surface Science* **2016,** *370*, 328-334.

31.   Fry, R. A.; Tsomaia, N.; Pantano, C. G.; Mueller, K. T. ^{19}F MAS NMR quantification of accessible hydroxyl sites on fiberglass surfaces. *Journal of the American Chemical Society* **2003,** *125* (9), 2378-2379.

32.   Benninghoven, A. Some aspects of secondary ion mass spectrometry of organic compounds. *International Journal of Mass Spectrometry and Ion Physics* **1983,** *53*, 85-99.

33.   Benninghoven, A. Surface analysis by secondary ion mass spectrometry (SIMS). *Surface Science* **1994,** *299*, 246-260.

34.   Van der Heide, P., *Secondary ion mass spectrometry: an introduction to principles and practices*. John Wiley & Sons: 2014.

35.   Szakal, C.; Kozole, J.; Russo Jr, M. F.; Garrison, B. J.; Winograd, N. Surface sensitivity in cluster-ion-induced sputtering. *Physical review letters* **2006,** *96* (21), 216104.

36.   Brongersma, H.; De Ridder, M.; Gildenpfennig, A.; Viitanen, M. Insight in the outside: materials science at the atomic level using LEIS. *Journal of the European Ceramic Society* **2003,** *23* (15), 2761-2767.

37.   Brongersma, H. H.; Grehl, T.; van Hal, P. A.; Kuijpers, N. C.; Mathijssen, S. G.; Schofield, E. R.; Smith, R. A.; ter Veen, H. R. High-sensitivity and high-resolution low-energy ion scattering. *Vacuum* **2010,** *84* (8), 1005-1007.

38.   Singh, B.; Smith, S. J.; Jensen, D. S.; Jones, H. F.; Dadson, A. E.; Farnsworth, P. B.; Vanfleet, R.; Farrer, J. K.; Linford, M. R. Multi-instrument characterization of five nanodiamond samples: a thorough example of nanomaterial characterization. *Analytical and bioanalytical chemistry* **2016,** *408* (4), 1107-1124.

39.   Jensen, D. S.; Kanyal, S. S.; Madaan, N.; Hancock, J. M.; Dadson, A. E.; Vail, M. A.; Vanfleet, R.; Shutthanandan, V.; Zhu, Z.; Engelhard, M. H.; Linford, M. R. Multi-instrument characterization of the surfaces and materials in microfabricated, carbon nanotube-templated thin layer chromatography plates. An analogy to 'The Blind Men and the Elephant'. *Surface and Interface Analysis* **2013,** *45* (8), 1273-1282.

40.   Mahoney, C. M., *Cluster secondary ion mass spectrometry: principles and applications*. John Wiley & Sons: 2013; Vol. 44.

41.   Cushman, C. V.; Brüner, P.; Zakel, J.; Major, G. H.; Lunt, B. M.; Smith, N. J.; Grehl, T.; Linford, M. R. Low energy ion scattering (LEIS). A practical introduction to its theory, instrumentation, and applications. *Analytical Methods* **2016,** *8* (17), 3419-3439.

42.   Engelhardt, H.; Bäck, W.; Menzel, D.; Liebl, H. Novel charged particle analyzer for momentum determination in the multichanneling mode: I. Design aspects and electron/ion optical properties. *Review of Scientific Instruments* **1981,** *52* (6), 835-839.

43.   Engelhardt, H.; Zartner, A.; Menzel, D. Novel charged particle analyzer for momentum determination in the multichanneling mode. II. Physical realization, performance tests, and sample spectra. *Review of Scientific Instruments* **1981,** *52* (8), 1161-1173.

44.   Ackermans, P.; Van Der Meulen, P.; Ottevanger, H.; Van Straten, F.; Brongersma, H. Simultaneous energy and angle resolved ion scattering spectroscopy. *Nuclear Instruments and Methods in Physics Research Section B: Beam Interactions with Materials and Atoms* **1988,** *35* (3-4), 541-543.

45.   Le Bourhis, E., *Glass: mechanics and technology*. John Wiley & Sons: 2014.

46.   Janssens, K. H., *Modern methods for analysing archaeological and historical glass*. John Wiley & Sons: 2013; Vol. 1.

47.   Mauro, J. C. Decoding the glass genome. *Current Opinion in Solid State and Materials Science* **2018,** *22* (2), 58-64.

48.   DiBenedetto, A. Tailoring of interfaces in glass fiber reinforced polymer composites: a review. *Materials Science and Engineering: A* **2001,** *302* (1), 74-82.

49.   Ballato, J.; Dragic, P. Rethinking optical fiber: new demands, old glasses. *Journal of the American Ceramic Society* **2013,** *96* (9), 2675-2692.

50.   Jensen, W. B. The origin of pyrex. *Journal of chemical education* **2006,** *83* (5), 692.

51.   Mysen, B. O.; Richet, P., *Silicate glasses and melts*. Elsevier: 2018.

52.   Morse, D. L.; Evenson, J. W. Welcome to the glass age. *International Journal of Applied Glass Science* **2016,** *7* (4), 409-412.

53.   De Forest, L., Space telegraphy. Google Patents: 1908.

54.   Fleming, J. A., Instrument for converting alternating electric currents into continuous currents. Google Patents: 1905.

55.   De Forest, L., Device for amplifying feeble electrical currents. Google Patents: 1907.

56.   Mauro, J. C.; Ellison, A. J.; Pye, L. D. Glass: the nanotechnology connection. *International Journal of Applied Glass Science* **2013,** *4* (2), 64-75.

57.   Zachariasen, W. H. The atomic arrangement in glass. *Journal of the American Chemical Society* **1932,** *54* (10), 3841-3851.

58.   McCloy, J. S. In *Methods for prediction of refractive index in glasses for the infrared*, Window and Dome Technologies and Materials XII, International Society for Optics and Photonics: 2011; p 80160G.

59.   Trivelpiece, C. L.; Rice, J. A.; Clark, N. L.; Kabius, B.; Jantzen, C. M.; Pantano, C. G. Corrosion of ISG fibers in alkaline solutions. *Journal of the American Ceramic Society* **2017,** *100* (10), 4533-4547.

60.   Seddon, A. Chalcogenide glasses: a review of their preparation, properties and applications. *Journal of Non-Crystalline Solids* **1995,** *184*, 44-50.

61.   Wong, H.-S. P.; Raoux, S.; Kim, S.; Liang, J.; Reifenberg, J. P.; Rajendran, B.; Asheghi, M.; Goodson, K. E. Phase change memory. *Proceedings of the IEEE* **2010,** *98* (12), 2201-2227.

62.   Kaur, G.; Pandey, O. P.; Singh, K.; Homa, D.; Scott, B.; Pickrell, G. A review of bioactive glasses: their structure, properties, fabrication and apatite formation. *Journal of Biomedical Materials Research Part A: An Official Journal of The Society for Biomaterials, The Japanese Society for Biomaterials, and The Australian Society for Biomaterials and the Korean Society for Biomaterials* **2014,** *102* (1), 254-274.

63.   Chen, M. A brief overview of bulk metallic glasses. *NPG Asia Materials* **2011,** *3* (9), 82.

64.   M Axinte, E.; PI Chirileanu, M. Recent progress in the industrialization of metallic glasses. *Recent Patents on Materials Science* **2012,** *5* (3), 213-221.

65.   Wang, L.-M. Enthalpy relaxation upon glass transition and kinetic fragility of molecular liquids. *The Journal of Physical Chemistry B* **2009,** *113* (15), 5168-5171.

66.   Takahashi, H.; Sato, K.; Sakata, S.; Okada, T. Charge leakage characteristic of glass substrate for liquid crystal display. *Journal of electrostatics* **1995,** *35* (4), 309-322.

67.   Pulker, H.; Pulker, H., *Coatings on glass*. Elsevier: 1999; Vol. 20.

68.   Mohelnikova, J. Materials for reflective coatings of window glass applications. *Construction and Building Materials* **2009,** *23* (5), 1993-1998.

69.   Arbab, M.; Finley, J. J. Glass in architecture. *International Journal of Applied Glass Science* **2010,** *1* (1), 118-129.

70.   Chabas, A.; Lombardo, T.; Cachier, H.; Pertuisot, M.; Oikonomou, K.; Falcone, R.; Verita, M.; Geotti-Bianchini, F. Behaviour of self-cleaning glass in urban atmosphere. *Building and environment* **2008,** *43* (12), 2124-2131.

71.   Lu, S. In *59.3: Functional Transparent Coatings for Displays*, SID Symposium Digest of Technical Papers, Wiley Online Library: 2015; pp 887-890.

72.   Mishra, N. N.; Retterer, S.; Zieziulewicz, T. J.; Isaacson, M.; Szarowski, D.; Mousseau, D. E.; Lawrence, D. A.; Turner, J. N. On-chip micro-biosensor for the detection of human CD4+ cells based on AC impedance and optical analysis. *Biosensors and Bioelectronics* **2005,** *21* (5), 696-704.

73.   Lines, M.; Perkins, R. T., Corrosion resistant wire-grid polarizer and method of fabrication. Google Patents: 2004.

74.   Bach, H. Advanced surface analysis of silicate glasses, oxides and other insulating materials: a review. *Journal of non-crystalline solids* **1997,** *209* (1), 1-18.

75.   Sprenger, D.; Bach, H.; Meisel, W.; Gütlich, P. XPS study of leached glass surfaces. *Journal of non-crystalline solids* **1990,** *126* (1-2), 111-129.

76.   Hench, L. Characterization of glass corrosion and durability. *Journal of non-crystalline solids* **1975,** *19*, 27-39.

77.   Hench, L.; Clark, D. E. Physical chemistry of glass surfaces. *Journal of Non-Crystalline Solids* **1978,** *28* (1), 83-105.

78. Little, L.; Klauser, H.; Amberg, C. An Infrared Study of the Adsorption of Butenes on Surfaces of Porous Vycor Glass. *Canadian Journal of Chemistry* **1961,** *39* (1), 42-60.

79. Low, M.; Ramasubramanian, N.; Ramamurthy, P.; Deo, A. Infrared spectrum, surface reaction, and polymerization of adsorbed hydrogen cyanide on porous glass. *The Journal of Physical Chemistry* **1968,** *72* (7), 2371-2378.

80. Hubert, M.; Faber, A. J. On the structural role of boron in borosilicate glasses. *Physics and Chemistry of Glasses-European Journal of Glass Science and Technology Part B* **2014,** *55* (3), 136-158.

81. Kobayashi, D.; Yamamoto, Y.; Isemura, T. Time-of-flight SIMS depth profiling of Na in SiO2 glass using C60 sputter ion beam. *Surface and Interface Analysis* **2013,** *45* (1), 113-116.

82. Synowicki, R. A.; Johs, B. D.; Martin, A. C. Optical properties of soda-lime float glass from spectroscopic ellipsometry. *Thin Solid Films* **2011,** *519* (9), 2907-2913.

83. Williams, K.; Johnson, C.; Nikolov, O.; Thomas, M.; Johnson, J.; Greengrass, J. Characterization of tin at the surface of float glass. *Journal of non-crystalline solids* **1998,** *242* (2-3), 183-188.

84. Frischat, G.; Müller-Fildebrandt, C.; Moseler, D.; Heide, G. On the origin of the tin hump in several float glasses. *Journal of non-crystalline solids* **2001,** *283* (1-3), 246-249.

85. Hayashi, Y.; Matsumoto, K.; Kudo, M. The diffusion mechanism of tin into glass governed by redox reactions during the float process. *Journal of non-crystalline solids* **2001,** *282* (2-3), 188-196.

86. Takeda, S.; Yamamoto, K.; Hayasaka, Y.; Matsumoto, K. Surface OH group governing wettability of commercial glasses. *Journal of non-crystalline solids* **1999,** *249* (1), 41-46.

87. Kolluru, P. V.; Green, D. J.; Pantano, C. G.; Muhlstein, C. L. Effects of surface chemistry on the nanomechanical properties of commercial float glass. *Journal of the American Ceramic Society* **2010,** *93* (3), 838-847.

88. Wood, J. G.; Prabakar, S.; Mueller, K. T.; Pantano, C. G. The effects of antimony oxide on the structure of alkaline-earth alumino borosilicate glasses. *Journal of non-crystalline solids* **2004,** *349*, 276-284.

89. Kelso, J.; Pantano, C. Spectroscopic examination of clean glass surfaces at elevated temperatures. *Journal of Vacuum Science & Technology A: Vacuum, Surfaces, and Films* **1985,** *3* (3), 1343-1346.

90. Gin, S.; Abdelouas, A.; Criscenti, L. J.; Ebert, W. L.; Ferrand, K.; Geisler, T.; Harrison, M. T.; Inagaki, Y.; Mitsui, S.; Mueller, K. T. An international initiative on long-term behavior of high-level nuclear waste glass. *Materials Today* **2013,** *16* (6), 243-248.

91. Gin, S.; Ryan, J. V.; Schreiber, D. K.; Neeway, J.; Cabié, M. Contribution of atom-probe tomography to a better understanding of glass alteration mechanisms: Application to a nuclear glass specimen altered 25 years in a granitic environment. *Chemical Geology* **2013,** *349*, 99-109.

92. Vienna, J. D.; Ryan, J. V.; Gin, S.; Inagaki, Y. Current understanding and remaining challenges in modeling long-term degradation of borosilicate nuclear waste glasses. *International Journal of Applied Glass Science* **2013,** *4* (4), 283-294.

93. Frugier, P.; Gin, S.; Minet, Y.; Chave, T.; Bonin, B.; Godon, N.; Lartigue, J.-E.; Jollivet, P.; Ayral, A.; De Windt, L. SON68 nuclear glass dissolution kinetics: Current state of knowledge and basis of the new GRAAL model. *Journal of Nuclear Materials* **2008,** *380* (1-3), 8-21.

94. Verney-Carron, A.; Gin, S.; Frugier, P.; Libourel, G. Long-term modeling of alteration-transport coupling: application to a fractured Roman glass. *Geochimica et Cosmochimica Acta* **2010,** *74* (8), 2291-2315.

95.   Verney-Carron, A.; Gin, S.; Libourel, G. A fractured roman glass block altered for 1800 years in seawater: Analogy with nuclear waste glass in a deep geological repository. *Geochimica et Cosmochimica Acta* **2008,** *72* (22), 5372-5385.

96.   Crovisier, J.-L.; Advocat, T.; Dussossoy, J.-L. Nature and role of natural alteration gels formed on the surface of ancient volcanic glasses (Natural analogs of waste containment glasses). *Journal of Nuclear Materials* **2003,** *321* (1), 91-109.

97.   Gin, S.; Neill, L.; Fournier, M.; Frugier, P.; Ducasse, T.; Tribet, M.; Abdelouas, A.; Parruzot, B.; Neeway, J.; Wall, N. The controversial role of inter-diffusion in glass alteration. *Chemical Geology* **2016,** *440*, 115-123.

98.   Doremus, R. H. Interdiffusion of hydrogen and alkali ions in a glass surface. *Journal of Non-Crystalline Solids* **1975,** *19*, 137-144.

99.   Smit, W.; Stein, H. Interdiffusion of hydrogen and alkali ions in glass surfaces. *Journal of Non-Crystalline Solids* **1979,** *34* (3), 357-370.

100.   McGrail, B. P.; Icenhower, J. P.; Shuh, D.; Liu, P.; Darab, J. G.; Baer, D. R.; Thevuthasen, S.; Shutthanandan, V.; Engelhard, M. H.; Booth, C. The structure of Na2O–Al2O3–SiO2 glass: impact on sodium ion exchange in H2O and D2O. *Journal of Non-Crystalline Solids* **2001,** *296* (1-2), 10-26.

101.   Hellmann, R.; Cotte, S.; Cadel, E.; Malladi, S.; Karlsson, L. S.; Lozano-Perez, S.; Cabié, M.; Seyeux, A. Nanometre-scale evidence for interfacial dissolution–reprecipitation control of silicate glass corrosion. *Nature materials* **2015,** *14* (3), 307-311.

102.   Geisler, T.; Nagel, T.; Kilburn, M. R.; Janssen, A.; Icenhower, J. P.; Fonseca, R. O.; Grange, M.; Nemchin, A. A. The mechanism of borosilicate glass corrosion revisited. *Geochimica et Cosmochimica Acta* **2015,** *158*, 112-129.

103.   Takeda, S.; Fukawa, M. Surface OH groups governing surface chemical properties of SiO 2 thin films deposited by RF magnetron sputtering. *Thin Solid Films* **2003,** *444* (1), 153-157.

104.   Takeda, S.; Fukawa, M. Role of surface OH groups in surface chemical properties of metal oxide films. *Materials Science and Engineering: B* **2005,** *119* (3), 265-267.

105.   Erkelens, J.; Linsen, B. Quantitative determination of hydroxyl groups and water for silica. *Journal of Colloid and Interface Science* **1969,** *29* (3), 464-468.

106.   Sulpizi, M.; Gaigeot, M.-P.; Sprik, M. The silica–water interface: how the silanols determine the surface acidity and modulate the water properties. *Journal of chemical theory and computation* **2012,** *8* (3), 1037-1047.

107.   Le Grange, J.; Markham, J.; Kurkjian, C. Effects of surface hydration on the deposition of silane monolayers on silica. *Langmuir* **1993,** *9* (7), 1749-1753.

108.   Opila, R.; Legrange, J.; Markham, J.; Heyer, G.; Schroeder, C. Effects of surface hydration on the deposition of silane monolayers on silica optical fiber. *Journal of adhesion science and technology* **1997,** *11* (1), 1-10.

109.   Rai, A.; Pinto, S.; Evangelista, M. B.; Gil, H.; Kallip, S.; Ferreira, M. G.; Ferreira, L. High-density antimicrobial peptide coating with broad activity and low cytotoxicity against human cells. *Acta biomaterialia* **2016,** *33*, 64-77.

110.   Rabnawaz, M.; Liu, G.; Hu, H. Fluorine-Free Anti-Smudge Polyurethane Coatings. *Angewandte Chemie International Edition* **2015,** *54* (43), 12722-12727.

111.   Pujari, S. P.; Scheres, L.; Marcelis, A. T.; Zuilhof, H. Covalent surface modification of oxide surfaces. *Angewandte Chemie International Edition* **2014,** *53* (25), 6322-6356.

112.   Isaienko, O.; Borguet, E. Hydrophobicity of hydroxylated amorphous fused silica surfaces. *Langmuir* **2013,** *29* (25), 7885-7895.

113.   Rodrigues, A.; Fearn, S.; Palomar, T.; Vilarigues, M. Early stages of surface alteration of soda-rich-silicate glasses in the museum environment. *Corrosion Science* **2018,** *143*, 362-375.

114.   Fearn, S.; McPhail, D.; Hagenhoff, B.; Tallarek, E. TOF-SIMS analysis of corroding museum glass. *Applied surface science* **2006,** *252* (19), 7136-7139.

115.   Melcher, M.; Wiesinger, R.; Schreiner, M. Degradation of glass artifacts: application of modern surface analytical techniques. *Accounts of chemical research* **2010,** *43* (6), 916-926.

116.   Krasnoslobodtsev, A. V.; Smirnov, S. N. Effect of water on silanization of silica by trimethoxysilanes. *Langmuir* **2002,** *18* (8), 3181-3184.

117.   Behrens, S. H.; Grier, D. G. The charge of glass and silica surfaces. *The Journal of Chemical Physics* **2001,** *115* (14), 6716-6721.

118.   Tarlov, M. J.; Evans, J. F.; Newman, J. G. Static SIMS and XPS study of water plasma exposed tin oxide films. *Applied surface science* **1993,** *64* (2), 115-125.

119.   Schaut, R. A. The effect of boron oxide on the composition, structure, and adsorptivity of glass surfaces. **2008**.

120.   De Bardi, M.; Hutter, H.; Schreiner, M. ToF-SIMS analysis for leaching studies of potash–lime–silica glass. *Applied Surface Science* **2013,** *282*, 195-201.

121.   Crobu, M.; Rossi, A.; Mangolini, F.; Spencer, N. D. Chain-length-identification strategy in zinc polyphosphate glasses by means of XPS and ToF-SIMS. *Analytical and bioanalytical chemistry* **2012,** *403* (5), 1415-1432.

122.   Mitchell, D.; Graham, M. Quantitative SIMS analysis of hydroxyl ion content in thin oxide films. *Journal of The Electrochemical Society* **1986,** *133* (5), 936-938.

123.   Mitchell, D.; Sproule, G.; Graham, M. Measurement of hydroxyl ions in thin passive oxide films using secondary ion mass spectrometry. *Applications of Surface Science* **1985,** *21* (1-4), 199-209.

124.   Liu, Y.; Guan, Y.; Zhang, Y.; Rossman, G. R.; Eiler, J. M.; Taylor, L. A. Direct measurement of hydroxyl in the lunar regolith and the origin of lunar surface water. *Nature Geoscience* **2012,** *5* (11), 779.

125.   Aubaud, C.; Withers, A. C.; Hirschmann, M. M.; Guan, Y.; Leshin, L. A.; Mackwell, S. J.; Bell, D. R. Intercalibration of FTIR and SIMS for hydrogen measurements in glasses and nominally anhydrous minerals. *American Mineralogist* **2007,** *92* (5-6), 811-828.

126.   Hauri, E. SIMS analysis of volatiles in silicate glasses, 2: isotopes and abundances in Hawaiian melt inclusions. *Chemical Geology* **2002,** *183* (1), 115-141.

127.   Stevie, F., *Secondary ion mass spectrometry: Applications for depth profiling and surface characterization*. Momentum Press: 2015.

128.   Cushman, C. V.; Brüner, P.; Zakel, J.; Major, G.; Lunt, B. M.; Grehl, T.; Smith, N. J.; Linford, M. R. A Pictorial View of LEIS and ToF-SIMS Instrumentation. **February, 2016**.

129.   Cushman, C. V.; Fisher, L. S.; Zakel, J.; Linford, M. R. Sample Charging in ToF-SIMS: How it Affects the Data that are Collected and How to Reduce it. *Vacuum Technology & Coating* **March, 2018**.

130.   Delcorte, A.; Leblanc, C.; Poleunis, C.; Hamraoui, K. Computer Simulations of the Sputtering of Metallic, Organic, and Metal–Organic Surfaces with Bi n and C60 Projectiles. *The Journal of Physical Chemistry C* **2013,** *117* (6), 2740-2752.

131.   Delcorte, A.; Bertrand, P.; Arys, X.; Jonas, A.; Wischerhoff, E.; Mayer, B.; Laschewsky, A. ToF-SIMS study of alternate polyelectrolyte thin films: Chemical surface characterization and molecular secondary ions sampling depth. *Surface Science* **1996,** *366* (1), 149-165.

132. Bottazzi, P.; Ottolini, L.; Vannucci, R. SIMS analyses of rare earth elements in natural minerals and glasses: An investigation of structural matrix effects on ion yields. *Scanning* **1992**, *14* (3), 160-168.

133. Bojan, V.; Büyüklimanli, T.; Pantano, C. G. Quantification of SIMS data for multicomponent glasses. *Surface and interface analysis* **1994**, *21* (2), 87-94.

134. Takizawa, K.; Ohno, M.; Saito, H.; Kobayashi, M.; Sagara, H. SIMS Analysis of Borosilicate Glasses using Sensitivity Factor Calculation. *Journal of the Mass Spectrometry Society of Japan* **1980**, *28* (2), 161-168.

135. Pantano, C. G., Chemical Properties of Real and Ideal Glass Surfaces. In *Materials Characterization for Systems Performance and Reliability*, Springer: 1986; pp 127-148.

136. Pacholski, M. L. Principal component analysis of TOF-SIMS spectra, images and depth profiles: an industrial perspective. *Applied surface science* **2004**, *231*, 235-239.

137. Graham, D. J.; Castner, D. G. Multivariate analysis of ToF-SIMS data from multicomponent systems: the why, when, and how. *Biointerphases* **2012**, *7* (1), 49.

138. Graham, D. J.; Wagner, M. S.; Castner, D. G. Information from complexity: Challenges of TOF-SIMS data interpretation. *Applied surface science* **2006**, *252* (19), 6860-6868.

139. Pei, L.; Jiang, G.; Tyler, B. J.; Baxter, L. L.; Linford, M. R. Time-of-flight secondary ion mass spectrometry of a range of coal samples: a chemometrics (PCA, cluster, and PLS) analysis. *Energy & Fuels* **2008**, *22* (2), 1059-1072.

140. Tyler, B. J.; Rayal, G.; Castner, D. G. Multivariate analysis strategies for processing ToF-SIMS images of biomaterials. *Biomaterials* **2007**, *28* (15), 2412-2423.

141. Kramer, R., *Chemometric techniques for quantitative analysis*. CRC Press: 1998.

142. Chatterjee, S.; Singh, B.; Diwan, A.; Lee, Z. R.; Engelhard, M. H.; Terry, J.; Tolley, H. D.; Gallagher, N. B.; Linford, M. R. A perspective on two chemometrics tools: PCA and MCR, and introduction of a new one: Pattern recognition entropy (PRE), as applied to XPS and ToF-SIMS depth profiles of organic and inorganic materials. *Applied Surface Science* **2018**, *433*, 994-1017.

143. Gallagher, N. B.; Shaver, J. M.; Martin, E. B.; Morris, J.; Wise, B. M.; Windig, W. Curve resolution for multivariate images with applications to TOF-SIMS and Raman. *Chemometrics and intelligent laboratory systems* **2004**, *73* (1), 105-117.

144. Garrido, M.; Rius, F.; Larrechi, M. Multivariate curve resolution–alternating least squares (MCR-ALS) applied to spectroscopic data from monitoring chemical reactions processes. *Analytical and bioanalytical chemistry* **2008**, *390* (8), 2059-2066.

145. Felten, J.; Hall, H.; Jaumot, J.; Tauler, R.; De Juan, A.; Gorzsás, A. Vibrational spectroscopic image analysis of biological material using multivariate curve resolution–alternating least squares (MCR-ALS). *Nature protocols* **2015**, *10* (2), 217.

146. Van der Heide, P., *X-ray photoelectron spectroscopy: an introduction to principles and practices*. John Wiley & Sons: 2011.

147. Gupta, V.; Ganegoda, H.; Engelhard, M. H.; Terry, J.; Linford, M. R. Assigning Oxidation States to Organic Compounds via Predictions from X-ray Photoelectron Spectroscopy: A Discussion of Approaches and Recommended Improvements. *Journal of Chemical Education* **2014**, *91* (2), 232-238.

148. Cushman, C. V.; Chatterjee, S.; Major, G. H.; Smith, N. J.; Roberts, A.; Linford, M. R. Trends in Advanced XPS Instrumentation. I. Overview of the Technique, Automation, High Sensitivity, Snapshot Spectroscopy, Gas Cluster Ion Beams, and Multiple Analytical Techniques on the Instrument. *Vacuum Technology & Coating* **November, 2016**, 20-28

149. Paynter, R. An ARXPS primer. *Journal of Electron Spectroscopy and Related Phenomena* **2009,** *169* (1), 1-9.

150. Smith, G. C. Evaluation of a simple correction for the hydrocarbon contamination layer in quantitative surface analysis by XPS. *Journal of electron spectroscopy and related phenomena* **2005,** *148* (1), 21-28.

151. Kelso, J.; Pantano, C.; Garofalini, S. A comparison of ion scattering spectra and molecular dynamics simulations at the surface of silicate glasses. *Surface science* **1983,** *134* (3), L543-L549.

152. Almeida, R. M.; Hickey, R.; Jain, H.; Pantano, C. G. Low-Energy Ion Scattering spectroscopy of silicate glass surfaces. *Journal of Non-Crystalline Solids* **2014,** *385*, 124-128.

153. Almeida, R. M.; Jain, H.; Pantano, C. G. Low-Energy Ion-Scattering Spectroscopy of Modified Silicate Glasses. *Journal of the American Ceramic Society* **2016,** *99* (4), 1259-1265.

154. Amma, S. i.; Kim, S. H.; Pantano, C. G. Analysis of water and hydroxyl species in soda lime glass surfaces using attenuated total reflection (ATR)-IR spectroscopy. *Journal of the American Ceramic Society* **2016,** *99* (1), 128-134.

155. Xing, Y.; Dementev, N.; Borguet, E. Chemical labeling for quantitative characterization of surface chemistry. *Current Opinion in Solid State and Materials Science* **2007,** *11* (5-6), 86-91.

156. Myalitsin, A.; Urashima, S.-h.; Nihonyanagi, S.; Yamaguchi, S.; Tahara, T. Water structure at the buried silica/aqueous interface studied by heterodyne-detected vibrational sum-frequency generation. *The Journal of Physical Chemistry C* **2016,** *120* (17), 9357-9363.

157. Fan, H.-F.; Li, F.; Zare, R. N.; Lin, K.-C. Characterization of two types of silanol groups on fused-silica surfaces using evanescent-wave cavity ring-down spectroscopy. *Analytical chemistry* **2007,** *79* (10), 3654-3661.

CHAPTER 2: Time-of-Flight Secondary Ion Mass Spectrometry of Wet and Dry Chemically Treated Display Glass Surfaces

2.1 Statement of Attribution

This document was originally published as Cushman, C. V.; Zakel, J.; Sturgell, B. S.; Major, G. I.; Lunt, B. M.; Bruner, P.; Grehl, T.; Smith, N. J.; Linford, M. R. Time-of-flight secondary ion mass spectrometry of wet and dry chemically treated display glass surfaces. *Journal of the American Ceramic Society* **2017,** *100* (10), 4770-4784. [1]

It has undergone minor edits prior to publication here, including changes to paragraph breaks and updated Figure labels.

2.2 Abstract

Display glasses meet the demands of the flat panel display industry vis-à-vis their composition, flatness, and forming processes. Here we report the high-resolution time-of-flight secondary ion mass spectrometry (ToF-SIMS) characterization of Corning® Eagle XG®, a widely used display glass, and subsequent chemometric analyses of these data. Samples analyzed included the as-formed glass, fracture surfaces from remelt bars, and as-formed surfaces subsequently exposed to process-relevant treatments including strong acids and bases, two industrial detergents, and an atmospheric-pressure plasma treatment. Elemental signals in the positive ion ToF-SIMS spectra respond to surface treatments. Acidic conditions leach non-silica components from the surfaces, while basic treatments extract these species less efficiently. The detergents leave residues of Na^+ and K^+. The atmospheric pressure (AP) plasma treatment had little effect on the surface

composition, while the melt surface differs significantly from the bulk fracture surface. Above ca. 75 m/z, the negative ion spectra are dominated by two series of homologous cluster ions with compositions of $Si_nO_{2n+2}Al^-$ and $Si_mHO_{2m+1}^-$. The presence of these clusters suggests that analogous structures exist at the near surface regions of the samples. In a series of MCR analyses, two or three MCR components captured > 95% of the variance in the data for these samples.

2.3 Introduction

Flat panel displays (FPDs) are ubiquitous in modern electronic devices. They are frequently found in televisions, laptops, smartphones, and tablets, to name only a few applications. FPDs are microfabricated devices. They can be made on glass, plastic, or other substrates. Of these, glass is currently the dominant substrate because of its superior material properties.[2-5] Current estimates for display glass production are ca. 460 million m^2/year.[3] The requirements on display glasses are stringent. Glass substrates for FPDs must (i) have a highly uniform, flat geometry, free from curvature, waves, or large deviations in thickness, (ii) have an excellent surface finish, including a low surface roughness and low particulate contamination, (iii) remain rigid throughout processing, (iv) be dimensionally stable at the highest processing temperatures used during display fabrication, (v) be chemically compatible with the circuitry manufactured on it, (vi) have excellent optical properties, and (vii) be able to withstand the harsh chemistries used during display fabrication.[2-3, 6] These requirements have resulted in the development of highly-engineered glass compositions that provide the desired bulk glass properties for display manufacture, as well as specialized forming processes to provide the precise geometry and surface finish required for microfabrication.[2] In general, these requirements are becoming increasingly demanding as

displays become larger, pixel size becomes smaller, and display glass panels become thinner.[3-4] Detailed reviews on the development of display glass can be found in the technical literature.[2, 6]

Surface chemistry influences important processes relevant to display manufacturing including thin film and particulate adhesion, the rate of surface contamination, charge build-up and discharge, conductivity, surface reactivity, chemical durability, glass strength, crack propagation, and water adsorption.[7-14] Because surface chemistry has such a profound influence on these properties, it has been identified as an important, but underrepresented, area of study for advancing the future of glass science.[15-16] That is, while the influence of surface chemistry on glass properties is recognized, its direct effect on the display fabrication process remains poorly understood. This is in part because few detailed surface characterizations of real-world display glasses have been reported. Nevertheless, the surface characterization of display glasses represents a significant challenge. For example, glass surface composition may vary from the bulk composition for a variety of reasons, including the loss of volatile species during glass formation, species migration to minimize surface free energy, and chemical/structural differences resulting from the difference in environment between the glass/air interface and the bulk glass.[17-20] In addition, the surface composition of display glasses is modified by exposure to production-line chemistries, with examples including acids, bases, detergents, plasmas, or adsorption or incorporation of tin on the surface of glasses made by the float process.[2, 21] The modifying effects of these treatments are complex and depend strongly on glass composition.[22-23] Therefore, any attempt to understand the surface chemistry of display glasses as it relates to display fabrication must take these factors into account.

Time-of-flight secondary ion mass spectrometry (ToF-SIMS) is a powerful tool for understanding the surface chemistry of materials. It has been applied extensively to glass surfaces,

especially in the areas of artifact identification/preservation and the chemical leaching of nuclear glasses.[18, 24-28] ToF-SIMS is sensitive to all the elements, including hydrogen, as well as their isotopes, giving it an advantage over other high-vacuum surface analysis techniques like low-energy ion scattering (LEIS) and X-ray photoelectron spectroscopy (XPS).[29-30] However, hydrogen detected by SIMS may come from various sources, including the adventitious hydrocarbon contamination on a sample surface. In addition, ToF-SIMS provides chemical information about materials vis-à-vis molecular fragments, giving it another advantage over comparable surface analysis techniques. SIMS is a very surface sensitive technique. The depth of analysis in static ToF-SIMS ranges from a few monolayers to the outer several nanometers of a material, depending on the sample analyzed and the analysis beam parameters.[31-34] Perhaps its most significant drawback is its matrix effect, which limits its use to semi-quantitative/qualitative measurements for complex matrices like glass.[31] This limitation is relaxed in the comparative analysis of a series of similar samples with similar matrices, such as those studied here.

ToF-SIMS spectra are generally complex, often containing hundreds or thousands of peaks.[35] Accordingly, ToF-SIMS spectral analysis sometimes focuses on only a small subset of the chemically relevant information. In the hands of a skilled operator, this approach can yield useful conclusions. However, it often ignores much of the information in the spectra. In contrast, statistical/chemometric techniques can consider much larger fractions of the information in data sets.[36] Among these, principal components analysis (PCA), hierarchical cluster analysis (HCA), and multivariate curve resolution (MCR) are widely used for categorizing/comparing spectra.[35, 37-43] A recent review discusses some of the numerous applications of chemometrics to ToF-SIMS data analysis.[36] Among the various chemometrics methods, MCR has the advantage that its loadings (pure component spectra) are presented with positive values, giving plots that look like

spectra and can be more intuitively interpreted. In contrast the orthogonality constraints of PCA often lead to negative (and positive) scores and loadings, which are often more abstract. Both PCA and MCR use 'scores' plots and 'loadings' plots to visualize data sets. An important goal of an MCR analysis is to define and identify the number of 'pure' component spectra that define a data set.[38] In MCR, loadings plots show which spectral features are associated with a certain pure component spectrum, while scores plots show how much of each pure component spectrum a sample contains. Accordingly, scores plots are often useful on their own for showing the degree of similarity or difference between certain sample types and for visualizing trends in data. However, loadings plots must be used to understand the chemical significance of scores plots.

In this study, we use ToF-SIMS to analyze Corning Eagle XG® a widely used display glass, with an aim towards understanding how its surface chemistry evolves during the manufacturing process. Eagle XG® is an alkali-free alkaline-earth modified boroaluminosilicate glass, manufactured using Corning Incorporated's fusion draw process. A description of the fusion-draw process and the development of this glass composition can be found elsewhere.[2] The glass surface was analyzed in its as-formed state, prior to any chemical treatments, and after exposure to certain model aqueous chemistries such as HCl, HF, two industrial detergents, and a model base (tetramethyl ammonium hydroxide, TMAH), as well as to an atmospheric-pressure plasma. We also analyzed a fracture surface to better understand the differences between the bulk composition and that of the as-formed surface. We first discuss the effects of the chemical treatments on the elemental composition of the glass.

HCl depletes the surface of B, Al, Mg, Ca, and Sr, leaving a surface that is relatively rich in silica. TMAH and the industrial detergents deplete these species to a lesser extent, and the detergents are a source of Na and K contamination. The fracture surface shows a significantly

higher concentration of B, Al, Mg, Ca, and Sr relative to the as-formed surface, suggesting that a silica-rich surface layer results during the glass forming process. We present multivariate curve resolution (MCR) analyses of the elemental compositions of the sample surface, and also of two homologous series of negative cluster ions. Based on widely accepted models of the SIMS process, these complex cluster ions are likely to be intact pieces of the glass network.[32, 44] In the case of the $Si_nO_{2n+2}Al^-$ type clusters, small peaks at lower mass show silicon substituted by additional aluminum, which suggests glass surface heterogeneity. For the fracture surface, there was a much higher fraction of $Si_nO_{2n+2}Al^-$ type clusters, while clusters of the form $Si_mHO_{2m+1}^-$ were dominant in the HCl-leached surface. The untreated surface fell somewhere between these two extremes. Our motivation for performing this work is to understand the surface composition of this important microfabrication substrate as it evolves during exposure to production-line chemistries. This work will serve as a foundation for future studies exploring the link between glass surface composition and surface-mediated processes and material properties such as reactivity, contamination, particulate adhesion, and static charge buildup and discharge. It will also help us understand how these properties/processes in turn impact the display fabrication process.

2.4 Introduction to Multivariate Curve Resolution (MCR)

Here, we provide a basic introduction to MCR. A more detailed description of the algorithms and constraints associated with this technique can be found elsewhere.[38]

MCR has its roots in classical least squares (CLS) analysis. In a simple embodiment of CLS, a pure spectrum is presumed to consist of component spectra, such that

$$(2.1)\ A = S \cdot C,$$

where **A** is the mixture (measured) spectrum, **S** is a matrix of pure component spectra, which are also measured, and **C** is a vector that corresponds to the weights or concentrations of the pure spectra. For completeness, we could write Equation (2.1) as

(2.2) $A = S \cdot C + E,$

where we have added, **E**, an error matrix. We assume here that the errors are randomly and normally distributed. If the error matrix, **E**, is ignored, we can solve Equation (2.1) for **C** to obtain:

(2.3) $C = (S^T S)^{-1} S^T A.$

Thus, if the pure component spectra are known, a best fit for **C** can be obtained. Note that this approach requires that the pseudo-inverse of **S**, $(S^T S)^{-1} S^T$, not be ill-conditioned.

Consider now the situation in which we have collected a series of mixture spectra, **A**, that we believe are based on a set of pure components, **S**, but where these pure spectra are unknown. Writing the problem in matrix notation for two pure components (more might be possible), we have:

(2.4) $\begin{bmatrix} A_{11} & & A_{1m} \\ A_{21} & & A_{2m} \\ A_{31} & \cdots & A_{3m} \\ \vdots & & \vdots \\ A_{n1} & & A_{nm} \end{bmatrix} = \begin{bmatrix} S_{11} & S_{12} \\ S_{21} & S_{22} \\ S_{31} & S_{32} \\ \vdots & \vdots \\ S_{n1} & S_{n2} \end{bmatrix} \begin{bmatrix} C_{11} & & C_{1m} \\ C_{21} & \cdots & C_{2m} \end{bmatrix},$

where we are again ignoring the error matrix, **E**. We again call the matrix on the left side of this equation **A**, and the first and second matrices on the right side of this expression **S** and **C**, respectively. Thus, we can write Equation (2.4) in an abbreviated fashion as:

(2.5) $A = S \cdot C.$

This equation is identical in form to Equation (2.1). However, as noted, both **S** and **C** are unknown in Equation (2.5). This is the fairly complex situation contemplated in MCR. However,

in a rather clever way, MCR finds the matrices $\mathbf{S}$ and $\mathbf{C}$ from the matrix $\mathbf{A}$, as follows. We first solve Equation (2.5) separately for both $\mathbf{C}$ and $\mathbf{S}$. Solving Equation (2.5) for $\mathbf{C}$ yields

$$(2.6) \quad \mathbf{C} = (\mathbf{S}^T\mathbf{S})^{-1}\mathbf{S}^T\mathbf{A},$$

and solving it for $\mathbf{S}$ gives:

$$(2.7) \quad \mathbf{S} = \mathbf{A}\mathbf{C}^T(\mathbf{C}\mathbf{C}^T)^{-1}.$$

At this point, we tell the MCR algorithm how many pure spectra, $\mathbf{S}$, should be in the system. The algorithm creates guesses for these pure spectra, and this estimate for the $\mathbf{S}$ matrix is inserted into Equation (2.6). The solution of this equation then yields a guess for the concentrations, $\mathbf{C}$. This $\mathbf{C}$ matrix is then inserted into Equation (2.7) to yield a new guess for $\mathbf{S}$. This process is continued, iteratively taking the result from one equation and inserting it into the other, until the results for $\mathbf{S}$ and $\mathbf{C}$ converge. Non-negativity constraints are imposed on the elements of $\mathbf{C}$ and $\mathbf{S}$ in this process. These constraints have a very important effect on the outcome of MCR – they make the pure spectra look like real spectra, which significantly increases the interpretability of the technique. Of course, these constraints are consistent with the fact that negative concentrations and absorbances are unphysical. The quality of the initial guesses has an important impact on the outcome of an MCR analysis, and various approaches exist for establishing these initial guesses. For example, the spectra that fall on the outer extremes of the hyperspace of the data are often representative of the pure components, and can be used as initial guesses.[38] In MCR, it is assumed that the components give a linear response, and that the noise across the spectrum, i.e., the error matrix $\mathbf{E}$, is homoscedastic. Appropriate preprocessing of the data may be required to correct for heteroscedasticity, non-linearity, and instrumental variation in response.[36] To determine the number of pure components in a system before performing MCR, it is common to use another chemometrics method, e.g., PCA.

2.5 Experimental

Untreated Eagle XG® samples were taken directly from the production line prior to any chemical or physical treatment and shipped in sealed containers that preserved one side of the glass in a clean and stable environment. This surface represented the cleaner "A-side" of the substrate, i.e., the side upon which transistors are constructed during panel manufacturing. Storage and transport in these containers effectively maintained a very low concentration of adventitious hydrocarbon at the sample surface, as confirmed by XPS to be about 4 - 5 atom%. These untreated Eagle XG® samples were packaged at a Corning facility in a cleanroom environment, with a controlled relative humidity of $40 \pm 10\%$. Samples of Eagle XG® extracted from these containers were subjected to wet chemical treatments using the chemistries and concentrations listed in Table 2.1. The industrial detergents here are alkaline mixtures containing some or all of the following bases: sodium hydroxide, potassium hydroxide, and tetramethyl ammonium hydroxide (TMAH). They additionally contain a proprietary mix of surfactants and chelators. 'Detergent 1', was provided to us by Corning Incorporated. Samples were treated by mixing/diluting a reagent or detergent with deionized water in a perfluorinated alkane (PFA) vial to a final volume of 50 mL. Ca. 20 mm x 90 mm pieces of Eagle XG® were chemically modified with each treatment. These were then cut to smaller sizes for storage and transportation to the analysis facility and for loading into the analysis instrument. The reagents were measured and delivered with 1 mL HDPE (high density polyethylene) syringes. The precision of this delivery method was verified gravimetrically using an analytical balance. After mixing, a vial was capped and agitated. For the samples treated at 60 °C, the vial was then submerged in a temperature-controlled water bath, and the temperature

was allowed to equilibrate for 20 – 30 minutes prior to sample introduction. No equilibration was necessary for the HF treatment, which was carried out at room temperature (the reagents were already at room temperature).

Table 2.1. Sample treatment conditions

Reagent	Grade	Supplier	Conc.	pH	Temp. (°C)	Time (m)
HCl	Optima®	Fisher Scientific	0.1 M	1*	60	10
HF	ACS	EMD	0.1 M	2*	20	10
TMAH	TraceSelect® Ultra	Fluka	0.1 M	11*	60	10
Detergent 1	N/R	N/R	1% v/v	12	60	10
Detergent 2	N/R	N/R	N/R	N/R	N/R	N/R

N/R = not reported. *Calculated pH.

After the wet chemical treatments, the samples were rinsed by decanting the solution in the PTFE vial, refilling it with deionized water, and decanting/refilling it again several times. The samples were then removed from the vial, rinsed for 1 minute with a spray of deionized water from a wash bottle, and blown dry with nitrogen. These samples were packaged in pre-cleaned glass vials for transport to the analysis facility. The samples treated at BYU were handled and packaged at the ambient humidity at Brigham Young University in Provo, Utah, where the building humidity was uncontrolled. Samples treated with another industrial detergent, designated 'Detergent 2' and/or atmospheric-pressure (AP) plasma, as well as control samples subjected to neither treatment, were also prepared at a Corning facility and shipped to us in the same type of storage containers described above for analysis. Detailed conditions of the AP plasma treatment were not quantified, but could be generally described as a plasma-cleaning in a mixture of clean dry air and nitrogen carried out at atmospheric pressure. All samples were extracted from their containers just prior to analysis. Samples used here come from two shipments of glass produced at the same production facility. Those labeled 'Untreated 1', 'HCl', 'HF', 'TMAH', and 'Detergent 1', came from one shipment, while 'Untreated 2', 'Detergent 2', 'Plasma' and 'Detergent 2 + Plasma' came

from another. For the fracture surface, 5 x 5 mm rectangular bars cut from annealed patties of remelted Eagle XG® were prepared. These were mounted in a cross-sectional holder, scored with a glass cutter, and fractured in air immediately prior to loading into the vacuum chamber for analysis.

ToF-SIMS was performed at the headquarters of IONTOF GmbH in Münster, Germany using af ToF-SIMS 5 instrument equipped with a bismuth cluster ion source. 30 keV Bi_3^+ clusters were used to probe the sample. A 100 x 100 μm area was analyzed. The samples received an ion dose of ca. 10^8 ions/cm^2, which was well below the static limit of 10^{13} ions per cm^2. Charge compensation was accomplished with an electron flood gun. Various normalization schemes for these ToF-SIMS signals for the radar plots (vide infra) were explored prior to data visualization, including normalization of each peak to the sum of the peak areas selected from that spectrum, normalization to the total ion count from the spectrum, and normalization to a signal from an isotope of Si^+. Of these, the total ion current proved unsatisfactory – it showed widely varying compositions from samples that were expected to be very similar. This may have been due to different levels of hydrocarbon contamination, which dominated the ion count. Normalization to the total area of the selected peaks appeared to work well in some cases, but also yielded some anomalous results, e.g., at least one signal (boron) appeared in high concentration that was shown by XPS to be in low concentration, and the normalized 30Si+ signal varied radically between the HCl and HF treated samples using this normalization scheme, while the raw 30Si+ signals varied by only ca. 1.6% between the two samples. Accordingly, we chose not to use this normalization scheme for plotting the data. The $^{28}Si^+$, $^{29}Si^+$ and $^{30}Si^+$ peaks were also considered as references. Of these, the $^{28}Si^+$ peak was too large – it showed more than one count per shot of primary ions (the detector was saturated). While a Poisson correction performed by the software may correct

for the effects of detector saturation, it is preferable to use a peak that does not require a numerical correction. Accordingly, the $^{29}Si^+$ and $^{30}Si^+$ peaks were considered. The $^{29}Si^+$ peak overlapped with the $^{28}SiH^+$ signal, while the $^{30}Si^+$ peak was well-resolved from neighboring peaks. The results obtained with the $^{30}Si^+$ signal agreed with our expectations of the materials, and were therefore chosen as the reference.

MCR was performed using the PLS toolbox version 8.1 (Eigenvector Research, Manson, WA) for Matlab (2015B version 8.6.0.2672246, Mathworks, Inc, Natick, MA). The analyses were performed on series of manually integrated peaks from the positive and negative ion spectra (see Appendix 1, Table A1.1). The first data set that was analyzed consisted of elemental signals from both the positive and negative ion spectra. The second analysis focused on higher mass (m/z > 75) cluster ions in the negative ion spectra. The third analysis included all of the integrated peaks from the positive and negative ion spectra. For each analysis, peak areas were assembled into a data matrix with signals from the different spectra (samples) in rows. The data were then preprocessed in two steps. In the first, all of the peak areas from a spectrum were normalized to an area of 1. In the cases where the MCR analysis included both positive and negative ion data, the positive and negative ion peak lists were normalized separately, such that all of the peaks in the separate data set summed to unity. This normalization, a row operation, was performed to account for signal intensity variation between the samples, etc. In the second step, a column operation, the data were Poisson-scaled, i.e. each column of normalized integrated peak areas was divided by the square root of their mean. This was done to account for the heteroscedastic (non-constant) nature of the noise inherent in ToF-SIMS data.[36, 45] To determine the number of pure components for MCR, a principal components analysis (PCA) was first performed. Here the data were normalized using the procedure outlined above, Poisson-scaled, and then mean-centered. In general, failure to mean-

center would unnecessarily introduce an additional PC into the model that would account for the distance between the mean of the data points and the origin, but not provide meaningful chemical information. The eigenvalue plots obtained by PCA were used to make an initial guess for the number of components in the MCR analyses. In all cases, PCA suggested 2-4 components.

2.6 Results and Discussion

2.6.1 Analysis of the Positive Ion Spectra

Positive ion ToF-SIMS detected all of the major elemental constituents of Eagle XG®, i.e., Si, Al, B, Mg, Ca, and Sr, as well as trace components at the surface like Na and K (see Figure 2.1). In addition, the spectra showed cluster ions in both the positive and negative ion spectra, e.g., $SiOH^+$, $SiH_2O_2^+$, $CaOH^+$, and two homologous series of negatively charged cluster ions that will be discussed below. The sample used to obtain the data in Figure 2.1 was removed from its sealed carrier just prior to analysis. Complementary XPS measurements of these surfaces generally showed less than 4 atom% adventitious hydrocarbon, as averaged over the information depth of XPS. Nevertheless, as is common in ToF-SIMS, hydrocarbon signals are found throughout the positive ion spectra of these surfaces, which accords with the greater surface sensitivity of the latter technique. Fortunately, the mass resolution in the spectra was 6500 - 7500 for most peaks, which was sufficient to distinguish between peaks with nominally identical m/z values (see Figure 2.2). Table A1.1 lists ions generated from the untreated surface, which appear to varying degrees in all of the spectra.

The elements identified in our spectral analyses were designated as major or minor components based on prior knowledge of the bulk glass composition. Various normalization schemes were considered for the resulting radar plots (vide supra). Figures 2.3 and 2.4 show a series of radar plots that compare the major and minor components, respectively, of the elements in the differently treated samples. The signals along each axis in these radar plots were linearly scaled so that the highest intensity peak had a value of unity. Figure 2.3A shows that both the HF and HCl treated surfaces were depleted (leached) of all major non-silica constituents relative to the untreated surface. Moreover, under the conditions explored herein, HCl appeared to leach the surface somewhat more effectively than HF. This observation accords with the expectation that mineral acids like HCl will efficiently leach network-modifying species, as well as soluble network-formers, leaving behind a silica-rich hydrated surface layer. HF-based chemistries meanwhile tend toward fluoride attack of the oxide network, and, in general, more congruent dissolution.[46] Our findings reveal however that, at the information depth of ToF-SIMS, a finite degree of leaching occurs in the acidic HF solution ahead of the dissolution front, leaving behind an ostensibly thin, but detectably altered, surface layer. Figure 2.4a similarly shows that HCl and HF leach the surface of its minor components, although HCl again appears to be quite a bit more effective. The HF treatment leaves behind Sn and K relative to the untreated surface. The source of potassium on these surfaces is not entirely clear, although again it is to be noted that differences in these normalized ion signals are comparative only, and likely represent a very small actual quantity on the surface.

Turning now to alkaline treatments, Figure 2.3B shows that TMAH and the detergents have a similar leaching effect on Ca, Mg, Sr, and B at the information depth of ToF-SIMS. As was the case for the HCl-treated surface, the network modifiers were somewhat more strongly leached than

boron, a network former. Interestingly, neither TMAH nor Detergent 2 appeared to substantially extract aluminum in a preferential sense from the surface, and the relative concentration of aluminum actually increased after the wash with Detergent 1. As for the minor/trace components, Figure 2.4B shows that TMAH and the detergents deplete the surfaces of Li^+, Sn^+, and Cs^+. However, it is significant that the detergents increase the surface concentrations of K and/or Na to ca. 40 times the levels found on the untreated surface. This observation is attributable to the fact that most commercial detergents designed to clean glass are alkaline in nature, and often contain mixtures of alkali hydroxides (NaOH, KOH) to enable slight dissolution of the glass and good cleaning efficiency. As a result, the increase in residual Na and/or K contaminants is clearly one way that commercial detergents can affect the glass surface after washing. That said, ToF-SIMS is exquisitely sensitive to these elements, and these concentrations may still be vanishingly small from a practical point of view, noting that these alkali metals are present at only trace levels in the bulk glass.

Figure 2.3C shows results from untreated/as-formed samples, versus those exposed to an atmospheric pressure (AP) plasma with or without a detergent wash. The yellow trace in Figure 2.3C comes from a sample that was washed with Detergent 2. The green trace represents a similar sample that was also detergent washed, but that underwent an additional AP plasma treatment. The results from these analyses are essentially identical. In a similar fashion, the blue trace in the figure is derived from an untreated sample, and the black trace is from a similar unwashed sample that was plasma-treated. These results are nearly identical. We conclude that the AP plasma had little or no effect on the inorganic composition of the surfaces here – it is probably helpful in removing organic contamination, but that capability was not probed here. The Untreated 1 and Untreated 2 samples in this figure came from different production batches. The corresponding traces in Figure

2.3C are fairly close together and have the same shape. The relatively small differences between them may be due to batch-to-batch variability or differences in the environments the samples were exposed to in transit to analysis. Figure 2.4C similarly shows that the 'Detergent 2' and 'Detergent 2 + Plasma' and also the 'Untreated 2' and 'Plasma' surfaces are very similar. Also, Detergent 2 leaves strong Na and K residues on the samples. The 'Untreated 2' and 'Plasma' samples again follow the shape of the 'Untreated 1' sample fairly well, except at the Cs signal, but this signal was quite weak and is clearly a very minor/trace species on the glass surface.

Figure 2.3D shows considerable differences between the as-formed and fracture Eagle XG® surfaces, the latter being taken to be representative of the bulk glass composition. These findings indicate that all of the major components in the as-formed surface are significantly depleted relative to the bulk composition. While the measured differences are not quite so large in Figure 2.4D, and the K signal from the two surfaces is essentially the same, the untreated surface is again noticeably depleted of most inorganic ion species compared to the fracture surface. These stark differences between surface and bulk composition have previously been observed to occur as a function of forming operation, thermal history, and surface preparation,[18-19] and this system is no exception: knowledge of the bulk composition of a glass is insufficient to understand its surface. That is, the results presented herein demonstrate that it is difficult to infer the surface composition from the bulk composition and vice versa.

2.6.2 Analysis of the Negative Ion Spectra

The low mass region of the negative ion spectrum in Figure 2.5 is dominated by peaks attributable to the elements and small cluster ions, e.g., H^-, O^-, C_2H^-, SiO^-, and $SiOH^-$. However,

the most interesting features in this spectrum occur at higher mass, where two homologous series of peaks appear. These ions have formulas $Si_nO_{2n+2}Al^-$ and $Si_mHO_{2m+1}^-$, where ions with m and n values of 1 – 6 are shown in Figure 2.5. As a guide to the eye, these peaks are enclosed in dashed red lines. Interestingly, as seen in the high-resolution views (see Figure 2.6), these peaks do not appear alone. As expected, to their high mass side we see isotope peaks, i.e., the same clusters but with ^{29}Si or ^{30}Si, or the base cluster with an additional proton. In the case of the $Si_nO_{2n+2}Al^-$ cluster ions, peaks at lower mass are present that are attributable to Si substituted by Al (most often both have tetrahedral coordination in glassy networks).[47-48] The peak envelopes containing the $Si_mHO_{2m+1}^-$ ions appear to be composed of overlapping signals from the unprotonated and protonated clusters with their associated isotopologues. Similar cluster ions have been observed in ToF-SIMS spectra of silicon's native oxide.[49] These assignments were confirmed by a classical least squares fit of the peak envelope to the isotope patterns of the given protonated and deprotonated ions, e.g., SiO_3^-, SiO_3H. Appendix 1, Figure A1.1, compares these fits to the raw data for the untreated sample. The Appendix 1 also includes a spreadsheet showing all of the CLS fits for the samples not shown in the figure.

2.6.3 MCR Analysis of the ToF-SIMS Spectra

While the manual analysis of the data above proved useful, it considered only a handful of peaks out of the hundreds present. MCR allowed us to examine a greater number of signals, and to visualize how the samples group vis-à-vis the expected variable reduction. We narrowed the scope of our MCR analysis to three sets of peaks that had been individually integrated. In the first analysis, we selected all of the elemental peaks we could identify in both the positive and negative

ion spectra, with the goal of understanding how the elemental compositions of the samples evolve with chemical treatment. In the second analysis, the high-mass (m/z ≥ 75) clusters in the negative ion spectra were analyzed. The third and final analysis used all of the integrated peaks listed in Table A1.1. The advantage of narrowing the focus of these analyses is that it greatly simplifies interpretation and reduces the chance of modeling peaks/regions that are not of interest, e.g., hydrocarbon peaks, or regions where there is only baseline signal. The potential drawback to this approach is that some of the variance in the spectra is still not considered.

For the first analysis (the elemental analysis), the exploratory PCA suggested 2 – 3 components. However, the corresponding two-component MCR model, shown in Appendix 1, placed the fracture surface at one end of a continuum and the HCl-treated and untreated surfaces at the other. This result was inconsistent with our radar plots, which showed significant differences between the untreated and HCl-treated surfaces. Also in this model, the Q-residuals for the fracture surface fell outside of its 95% confidence interval. The three-component MCR analysis of the data is shown in Figure 2.7. Here, most of the samples fall on a line/trajectory between the fracture surface, which is expected to be the least leached/richest in network modifiers, and the HCl-treated sample, which is the most modifier-leached/silica-rich. The samples treated with detergents fall on a different trajectory due to the presence of Na and K contamination. These results agree with our radar plots (see Figures 2.3-2.4). In this three-component model, one sample ('Detergent 1') had Q-residuals outside of the 95% confidence limits due to a high concentration of Na on this sample, which was poorly captured by the model.

The pure component loadings for the three-component model of the elemental species are shown together with the peak selections corresponding to the 'HCl', 'Fracture', and 'Detergent 2 + Plasma' samples in Figure 2.8. Component 1 closely matches the elemental composition of the

'HCl' sample, Component 2 is quite similar to the 'Fracture' surface, and Component 3 closely resembles the 'Detergent 2 + Plasma' surface. Samples with high scores on Component 1 have relatively high concentrations of H^+, Si^+, H^-, O^-, and Si^-, and low concentrations of Na^+, K^+ Mg^+, Ca^+, Sr^+ and Al^+. Accordingly, Component 1 represents the degree of leaching from the glass surface. Samples with high scores on Component 2 have high concentrations of Mg^+, Al^+, Ca^+, and B^+, and low Si^+, H^+, Na^+, and K^+ signals. This component is essentially measuring the concentration of the modifiers/non-silica species. Therefore, samples falling on the trajectory between Components 1 and 2 are ordered according to their degree of leaching. Component 3 shows high Na^+ and K^+, moderate levels of H^+, Al^+, Si^+, and relatively low levels of H^- and O^-. It captures the surface contaminants introduced by detergent treatment. While Li, Ti, Sn, Cl, and Br were detected in trace amounts on the sample surfaces, they appear to contribute little to this model.

MCR was next performed on the high-mass (m/z >75) cluster ions in the negative ion spectra. Based on the widely accepted precursor model and subsequent modifications thereof, the higher mass cluster ions are likely to be intact pieces of the glass network.[32, 44] Therefore, these species represent an interesting subject for analysis. An initial exploratory analysis by PCA suggested 2-3 principal components for this model. Both two- and three-component MCR models could discriminate between sample treatments. The two-component scores plot, shown in Figure 2.9, was the easiest to interpret. This model placed the samples on a continuum ranging from the fracture surface to the HCl-treated surface.

The loadings for these components (see Appendix 1) closely resemble the corresponding 'spectra' from the fracture and HCl-treated surfaces. Samples closer to the HCl-treated surface in the scores plot were richer in $Si_mHO_{2m+1}^-$ clusters, while samples closer to the fracture surface were richer in $Si_nO_{2n+2}Al^-$ clusters. While the small peaks surrounding the major cluster ion peaks were

included in the model, they had little influence due to their low intensities, such that the model focused primarily on the main peaks in the homologous series described above (see also Appendix 1). As expected, the $Si_nO_{2n+2}Al^-$ clusters are correlated with each other in one component (appear with significant intensities), while the $Si_mHO_{2m+1}^-$ clusters are correlated with each other in the second. In this analysis, the HF-treated sample is relatively similar to the HCl-treated sample. The untreated, plasma-treated, TMAH-treated, and detergent treated samples fall somewhere in the middle of the trajectory, indicating that these treatments have little effect on the generated cluster ions relative to the untreated surface. The 'Detergent 1' sample falls closer to the fracture surface than the other samples. This agrees with the radar plots, which show aluminum enrichment for this sample. In summary, this analysis suggests that the cluster ions formed by ToF-SIMS are sensitive to surface treatment, and indicate that the glass structure within the information depth of the sample surfaces also varies as a function of chemical treatment. In the three-component MCR model (see Appendix 1) the Fracture and HCl-treated surfaces are found at the extremes of two of the components, and the detergent treated, plasma-treated, and untreated surfaces are described more fully by the third component.

In a final MCR analysis, all of the peaks listed in Table A1.1 were considered in a single model with the goal of understanding the variance within the samples while considering as many signals as possible. Here, the exploratory PCA analysis indicated up to four PCs, and an MCR model using four components was initially attempted (see Appendix 1). It provided good discrimination between all sample types. However, the fourth component mostly captured the difference between samples treated with Detergents 1 and 2. Given that the fourth component was only useful for one of the samples, a three-component model was selected. The scores plot for this model is shown in Figure 2.10. The sample groupings on this plot are similar to those obtained in

the first MCR analysis. Here, the 'HCl', 'Plasma + Detergent 2' and 'Fracture' samples have the highest scores on Components 1, 2, and 3, respectively. The chemically treated samples fall along a trajectory between Components 1 and 2, while the untreated/plasma treated samples and the fracture surface fall on a trajectory between Components 1 and 3. The loadings plots for this model (Figure 2.11) show that the elemental species from the positive and negative ion spectra as well as the high mass cluster ions in the negative ion spectra are strongly influential in this model. The fact that the groupings here correspond so closely to those in the elemental MCR analysis indicates a strong correlation between the elemental composition of the samples and the cluster ions generated from them.

2.7 Conclusion

The surface composition of nominally-alkali-free display glasses like Eagle XG® can change markedly in response to aqueous production-line chemistries. For example, acids leach the surface of non-silica components, while bases/detergents studied here deplete Ca, Mg, Sr, and B, to a lesser extent than the acids. Treatment with 'Detergent 1' leaves the surface enriched in aluminum, and treatment with either of two detergents leaves a residue of sodium and/or potassium (ca. a 40-fold increase relative to the untreated surface). However, the ToF-SIMS results here are insufficient to establish absolute concentrations of these species, which may be quite low given the exquisite sensitivity of the technique to the alkali metals. We observe significant differences between the compositions of the fracture and as-formed surfaces, wherein the as-formed surface is depleted in all of the major non-silica glass constituents (Al, B, Mg, Ca, Sr). The difference between these two surfaces is greater than those between the as-formed surface and any of the

chemically-treated surfaces, which suggests that the as-formed surface of Eagle XG$^{\circledR}$ naturally forms a silica-rich surface layer on some scale during production.

The negative ion spectrum contains two series of homologous cluster ions with formulas $Si_nO_{2n+2}Al^-$ and $Si_mHO_{2m+1}^-$, n = 1 – 6 and m = 1 – 6. These dominant peaks show their corresponding isotopologues, and the $Si_nO_{2n+2}Al^-$ ions appear with a series of peaks at lower mass that can be attributed to substitution of the Si in the clusters with Al. These peaks are likely representative of near-surface structural units. An MCR analysis of these peaks shows that their composition changes in response to surface treatment, with the fracture surface showing a relatively high concentration of $Si_nO_{2n+2}Al^-$ clusters, and the leached surfaces showing a higher fraction of $Si_mHO_{2m+1}^-$ ions. There appears to be little difference in the cluster ions between the untreated, plasma-treated, and 'Detergent 2' samples. However, the 'Detergent 1' sample, which showed aluminum enrichment in the radar plot analysis, also appears to have a higher fraction of $Si_nO_{2n+2}Al^-$ ions than the untreated surface. These results suggest that these cluster ions are indicative of the near-surface glass structure.

In general, the MCR analyses performed herein provided a useful way to visualize how the samples group and to quickly understand what differentiates them. In all cases, the samples appear to group based on their degree of leaching, with the fractured surface falling at one end of a continuum, and the HCl-treated sample falling at another. For the elemental analysis and that of all the integrated peaks, a third dimension was needed in the models to account for surface contaminants introduced by the detergents. Here, the untreated surface appears roughly in the middle of a continuum between the fracture surface and the HCl-treated surface, indicating that it is relatively depleted of non-silica glass constituents compared to the bulk composition, and that acidic conditions further leach elements from its surface. The final MCR analysis, which

considered all of the integrated peaks in Table A1.1, gave groupings very similar to those in the elemental analysis. This, together with the loadings plots from the model, suggests that the cluster ion composition and the elemental composition are closely correlated.

The ultimate goal of this analysis is to provide a framework for understanding the link between display glass surface composition and surface attributes critical to performance in end use. Careful characterizations, like this one, are important first steps to understanding the glass surface so that topics like glass contamination behavior or surface reactivity can be understood as a function of surface composition.

2.8 Acknowledgments

2.9 Figures
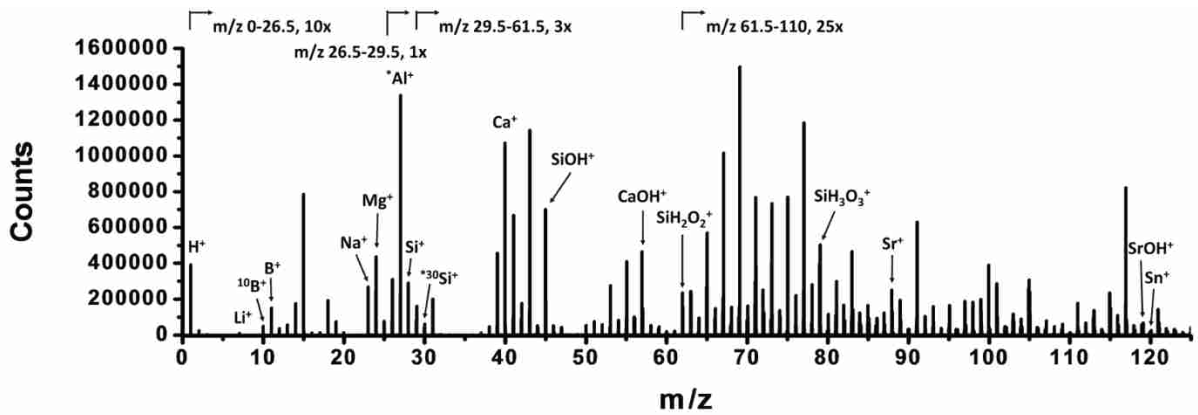
Figure 2.1. Positive ion ToF-SIMS spectrum for the untreated surface of Eagle XG®. The peak for Al in this low-resolution view appears large because of an interfering hydrocarbon peak.
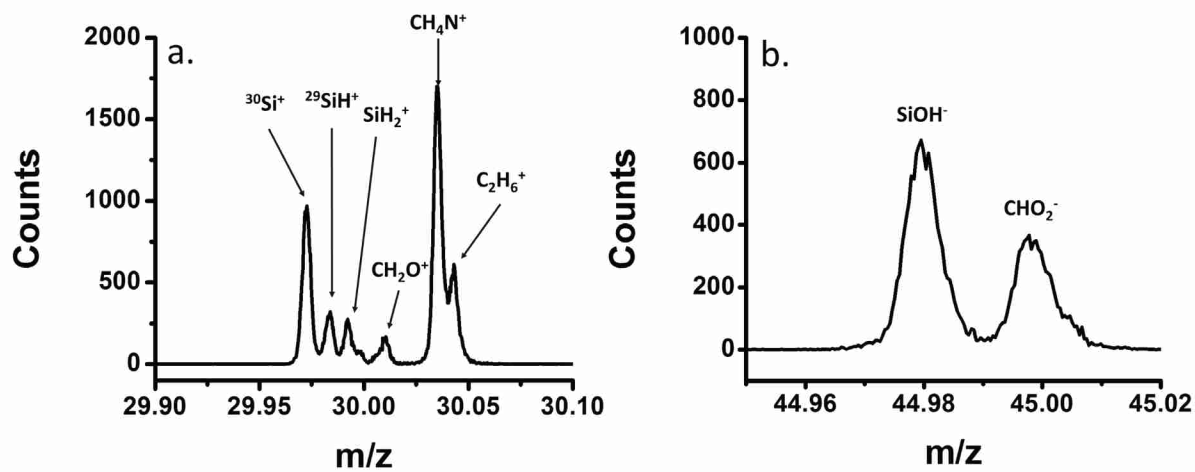
Figure 2.2. High resolution mass spectra from the untreated Eagle XG® surface, showing differentiation between organic and inorganic species for the (a) positive and (b) negative ion spectra.
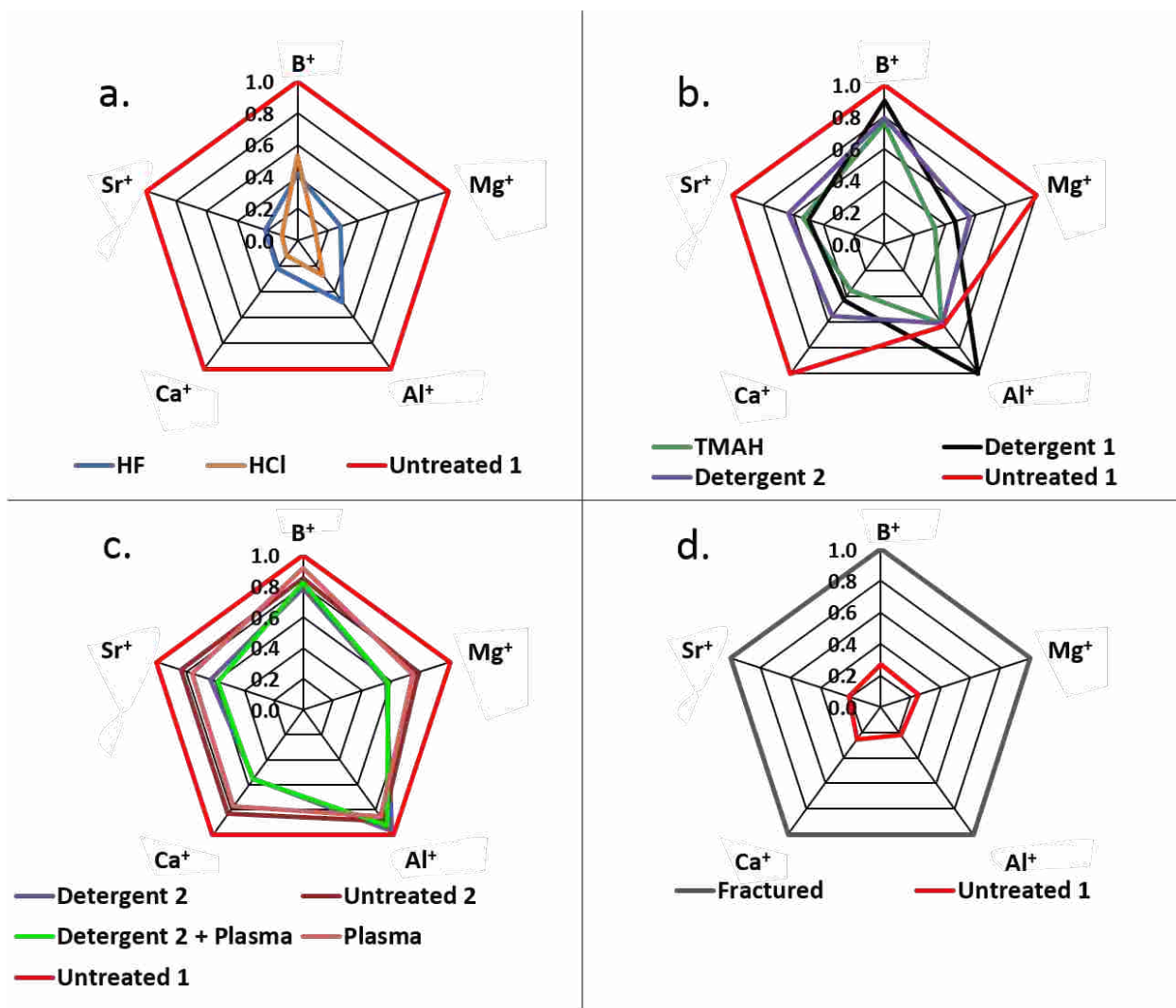
Figure 2.3. Radar plots comparing relative ToF-SIMS ion elemental signals for the major glass components (network formers and modifiers) from different Eagle XG® surfaces, as normalized to the $^{30}Si^+$ signal.
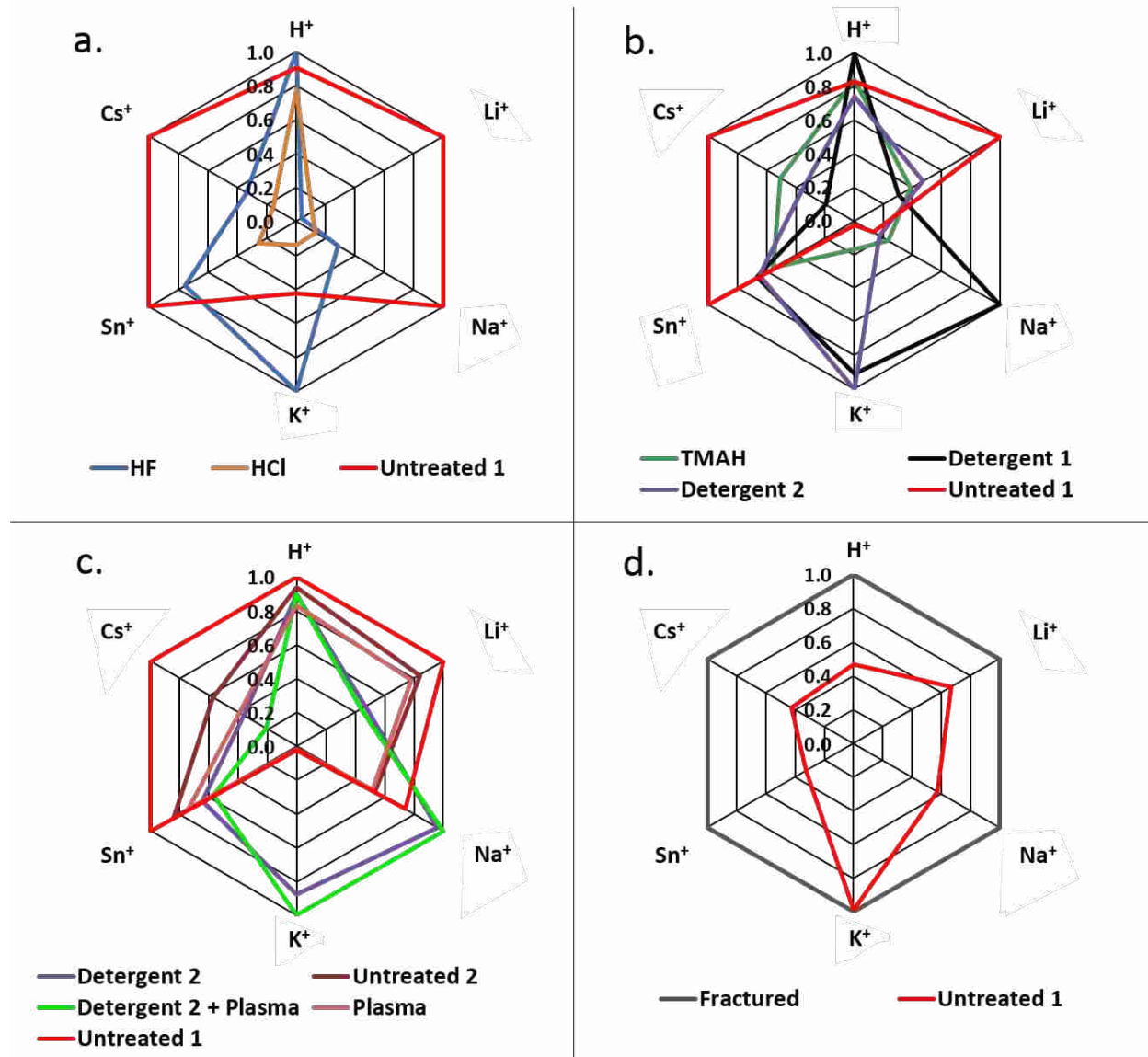
Figure 2.4. Radar plots comparing relative ToF-SIMS ion signals for minor and contaminant species from different Eagle XG surfaces, as normalized to the $^{30}Si^+$ signal.
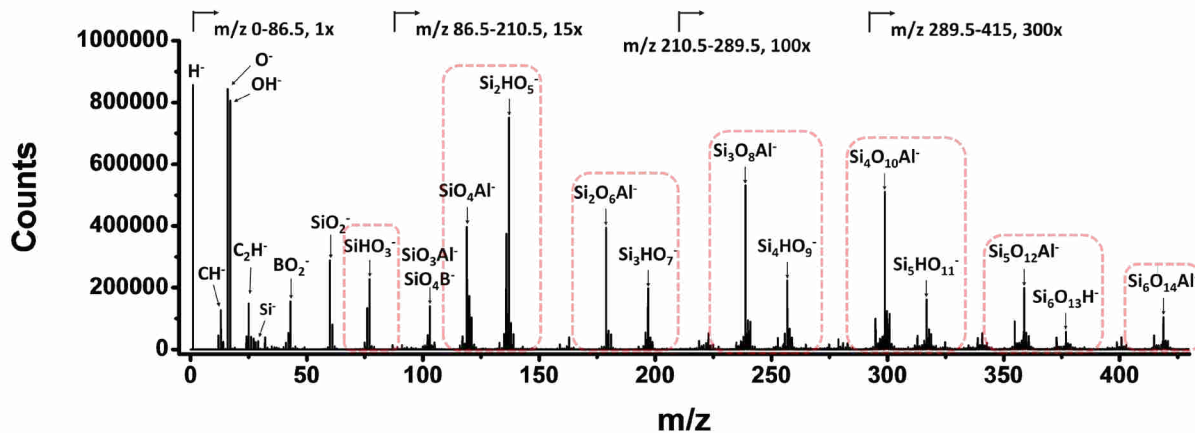
Figure 2.5. Low resolution negative ion mass spectrum of untreated Eagle XG®. Red squares are a guide to the eye to show peaks in homologous series.
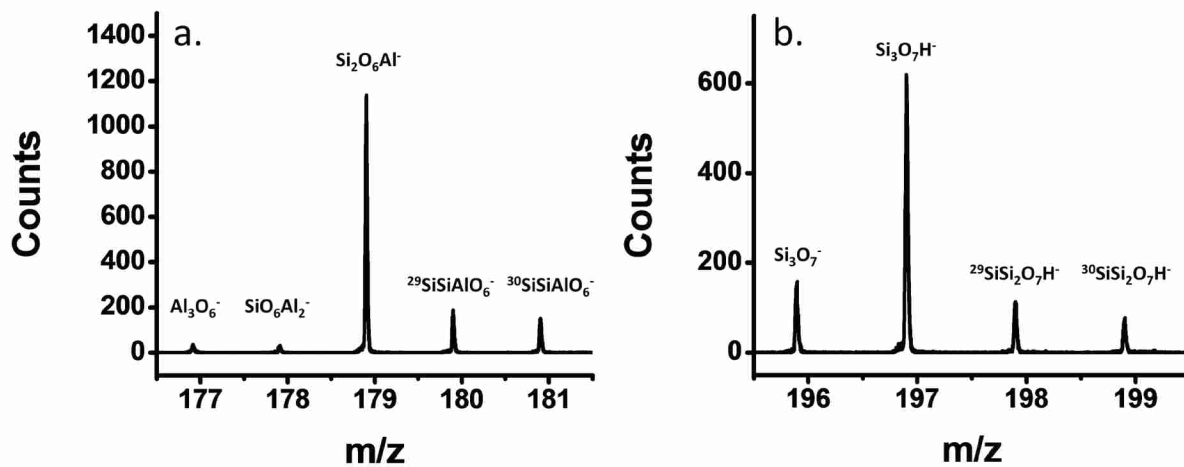
Figure 2.6. High resolution views of the peaks surrounding a $Si_2O_6Al^-$ cluster (a) and a $Si_3O_7H^-$ cluster (b).
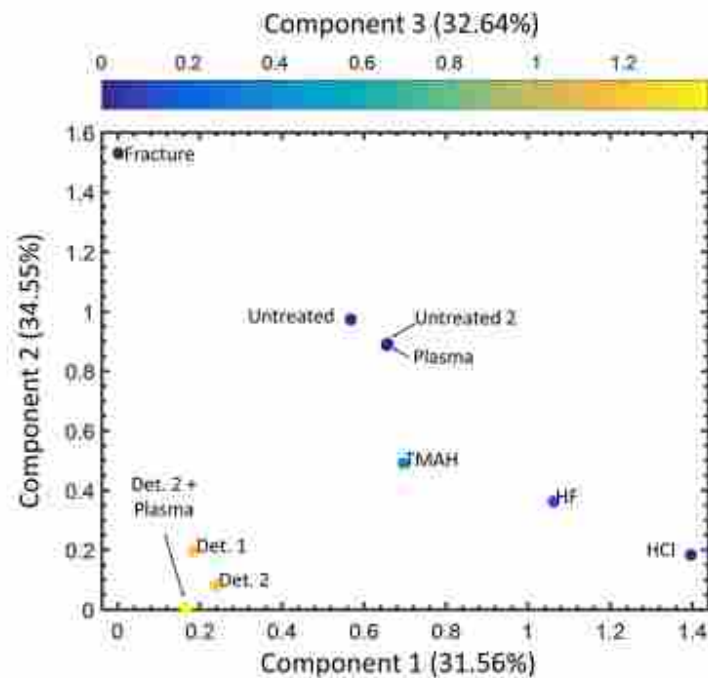
Figure 2.7. Scores plot for the MCR analysis of the elemental components of glass samples. The loadings for the pure component spectra are shown in Figure 2.8.
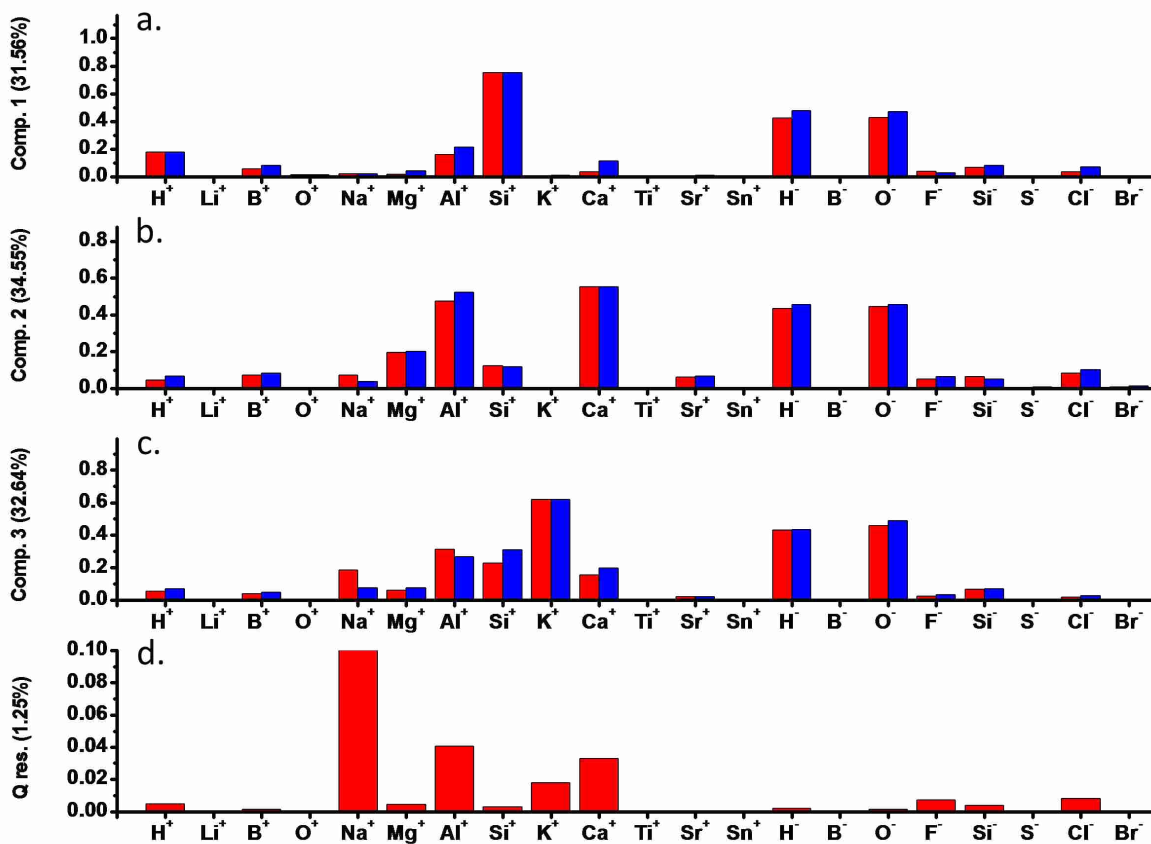
Figure 2.8. Loadings plots for MCR analysis of elemental species shown in Figure 2.7, compared to selected preprocessed spectral data. (a) Component 1 (red) compared to 'HCl' sample (blue). (b) Component 2 compared to 'Fracture' sample. (c) Component 3 compared to 'Detergent 2 + Plasma' sample. Here, the preprocessed spectral data has been divided by a scaling factor so that the most intense peaks in each graph have the same intensity.
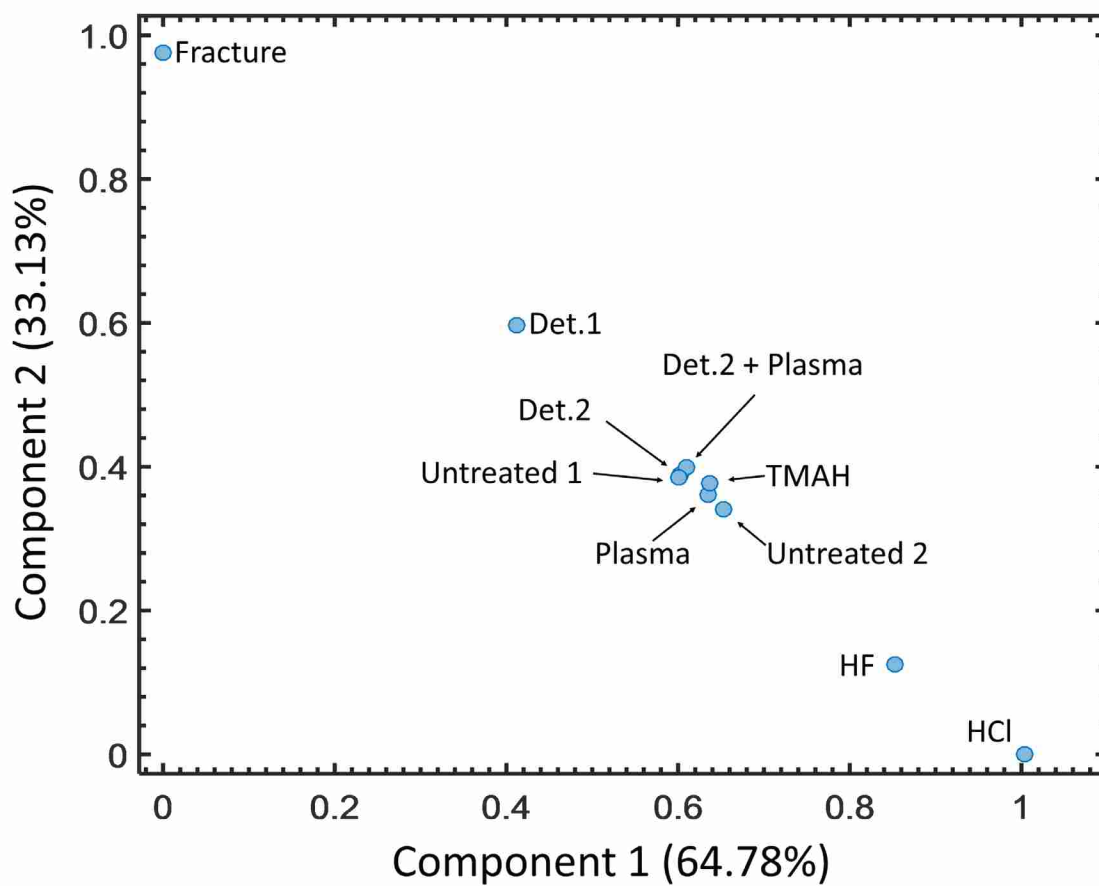
Figure 2.9. Scores on two component MCR of negative cluster ions. The loadings for the pure component spectra are shown in Figure A1.3 of Appendix 1.
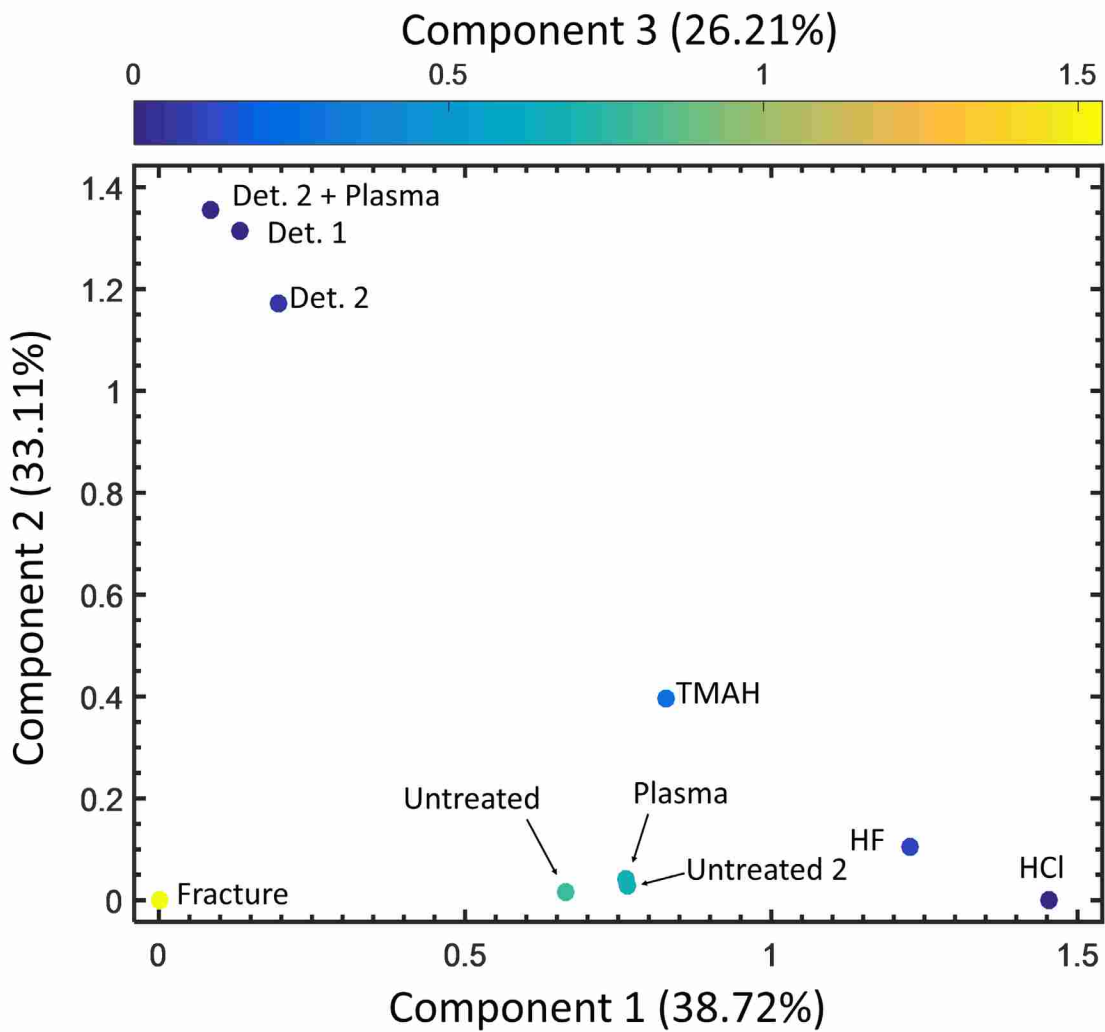
Figure 2.10. Scores for 3 component MCR of all integrated species shown in Table A1.1. The loadings

for the pure component spectra are shown in Figure 2.11.
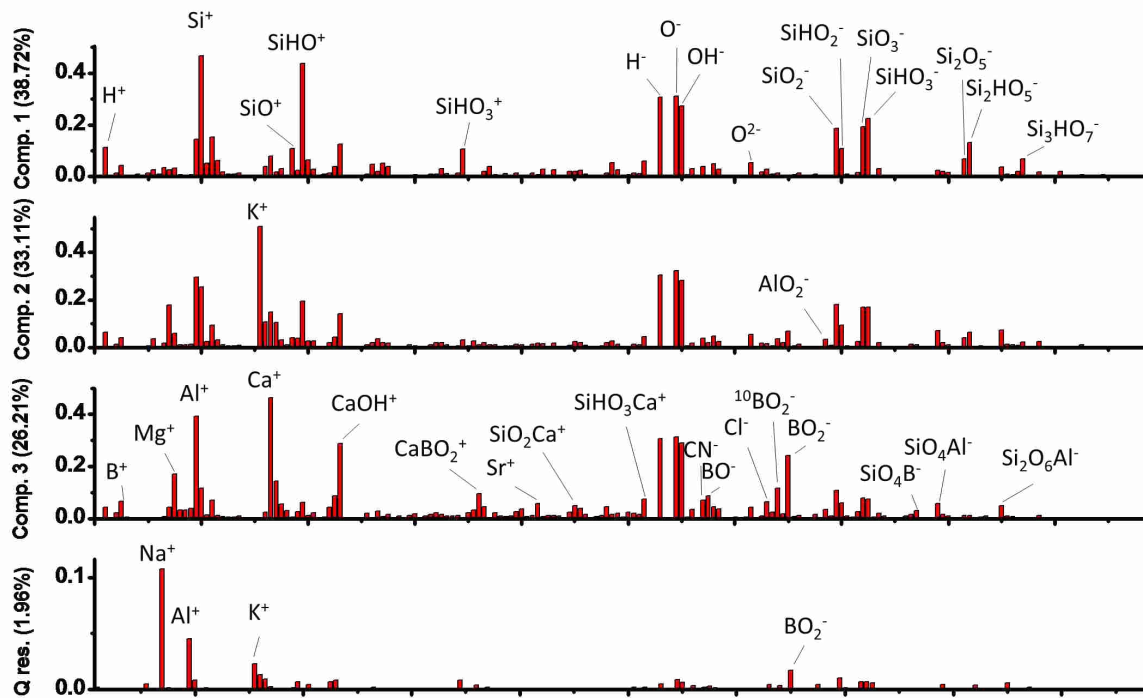
Figure 2.11. Loadings plot associated with MCR analysis shown in Figure 2.10, with prominent peaks labeled.

2.10 References

1.   Cushman, C. V.; Zakel, J.; Sturgell, B. S.; Major, G. I.; Lunt, B. M.; Bruner, P.; Grehl, T.; Smith, N. J.; Linford, M. R. Time-of-flight secondary ion mass spectrometry of wet and dry chemically treated display glass surfaces. *Journal of the American Ceramic Society* **2017,** *100* (10), 4770-4784.

2.   Ellison, A.; Cornejo, I. A. Glass Substrates for Liquid Crystal Displays. *International Journal of Applied Glass Science* **2010,** *1* (1), 87-103.

3.   Choi, Y. S.; Yun, J. U.; Park, S. E. Flat Panel Display Glass: Current Status and Future. *Journal of Non-Crystalline Solids* **2016,** *431*, 2-7.

4.   Hamilton, L. L. Display Innovations Through Glass. *Japanese Journal of Applied Physics* **2016,** *55*, 03CA01.

5.   Bocko, P. L.; Trott, G. R. In *Glass for the Future: Displays and Semiconductors*, 2013 Symposium on VLSI Circuits, IEEE: 2013; pp C86-C89.

6.   Kloss, T.; Lautenschläger, G.; Schneider, K. Advances in the Process of Floating Borosilicate Glasses and some Recent Applications for Specialty Borosilicate Float Gslasses. *Glass technology* **2000,** *41* (6), 177-181.

7.   Hair, M. L. Hydroxyl groups on silica surface. *Journal of Non-Crystalline Solids* **1975,** *19*, 299-309.

8.   Takeda, S.; Yamamoto, K.; Hayasaka, Y.; Matsumoto, K. Surface OH group governing wettability of commercial glasses. *Journal of non-crystalline solids* **1999,** *249* (1), 41-46.

9.   Wikby, A. Chemical and electrical properties of the surface layers of some glass electrodes. *Electrochimica Acta* **1974,** *19* (7), 329-336.

10.   Wiederhorn, S. Influence of Water Vapor on Crack Propagation in Soda-Lime Glass. *Journal of the American Ceramic Society* **1967,** *50* (8), 407-414.

11.   Wondraczek, L.; Mauro, J. C.; Eckert, J.; Kühn, U.; Horbach, J.; Deubener, J.; Rouxel, T. Towards ultrastrong glasses. *Advanced Materials* **2011,** *23* (39), 4578-4586.

12.   Striepe, S.; Deubener, J.; Smedskjaer, M. M.; Potuzak, M. Environmental effects on fatigue of alkaline earth aluminosilicate glass with varying fictive temperature. *Journal of Non-Crystalline Solids* **2013,** *379*, 161-168.

13.   Leed, E. A.; Sofo, J. O.; Pantano, C. G. Electronic structure calculations of physisorption and chemisorption on oxide glass surfaces. *Physical Review B* **2005,** *72* (15), 155427.

14.   Agnello, G.; Hamilton, J.; Manley, R.; Streltsova, E.; LaCourse, W.; Cormack, A. Investigation of Contact-Induced Charging Kinetics on Variably Modified Glass Surfaces. *Applied Surface Science* **2015,** *356*, 1189-1199.

15.   Mauro, J. C.; Philip, C. S.; Vaughn, D. J.; Pambianchi, M. S. Glass science in the United States: current status and future directions. *International Journal of Applied Glass Science* **2014,** *5* (1), 2-15.

16.   Mauro, J. C. Grand challenges in glass science. *Frontiers in Materials* **2014,** *1*, 20.

17.   PANTANO, C. G.; BEALL, D. M.; CERMIGNANI, W. Surface Studies of Borate Glasses. *BORATE GLASSES, CRYSTALS & MELTS* **1997**, 239.

18.   Bach, H. Advanced surface analysis of silicate glasses, oxides and other insulating materials: a review. *Journal of non-crystalline solids* **1997,** *209* (1), 1-18.

19.   Schaut, R. A.; Lobello, R. A.; Mueller, K. T.; Pantano, C. G. Characterization of boroaluminosilicate glass surface structures by B K-edge NEXAFS. *Journal of Non-Crystalline Solids* **2011,** *357* (19), 3416-3423.

20.   Wood, J. G.; Prabakar, S.; Mueller, K. T.; Pantano, C. G. The effects of antimony oxide on the structure of alkaline-earth alumino borosilicate glasses. *Journal of non-crystalline solids* **2004,** *349,* 276-284.

21.   Synowicki, R. A.; Johs, B. D.; Martin, A. C. Optical properties of soda-lime float glass from spectroscopic ellipsometry. *Thin Solid Films* **2011,** *519* (9), 2907-2913.

22.   Hench, L.; Clark, D. E. Physical chemistry of glass surfaces. *Journal of Non-Crystalline Solids* **1978,** *28* (1), 83-105.

23.   Hench, L. Characterization of glass corrosion and durability. *Journal of non-crystalline solids* **1975,** *19,* 27-39.

24.   Melcher, M.; Wiesinger, R.; Schreiner, M. Degradation of glass artifacts: application of modern surface analytical techniques. *Accounts of chemical research* **2010,** *43* (6), 916-926.

25.   Portal, S.; Sempere, R. Study of alkali silicate glass corrosion using spectroscopic ellipsometry and secondary ion mass spectrometry. *Physics and Chemistry of Glasses* **2003,** *44* (4), 303-307.

26.   De Bardi, M.; Hutter, H.; Schreiner, M. ToF-SIMS analysis for leaching studies of potash–lime–silica glass. *Applied Surface Science* **2013,** *282,* 195-201.

27.   Cailleteau, C.; Angeli, F.; Devreux, F.; Gin, S.; Jestin, J.; Jollivet, P.; Spalla, O. Insight into silicate-glass corrosion mechanisms. *Nature materials* **2008,** *7* (12), 978-983.

28.   Geisler, T.; Janssen, A.; Scheiter, D.; Stephan, T.; Berndt, J.; Putnis, A. Aqueous corrosion of borosilicate glass under acidic conditions: a new corrosion mechanism. *Journal of Non-Crystalline Solids* **2010,** *356* (28), 1458-1465.

29.   Cushman, C. V.; Brüner, P.; Zakel, J.; Major, G.; Lunt, B. M.; Grehl, T.; Smith, N. J.; Linford, M. R. Low Energy Ion Scattering (LEIS). A Practical Introduction to its Theory, Instrumentation, and Applications. *Analytical Methods* **2016**.

30.   Gupta, V.; Ganegoda, H.; Engelhard, M. H.; Terry, J.; Linford, M. R. Assigning Oxidation States to Organic Compounds via Predictions from X-ray Photoelectron Spectroscopy: A Discussion of Approaches and Recommended Improvements. *Journal of Chemical Education* **2014,** *91* (2), 232-238.

31.   Benninghoven, A. Surface analysis by secondary ion mass spectrometry (SIMS). *Surface Science* **1994,** *299,* 246-260.

32.   van der Heide, P., Sputtering and Ion Formation. In *Secondary Ion Mass Spectrometry*, John Wiley & Sons, Inc.: 2014; pp 44-143.

33.   Delcorte, A.; Leblanc, C.; Poleunis, C.; Hamraoui, K. Computer Simulations of the Sputtering of Metallic, Organic, and Metal–Organic Surfaces with Bi n and C60 Projectiles. *The Journal of Physical Chemistry C* **2013,** *117* (6), 2740-2752.

34.   Szakal, C.; Kozole, J.; Russo Jr, M. F.; Garrison, B. J.; Winograd, N. Surface sensitivity in cluster-ion-induced sputtering. *Physical review letters* **2006,** *96* (21), 216104.

35.   Graham, D. J.; Wagner, M. S.; Castner, D. G. Information from complexity: Challenges of TOF-SIMS data interpretation. *Applied surface science* **2006,** *252* (19), 6860-6868.

36.   Graham, D. J.; Castner, D. G. Multivariate analysis of ToF-SIMS data from multicomponent systems: the why, when, and how. *Biointerphases* **2012,** *7* (1), 49.

37.   Pacholski, M. L. Principal component analysis of TOF-SIMS spectra, images and depth profiles: an industrial perspective. *Applied surface science* **2004,** *231,* 235-239.

38.   Gallagher, N. B.; Shaver, J. M.; Martin, E. B.; Morris, J.; Wise, B. M.; Windig, W. Curve resolution for multivariate images with applications to TOF-SIMS and Raman. *Chemometrics and intelligent laboratory systems* **2004,** *73* (1), 105-117.

39.   Pei, L.; Jiang, G.; Tyler, B. J.; Baxter, L. L.; Linford, M. R. Time-of-flight secondary ion mass spectrometry of a range of coal samples: a chemometrics (PCA, cluster, and PLS) analysis. *Energy & Fuels* **2008,** *22* (2), 1059-1072.

40.   Zhang, F.; Gates, R. J.; Smentkowski, V. S.; Natarajan, S.; Gale, B. K.; Watt, R. K.; Asplund, M. C.; Linford, M. R. Direct adsorption and detection of proteins, including ferritin, onto microlens array patterned bioarrays. *Journal of the American Chemical Society* **2007,** *129* (30), 9252-9253.

41.   Yang, L.; Bennett, R.; Strum, J.; Ellsworth, B. B.; Hamilton, D.; Tomlinson, M.; Wolf, R. W.; Housley, M.; Roberts, B. A.; Welsh, J. Screening phosphatidylcholine biomarkers in mouse liver extracts from a hypercholesterolemia study using ESI-MS and chemometrics. *Analytical and bioanalytical chemistry* **2009,** *393* (2), 643-654.

42.   Yang, L.; Shirahata, N.; Saini, G.; Zhang, F.; Pei, L.; Asplund, M. C.; Kurth, D. G.; Ariga, K.; Sautter, K.; Nakanishi, T. Effect of surface free energy on PDMS transfer in microcontact printing and its application to ToF-SIMS to probe surface energies. *Langmuir* **2009,** *25* (10), 5674-5683.

43.   Lee, M. V.; Hoffman, M. T.; Barnett, K.; Geiss, J.-M.; Smentkowski, V. S.; Linford, M. R.; Davis, R. C. Chemomechanical nanolithography: nanografting on silicon and factors impacting linewidth. *Journal of nanoscience and nanotechnology* **2006,** *6* (6), 1639-1643.

44.   Benninghoven, A. Some aspects of secondary ion mass spectrometry of organic compounds. *International Journal of Mass Spectrometry and Ion Physics* **1983,** *53*, 85-99.

45.   Keenan, M. R.; Kotula, P. G. Accounting for Poisson noise in the multivariate analysis of ToF-SIMS spectrum images. *Surface and interface analysis* **2004,** *36* (3), 203-212.

46.   Spierings, G. Wet chemical etching of silicate glasses in hydrofluoric acid based solutions. *Journal of Materials Science* **1993,** *28* (23), 6261-6273.

47.   McKeown, D.; Waychunas, G.; Brown, G. EXAFS study of the coordination environment of aluminum in a series of silica-rich glasses and selected minerals within the Na_2O-Al_2O_3-SiO_2 system. *Journal of Non-Crystalline Solids* **1985,** *74* (2), 349-371.

48.   Jong, B.; Schramm, C.; Parziale, V. Polymerization of silicate and aluminate tetrahedra in glasses, melts, and aqueous-solutions. 4. aluminum coordination in glasses and aqueous-solutions and comments on the aluminum avoidance principle. *Geochimica Et Cosmochimica Acta* **1983,** *47*, 1223-1236.

49.   Kanyal, S. S.; Jensen, D. S.; Zhu, Z.; Linford, M. R. Silicon (100)/SiO2 by ToF-SIMS. *Surface Science Spectra* **2015,** *22* (2), 1-6.

CHAPTER 3: Low Energy Ion Scattering (LEIS) of As-Formed and Chemically Modified Display Glass and Peak-Fitting of the Al/Si LEIS Peak Envelope

3.1 Statement of Attribution

This document was originally published as Cushman, C. V.; Brüner, P.; Zakel, J.; Dahlquist, C.; Sturgell, B.; Grehl, T.; Lunt, B. M.; Banerjee, J.; Smith, N. J.; Linford, M. R. Low Energy Ion Scattering (LEIS) of As-Formed and Chemically Modified Display Glass and peak-fitting of the Al/Si LEIS peak envelope. *Applied Surface Science* **2018,** *455*, 18-31.[1]

3.2 Abstract

Flat panels displays (FPDs) are commonly manufactured on highly-engineered glass substrates known as display glasses. As FPD pixel sizes decrease and pixel densities increase, the surface composition and surface properties of these glasses have an increasingly important impact on device yield, influencing static electricity buildup and discharge, particulate adhesion, rate of contamination, and device lifetime. Here, we apply low energy ion scattering (LEIS) to the analysis of Eagle XG®, a widely used display glass. Surfaces were treated with production-line relevant chemistries including acids, bases, etchants, industrial detergents, and plasmas. The resulting surfaces were compared to as-formed melt surfaces, fracture surfaces, and fibers formed from remelted Eagle XG®. LEIS revealed the elemental composition of the outermost atomic layer of these materials, detecting all major Eagle XG® constituents except boron. The surface composition of the glass differed as a function of forming process used to fabricate it as well as surface treatment. The surface concentration of aluminum on the as-formed melt surface differs

significantly from the bulk composition (1-5% vs. 30-31% Al_2O_3 surface coverage, respectively). HCl treatment depleted the surface of all species except silica. HF treatment depleted modifier species from the glass surface to a lesser extent. An alkaline industrial detergent produced an increase in alumina relative to the as-formed glass surface (8-12% vs. 1-5% Al_2O_3 surface coverage, respectively). Treatment with an atmospheric-pressure plasma had no detectable impact on the elemental surface composition of the glass. Aluminum and silicon generally give overlapping signals in LEIS, and these signals could only be resolved here through a combination of optimized experimental conditions and data fitting. Various approaches to this data analysis were explored, including a guided least-squares approach referred to herein as informed sample model approach (ISMA), wherein the pure spectral components required for the fit were mathematically derived from the sample spectra. Most commercial display glasses contain both Al and Si, but there is little discussion of the deconvolution of these LEIS signals in the technical literature.

3.3 Introduction

Flat panel displays (FPDs) have become essential components of many modern electronic devices, including smartphones, laptops, tablets, and televisions. FPDs are most often fabricated on glass substrates due to their superior material properties, which include extraordinary flatness, low birefringence, high strength, rigidity (but also flexibility), and transparency.[2-3] Accordingly, specialized glass compositions and forming processes have been developed to meet the demands of the display industry.[3-4] These glasses must conform to stringent requirements, maintaining dimensional stability at high processing temperatures and withstanding harsh processing chemistries. Display glasses must also be compositionally compatible with the electronic circuits fabricated on them. Most display glasses are alkali-free borosilicates.[3-4]

The maximum sizes of FPDs continue to increase while their minimum pixel sizes decrease.[5] As these critical pixel dimensions become more demanding, surface-mediated processes and contamination have an increasingly important influence on FPD device yield. In particular, the composition and chemistry of display glass surfaces influence material attributes that include surface adhesion, particle contamination, wetting, static charge buildup, and reactivity.[6-9] Of these, particulate adhesion and electrostatic discharge have become important modes of FPD device failure during manufacturing.[5-6] However, to fundamentally understand these processes and their influence on FPD fabrication, it is necessary to know the surface compositions of glass substrates at a variety of depth scales. This is a challenging prospect. It is generally accepted that glass surface compositions can vary significantly from bulk compositions.[10-12] Furthermore, glass surfaces are relatively labile; their compositions typically change with exposure to production line chemistries, which may include acids, bases, detergents, etchants, and plasmas.[13-15] Thus, the surface composition of a display glass is a function of its production line history, and attempts to establish

the relationship between display glass surface composition, surface mediated-processes, and FPD device yield must take these effects into account.

There are numerous publications on the surface and material analysis of silicate glasses, which include glasses for nuclear waste storage and archeological and art specimens.[7, 16-18] Techniques for analyzing these surfaces have included X-ray photoelectron spectroscopy (XPS), time-of-flight secondary ion mass spectrometry (ToF-SIMS), spectroscopic ellipsometry, and atomic force microscopy.[10, 19-20] However, in spite of the growing technological importance of FPDs, there have been relatively few published studies on the surface composition and properties of display glasses. Thus, surface analytical studies probing display glass composition and chemical alterations of these surfaces are important for the glass community and for the advancement of display glass technology in general.

Low energy ion scattering (LEIS), also known as ion scattering spectroscopy (ISS), provides quantitative elemental analysis on the outermost atomic layer of a material.[14, 21-22] It is the only surface analytical technique that provides this information. Even otherwise surface sensitive techniques like XPS and ToF-SIMS probe at least a few molecular layers into a material and give information averaged over this depth, and thus cannot definitively establish the composition of the terminating atomic layer of a material. Therefore, LEIS can provide insight into surface-mediated processes that these other techniques may not. For example, the activity of catalytic materials often shows a direct correlation to compositional information from LEIS, even when it shows no such correlation to compositional data from XPS or ToF-SIMS.[23] To emphasize the enhanced sensitivity of modern LEIS instrumentation, it is often referred to as high-sensitivity LEIS (HS-LEIS).[24-26]

ISS has previously been used to analyze fused silica and sodium silicate glasses.[27] These studies revealed that the fracture surface of fused silica is oxygen-terminated, and that the fracture surface of sodium silicate glasses has a higher-than-bulk concentration of sodium. The authors hypothesized that sodium migrated toward the fracture surface to shield negatively charged oxygens and also dangling bonds formed in the fracture process. A follow-up study used *in situ* heating during LEIS to monitor the surface composition of a fracture surface as a function of temperature.[28] Here, during heating below the glass transition temperature, modifier species were depleted from the sample surface. However, above this temperature, the network modifiers diffused from the bulk toward the surface to give a composition very similar to the original fracture surface. Other recent studies have used HS-LEIS to study mixed alkali silicate glasses and silicate glasses containing both alkali and alkaline earth modifiers.[29-30] These reports compared the melt-formed and fracture surfaces of these glasses to their bulk compositions, albeit in all cases after Ar^+ ion sputter cleaning. It was determined here that all modifiers were depleted at the glass melt surface relative to the bulk composition, and that the fracture surface was enriched in alkali species relative to the bulk composition. In addition, both studies showed that barium was not as prone to fracture-induced migration as were the alkali species. These studies provide ample evidence that a bulk glass composition is not predictive of its surface composition, and that the surface composition of a glass can be strongly affected by its processing history. In summary, mobile network modifiers are easily depleted from glass melt surfaces, and fracture surfaces are not necessarily representative of bulk glass compositions at the length-scale of LEIS analysis.

This LEIS analysis is part of our ongoing wider effort to characterize display glass surfaces and other glass materials with a variety of surface-analytical tools, including ToF-SIMS,[11] and spectroscopic ellipsometry.[31-33] In particular, the objective of this project is to create a foundation

111

for understanding the link between display glass surface composition and surface-mediated phenomena that affect the FPD manufacturing process and device performance. With a sufficiently accurate and quantitative understanding of the surface of the glass, it should be possible to estimate the average areal densities of important functional groups at the glass surface, e.g., the number of silanols, boronols, aluminols, and non-bridging oxygens. Such calculations for glass surfaces have previously been made from XPS measurements.[34] However, given the greater surface sensitivity of LEIS, calculations based on this technique should be even more predictive of surface functional group concentrations, assuming one can detect all the elements of interest.

Here, for the first time, we apply HS-LEIS to the analysis of a multicomponent display glass, Corning Eagle XG®. Samples analyzed include the as-formed melt glass surface, as well as the same melt surfaces exposed to two important acids, a base, two detergents, and an atmospheric-pressure (AP) plasma. These surface treatments were chosen because similar chemistries are often used industrially to prepare display glass panels for FPD fabrication. We compared these chemically-treated glass surfaces to a fracture surface of remelted glass from the same stock with an operationally identical bulk composition (hereafter referred to as "Fracture"). We also wished to better understand and describe the limitations and capabilities of LEIS for glass analysis. Indeed, while the above-mentioned LEIS studies focused on relatively simple model glass systems,[27-30] most silicate glasses used industrially are significantly more complex, and such multicomponent matrices create analytical challenges. For example, Eagle XG® contains oxides of Si, Al, B, Mg, Ca, Sr, and Sn. This material is an especially challenging sample for LEIS due to nearly overlapping signals from Al and Si, which results from their similar masses. Fortunately, recent advances in LEIS instrumentation have improved the resolution of the technique sufficiently to at least partially resolve these and other such pairs of elements through optimization of instrument

112

parameters and data fitting.[25, 35] Below, we discuss our approach to this deconvolution and the challenges associated with it. Another analytical challenge is to obtain appropriate reference materials for quantitative analysis, especially with calcium. Finally, due to factors that include low concentrations and low cross sections, some species of interest may not be directly detectable by LEIS. In analysis of Eagle XG®, this unfortunately included boron—an important network former.

3.4 Theory of LEIS

The theory and applications of LEIS have been discussed in several recent review articles.[14, 22, 24-25] Here, we provide only a very short introduction. In LEIS, a beam of low energy (< 10 keV) noble gas ions probes a sample surface, and the kinetic energies of the backscattered ions are measured at a selected backscattering angle. This backscattering process can be modeled as a single inelastic collision between two bodies,[21] where the following governing equation for LEIS is obtained from the classical equations for the conservations of mass and energy:

$$(3.1) \quad E_S = k \cdot E_P = \left(\frac{\cos \Theta + \sqrt{\left(\frac{M_S}{M_P}\right)^2 - \sin^2\Theta}}{1 + \frac{M_S}{M_P}} \right)^2 \cdot E_P, \quad \frac{M_S}{M_P} \geq |\sin\Theta|.$$

Here, E_S is the energy of the backscattered ion, E_P is the energy of the primary ion, Θ is the angle through which backscattering occurs, M_S is the mass of the species at the sample surface, and M_P is the mass of the projectile ion. In a typical LEIS experiment, E_P, M_P, and Θ are fixed and E_S is measured, such that Equation (3.1) can be solved for the remaining unknown, M_S. Accordingly, LEIS identifies elements at a surface by their masses. LEIS is surface sensitive because only the backscattered ions (not the neutrals) are detected, and only noble gas ions that backscatter from the outermost atomic layer of a material have short enough interaction times to avoid

neutralization.[22] These elemental surface signals appear as Gaussian peaks, and they are quantitative; with few exceptions, their areas scale linearly with surface coverage. Thus, unlike ToF-SIMS, LEIS is generally free from matrix effects.[22] For some sample systems, LEIS can also provide information about the subsurface distribution of species. This information is obtained from ions that penetrate into a material and backscatter below the surface. As these ions enter the material, they are almost immediately neutralized, but as they exit, a fraction of them is re-ionized and subsequently detected. These ions lose energy as they travel through the material, and the resulting signals appears as a tail on the low-energy side of the corresponding LEIS surface peaks.[14, 22]

LEIS (ISS) has existed as a technique for several decades.[21] However, recent advances in its instrumentation, especially the invention and development of the double-toroidal analyzer, have dramatically improved the resolution and sensitivity of the method.[22, 25, 36-38] A dedicated LEIS instrument with a double toroidal analyzer (see Figure 3.1) is now commercially available.[25] This unique instrumental geometry allows ions to be collected over a 360 degree azimuthal angle while maintaining a narrow range of backscattered angles. These improvements lead to ca. 3 orders of magnitude better sensitivity while providing higher mass resolution than previous LEIS/ISS instruments based on concentric mirror or hemispherical analyzers.[22, 25] This so-called high-sensitivity LEIS (HS-LEIS) has been used to probe a number of materials, including solid-oxide fuel cells, catalysts, extreme UV optics, semiconductors, and films deposited by atomic layer deposition.[39-43]

3.5 Experimental

3.5.1 Materials and Sample Preparation

The sample system for this study was Eagle XG®, a widely used display glass. Eagle XG® is an alkali-free, alkaline-earth modified boroaluminosilicate glass manufactured using Corning Incorporated's patented fusion draw process. A discussion of the development of this composition and the fusion draw process can be found elsewhere.[3] Pieces of Eagle XG® (0.5 mm thick) were taken from the production line immediately after forming and prior to any washing steps and shipped to us in containers that preserved one side of the glass in a sealed environment. These pristine native melt surfaces (hereafter referred to as "Untreated") were analyzed, in addition to pristine samples that were subsequently treated with HCl, HF, tetramethylammonium hydroxide (TMAH), and an industrial alkaline detergent (Detergent 1). In order to understand the effects of plasma on the surface composition, a series of samples that had been exposed to an atmospheric-pressure plasma and/or an additional industrial detergent (Detergent 2), as well as an untreated control sample (Untreated 2) were also analyzed. The conditions of the various wet chemical treatments explored herein are summarized in Table 3.1. In addition to these samples, 100 x 5 x 5 mm bars of remelted Eagle XG®, also prepared by Corning Incorporated, were used to create and evaluate fracture surfaces. Glass fibers (16-19 μm diameter) formed from remelted Eagle XG® were similarly analyzed. The N_2 BET surface area of these fibers was 1.10 m^2/g.

Samples treated with HCl, TMAH, Detergent 1, and HF were prepared at Brigham Young University (BYU), while those treated with Detergent 2 and/or atmospheric-pressure plasma were prepared at a Corning production facility and shipped in sealed containers. For the samples

prepared at BYU, pieces of Eagle XG® were removed from their sealed containers, cut into ca. 2 cm x 5 cm pieces, and inserted into perfluorinated alkane (PFA) vials containing 50 mL of reagent. For the treatments carried out with heated solutions, the reagents were heated for 20 minutes in a heated water bath prior to sample introduction. For the HF treatment, all reagents, including water, were equilibrated to room temperature prior to sample immersion. Ultrapure water (18 MΩ) was used as the diluent for all wet chemical treatments. Immediately following a wet chemical treatment, the contents of the reaction vials were exchanged with ultrapure water several times, after which the samples were removed and rinsed with a spray of ultrapure water for ca. 1 minute. Finally, the samples were blown dry and stored in sealed, precleaned glass vials until analysis. The Corning Incorporated manufacturing facility was maintained at a relative humidity of $40 \pm 10\%$. The humidity at BYU was uncontrolled.

Table 3.1. Reagents and conditions for wet chemical treatments of Eagle XG®

Reagent	Grade	Supplier	Conc.	pH	Temp. (°C)	Time (m)
Detergent 1	N/R	N/R	1% v/v	12	60	10
Detergent 2	N/R	N/R	N/R	N/R	N/R	N/R
HCl	Optima®	Fisher Scientific	0.1 M	1*	60	10
HF	ACS	EMD	0.1 M	2*	20	10
TMAH	TraceSelect® Ultra	Fluka	0.1 M	11*	60	10

N/R = Not reported. *Calculated pH.

3.5.2 LEIS Analysis

LEIS was performed at the IONTOF GmbH headquarters in Münster, Germany using a Qtac[100] HS-LEIS instrument. Untreated and chemically treated samples were removed from their sealed containers, cut into ca. 1 cm x 1 cm pieces, loaded onto the analysis stage, and immediately introduced into the instrument for analysis. The cumulative exposure time of sample surfaces outside their sealed vessels to the air was on the order of a few minutes. Fracture bar samples were fractured in ambient air and loaded into the instrument's preparation chamber as quickly as possible, experiencing ca. 1 min or less of air exposure. For the analysis of the fibers, a large bundle of them was simply clamped into a sample holder. Once in the instrument, samples were cleaned *in situ* with the downstream products of an oxygen plasma, i.e. atomic oxygen, immediately prior to analysis. This downstream approach ensured that radical/activated species did not impinge on sample surfaces with high kinetic energy. Accordingly, organic surface contamination was removed under gentle conditions that minimized surface rearrangement, sputter damage, and any increase in sample temperature. Atomic oxygen is widely used for removing adventitious hydrocarbon from surfaces for LEIS and for other purposes.[24, 44-46] This surface cleaning is important because adventitious hydrocarbons, which are H-terminated, do not give a

LEIS signal for most angles of analysis.[22] Instead, they have the effect of attenuating all LEIS signals due to hydrogen's low mass (see Equation 3.1), which causes forward scattering, not backscattering, of incident noble gas ions except at very shallow backscattering angles. Cleaning with atomic oxygen typically oxidizes surface species to their highest oxidation state. However, because the components of these display glass surfaces are, in general, already expected to be in their highest oxidation states and are devoid of highly-mobile modifier ions like Na^+, this treatment probably does not measurably perturb/alter their surface chemistry. In practice, samples were exposed to increasing doses of atomic oxygen until additional cleaning resulted in little or no change in the spectra. Figure 3.2 shows LEIS spectra for as-received Eagle XG® samples exposed to increasing doses of atomic oxygen. For the first 10 minutes, significant increases in signal are observed. However, after another five minutes the change in the oxygen and Al/Si peak areas were less than 5%. Based on these results, all samples in this study were exposed to 15 minutes of atomic oxygen cleaning prior to analysis.

All samples were analyzed using 3 keV $^4He^+$. To provide better mass resolution, positive identification, and easier quantitation of the higher mass species, the surfaces were also analyzed with 5 keV Ne^+.[14] For all analyses, a 2 mm x 2 mm area was probed. To avoid beam-induced sputter damage, the ion doses were kept below 1×10^{14} ions/cm^2 and 1×10^{13} ions/cm^2 for analyses performed with $^4He^+$ and Ne^+, respectively, i.e., these analyses were performed below the static limit. To establish the reproducibility of the technique, three replicate analyses were performed on Eagle XG® fracture surfaces using both 3 keV He^+ and 5 keV Ne^+. One of these replicates showed zinc contamination, likely from the tool used to break the fracture bars. This replicate was excluded from the analysis. The remaining replicates are shown in Figures 3.3a – 3.3b. The absolute percent differences in peak areas between these replicates are listed in Table 3.2.

Table 3.2. Percent differences between peak areas for the two replicate Eagle XG® fracture surfaces highlighted in Figure 3.3.

Species	O	Al/Si	Ca	Sr	Sn
% Difference	14	10	9	5	18

A subset of the samples was also analyzed with 6 keV $^4He^+$ with the goal of resolving the Al and Si signals. These samples included Untreated Eagle XG®, a fracture surface of remelted Eagle XG®, and samples treated with Detergent 1 and HCl. SiO_2 grown thermally on a silicon wafer was used as the SiO_2 reference for this analysis, and Al_2O_3 deposited by atomic layer deposition (ALD) on an Eagle XG® substrate was used as the Al_2O_3 reference. This film of alumina was sufficiently thick that no signals from the Eagle XG® substrate were present in the corresponding LEIS spectrum. A film of MgO grown on a magnesium substrate was used as the magnesium reference. Peak fitting, including a guided form of linear least squares analysis referred to herein as informed sample model approach (ISMA), was performed on these samples to resolve the Al and Si signals. All data fitting was performed with CasaXPS (Version 2.3. 18PRI.0).

3.5.3 Sample Charging and Spectral Calibration

Sample charging in LEIS can result in shifted peaks, distorted spectra, and in extreme cases, a complete loss of signal. Given that our samples are insulators, a low energy electron flood gun was used for charge compensation (ca. 4 µA of current at 12 eV of electron energy). While the flood gun dramatically reduced the effects of sample charging, some peak shifting between the spectra remained. Peak shifting in LEIS due to sample charging can be modeled by Equation (3.2),

$$(3.2) \quad E' = E + U\left(1 - \frac{E}{E_0}\right),$$

where E' is the measured backscattered energy of a LEIS signal, E is the expected energy of that signal in the absence of charging, E_0 is the energy of the analysis beam, and U is the voltage at the sample surface. A consequence of Eq. 2 is that peak shifting due to sample charging is not a constant value across a LEIS spectrum, but rather a function of the backscattering energy. In practice, a spectrum can be calibrated by calculating U based on the known analysis beam energy and the measured position of a reference peak. The spectrum can then be replotted on a shifted energy scale by solving Equation (3.2) for E. All spectra shown here were calibrated according to the above-described method, using the oxygen signals as the reference peaks. The oxygen signal was chosen for sample calibration because it was a strong signal that was free from spectral interferences.

3.6 Quantitation and Data Treatment

Quantitation in LEIS is usually straightforward. With very few exceptions, LEIS is free from matrix effects and gives linear signal responses.[22] Each element has a unique backscattering cross-section, so reference materials are often used to establish LEIS surface coverages.[24] In the case of the glass studied here, elements were expected to be in their typical, highest oxidation states, and, where possible, oxide surfaces were used as reference materials. The surface coverage of an oxide is assumed to scale linearly with the metal peak for that oxide. For example, if an SiO_2 reference material gives a silicon peak area of 1000 arbitrary units, and a sample gives a silicon peak area of 100 arbitrary units, the surface is said to have 10% SiO_2 coverage. With this approach to quantitation, it is assumed that the areal population of the topmost surface atoms is comparable

in both reference and sample, and this assumption may be imperfect in the case of glass. For example, aluminum is expected to be tetrahedrally coordinated in the glass samples studied here, but the ALD-deposited Al_2O_3 used as a reference material likely contains both tetrahedrally and octahedrally coordinated aluminum.[47] Nevertheless, describing glass species in terms of their respective surface oxide coverages provides a useful interpretation of LEIS data that has solid support in the literature.[14, 22, 48-49]

LEIS is well-suited to the analysis of powders and otherwise rough samples like bundled fibers, because it is relatively insensitive to sample roughness.[22] However, in some cases, rough samples result in attenuated signals due to shadowing effects.[50] A previous analysis of several different powders demonstrated that roughness has the effect of attenuating all LEIS signals, such that the absolute signal magnitude is diminished but the ratios between given elements remained constant.[50] For these samples, a corrective geometry factor is necessary. This factor can be assigned so that a reference peak in a rough sample gives the same response as in a comparable smooth sample. The glass fiber samples analyzed here required such a geometry factor. Because the fracture surface and the planar samples all gave approximately the same oxygen intensity in the 3 keV $^4He^+$ spectra, the spectrum from the glass fiber sample was scaled so that it had the same oxygen intensity as these other samples. The resulting geometry factor was 1.9, and this same factor was applied to the 5 keV Ne^+ spectrum for this sample.

Most element pairs are well resolved in LEIS, so peak fitting of LEIS data is relatively rare. However, a significant challenge for the current glass samples is that Al and Si have similar masses and give strongly overlapping signals. Accordingly, to quantify Al_2O_3 and SiO_2 surface coverages, these signals must be resolved via data fitting. In situations in LEIS data analysis where peak fitting has been required, the background has often been fit with an error function, and the LEIS surface

signals are fit with symmetric shapes including Gaussian and Lorentzian lineshapes.[49] However, one recent publication used asymmetric line shapes and the Shirley background commonly employed in XPS.[51-52] In addition, at least one publication argues that asymmetry is inherent in LEIS signals.[49] Linear least squares (LLS) analysis has previously been used to fit LEIS spectra with overlapping signals.[45] We attempted to fit our Al/Si LEIS peak envelopes using both ISMA and by fitting with synthetic lineshapes. A detailed discussion of these efforts is provided below. While LEIS results for samples containing both aluminum and silicon have previously been reported,[35, 53] we are not aware of any publication that discusses the challenge of resolving these significantly overlapping signals. Accordingly, we hope that our thorough treatment of this issue will provide a useful point of reference for future LEIS analyses of commercial glasses, given that many of them contain both aluminum and silicon.

3.6.1 Introduction to Linear Least Squares and Informed Sample Model Approach (ISMA)

LLS assumes that sample spectra can be represented as a linear combination of basis spectra, per Equation (3.3),

$$(3.3) \quad \boldsymbol{A} = \boldsymbol{S} \cdot \boldsymbol{C},$$

where $\mathbf{C}$ is a matrix containing the concentrations or weighting factors for the basis spectra in the matrix $\mathbf{S}$.

Equation (3.3) can be solved for $\mathbf{C}$ according to Equation (3.4),

$$(3.4) \quad \boldsymbol{C} = (\boldsymbol{S}^T \boldsymbol{S})^{-1} \boldsymbol{S}^T \boldsymbol{A}.$$

Accordingly, if $\boldsymbol{A}$ and $\boldsymbol{S}$ are known, the concentrations or weightings of the reference spectra in each sample spectrum can be easily determined. Linear least squares assumes good alignment and good agreement between peak shapes and peak widths between spectra. An

advantage of this approach is that no synthetic peaks need to be created. Instead, the peak shapes are represented entirely by the reference spectra.

Informed sample model approach (ISMA) is useful in situations where some of the basis spectra in an LLS analysis cannot be obtained by analyzing reference materials. ISMA relies to a degree on the analyst's *a priori* knowledge of a sample to mathematically derive pure spectral components from a series of related samples. This approach has much in common with the multivariate curve resolution (MCR) approach used in Chapter 2. The difference between MCR and ISMA is that the component spectra in MCR are derived entirely by an iterative fitting algorithm while ISMA requires significantly more user input. In ISMA, the analyst performs weighted subtractions according to Equation (3.5),

(3.5) $\boldsymbol{S_R} = \boldsymbol{S_1} - C_2 \cdot \boldsymbol{S_2},$

where $\boldsymbol{S_R}$ is the user-derived reference spectrum, $\boldsymbol{S_1}$ and $\boldsymbol{S_2}$ are spectra of sample materials, and C_2 is a scalar weighting factor. Assuming that an ensemble of appropriate sample spectra with varying concentrations of the species of interest are available, pure basis set components can often be derived by application of Equation (3.5) to the correct samples. Sample spectra can then be fit using a linear combination of basis spectra as in Equation (3.4), i.e., once the basis sets are mathematically derived, a simple LLS analysis is performed. A very similar analytical approach has been used to deconvolve complex XPS peak envelopes, where it was called informed amorphous sample model (IASM). This name reflected the fact that basis spectra were mathematically constructed from measurements of polycrystalline reference materials and then used for quantitation of amorphous samples.[55-56] However this analytical approach could potentially be applied to any analysis where a linear response can be assumed and there are a sufficient number and variety of spectra to extract the desired information. Accordingly, we have

used the more generally-applicable name of informed sample model approach (ISMA). The technique has also been called by this name in online tutorial videos and training seminars.

3.6.2 Peak Fitting Lineshapes and Constraints

For all peak fitting performed on the 6 keV spectra, a Shirley background was applied and the peaks were represented by an LF line shape. The LF line shape is a function of four parameters $LF(\alpha, \text{ß}, w, m)$. It is based on a Voigt function (convolution of Gaussian and Lorentzian line shapes) with additional parameters to suppress the Lorentzian tails to different degrees on either side of the peak. It also includes a parameter to control the width of the Gaussian function in the convolution. Here, the Lorentzian line shape is given by

$$(3.6) \quad L(x) = \frac{1}{1 + 4\left(\frac{x-E}{F}\right)^2}$$

where E is the peak position and F is the FWHM of the peak. The parameters α and ß modify the Lorentzian contribution to the final lineshape according to

$$(3.7) \quad LF(\alpha, \text{ß}, w, m) = f(x) = \begin{cases} G(m, x) * [L(x)]^{\alpha \to A}, & x < E \\ G(m, x) * [L(x)]^{\text{ß} \to A}, & x \geq E \end{cases}$$

The parameters α and ß are forced to smoothly increase to a constant value A as the energy x approaches $E \pm w$. In CasaXPS, the parameter A is fixed at a value of 3. The parameter m controls the width of the Gaussian convolved with the Lorentzian curve. Setting the parameters α and ß equal to one another results in a symmetric shape, while setting them to different values imparts asymmetry to the peak. A more detailed description of this lineshape can be found in the CasaXPS software documentation, which is available online.

The widths of the oxygen peaks for a given sample were determined by fitting them with an LF(1,1,25,280) line shape. Both symmetric and asymmetric LF shapes were investigated for fitting the Al and Si peak shapes, and both gave similar quantitative results. However, the asymmetric shapes gave lower residuals for the reference materials, and were used in all subsequent fits. The Al contribution was fit using an LF(1.05,1.2,25,280) and the Si contribution was fit using an LF(1.1,0.91,28,400).

The peak positions in the fits were constrained to those of the reference materials. Two different sets of peak width constraints are discussed below: fits with widths constrained to those of the reference materials, and fits where a fixed width ratio was used between the oxygen peaks and the Al/Si peaks, based on the ratios obtained from the reference materials. The Al/O width ratio was determined to be 1.335, and the Si/O width ratio was determined to be 1.615.

3.7 Results and Discussion

All major components of Eagle XG$^®$ except boron were detected by LEIS in at least some of the samples. Acquisitions using a range of different spectrometer settings were required to resolve signals from some of these species. Boron is difficult to detect in LEIS because it has a low backscattering cross-section and because it occurs in a spectral region with a high background due to sputtered particles. Accordingly, boron was below the detection limit in all the samples analyzed here. Detection limits in LEIS depend on the angle of analysis, so in theory boron detection may be improved by analyzing at a shallower backscattering angle than the 145° used here. However, this angle, which optimizes a tradeoff between mass resolution and detection limits for most species, is fixed in the instrument analyzer. We additionally note that other surface sensitive techniques like X-ray photoelectron spectroscopy and Auger electron spectroscopy can

be useful for quantifying boron at sample surfaces, albeit with lower surface sensitivity than LEIS.[57] Mg was only detected/quantified on the fracture surface of Eagle XG®. Due to its proximity to the Al/Si envelope, it was difficult to assign an appropriate background to fit this peak with synthetic lineshapes, and, accordingly, we report only the quantity obtained via ISMA analysis.

3.7.1 Analysis of the 3 keV ^{4}He$^+$ and 5 keV Ne$^+$ Spectra

3 keV He$^+$ LEIS spectra for selected glass samples are shown in Figure 3.4a. Well-resolved peaks corresponding to oxygen and calcium can be seen. In contrast, Al and Si are poorly resolved due to their similar masses, resulting in a single broad peak. While Sr is detected under these settings, it is better resolved from neighboring peaks and identified with more certainty in the 5 keV Ne$^+$ spectrum shown in Figure 3.5a. Figure 3.4b shows a zoomed-in view of the Ca peak envelope from Figure 3.4a. Here, the amount of Ca in the samples varies as a function of the chemical treatments applied to the surface. The fracture surface has the most Ca, and the Untreated melt surface has significantly less Ca than the fracture surface. The HCl and HF-treated samples have the lowest amounts of Ca, while samples treated with TMAH and Detergent 1 solutions—both of which are strongly basic—show Ca depletion to a much lesser degree. Ca^{2+} in glass is most often charge-balanced by non-bridging oxygens. However, CaO is not a suitable reference material for LEIS because it readily reacts with water, giving it unpredictable surface stoichiometry. Accordingly, we used the more stable CaF$_2$ as a reference material, and its spectrum is also shown in Figure 3.4. While this is a less-than-ideal mimic of Ca speciation in glass, it provides a point of reference for comparing these samples and also for comparing results from this study to future

126

LEIS analyses. The quantitative values provided for calcium in Table 3.3 are given as an area percentage of the CaF_2 reference material.

Table 3.3. Quantitative results for Ca, Sr, and Sn for all Eagle XG® samples calculated from peak areas from 3 keV ^{4}He$^+$ and 5 keV Ne$^+$ LEIS spectra. n/d = not detected.

Sample	Ca (% of ref.)	SrO % Cov.	SnO2 % Cov.
Fracture	10.6	2.1	0.12
Fiber	8.2	1.7	0.26
Untreated	3.6	0.7	0.16
Untreated 2	3.6	0.6	0.08
Det.2 + Plasma	3.5	0.4	0.09
Plasma	3.2	0.6	0.08
Det. 1	2.6	0.5	0.15
Det 2.	2.5	0.3	0.11
TMAH	1.8	0.4	0.08
HF	1.1	0.1	0.21
HCl	n/d	n/d	0.04

Figure 3.5 shows the Sr and Sn LEIS signals from treated and Untreated Eagle XG glass®. Here SrO and SnO$_2$ were used as the reference materials for Sr and Sn, respectively, and the Sr and Sn peaks are well resolved. Quantitative results obtained from these data are reported as SrO and SnO$_2$ surface coverage in Table 3.3. The compositional trends in Sr surface coverage here are the same as for Ca surface coverage; the fracture surface has the most Sr in this sample set, the Untreated surface has significantly less Sr than the fracture surface, and the samples treated with HCl and HF are almost entirely devoid of Sr. Samples treated with TMAH and Detergent 1 are only moderately depleted in Sr. The coverage of Sn does not follow the same trend as the Ca and Sr coverages. Here, the Untreated and fracture surfaces have about the same amount of Sn, while the HF-treated sample has the most Sn. Similar to the Ca and Sr results, the HCl-treated surface is the most strongly depleted of Sn.

3.7.2 Analysis of Si/Al (and O and Mg) Envelopes for Selected Samples Using 3 keV and 6 keV ^{4}He$^+$

Because of their similar masses, Al and Si give interfering signals in the 3 keV ^{4}He$^+$ LEIS spectra shown in Figure 3.4a. Given that most other LEIS element pairs are easily resolved, there are relatively few publications that deal with the deconvolution of LEIS signals, and even fewer that focus specifically on overlapping aluminum and silicon signals. One recent publication showed quantitative results for alumina in silicate zeolite materials, but provided little discussion of the data fitting process employed.[35] The quantitation of Al and Si in samples of atomic layer-deposited alumina on silicon wafers was reported in 2015 in a conference presentation. However, again, this presentation gave quantitative results while providing little discussion of the data fitting process.[53] Motivated by these precedents, we attempted to deconvolute the Al and Si signals in the spectra from our fracture sample, Untreated sample, and samples treated with Detergent 1 and HCl. These surfaces were chosen because they showed the widest variation in surface aluminum concentration in our previous ToF-SIMS analysis.[11] These samples were analyzed using both 3 keV and 6 keV ^{4}He$^+$ beams. Additional reference materials for this analysis included thermally grown SiO_2 as the silica reference and a fully-closed, ALD-deposited Al_2O_3 film on a different substrate as the alumina reference. The 3 keV settings generally give better sensitivity than the 6 keV settings, as evidenced by the higher count rate, but the separation between the Al and Si reference peaks is only ca. 31% of the silica peak's FWHM with 3 keV ^{4}He$^+$ while it is 55% for 6 KeV ^{4}He$^+$. Accordingly, the analyses at 6 keV greatly improve the ability to resolve contributions from aluminum and silicon in these samples. The increase in peak separation at 6 keV can be explained by Eq. 1, where the backscattered energy varies directly with the primary ion energy, resulting in greater peak separations at higher analysis energies. This effect was counteracted to

some degree by a greater degree of peak broadening at the higher energies, which is also observed in Figure 3.6b. The differing count rates between the 3 keV ^{4}He$^+$ and 6 keV ^{4}He$^+$ spectra is the result of differing back scattering, neutralization, and reionization cross sections between the spectra as a function of incident ion energy.[58] The Al/Si envelopes obtained with 6 keV ^{4}He$^+$ from the Eagle XG$^®$ samples and corresponding reference materials are shown in Figure 3.7a, and the oxygen envelopes for these samples recorded under the same conditions are shown in Figure 3.7b. In addition to the Al/Si signal, a small contribution corresponding to Mg can be seen here for the fracture surface.

We tried two basic approaches to resolve the overlapping signals in Figure 3.7: peak fitting with synthetic line shapes, and ISMA. We have made no attempt to account for possible double-scattering events in any of these fits because we see no double scattering peaks near other well-isolated signals like oxygen. For fitting with the synthetic line shapes, we report results obtained using two different sets of fitting constraints. The data here were fit using a Shirley background and two peaks that represent spectral contributions from Al and Si. To reduce the influence of noise on the background intensity, an average of the neighboring ±15 data points were used to determine the intensity of each background end point. Fits were attempted using both Gaussian and asymmetric Gaussian/Lorentzian (LF) lineshapes. Both types of line shapes gave very similar quantitative results, but the asymmetric shapes gave lower residuals, and accordingly, they were used in all fits. For the asymmetric shapes, the magnitude of the Gaussian and Lorentzian contributions and the degree of asymmetry were determined by fitting the line shapes to the SiO_2 and Al_2O_3 reference spectra. Once good fits were obtained for the reference materials, the resulting lineshapes were used to represent the Al and Si contributions in the subsequent fits. An

LF(1.1,0.91,28,400) was used for the Si peak, and an LF(1.05,1.2,25,280) was used for the Al peak.

The constraints on the parameters in this analysis had an important effect on the outcomes of the peak fits. When the peak positions and widths were unconstrained, the fits yielded positions and widths that differed significantly from those of the reference spectra. Even when the Al and Si peak positions and widths were constrained to a relatively narrow window, e.g., ± 7 eV for width and ± 5 eV for position, the fits placed the positions and widths at their constraint limits for all the samples. This suggested that these envelopes could not be uniquely fit with unconstrained peak positions and widths, i.e., obtaining a reasonable fit would require reasonable constraints. We first attempted to constrain the peak positions and widths in the sample fits to those of the reference spectra. While this is the most obvious approach, it assumes no variation in peak widths due to sample charging. A fit for the Detergent 1-treated sample spectrum using this approach is shown in Figure 3.8a, and a fit to the Untreated samples is shown in Figure 3.9a. The quantitative results from this fitting approach are listed in Table 3.4. Figures showing the fits to the remainder of the samples obtained with this approach are in the Supporting Information.

Table 3.4. Surface coverages of Al_2O_3 and SiO_2 by the different fitting approaches taken in this work for the samples shown in Figure 3.7, wherein % coverage of individual species is defined relative to reference materials.

Sample	Approach 1 (fixed width)		Approach 2 (width ratio)		ISMA		
	% Al_2O_3	% SiO_2	% Al_2O_3	% SiO_2	% Al_2O_3	% SiO_2	% MgO
Fracture	31.1	77.1	29.7	80.8	29.7	79.5	8.8
Untreated	4.6	79.4	2.8	83.9	1.1	80.9	n/d
Det. 1	12.0	87.8	10.9	90.2	7.8	89.9	n/d
HCl	0.0	89.0	0.0	91.2	0.0	86.3	n/d

To determine the degree to which the peak widths might vary between the spectra, we performed an analysis of the oxygen peak envelope shown in Figure 3.7b. This analysis indicated that the oxygen peak widths varied over a range of 7.5 eV, i.e., ca. 12% of the average oxygen peak width for these samples. This variation in peak width is probably due to sample charging. To account for these variations, we attempted a second fit wherein the peak widths of the aluminum and silicon contributions were constrained to a fixed ratio relative to their corresponding oxygen peaks. The Al/O width ratio determined from the alumina reference was 1.335, and the Si/O width ratio determined from the thermal silicon oxide was 1.615. Fits for the Detergent 1-treated and Untreated samples using these constraints can be seen in Figures 3.8b and 3.9b, respectively, and the quantitative results for these fits are presented in Table 3.4. The fits to the remainder of the samples fitted in this manner are given in the Supporting Information.

We initially attempted an LLS fit of the Al/Si region of our sample data using reference spectra from Al_2O_3, SiO_2, and MgO as the basis sets. However, this three-component LLS fit gave poor results because the shape of the background in the Eagle XG® samples is poorly captured by

the reference materials. The difference in backgrounds between samples is easily observed in Figure 3.7a, where the Eagle XG® fracture surface gives a significantly higher background than all the other spectra. This difference in background intensity is probably the result of background contributions from Ca and Sr, which are more abundant in the fracture surface than in the other samples. Accordingly, we hypothesized that a successful least squares fit of these spectra would require a basis set containing background contributions from species outside of the spectral range that could be derived by ISMA. That is, it was assumed that the Eagle XG® sample spectra could be represented by four basis spectra: an Al_2O_3 spectrum, an SiO_2 spectrum, a spectrum representing background contributions from other elements in Eagle XG®, and a contribution for Mg (detected only in the fracture surface). Since the fracture surface had the highest Mg, Ca and Sr concentrations, it was used to derive the Eagle XG® background spectum. To do this, the SiO_2 spectrum was first subtracted from the fracture spectrum, leaving contributions from Al_2O_3, Mg, and the Eagle XG® background. The Al_2O_3 spectrum was then subtracted, presumably leaving only contributions from Mg and the Eagle XG® background. Finally, an MgO reference spectrum was subtracted from the fracture spectrum, leaving only the background contribution from the other elements of Eagle XG® in this spectral region. This process can be represented mathematically as

(3.8) $\quad \boldsymbol{S_b} = \boldsymbol{S_{frac}} - C_{SiO_2} \cdot \boldsymbol{S_{SiO_2}} - C_{Al_2O_3} \cdot \boldsymbol{S_{Al_2O_3}} - C_{MgO} \cdot \boldsymbol{S_{MgO}}$,

where $\mathbf{S_b}$ is the Eagle XG® background spectrum, $\boldsymbol{S_{SiO_2}}$ is the SiO_2 reference spectrum, $\boldsymbol{S_{Al_2O_3}}$ is the Al_2O_3 reference spectrum, and $\boldsymbol{S_{MgO}}$ is the magnesium reference spectrum. C_{SiO_2}, $C_{Al_2O_3}$, and C_{MgO} are the manually-assigned weighting factors. The three reference spectra and the ISMA-derived background spectrum are shown in Figure 3.10. Using these spectra, we performed LLS fits of our samples. The raw data vs. the ISMA LLS fits for the Detergent 1 and Untreated samples

are shown in Figures 3.8c and 3.9c, respectively, together with the contributions from each of the reference spectra. The fits to the remainder of the samples fitted in this manner are shown in the supporting information. To quantify the Al and Si in each sample, simple peak area measurements were taken from the Al and Si contributions to the fit data using Shirley backgrounds. These backgrounds can also be seen in Figure 3.8c and 3.9c. The quantitative results from this fit are given in Table 3.4, together with the results from the other two approaches. One consequence of using the fracture sample to derive our basis sets is that it is fit perfectly with no residuals, i.e., the quantitative results obtained for the fracture surface are the direct consequence of the weightings of the SiO_2, Al_2O_3, and MgO reference spectra that were manually subtracted from it during ISMA to derive the Eagle XG® background spectrum. However, in spite of this being a manual process, the quantities of Al and Si measured in the fracture surface by this method are in decent agreement with the quantities obtained by peak fitting, indicating that a reasonable subtraction was performed.

Each of the fitting approaches considered herein has its advantages and drawbacks. Peak fitting is sensitive to the choice of background and the positioning of the background endpoints. For peak fitting with synthetic line shapes, it is assumed that the data are well-modeled by the line shapes chosen. The advantage of ISMA over peak fitting with synthetic line shapes is that the peak shapes are determined entirely by the reference spectra, and the analyst does not need to assign background shapes or endpoints in the initial fit, though backgrounds may be applied to the spectral contributions during quantitation. We have assumed here that an accurate representation of background contributions from elements other than Al, Si, and Mg can be derived from the Eagle XG® fracture surface via a process of manual subtraction. This subtraction process relies on the skill and experience of the analyst. An advantage of this approach is that an analyst may have

knowledge about the samples or the analytical technique that are not easily considered by fitting algorithms. One potential drawback is that different analysts may get different results.

While each fitting approach attempted has its theoretical merits, we believe it is significant that they all give very similar results. For example, the residuals for the different fitting approaches for the Detergent 1 and the untreated samples are shown in Figures 3.8d and 3.9d, respectively (residuals for the remainder of the samples are shown in the Supporting Information). Indeed, for most of the samples, the difference in residuals between the fixed-width synthetic peak fits and the ratioed-width peak fits are very small. The residuals for the ISMA LLS fits also gave very similar residuals to the two synthetic peak fitting approaches. In terms of aluminum coverage, all three approaches rank the samples as Fracture (most) > Detergent 1> Untreated > HCl (least). This is in good agreement with Chapter 2. The quantitative differences in coverage obtained between the two sets of constraints used for fitting with synthetic lineshapes are subtle, while the ISMA analysis gives systematically lower Al in all the samples than the other two approaches. As expected, all three approaches indicate that the HCl-treated surface has an aluminum content below the detection limit. However, surprisingly, and perhaps very significantly, they also reveal aluminum concentrations on the Untreated sample in the range of 1 – 5%. In contrast, the Fracture surface shows a much higher concentration of this element (29 – 31% Al). Thus, the outermost atomic-layer of natively-formed Eagle XG® is strongly depleted in aluminum. This result will have important future consequences for modeling and thinking about Eagle XG® and similar aluminosilicate glasses. For example, because the natively formed surface of Eagle XG® appears to be strongly depleted of aluminum to merely 1-5% percent, and because –OH groups, including aluminols are very important in glass surface chemistry, one can probably conclude that aluminols play a minor role at most in the apparent surface chemistry of this glass in its as-formed condition.

That said, our fitting results also reveal significantly increased aluminum for the Detergent 1-treated surface relative to the Untreated surface, which is in good agreement with Chapter 2. This latter result has similarly important practical implications, since most display glass sheets are cleaned in detergent media—usually at alkaline pH—at some point in their production path in order to reduce particles from handling. It follows then that the process of washing the as-formed surfaces in alkaline detergent media "recovers" the concentration of Al at the outermost atomic layer to a level closer to that of the bulk. Processes downstream of washing thus experience a somewhat different surface, in which Al may play a more important role in governing apparent surface chemistry.

The fitting approaches taken herein also allow the samples to be ranked according to their silicon concentrations. However, the amount of silicon in each sample varies by less than 10% between the various chemical treatments. That is, the SiO_2 coverage remains relatively constant as a function of surface treatment while the concentrations of the other constituents can vary dramatically. We also note that the SiO_2 surface coverage falls significantly short of that of the reference material for all the samples. This includes those entirely depleted of other surface species, e.g., the HCl sample.

3.7.3 Discussion of Quantitative Results

The data in Tables 3.3 and 3.4 provide several interesting insights regarding the surface composition of treated and Untreated Eagle XG®. First, there are stark compositional differences between the Eagle XG® Fracture surface and the as-formed, Untreated surface. The Untreated surface has approximately half as much Ca and Sr as the Fracture surface. In addition, Mg is

detected at the Fracture surface, but it is below the detection limit in the other surfaces (the Untreated surface, the Detergent 1-treated surface, and the HCl-treated surface), where quantitation was only attempted in the 6 keV ^{4}He$^+$ spectra. These LEIS results are consistent with previous ones that have indicated that glass fracture and melt surfaces can have significantly different compositions.[27-30] Modifier depletion layers are common at silicate glass surfaces.[13] They are also known to form in glass held at elevated temperatures below the glass transition temperature.[28] These observations are especially applicable to glasses with higher vapor pressure constituents, with the alkali metals and boron being typical examples. It is noteworthy that the marked discrepancy between fracture- and melt-formed surface compositions also applies to alkaline-earth species at the outermost surfaces of these nominally alkali-free glasses. In summary, the results in Tables 3.3 and 3.4 emphasizes that it is generally *not* possible to infer surface composition from bulk composition, and vice versa, and moreover that differences between the bulk and the surface are amplified as the information depth of the interrogation technique decreases.[11] In this regard, LEIS provides the ultimate sensitivity to such discrepancies in bulk vs. surface composition of a given glass.

Interestingly, glass fibers formed from remelted Eagle XG® had a composition more similar to the fracture surface than the Untreated surface, where they was only a minor depletion of Ca and Sr for this sample (Al and Mg were not quantified). While the Untreated, fracture, and fiber samples have the same nominal bulk compositions, they exhibit different surface compositions depending on their thermal histories and the glass forming process used to make them. These observations emphasize that the forming process used to make a glass melt surface also has a strong impact on its final surface composition, especially at the monolayer scale of LEIS. For the results shown here, the thermal history of the glass may be an important factor, given that

species have a longer time to evaporate or migrate inward the longer that a glass spends at high temperatures.[28, 59] It has also been noted elsewhere that the atmosphere surrounding the glass at elevated temperatures plays an important role in its final surface composition.[59] Attempts to understand the correlation between glass surface and bulk properties and composition must take these issues into account.

Some of the wet chemical treatments considered in this study have the expected effects on the glass surface while others alter the sample surfaces in more unexpected ways. For example, our results show that leaching with HCl removes Ca, Sr, Al, and Sn from the sample surface. Strong depletion of these species was also seen in our previous ToF-SIMS analysis.[11] However, at least some of each of these species was present by ToF-SIMS, while all of them except Sn are depleted to below their detection limits in the LEIS analysis. This difference is most likely due to LEIS's greater surface sensitivity; it suggests that these species are readily depleted from the outermost atomic layer seen by LEIS, while some quantity of them remain immediately below the surface to be detected by ToF-SIMS with its ca.1 nm information depth. In contrast to the leaching behavior expected for HCl, HF is generally expected to exhibit closer-to-congruent network dissolution resulting in a composition similar to a fracture surface. Instead, the HF-treated sample shows significant depletion of Ca and Sr, suggesting that a finite amount of leaching occurs in a thin layer ahead of the HF etching front for the conditions studied here. This is an important result. It suggests that selection of the acid, and presumably its concentration and reaction time, can be used to tune surface properties/composition. These changes could be "missed" when viewed through the lens of less-sensitive analytical techniques. Another study has also noted some degree of preferential extraction for glass surfaces treated with dilute HF.[60]

Detergent 1 also gives some intriguing results. This detergent solution contains strong bases, including sodium hydroxide and tetramethyl ammonium hydroxide, and has a measured pH of 12 with no appreciable Al in its formulation. Accordingly, it would also be expected to interact with the glass primarily through a congruent dissolution mechanism. Instead, it changes the Ca and Sr concentrations at the outermost surface slightly, while dramatically increasing the Al compared to the Untreated surface. Based on the well-established observation that alkaline-pH media typically interact with silicate glasses through a relatively slow, congruent dissolution mechanism (on the order of 1-10Å/min under the conditions studied), a logical interpretation of the "recovery" of Al by alkaline-solution exposure is that the Al depletion on the native melt surface extends only to a vanishingly-thin depth on the order of a one-or-so monolayers, which is then dissolved away upon base-washing to expose more of the underlying glass with greater Al concentrations. An alternative possibility is that Al increases in concentration as a result of selective extraction of other surface species, leaving an Al rich film, and/or possibly through re-deposition of dissolved Al from solution. Precipitation of Al rich phases from strongly basic solutions has been observed in some previous glass corrosion studies, albeit on a much longer time scale than that studied here.[18] However, the detergents in question contain chelating components to help prevent such redeposition. In summary, these results show that washing display glass surfaces with common cleaning chemistries can significantly alter their surface compositions, sometimes in surprising ways—especially at the scale of the outermost monolayer. Attempts to understand how display glass composition affects FPD production and performance must take these effects into account, since both glass manufacturers and panel makers typically wash glass in similar media. Finally, as suggested by the multiple spots analyzed by ToF-SIMS and LEIS, the

increase in Al concentration we detected appears to take place uniformly across the surface, though more exhaustive surface imaging would be needed to fully confirm this conclusion.

Tin is added to Eagle XG® in small quantities as a fining agent.[3] And while there are clear trends in the amounts of Ca, Sr, and Al at the various Eagle XG® surfaces, any trends in the Sn concentrations at these surfaces are less obvious. For example, the Untreated sample has more Sn at its surface than the fracture sample. As is the case for Ca and Sr, the HCl-treated sample has the lowest concentration of Sn, suggesting that Sn is leached from the surface by this treatment. In contrast, the HF treated sample had the most tin of any of the samples by a significant margin, in spite of the fact that HF had a depleting effect on Ca and Sr. Here, SnO_2 may resist attack by the HF,[61] leaving a Sn-enriched surface. It is also possible that the solution used for HF treatment contributed small amounts of Sn contamination. However, the grade of reagent used here is certified to have < 5 ppm of heavy metal contaminants, including Sn. Other surface treatments had a relatively minor effect on Sn, generally depleting it slightly relative to the Untreated surface.

Of all the treatments studied here, atmospheric-pressure (AP) plasma appears to have the lowest impact on the elemental composition of the outermost atomic layer of Eagle XG®. This sample subset included samples that were treated with AP plasma ('Plasma'), and/or washed with a detergent, i.e., 'Detergent 2', 'Detergent 2 + Plasma', and 'Untreated 2'. All of these samples have approximately the same levels of Ca, Sr, and Sn, regardless of treatment. Accordingly, we conclude that the AP plasma conditions used here do not alter the elemental surface composition of the glass. Likewise, Detergent 2 appears to have no effect on Ca, Sr, or Sn concentration in the glass (Al was not quantified for this sample). While seemingly a trivial result, these findings are actually significant in that they demonstrate the possibility of applying such techniques (e.g. organic removal) *without* any significant alteration of the underlying glass composition—even at

the monolayer scale. That said, it should be recognized that AP plasmas may alter the glass surface in other ways, e.g., by the removal of adventitious hydrocarbon or by altering the hydroxylation state of the glass. LEIS is relatively insensitive to these types of changes, especially considering that atomic oxygen was used to clean these samples prior to analysis. Nonetheless, the degree of hydrocarbon coverage and the surface hydroxylation of the glass are both expected to have a strong impact on glass surface properties. For example, one study demonstrated that a thin overlayer of carbonaceous material can dramatically reduce the contact-induced charging of a glass surface,[6] while another argues that surface hydroxyls govern the rate of contamination on glass surfaces.[7] While LEIS is a powerful tool for understanding the elemental surface compositions of materials, these important aspects of glass surface chemistry are somewhat of a "blind spot" for LEIS.

In general, the LEIS results reported herein are in good agreement with our previously published ToF-SIMS analysis of the same materials, while they also address several of its shortcomings. ToF-SIMS suffers from a significant matrix effect, where, in most cases, it is semi-quantitative at best. In contrast, LEIS generally gives linear responses, although there are a few examples of matrix effects with this technique. Accordingly, the LEIS results reported herein are expected to be much more quantitative than the SIMS results. In the case of Ca, no suitable oxide reference could be found to establish surface coverages. However, given that signal responses can be assumed to be linear in LEIS, relative quantitation is still possible here, e.g. it can be confidently stated that the Untreated surface has ca. 40% as much Ca as the Fracture surface, where we have provided surface coverages relative to a CaF_2 reference to facilitate comparisons between these surfaces and other glass compositions. This study also provides more surface sensitive measurements. That is, while ToF-SIMS is very surface sensitive, LEIS is even more so. Estimates for the depth of analysis in ToF-SIMS range from a few atomic layers to several nm, depending

on the sample and the ion beam conditions.[62-65] Meanwhile, LEIS is uniquely sensitive to the outermost atomic layer.[22] Accordingly, these results are more representative of the outermost surface than those from ToF-SIMS. For example, ToF-SIMS detects Ca in all the glass samples in our previous study, while LEIS shows a significant Ca signal in some of the samples and none in others. It follows that LEIS provides insights about glass that cannot be gained from other surface analytical techniques.

The previous ToF-SIMS analysis also addresses some of the shortcomings of this LEIS analysis. That is, there is some complementarity between these methods. For example, boron is not observed by LEIS due to instrumental limitations for this species, but it is easily detected by ToF-SIMS. Detection limits by ToF-SIMS are also better for most species in Eagle XG®, and it can be used to detect trace contaminants on the glass surface like Na and K, even if they can't be readily quantified. In addition, while the Al and Si signals are difficult to resolve by LEIS, they are well separated in SIMS, and SIMS has no trouble resolving silicon's isotopes. SIMS can also provide information about surface hydroxylation, hydrocarbon contamination, and molecular fragments that LEIS cannot. Thus, these two techniques provided complementary information that give a fairly complete picture of the surface composition of Eagle XG® glass, and show once again the power of a multi-technique approach to provide a more complete picture of a material.[66-68]

3.8 Conclusion

LEIS provides valuable information about the concentrations of Al, Si, network modifiers, and Sn at a display glass surface. Surface coverage estimates for Al, Si, Mg, Sr, and Sn were provided by comparing the glass surfaces to reference oxide materials. No suitable oxide surface

reference was available for Ca, so CaF_2 was used. These LEIS results are in good agreement with Chapter 2. However, ToF-SIMS yields a signal that is derived from several atomic layers, while LEIS directly measures the composition of the outermost atomic layer of a material. Accordingly, ToF-SIMS could not definitively conclude that various atomic species were or were not depleted from the Eagle XG® surface, and/or to what degree they are present at the outermost atomic layer of the material. XPS, which is generally considered to be less surface sensitive than ToF-SIMS, faces similar, and arguably even greater, limitations. In contrast, LEIS clearly shows that network modifiers are present at the as-formed Eagle XG® surface, albeit in depleted quantities relative to the bulk composition represented by the Fracture surface. Furthermore, these results show that a brief treatment in 0.1 m HCl depletes Ca, Sr, and Sn to below their LEIS detection limits. However, even with the modern instrument used here, LEIS has some limitations with regards to the analysis of boroaluminosilicate glasses. Its detection limits for B are poor, such that this element was not even detected in the Fracture surface. In addition, silicon and aluminum give overlapping signals, and even under optimized analysis conditions, these signals could only be resolved via peak fitting or least squares analysis. We have provided a detailed discussion of fitting approaches for resolving these signals and the underlying assumptions for each approach. While others have quantified these species by LEIS, to the best of our knowledge, we are the first to provide a detailed discussion of the deconvolution of these signals in the peer-reviewed literature. All in all, LEIS has provided detailed information about the surface composition of a real-world multicomponent display glass that will be valuable in future efforts to model its structure, composition, and influence on surface-mediated processes.

3.9 Acknowledgments

3.10 Figures
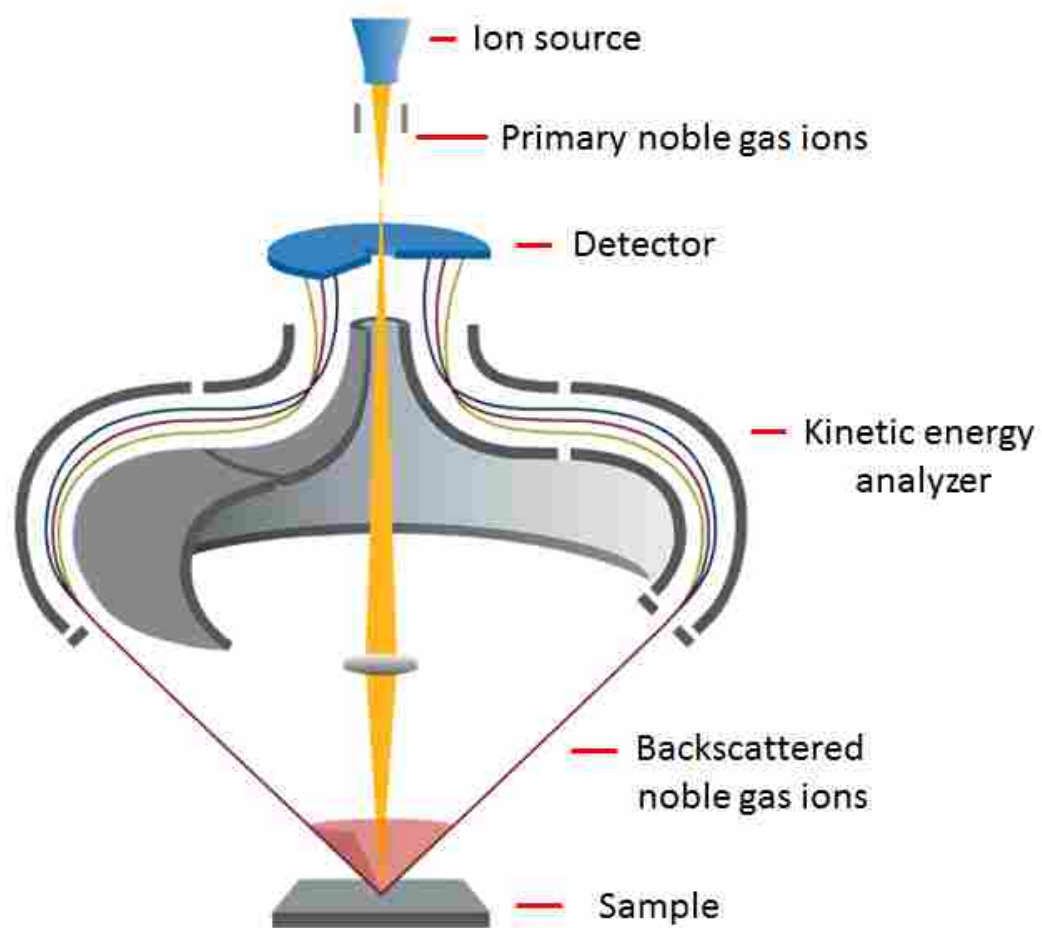
Figure 3.1. Representation of the Qtac[100] LEIS analyzer. Figure used with permission from ION-TOF, GmbH (Münster, Germany).
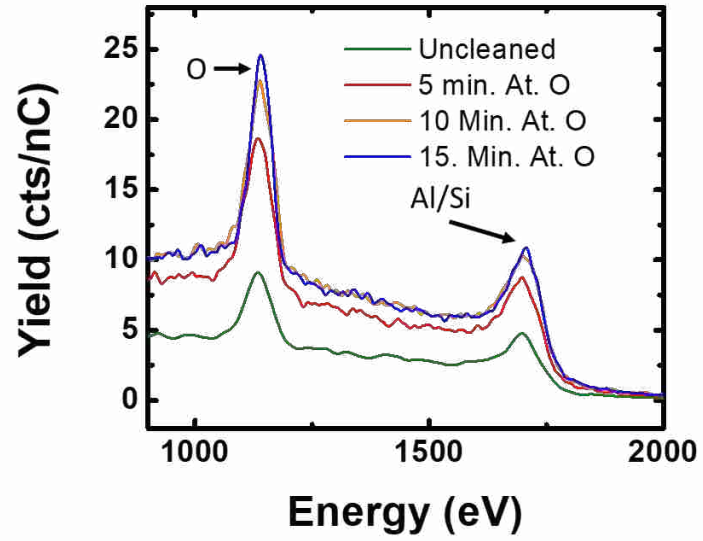
Figure 3.2. LEIS spectra of Eagle XG® exposed to increasing doses of atomic oxygen as obtained with 3 keV ^{4}He$^+$.
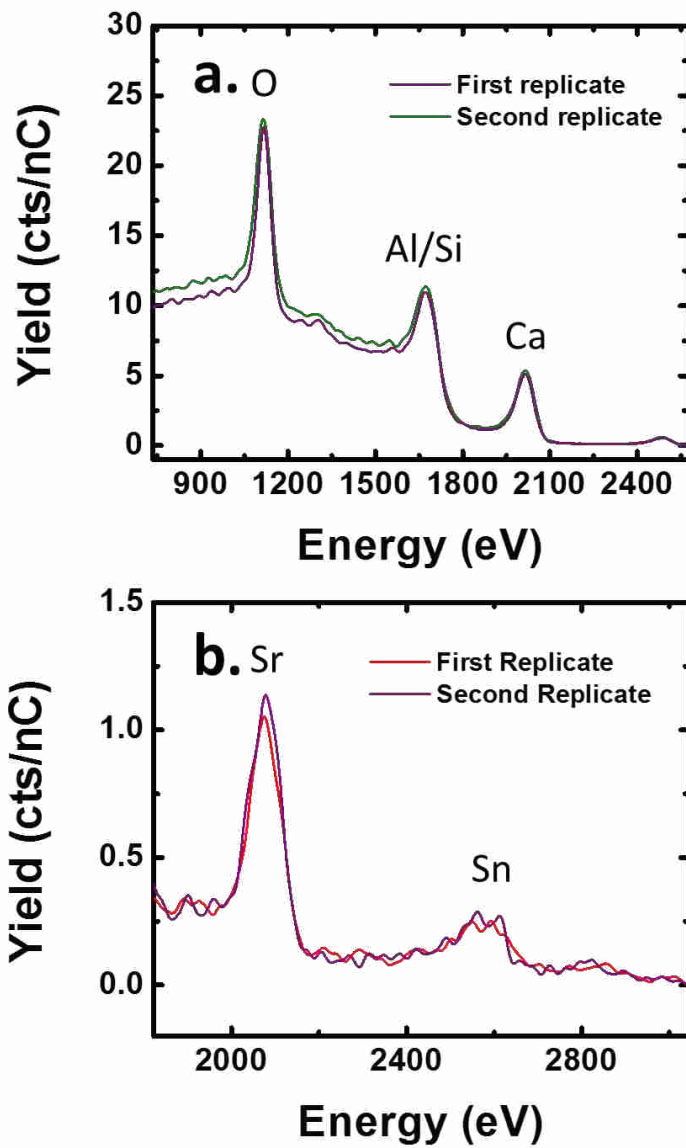
Figure 3.3. Replicate LEIS measurements of an Eagle XG® fracture surface obtained with (a) 3 keV ^{4}He$^+$ and (b) 5 keV Ne$^+$.
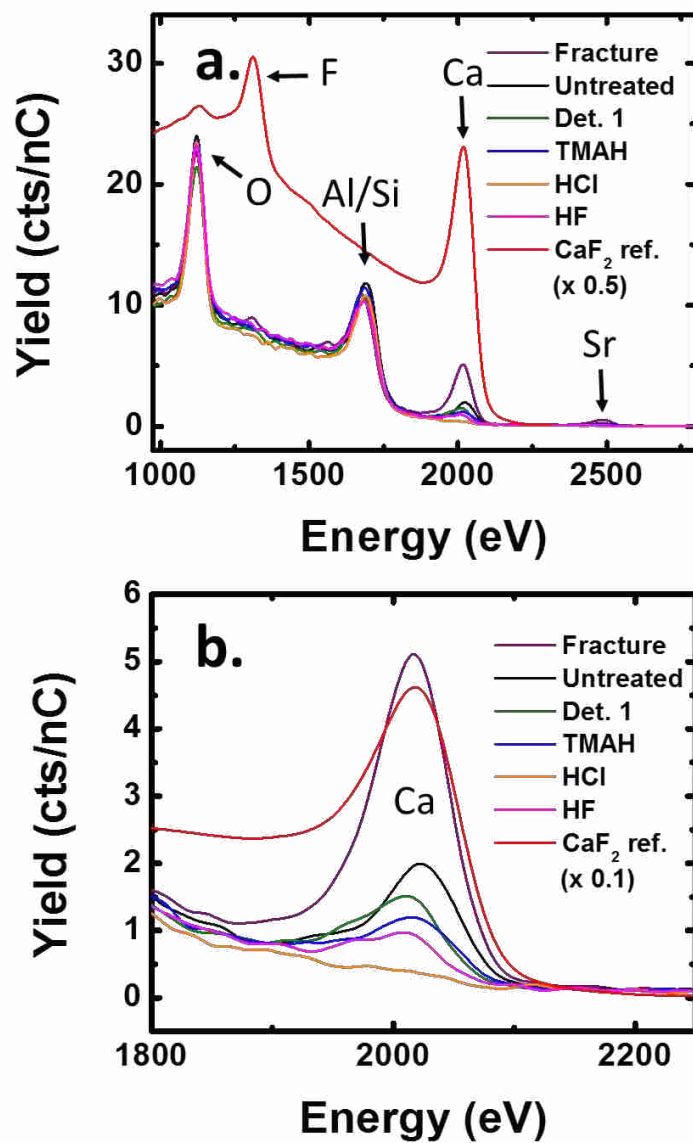
Figure 3.4. LEIS spectra taken with 3 keV He[+] of treated and Untreated Eagle XG® samples shown together with a spectrum of a CaF$_2$ reference material. (a) Wide energy range spectrum with selected peaks identified. (b) Zoomed-in view of the Ca peak.
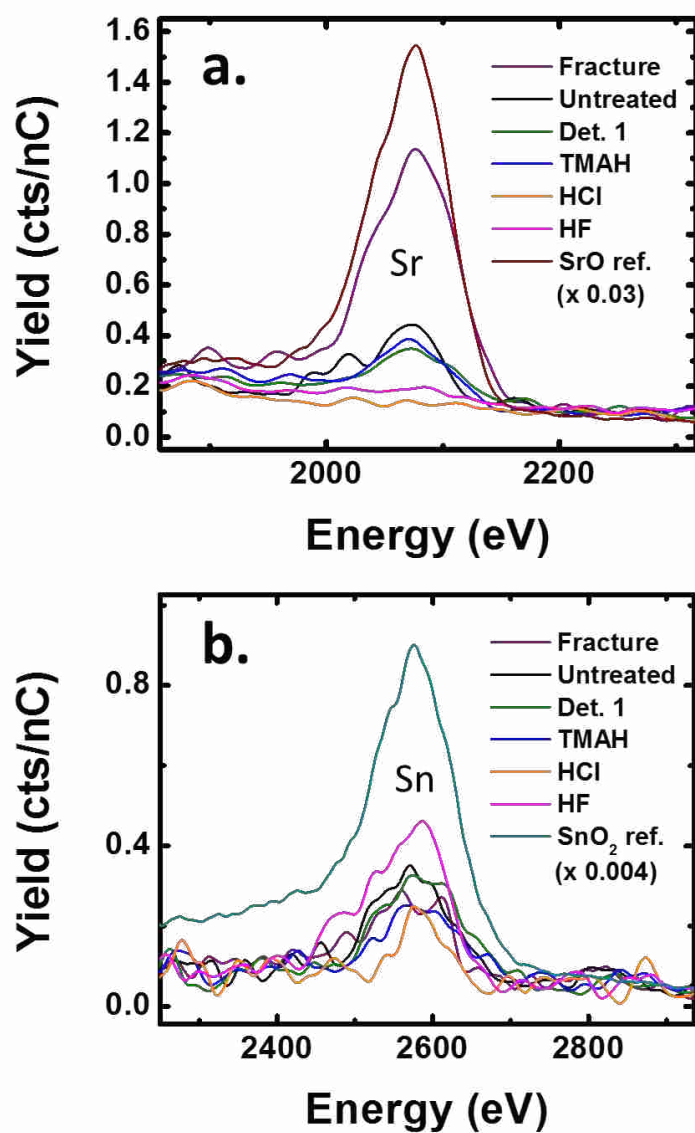
Figure 3.5. LEIS spectra taken with 5 keV Ne$^+$ of treated and Untreated Eagle XG$^®$ samples and reference materials. (a) Sr peak, and (b) Sn peak.
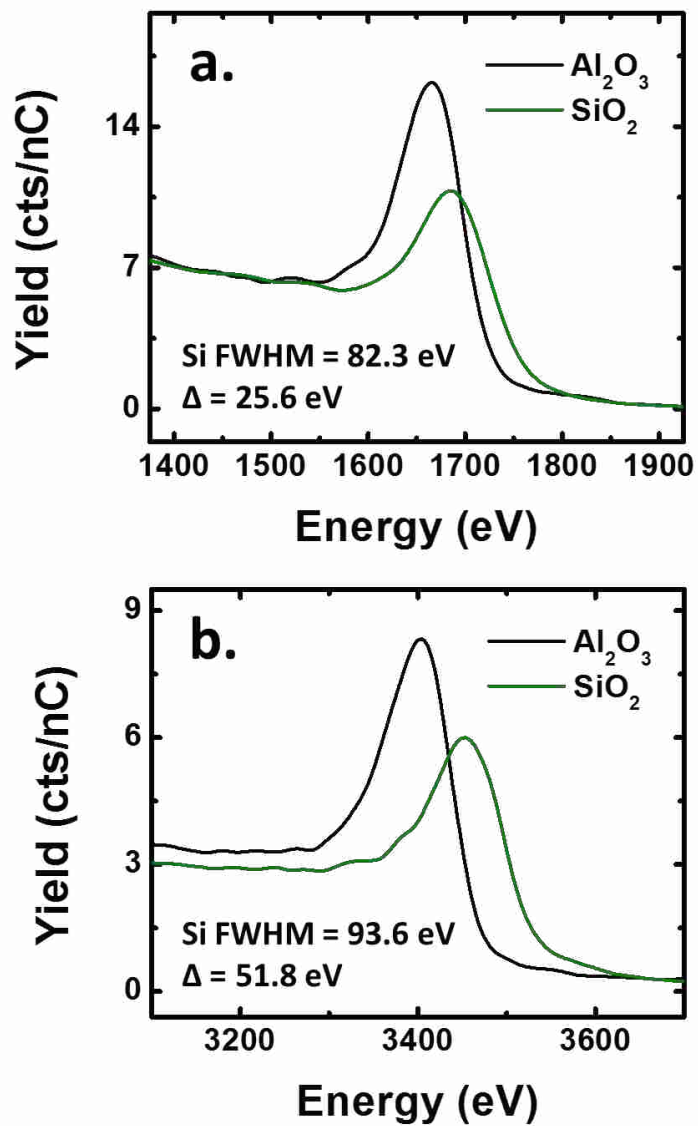
Figure 3.6. LEIS spectra showing aluminum and silicon peaks for Al_2O_3 and SiO_2 reference materials taken with (a) 3 keV $^4He^+$ and (b) 6 keV $^4He^+$, with peak separation (Δ) and the FWHM of the silicon peak noted in each plot.
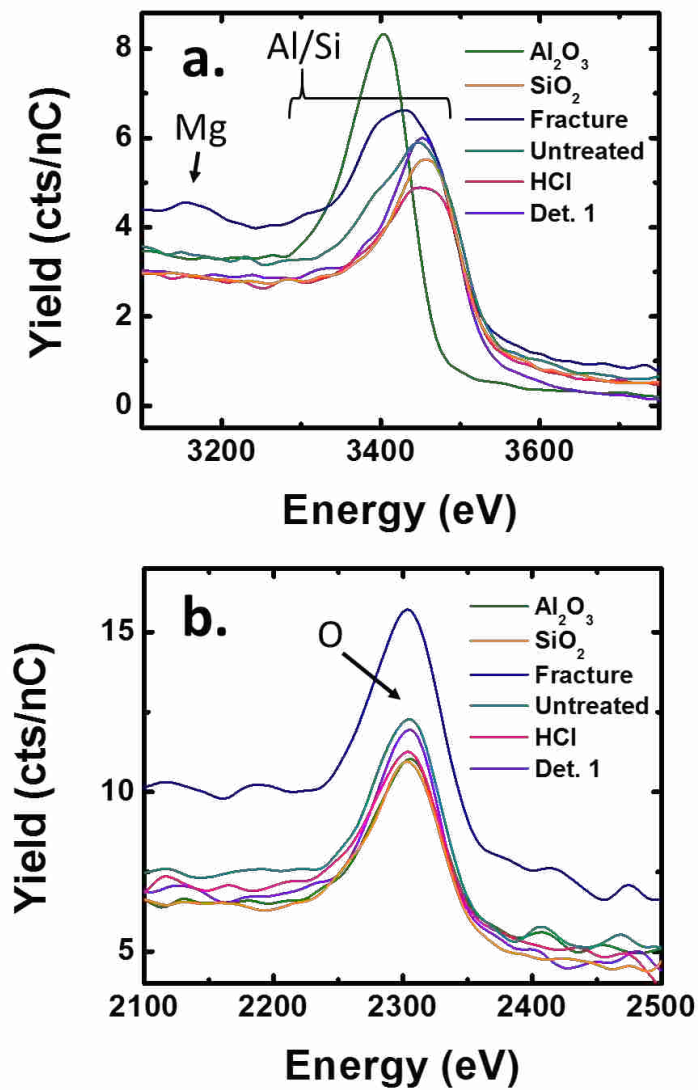
Figure 3.7. 6 keV ^{4}He$^+$ LEIS spectral regions of (a) the Al/Si signal and (b) the oxygen signal for selected Eagle XG® samples and reference materials.
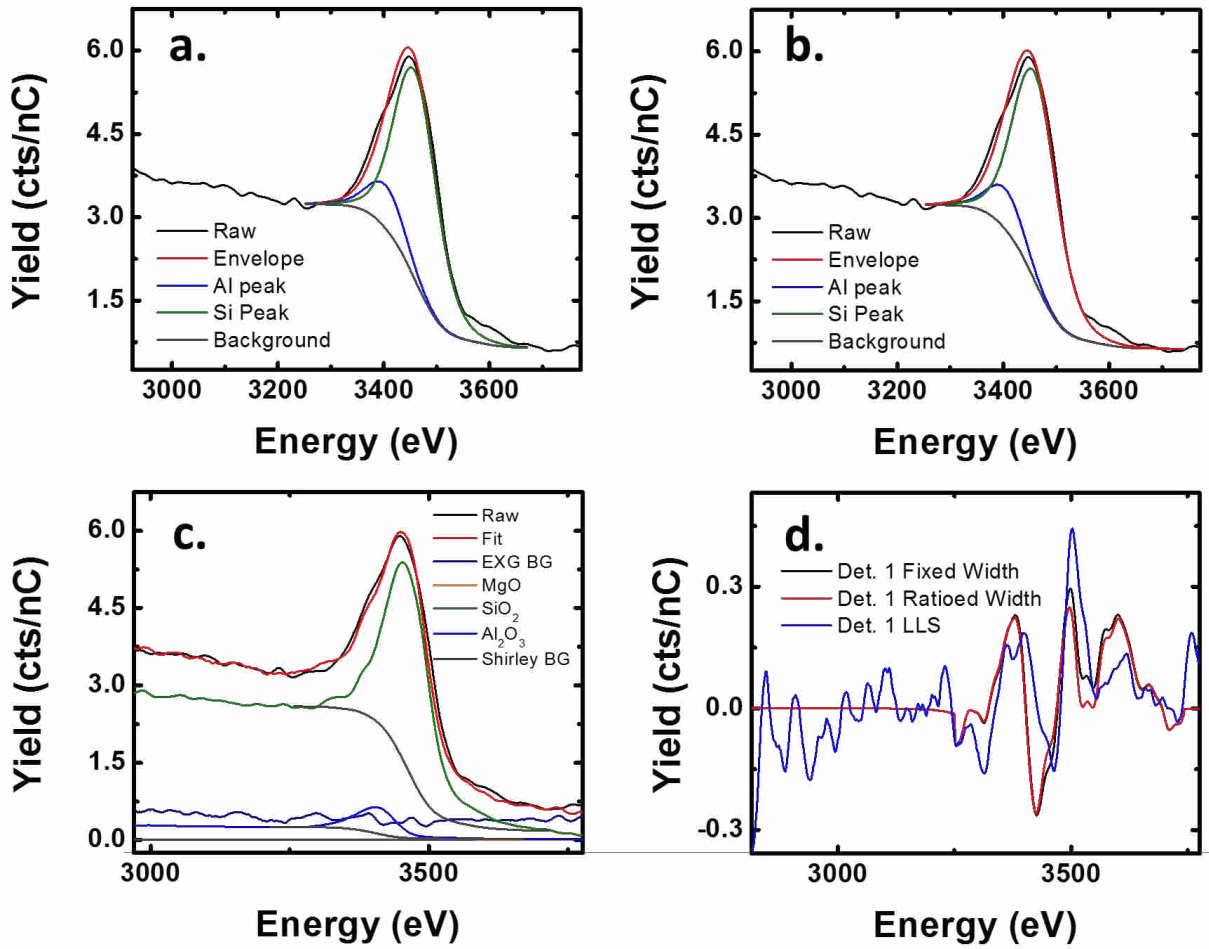
Figure 3.8. Fits to the Al/Si peak for Eagle XG® treated with Detergent 1. (a) Synthetic peak fitting with positions and widths fixed to values from reference materials. (b) Synthetic peak fitting based on reference materials, with peak widths set to a fixed ratio relative to the oxygen peak. (c) ISMA LLS fits, using the basis spectra shown in Figure 3.10. (d) Residuals for all three methods.
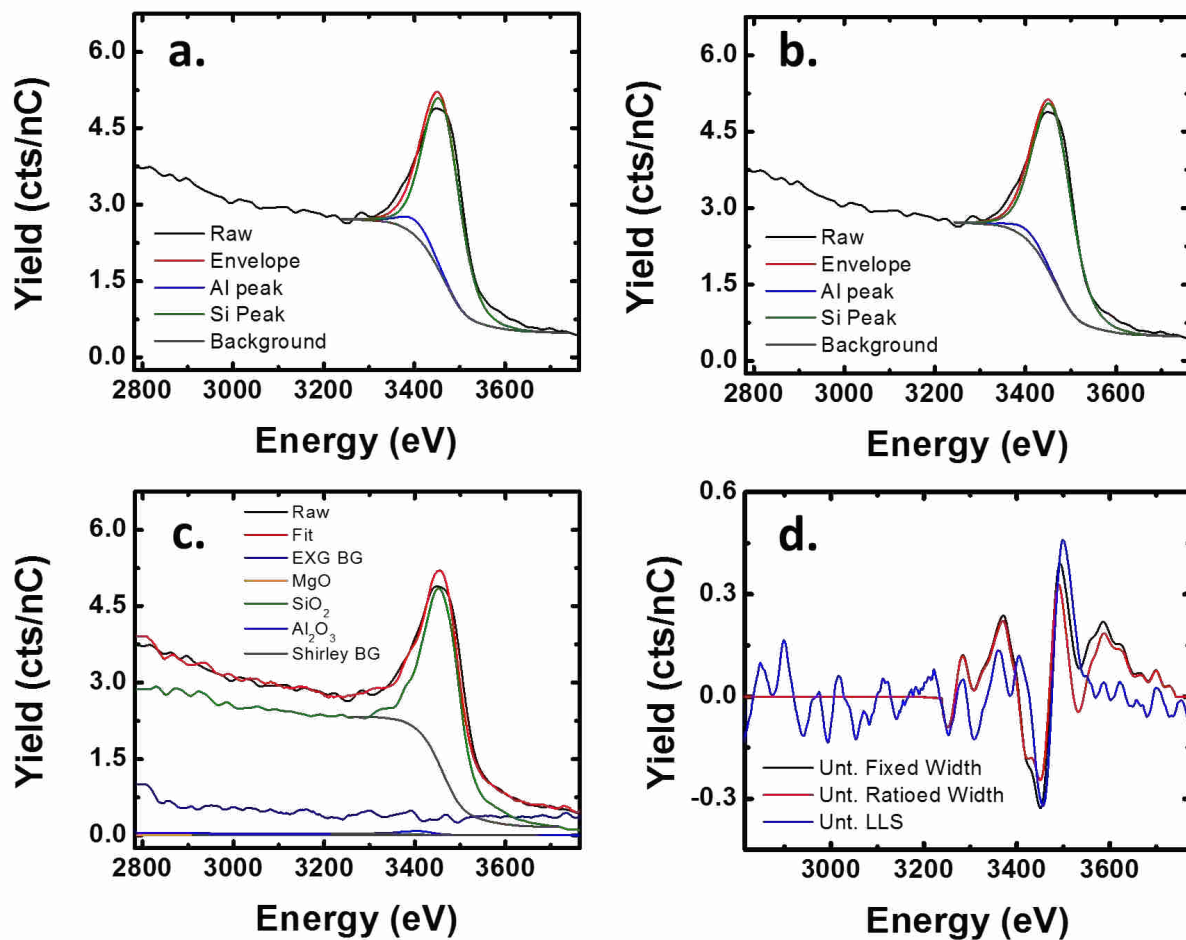
Figure 3.9. Fits to the Al/Si peak for Untreated Eagle XG®. (a) Synthetic peak fitting with positions and widths fixed to fits from reference materials. (b) Synthetic peak fitting based on reference materials, with peak widths set to a fixed ratio relative to the oxygen peak. (c) ISMA LLS fits, using the basis spectra shown in Figure 3.10. (d) Residuals for all three methods.
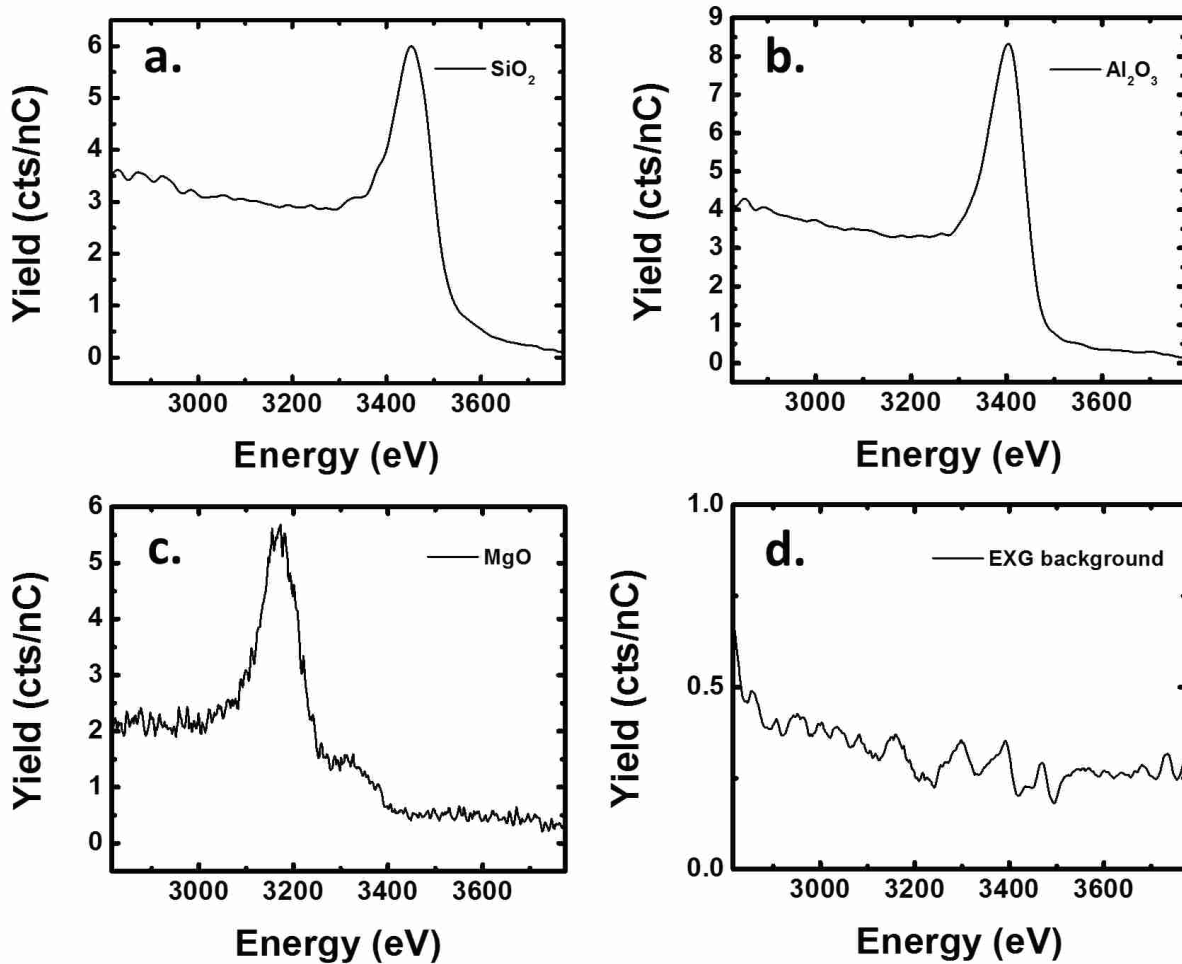
Figure 3.10. Spectra used as a basis set for ISMA LLS analysis. (a) SiO_2 reference material. (b) Al_2O_3 reference material. (d) MgO reference spectrum. (d) ISMA-derived Eagle XG® background spectrum.

3.11 References

1.   Cushman, C. V.; Brüner, P.; Zakel, J.; Dahlquist, C.; Sturgell, B.; Grehl, T.; Lunt, B. M.; Banerjee, J.; Smith, N. J.; Linford, M. R. Low Energy Ion Scattering (LEIS) of As-Formed and Chemically Modified Display Glass and peak-fitting of the Al/Si LEIS peak envelope. *Applied Surface Science* **2018,** *455*, 18-31.

2.   Hamilton, L. L. Display Innovations Through Glass. *Japanese Journal of Applied Physics* **2016,** *55*, 03CA01.

3.   Ellison, A.; Cornejo, I. A. Glass Substrates for Liquid Crystal Displays. *International Journal of Applied Glass Science* **2010,** *1* (1), 87-103.

4.   Kloss, T.; Lautenschläger, G.; Schneider, K. Advances in the Process of Floating Borosilicate Glasses and some Recent Applications for Specialty Borosilicate Float Gslasses. *Glass technology* **2000,** *41* (6), 177-181.

5.   Choi, Y. S.; Yun, J. U.; Park, S. E. Flat Panel Display Glass: Current Status and Future. *Journal of Non-Crystalline Solids* **2016,** *431*, 2-7.

6.   Agnello, G.; Hamilton, J.; Manley, R.; Streltsova, E.; LaCourse, W.; Cormack, A. Investigation of Contact-Induced Charging Kinetics on Variably Modified Glass Surfaces. *Applied Surface Science* **2015,** *356*, 1189-1199.

7.   Takeda, S.; Yamamoto, K.; Hayasaka, Y.; Matsumoto, K. Surface OH group governing wettability of commercial glasses. *Journal of non-crystalline solids* **1999,** *249* (1), 41-46.

8.   Hair, M. L. Hydroxyl groups on silica surface. *Journal of Non-Crystalline Solids* **1975,** *19*, 299-309.

9.   Bhattacharya, S.; Mittal, K. Mechanics of removing glass particulates from a solid surface. *Surface Technology* **1978,** *7* (5), 413-425.

10.   Bach, H. Advanced surface analysis of silicate glasses, oxides and other insulating materials: a review. *Journal of non-crystalline solids* **1997,** *209* (1), 1-18.

11.   Cushman, C. V.; Zakel, J.; Sturgell, B. S.; Major, G. I.; Lunt, B. M.; Bruner, P.; Grehl, T.; Smith, N. J.; Linford, M. R. Time-of-flight secondary ion mass spectrometry of wet and dry chemically treated display glass surfaces. *Journal of the American Ceramic Society* **2017,** *100* (10), 4770-4784.

12.   Pantano, C. G., Chemical Properties of Real and Ideal Glass Surfaces. In *Materials Characterization for Systems Performance and Reliability*, Springer: 1986; pp 127-148.

13.   Hench, L.; Clark, D. E. Physical chemistry of glass surfaces. *Journal of Non-Crystalline Solids* **1978,** *28* (1), 83-105.

14.   Cushman, C. V.; Brüner, P.; Zakel, J.; Major, G. H.; Lunt, B. M.; Smith, N. J.; Grehl, T.; Linford, M. R. Low energy ion scattering (LEIS). A practical introduction to its theory, instrumentation, and applications. *Analytical Methods* **2016,** *8* (17), 3419-3439.

15.   Sharma, A.; Jain, H.; Carnali, J. O.; Lugo, G. M. Influence of the Manufacturing Process on Corrosion Behavior of Soda-Lime-Silicate Glassware. *Journal of the American Ceramic Society* **2003,** *86* (10), 1669-1676.

16.   Melcher, M.; Wiesinger, R.; Schreiner, M. Degradation of glass artifacts: application of modern surface analytical techniques. *Accounts of chemical research* **2010,** *43* (6), 916-926.

17.	Geisler, T.; Janssen, A.; Scheiter, D.; Stephan, T.; Berndt, J.; Putnis, A. Aqueous corrosion of borosilicate glass under acidic conditions: a new corrosion mechanism. *Journal of Non-Crystalline Solids* **2010,** *356* (28), 1458-1465.

18.	Gin, S.; Jollivet, P.; Fournier, M.; Berthon, C.; Wang, Z.; Mitroshkov, A.; Zhu, Z.; Ryan, J. V. The fate of silicon during glass corrosion under alkaline conditions: a mechanistic and kinetic study with the international simple glass. *Geochimica et Cosmochimica Acta* **2015,** *151*, 68-85.

19.	Portal, S.; Sempere, R. Study of alkali silicate glass corrosion using spectroscopic ellipsometry and secondary ion mass spectrometry. *Physics and Chemistry of Glasses* **2003,** *44* (4), 303-307.

20.	Jellison, G.; Aytug, T.; Lupini, A.; Paranthaman, M.; Joshi, P. C. Optical properties of a nanostructured glass-based film using spectroscopic ellipsometry. *Thin Solid Films* **2016,** *617*, 38-43.

21.	Smith, D. P. Scattering of Low-Energy Noble Gas Ions from Metal Surfaces. *Journal of Applied Physics* **1967,** *38* (1), 340-347.

22.	Brongersma, H. H.; Draxler, M.; de Ridder, M.; Bauer, P. Surface composition analysis by low-energy ion scattering. *Surface Science Reports* **2007,** *62* (3), 63-109.

23.	Celaya Sanfiz, A.; Hansen, T. W.; Sakthivel, A.; Trunschke, A.; Schlögl, R.; Knoester, A.; Brongersma, H. H.; Looi, M. H.; Hamid, S. B. A. How important is the (001) plane of M1 for selective oxidation of propane to acrylic acid? *Journal of Catalysis* **2008,** *258* (1), 35-43.

24.	Ter Veen, H.; Kim, T.; Wachs, I.; Brongersma, H. Applications of high sensitivity-low energy ion scattering (hs-leis) in heterogeneous catalysis. *Catalysis Today* **2009,** *140* (3), 197-201.

25.	Brongersma, H. H.; Grehl, T.; van Hal, P. A.; Kuijpers, N. C.; Mathijssen, S. G.; Schofield, E. R.; Smith, R. A.; ter Veen, H. R. High-sensitivity and high-resolution low-energy ion scattering. *Vacuum* **2010,** *84* (8), 1005-1007.

26.	Téllez, H.; Aguadero, A.; Druce, J.; Burriel, M.; Fearn, S.; Ishihara, T.; McPhail, D. S.; Kilner, J. A. New perspectives in the surface analysis of energy materials by combined time-of-flight secondary ion mass spectrometry (ToF-SIMS) and high sensitivity low-energy ion scattering (HS-LEIS). *Journal of Analytical Atomic Spectrometry* **2014,** *29* (8), 1361-1370.

27.	Kelso, J.; Pantano, C.; Garofalini, S. A comparison of ion scattering spectra and molecular dynamics simulations at the surface of silicate glasses. *Surface science* **1983,** *134* (3), L543-L549.

28.	Kelso, J.; Pantano, C. Spectroscopic examination of clean glass surfaces at elevated temperatures. *Journal of Vacuum Science & Technology A: Vacuum, Surfaces, and Films* **1985,** *3* (3), 1343-1346.

29.	Almeida, R. M.; Hickey, R.; Jain, H.; Pantano, C. G. Low-Energy Ion Scattering spectroscopy of silicate glass surfaces. *Journal of Non-Crystalline Solids* **2014,** *385*, 124-128.

30.	Almeida, R. M.; Jain, H.; Pantano, C. G. Low-Energy Ion-Scattering Spectroscopy of Modified Silicate Glasses. *Journal of the American Ceramic Society* **2016,** *99* (4), 1259-1265.

31.	Cushman, C. V.; Sturgell, B. A.; Martin, A. C.; Lunt, B. M.; Smith, N. J.; Linford, M. R. Eagle XG® glass, optical constants from 230 to 1690 nm (0.73-5.39 eV) by spectroscopic ellipsometry. *Surface Science Spectra* **2016,** *23* (1), 55-60.

32.	Cushman, C. V.; Johnson, B. I.; Martin, A.; Lunt, B. M.; Smith, N. J.; Linford, M. R. Eagle XG® glass: Optical constants from 196 to 1688 nm (0.735–6.33 eV) by spectroscopic ellipsometry. *Surface Science Spectra* **2017,** *24* (2), 026001.

33.	Johnson, B. I.; Cushman, C. V.; Rowley, J.; Lunt, B. M.; Smith, N. J.; Martin, A.; Linford, M. R. Optical constants of SiO_2 from 196 to 1688 nm (0.735-6.33 eV) from 20, 40, and 60 nm

films of reactively sputtered SiO2 on Eagle XG ® glass by spectroscopic ellipsometry. *Surface Science Spectra* **2017,** *24* (2).

34.　　Banerjee, J.; Kim, S. H.; Pantano, C. G. Elemental areal density calculation and oxygen speciation for flat glass surfaces using x-ray photoelectron spectroscopy. *Journal of Non-Crystalline Solids* **2016,** *450*, 185-193.

35.　　Bare, S. R.; Knop-Gericke, A.; Teschner, D.; Hävacker, M.; Blume, R.; Rocha, T.; Schlögl, R.; Chan, A. S.; Blackwell, N.; Charochak, M. Surface analysis of zeolites: An XPS, variable kinetic energy XPS, and low energy ion scattering study. *Surface Science* **2016,** *648*, 376-382.

36.　　Ackermans, P.; Van Der Meulen, P.; Ottevanger, H.; Van Straten, F.; Brongersma, H. Simultaneous energy and angle resolved ion scattering spectroscopy. *Nuclear Instruments and Methods in Physics Research Section B: Beam Interactions with Materials and Atoms* **1988,** *35* (3-4), 541-543.

37.　　Engelhardt, H.; Bäck, W.; Menzel, D.; Liebl, H. Novel charged particle analyzer for momentum determination in the multichanneling mode: I. Design aspects and electron/ion optical properties. *Review of Scientific Instruments* **1981,** *52* (6), 835-839.

38.　　Engelhardt, H.; Zartner, A.; Menzel, D. Novel charged particle analyzer for momentum determination in the multichanneling mode. II. Physical realization, performance tests, and sample spectra. *Review of Scientific Instruments* **1981,** *52* (8), 1161-1173.

39.　　Burriel, M.; Wilkins, S.; Hill, J. P.; Muñoz-Márquez, M. A.; Brongersma, H. H.; Kilner, J. A.; Ryan, M. P.; Skinner, S. J. Absence of Ni on the outer surface of Sr doped La 2 NiO 4 single crystals. *Energy & Environmental Science* **2014,** *7* (1), 311-316.

40.　　Sanfiz, A. C.; Hansen, T. W.; Sakthivel, A.; Trunschke, A.; Schlögl, R.; Knoester, A.; Brongersma, H.; Looi, M. H.; Hamid, S. How important is the (001) plane of M1 for selective oxidation of propane to acrylic acid? *Journal of Catalysis* **2008,** *258* (1), 35-43.

41.　　Stokhof, M.; Sprey, H.; Li, W.-M.; Haukka, S.; Brongersma, H. LEIS study of ALD WNxCy growth on dielectric layers. *ECS Transactions* **2006,** *1* (10), 71-77.

42.　　de Rooij-Lohmann, V.; Kleyn, A.; Bijkerk, F.; Brongersma, H.; Yakshin, A. Diffusion and interaction studied nondestructively and in real-time with depth-resolved low energy ion spectroscopy. *Applied physics letters* **2009,** *94* (6), 063107.

43.　　Brongersma, H.; De Ridder, M.; Gildenpfennig, A.; Viitanen, M. Insight in the outside: materials science at the atomic level using LEIS. *Journal of the European Ceramic Society* **2003,** *23* (15), 2761-2767.

44.　　Harmsen, J.; Jansen, W.; Hoebink, J.; Schouten, J.; Brongersma, H. Coke deposition on automotive three-way catalysts studied with LEIS. *Catalysis letters* **2001,** *74* (3), 133-137.

45.　　Druce, J.; Ishihara, T.; Kilner, J. Surface composition of perovskite-type materials studied by Low Energy Ion Scattering (LEIS). *Solid State Ionics* **2014,** *262*, 893-896.

46.　　De Ridder, M.; Van Welzenis, R.; Brongersma, H. Surface cleaning and characterization of yttria-stabilized zirconia. *Surface and interface analysis* **2002,** *33* (4), 309-317.

47.　　Kimoto, K.; Matsui, Y.; Nabatame, T.; Yasuda, T.; Mizoguchi, T.; Tanaka, I.; Toriumi, A. Coordination and interface analysis of atomic-layer-deposition Al 2 O 3 on Si (001) using energy-loss near-edge structures. *Applied Physics Letters* **2003,** *83* (21), 4306-4308.

48.　　Shin, H. H.; McIntosh, S. On the H 2/D 2 isotopic exchange rate of proton conducting barium cerates and zirconates. *Journal of Materials Chemistry A* **2013,** *1* (26), 7639-7647.

49.　　De Ridder, M.; Van Welzenis, R.; van der Gon, A. D.; Brongersma, H.; Wulff, S.; Chu, W.-F.; Weppner, W. Subsurface segregation of yttria in yttria stabilized zirconia. *Journal of applied physics* **2002,** *92* (6), 3056-3064.

50.	Jansen, W.; Knoester, A.; Maas, A.; Schmit, P.; Kytökivi, A.; Denier vd Gon, A.; Brongersma, H. Influence of compaction and surface roughness on low-energy ion scattering signals. *Surface and interface analysis* **2004,** *36* (11), 1469-1478.

51.	Vári, G.; Óvári, L.; Kiss, J.; Kónya, Z. LEIS and XPS investigation into the growth of cerium and cerium dioxide on Cu (111). *Physical Chemistry Chemical Physics* **2015,** *17* (7), 5124-5132.

52.	Young, V. Y.; Welcome, N.; Hoflund, G. B. Theoretical investigation of the instrumental peak line shape in ion-scattering spectroscopy. *Physical Review B* **1993,** *48* (5), 2981.

53.	Hathaway, M.; Grehl, T.; Brüner, P.; Fartmann, M.; Brongersma, H. In *Nucleation and Growth of Few-Layer ALD Films on Various Substrates Studied by Low Energy Ion Scattering (LEIS) Spectrosopy*, AVS 62nd International Symposium, San Jose, CA, 2015.

54.	Chatterjee, S.; Singh, B.; Diwan, A.; Lee, Z. R.; Engelhard, M. H.; Terry, J.; Tolley, H. D.; Gallagher, N. B.; Linford, M. R. A perspective on two chemometrics tools: PCA and MCR, and introduction of a new one: Pattern recognition entropy (PRE), as applied to XPS and ToF-SIMS depth profiles of organic and inorganic materials. *Applied Surface Science* **2018,** *433*, 994-1017.

55.	Baltrusaitis, J.; Mendoza-Sanchez, B.; Fernandez, V.; Veenstra, R.; Dukstiene, N.; Roberts, A.; Fairley, N. Generalized molybdenum oxide surface chemical state XPS determination via informed amorphous sample model. *Applied Surface Science* **2015,** *326*, 151-161.

56.	d'Halluin, M.; Mabit, T.; Fairley, N.; Fernandez, V.; Gawande, M. B.; Le Grognec, E.; Felpin, F.-X. Graphite-supported ultra-small copper nanoparticles–Preparation, characterization and catalysis applications. *Carbon* **2015,** *93*, 974-983.

57.	Kiss, J.; Révész, K.; Solymosi, F. Segregation of boron and its reaction with oxygen on Rh. *Applied Surface Science* **1989,** *37* (1), 95-110.

58.	Draxler, M.; Gruber, R.; Brongersma, H.; Bauer, P. Velocity scaling of ion neutralization in low energy ion scattering. *Physical review letters* **2002,** *89* (26), 263201.

59.	Sekine, T.; Suzuki, T.; Yamamoto, K. Inward Migration of Glass-Modifier Cations During Heat Treatment Under an N2 Atmosphere. *Journal of the American Ceramic Society* **2015,** *98* (5), 1464-1470.

60.	Mellott, N.; Brantley, S.; Hamilton, J.; Pantano, C. Evaluation of surface preparation methods for glass. *Surface and interface analysis* **2001,** *31* (5), 362-368.

61.	Sundaram, K.; Bhagavat, G. X-ray and electron diffraction studies of chemically vapour-deposited tin oxide films. *Thin Solid Films* **1981,** *78* (1), 35-40.

62.	Benninghoven, A. Some aspects of secondary ion mass spectrometry of organic compounds. *International Journal of Mass Spectrometry and Ion Physics* **1983,** *53*, 85-99.

63.	Delcorte, A.; Leblanc, C.; Poleunis, C.; Hamraoui, K. Computer Simulations of the Sputtering of Metallic, Organic, and Metal–Organic Surfaces with Bi n and C60 Projectiles. *The Journal of Physical Chemistry C* **2013,** *117* (6), 2740-2752.

64.	Szakal, C.; Kozole, J.; Russo Jr, M. F.; Garrison, B. J.; Winograd, N. Surface sensitivity in cluster-ion-induced sputtering. *Physical review letters* **2006,** *96* (21), 216104.

65.	van der Heide, P., Sputtering and Ion Formation. In *Secondary Ion Mass Spectrometry*, John Wiley & Sons, Inc.: 2014; pp 44-143.

66.	Jensen, D. S.; Kanyal, S. S.; Madaan, N.; Hancock, J. M.; Dadson, A. E.; Vail, M. A.; Vanfleet, R.; Shutthanandan, V.; Zhu, Z.; Engelhard, M. H.; Linford, M. R. Multi-instrument characterization of the surfaces and materials in microfabricated, carbon nanotube-templated thin layer chromatography plates. An analogy to 'The Blind Men and the Elephant'. *Surface and Interface Analysis* **2013,** *45* (8), 1273-1282.

67.   Singh, B.; Smith, S. J.; Jensen, D. S.; Jones, H. F.; Dadson, A. E.; Farnsworth, P. B.; Vanfleet, R.; Farrer, J. K.; Linford, M. R. Multi-instrument characterization of five nanodiamond samples: a thorough example of nanomaterial characterization. *Analytical and bioanalytical chemistry* **2016,** *408* (4), 1107-1124.

68.   Diwan, A.; Singh, B.; Hurley, C. J.; Linford, M. R. Layer-by-layer deposition of nitrilotris (methylene) triphosphonic acid and Zr (IV): an XPS, ToF-SIMS, ellipsometry, and AFM study. *Surface and Interface Analysis* **2016,** *48* (2), 105-110.

Chapter 4: Angle-Resolved X-ray Photoelectron Spectroscopy Analysis of Chemically Treated Display Glass Surfaces

4.1 Statement of Attribution

This data was not published in a peer-reviewed journal at the time of publication. This data represents a work in progress. We have provided qualitative interpretation of the data here, which generally supports conclusions from other chapters in this dissertation. However, we plan to perform additional modeling before publishing these results in a peer-reviewed research journal.

I would like to acknowledge the contributions of George Major, Landon S. Fisher, Sean Chapman, Jeff Chapman, Adam Roberts, Paul Mack, Tim Nunney, Joy Banerjee, and Nicholas J. Smith, who have assisted with the collection and interpretation of this data.

4.2 Introduction

Angle-resolved X-ray photoelectron spectroscopy (AR-XPS) provides depth-resolved elemental compositional information about the outer *ca.* 6-10 nm of a sample.[1-4] Photoelectrons collected at different take off angles originate from different depths within the sample. Simple comparison between compositions measured at different take off angles can be used to detect and interpret compositional gradients near the sample surface. Mathematical modeling is required to derive quantitative depth scales for AR-XPS data. This process typically requires *a priori* knowledge about the composition and structure of the sample.[1, 4]

The complexity of the modeling for AR-XPS data scales with the complexity of the sample's composition. Relative depth and layer thicknesses are easily derived for samples with 2-3 discrete layers with well-defined stoichiometries.[1, 4] Continuous compositional gradients substantially increase the modeling complexity.[1, 5-8] The glass samples we analyzed likely have continuous compositional gradients based on the various glass corrosion mechanisms discussed in Chapter 1.[9-10] We can currently only provide qualitative interpretation of this AR-XPS data, but we may derive depth-resolved compositional profiles with additional work.

Even interpreted in a qualitative sense, the AR-XPS data presented here provides valuable insight into our samples. The results in Chapters 2 and 3 show clear differences between surface and bulk compositions of Eagle XG®, where the bulk composition was obtained by analyzing Eagle XG® fracture surfaces. However, the analyses in Chapters 2 and 3 provide no indication as to whether composition changes rapidly as a function of sample depth at the outer 10 nm. Even with the qualitative interpretation presented here, the AR-XPS data demonstrate a relatively steep compositional gradient over the outer *ca.* 10 nm of Eagle XG®. The surface composition also varies strongly as a function of the wet-chemical sample treatments used in this study, consistent with previous results.[11-12]

4.3 Theory of AR-XPS

The fundamental equation of XPS assumes that photoelectron kinetic energy is a function of the exciting photon energy, core-level electron binding energy, and work function of the XPS instrument, according to Equation (4.1),[13]

(4.1) $E_{photon} = E_{binding} + E_{kinetic} + E_{work}$,

where E_{photon} is the photon energy, $E_{binding}$ is the core-level binding energy, and E_{work} is the instrument work function. Core-level electron binding energies are characteristic of the elements. They scale with atomic number, Z, and increase with decreasing principal quantum number n.[13] XPS measures the kinetic energies of photoelectrons emitted from the sample surface, calculates their binding energy using Equation (4.1), and identifies and quantifies the elements present in the sample based on the binding energies and intensities of the photoelectron signals in the resulting spectra. XPS spectra are typically plotted according to the very simple assumptions of Equation (4.1).

Equation (4.1) does not account for energy lost from inelastic scattering. Photoelectrons that scatter inelastically before escaping the sample lose kinetic energy and, according to the simplified assumptions of Equation (4.1), are plotted at higher binding energy than photoelectrons from the same core-level that do not scatter inelastically. Electrons that do not undergo inelastic scattering give relatively sharp peaks in XPS spectra, while the inelastically scattered photoelectrons contribute to the stair-step background shapes common in XPS.[13]

AR-XPS analyzes the elemental composition of the outer *ca.* 10 nm of a sample. The surface sensitivity of XPS stems from the fact that free electrons only travel a short distance through a solid material before undergoing inelastic collisions. The inelastic mean free path (λ) of electrons through solid materials is a function of their kinetic energy and also depends on the

composition of the material they traverse.[1, 13] For lab-scale XPS instruments operating with aluminum anode X-ray sources, photoelectron kinetic energies of 0-1486 eV are possible, and λ from 1-3 nm are typical.[13] Changing the angle at which photoelectrons are collected varies the depth from which photoelectrons originate relative to sample normal. Figure 4.1 illustrates this schematically.

In Figure 4.1, it is assumed that photoelectrons can travel a maximum distance of 3λ through the sample. Their maximum depth of origin normal to the sample surface is given by $3\lambda\cos\Theta$, where Θ is the photoelectron take off angle relative to surface normal. Some sources define take off angle relative to surface horizontal, in which case the maximum depth of origin is given by $3\lambda\sin\Theta$. Assuming a typical λ of 3 nm, data recorded at a take off angle of 78.25° (the most surface sensitive take off angle used in this study) integrates information over a depth from 0 to 1.8 nm, while data recorded at normal incidence integrates information from 0-9 nm. Thus, data recorded at a higher take off angle provides compositional information nearer to the sample surface, while data recorded nearer to normal incidence provides information from a greater sample depth.

Different take off angles do not probe discrete sample volumes. For example, a take off angle of 76.25° integrates information from 0-2 nm relative to surface normal, while a take off angle of 23.75° integrates information from 0-8 nm, such that there is some overlap in information depth between the two take off angles.[1] In contrast, sputter depth profiling erodes the sample during the analysis, such that each scan records information from a discrete slice of the sample. As a result, interpreting AR-XPS data is generally more complicated than analyzing sputter depth profile data. The differences in sampling between these two methods are illustrated schematically in Figure 4.2.

Sputter depth profiling is usually used over greater information depths than AR-XPS. In ToF-SIMS, the analysis depth for each individual scan in a depth profile ranges from 0-3 nm, depending on numerous factors. By eroding the samples and taking many scans, depth profiles are routinely taken from depths ranging from *ca.* 20 nm to several hundred nanometers.[14-15] AR-XPS is limited to a maximum information depth of *ca.* 10 nm. AR-XPS is unique in its ability to provide depth-resolved information over this narrow information depth. This is possible because AR-XPS is a non-destructive process. In contrast, sputter depth profiling involves bombarding samples with a high-energy beam. The sample's composition is altered during this process through atomic mixing and preferential sputtering. Several seconds of sputter time may be required before the composition in the sputter volume reaches a steady state useful for compositional analysis.[15-16]

In Figure 4.2, we represented XPS sampling depths as tapered shapes to indicate that the greatest fraction of photoelectrons is collected within $1\lambda\cos\Theta$ of the surface. Photoelectron signal intensity attenuates through inelastic collisions as a function of depth according to the Beer-Lambert law, Equation (4.2),

(4.2) $I = I^0 e^{-d/\lambda cos\Theta}$,

where I is photoelectron intensity after attenuation and I^0 is the unattenuated photoelectron intensity of a layer of atoms at depth d within the sample measured normal to the sample surface.[1] Based on these assumptions, the photoelectron signal integrated from sample depths of $0\lambda\cos\Theta$ to $1\lambda\cos\Theta$ accounts for 63% of total photoelectron intensity in an XPS spectrum for a sample with homogeneous composition. Only 8.5% of total photoelectron peak intensity originates from a sample depth between $2\lambda\cos\Theta$ and $3\lambda\cos\Theta$. In summary, while the sampling depth of XPS is often stated to be $3\lambda\cos\Theta$, the majority of the signal in an XPS spectrum originates from within $1\lambda\cos\Theta$ of the surface.

Modeling AR-XPS data to obtain depth-resolved compositional profiles is challenging because the model must account for Beer's law attenuation of photoelectrons as a function of sample composition, structure, and photoelectron kinetic energy.[1] The fact that XPS data obtained at different take off angles provides overlapping information rather than discrete information, as shown in Figure 4.2, further complicates modeling. The complex mathematics underlying modeling of AR-XPS data are the subject of numerous publications and reviews and articles.[1-2, 4, 6-8] We limited ourselves to a qualitative interpretation due to the inherent complexity of modeling AR-XPS data.

Our data shows that AR-XPS is a powerful tool for understanding near-surface compositional gradients in multicomponent glasses. However, we are not aware of any publication using AR-XPS for this purpose. AR-XPS has been used to measure the growth of oxide films on various substrates including magnesium and iron, to measure the nitrogen profiles in thin silicon oxynitride films, and to characterize self-assembled monolayers, among other applications.[3, 5, 17-18] When samples consist of discrete layers with well-defined stoichiometries, AR-XPS often provides excellent film thickness measurements. AR-XPS can also be used to model compositional gradients in samples. In these cases a unique fitting solution is usually not possible, and the final fit results strongly depend on modeling assumptions and constraints.[1, 3] Compositional gradients are likely for our glass samples, and advanced modeling will be required to extract quantitative depth distributions from the data below. We hope to address this in the near future. However, even qualitative interpretation of the data gives useful insight into the near-surface composition of multicomponent display glass.

4.4 Experimental

Samples in this study were produced from Eagle XG® display glass harvested directly from a Corning production line and stored in airtight containers until the time of analysis. We have confirmed by XPS that this storage method maintains pristine surfaces with <5 atom % of adventitious carbon contamination. These samples were treated with the chemical treatments shown in Table 4.1, following the same protocols used in previous chapters of this dissertation. Following treatment, samples were stored in sealed glass vials until the time of analysis (*ca.* 1 week).

Table 4.1. Wet chemical treatment conditions.

Reagent	Grade	Supplier	Conc.	pH	Temp. (°C)	Time (m)
Industrial Detergent	N/R	N/R	1% v/v	12	60	10
HCl	Optima®	Fisher Scientific	0.1 M	1*	60	3.3, 10, or 100
HF	ACS	EMD	0.1 M	2*	20	10
TMAH	TraceSelect® Ultra	Fluka	0.1 M	11*	60	10

N/R = not reported. *Calculated pH.

All XPS data was acquired at ThermoFisher headquarters in East Grinstead, UK, using a ThermoFisher Thetaprobe instrument. This instrument acquires AR-XPS data at multiple angles in parallel using electron optics that disperse photoelectrons according to their take off angles across a position-sensitive detector, as shown in Figure 4.3. For this analysis, the data was retroactively partitioned into eight take off angle data channels. Two replicates were taken for each sample treatment, where a new sample was used for each replicate. The average compositions from two replicate measurements are reported at each angle for each species.

Data was collected from the Si 2p, Al 2p, B 1s, Ca 2p, Mg 1s, Sr 3d, O 1s, and Sn 3d transitions for each sample. Data was analyzed using the Avantage software package (ThermoFisher, East Grinstead, UK. Ver. 5.967). The peak areas at each transition were measured by applying a 'Smart' type background included in the analysis software package. This background is a variation of the commonly used Shirley background with the additional constraint that the background intensity should not exceed the data intensity at any point. The resulting peak areas were used to calculate the relative concentration in units of atom % and mole %.

We used the known bulk composition of an Eagle XG® fracture surface to derive elemental sensitivity factors. The bulk composition of Eagle XG® is proprietary, and is not published here. However, the AR-XPS analysis revealed no compositional gradients in the Eagle XG® fracture surface. Prior to quantitation, we corrected all data for signal attenuation from adventitious carbon overlayers following a published protocol.[19]

4.5 Results and Discussion

Figure 4.4 displays XPS results for Eagle XG® exposed to various sample treatments. Quantitative surface compositional information for Eagle XG® is considered confidential information. Therefore, the data in each plot has been scaled to the concentration for untreated Eagle XG® obtained at a take off angle of 23.75°, which is the least surface sensitive take off angle in this study. Thus normalized, the plots provide useful compositional comparison between the various sample treatments and present evidence of near-surface compositional gradients in these samples while protecting sensitive compositional information. Modifier, Al, and B concentrations generally decrease as the scans move to shallower analysis depths (greater take off angles) in

Figure 4.4b-f. In contrast, the concentration of Si increases near the sample surface in Figure 4.4a. These results are consistent with the previous LEIS and SIMS quantitative analyses, which suggest relatively Si rich surfaces form on most chemically treated Eagle XG® samples.[11-12] Significant scatter occurs in some of the plots, especially for the less-abundant species. Scatter in the B 1s data may be attributed to its relatively low photoemission cross-section. The Sr 3d transition proved challenging due to its low concentration and difficult background arising from proximity to the Si 2p and Al 2s transitions. Only small fractions of Sn and Mg were detected while excellent signals were obtained for Si, Ca, and Al.

Similar quantities of oxygen are detected in all Eagle XG® samples in Figure 4.4g. Oxygen concentration increases sharply in the more surface sensitive scans. Relative increases of *ca.* 8% in oxygen are seen for all samples between the least surface sensitive data, recorded at 23.75°, and the data with the greatest surface sensitivity, recorded at 76.25°. There are several possible explanations for this apparent compositional gradient. Oxidized adventitious hydrocarbon species (e.g., alcohols and carboxylic acids) contribute some oxygen to the sample surface. Also, physisorbed water contributes to the total measured oxygen. Without heating the samples, it is impossible to remove or account for oxygen from physisorbed water.[20] Surface hydroxyls also increase the amount of detected oxygen compared to unhdroxylated surfaces.[20-21] Water and hydrous species, e.g., hydronium, may also penetrate the glass to some extent, contributing to an oxygen gradient near the sample surface.[9]

Unfortunately, it is difficult to distinguish between oxygen from water and oxygen from the glassy network by XPS.[20] All of our samples, including the fracture surfaces used to derive the elemental sensitivity factors, were prepared in air and are likely to include a layer of physisorbed water and surface hydroxyls. This is a source of uncertainty in the elemental sensitivity factors for

oxygen, but will not affect the relative ratios of other elemental signals. Accordingly, the remainder of the discussion focuses on sample composition in terms of mole % of oxides, assuming that the concentrations of SiO_2, B_2O_3, Al_2O_3, SnO_2, CaO, MgO, and SrO scale with the Si 2p, B 1s, Al 2p, Sn 3d, Ca 2p, Mg 3d, and Sr 3d signals, respectively, applying stoichiometric factors where necessary. In other words, we have calculated the molar concentrations of these species without using the O 1s signal.

Molar percentages of each oxide as a function of take off angle are shown in Figure 4.5 for all samples. Again, all concentrations have been normalized to the intensity of the concentrations for the untreated Eagle XG® sample measured at a take off angle of 23.75° to protect sensitive compositional information. Removing the oxygen signal from our analysis and analyzing the data in terms of molar composition has simplified the interpretation of compositional trends in some cases. For example, Figure 4.4a shows a dip in Si concentration at intermediate take off angles while Figure 4.5a shows monotonically increasing SiO_2 concentration nearer to the surface. B_2O_3 concentration appears to decrease most sharply nearest to the surface for all samples, while more gradual decreases are seen for Al_2O_3 and CaO. Noisier data for MgO and SrO limit their interpretation, but concentrations for both species appear to decrease near the surface. SnO_2 is detected in small quantities, but the signal-to-noise ratio is too low for further interpretation.

This data suggests a significant compositional gradient occurs in the outer *ca.* 10 nm of Eagle XG®. This is a relatively shallow depth of modifier depletion. For example, there is a *ca.* 25% relative decrease Al_2O_3 concentration for untreated Eagle XG® between analyses performed at 23.75° and 76.25°. More advanced modeling of the data may reveal an even steeper compositional gradient. This result is in good agreement with our previous LEIS analysis, which showed very low Al_2O_3 surface coverage at the outermost atomic layer of untreated Eagle XG®.[11]

This study included samples exposed to 0.1 m HCl for different periods of time (3.3 minutes, 10 minutes, or 100 minutes). The depletion of modifiers, Al, and B for these samples follows the expected trend, with the greatest degree of depletion for the sample treated the longest. Interestingly, modifiers, Al, and B are also strongly depleted from the HF-treated sample, which gives only slightly higher concentrations than the sample treated with HCl for 3.3 minutes. This result agrees with the previous LEIS and ToF-SIMS analyses in Chapters 2 and 3. It suggests that both etching and ion exchange occur for HF-treated Eagle XG® under the described reaction conditions.

Detergent-treated Eagle XG® has increased Al_2O_3 compared to the as-formed surface, in agreement with our previous LEIS and ToF-SIMS analyses.[11-12] This sample has *ca.* 20% greater Al_2O_3 concentration than the untreated surface in the analysis performed at 23.75°, and *ca.* 40% greater aluminum concentration in the analysis performed at 76.25°. Possible explanations for this phenomenon include precipitation of an Al_2O_3-rich layer from solution on the glass surface, or etching of a Si-rich layer that naturally forms on Eagle XG® to reveal a more bulk-like Al_2O_3-rich composition.

Interestingly, while other samples shown monotonically decreasing Al_2O_3 concentrations towards more surface sensitive angles, the Al_2O_3 initially decreases at take off angles from 23.75° to 53.75° showing a flat or slightly increasing concentration after that. This may indicate the formation of an Al-rich layer on the surface of this sample, though mathematical modeling of the data is required to determine this conclusively.

4.6 Conclusion

We have analyzed chemically-treated display glass surfaces with AR-XPS. The results indicate a strong compositional gradient over the outer *ca.* 10 nm of the sample surface in all cases. The AR-XPS analysis shows a surface depleted of modifiers, Al, and B, and relatively rich in silica in good agreement with previous results.[11-12] Samples treated with industrial alkaline detergent have increased Al_2O_3 surface concentration compared to untreated Eagle XG® surfaces.

These results reinforce the conclusion that even short chemical treatments can result in important differences in the surface composition of Eagle XG®. They also show that a relatively steep compositional gradient occurs in the near-surface region of Eagle XG® during these short chemical treatments. This suggests that some of the noted differences between the LEIS and SIMS quantitative results in Chapters 2 and 3 may be due to the different information depths between the two techniques. They also demonstrate that understanding the surface composition of display glass as it relates to surface mediated processes requires extremely surface sensitive analyses. Here, XPS taken at 23.75° (analysis depth of *ca.* 8 nm) gave significantly different elemental compositions than those recorded at 76.25° (information depth of *ca.* 2 nm) in all cases. Therefore, standard XPS analysis does not accurately represent the composition of the outermost atomic layer of these display glass surfaces. The composition of the outermost atomic layer likely has the strongest influence on surface mediated processes on display glass surfaces. Therefore, understanding surface mediated processes requires extremely surface sensitive analysis.

Further modeling of this data may provide insight into glass alteration mechanisms at the Eagle XG® surface. For example, the mechanism of aluminum enrichment during treatment with alkaline industrial detergent remains unknown. A compositional depth profile of aluminum will improve our understanding. If the modeling reveals an Al_2O_3-rich film on top of a surface with

composition similar to untreated Eagle XG$^\circledR$, it may indicate that an Al_2O_3 enriched film precipitates from solution onto the surface of this sample. In contrast, a more gradual, continuous increase in Al_2O_3 concentration from surface to bulk would suggest that detergent treatment etches through an Al_2O_3-depleted/SiO_2-rich layer at the Eagle XG$^\circledR$ surface to reveal a more bulk-like composition. In principle, such modeling of our data is possible provided reasonable constraints can be applied to the fits, as indicated by other AR-XPS studies of diffusion.[1]

4.7 Figures
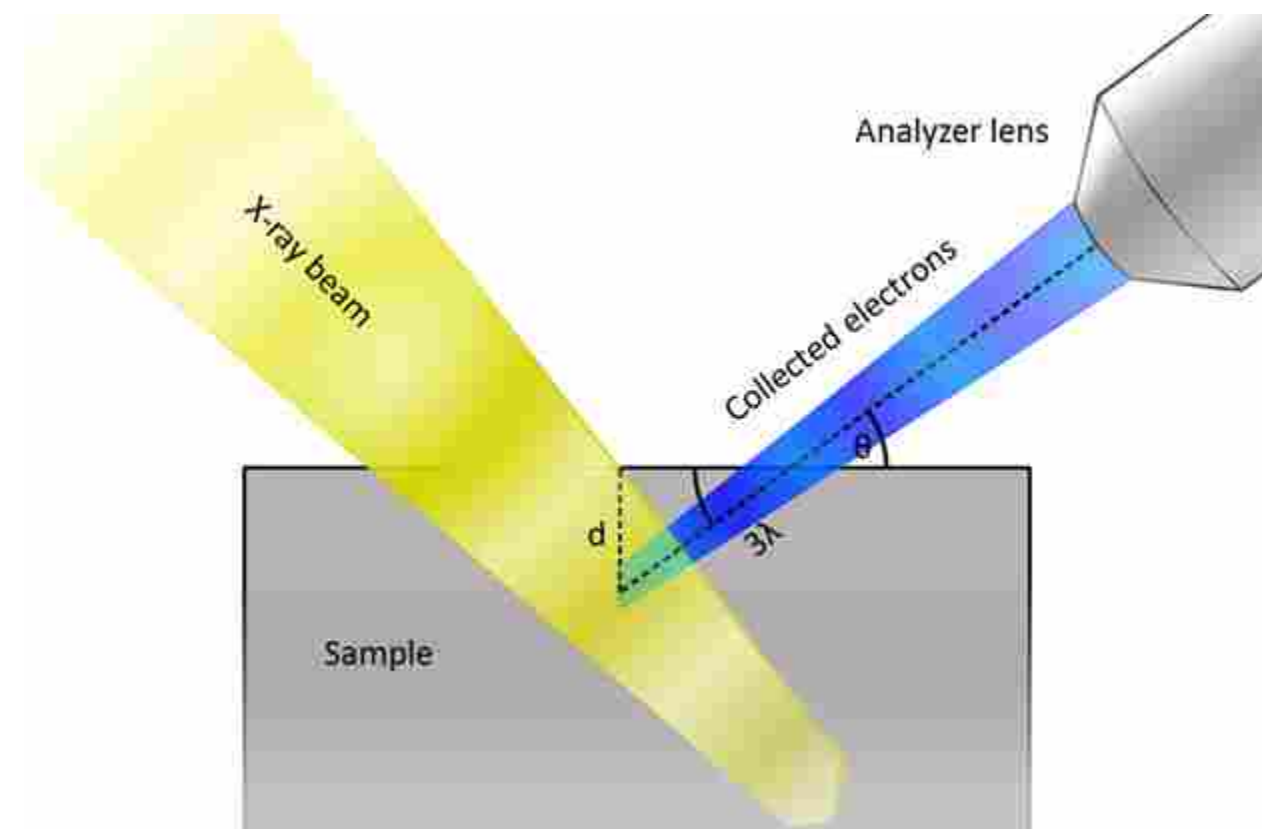
Figure 4.1. Schematic representation of the operating principle of AR-XPS.
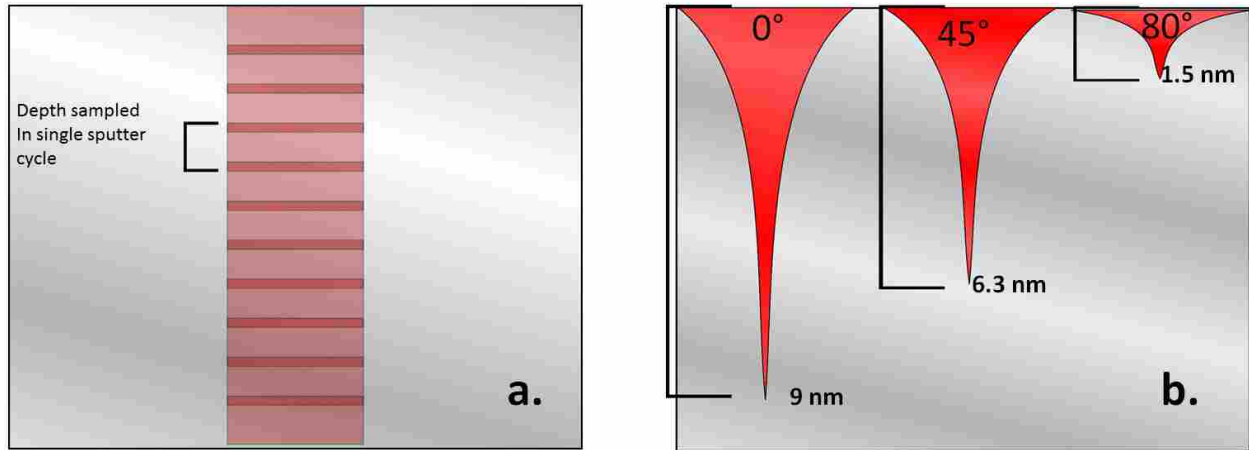
Figure 4.2. Schematic representation of sampling depths in sputter depth profiling and AR-XPS. (a.) Sampling in sputter depth profiling, where a discrete slice of sample is analyzed with every sputter cycle. (b.) Sampling in AR-XPS, where greater take off angles relative to surface normal analyze shallower depths. Note that the greatest fraction of photoelectrons always occurs within $1\lambda\cos\Theta$ of the sample surface, symbolized by the tapered shapes in the drawing.
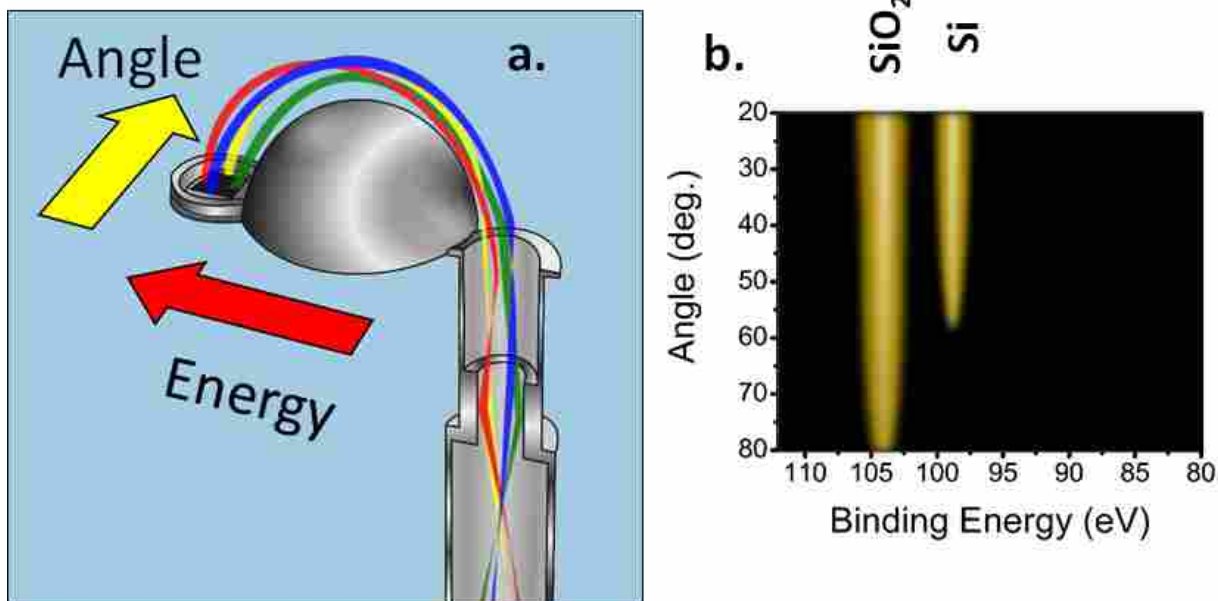
Figure 4.3. Overview of the ThermoFisher Thetaprobe XPS instrument. (a.) Electron optics in the instrument disperse the electrons across a 2-dimensional position sensitive detector. The electrons are dispersed according to energy in one axis and according to angle on the other axis. (b.) Schematic representation of the position sensitive detector using silicon oxide on silicon as an example. Electrons are dispersed by energy on the x-axis and by take off angle on the y-axis. At surface sensitive angles (nearer to 90°), only the SiO_2 is detected.
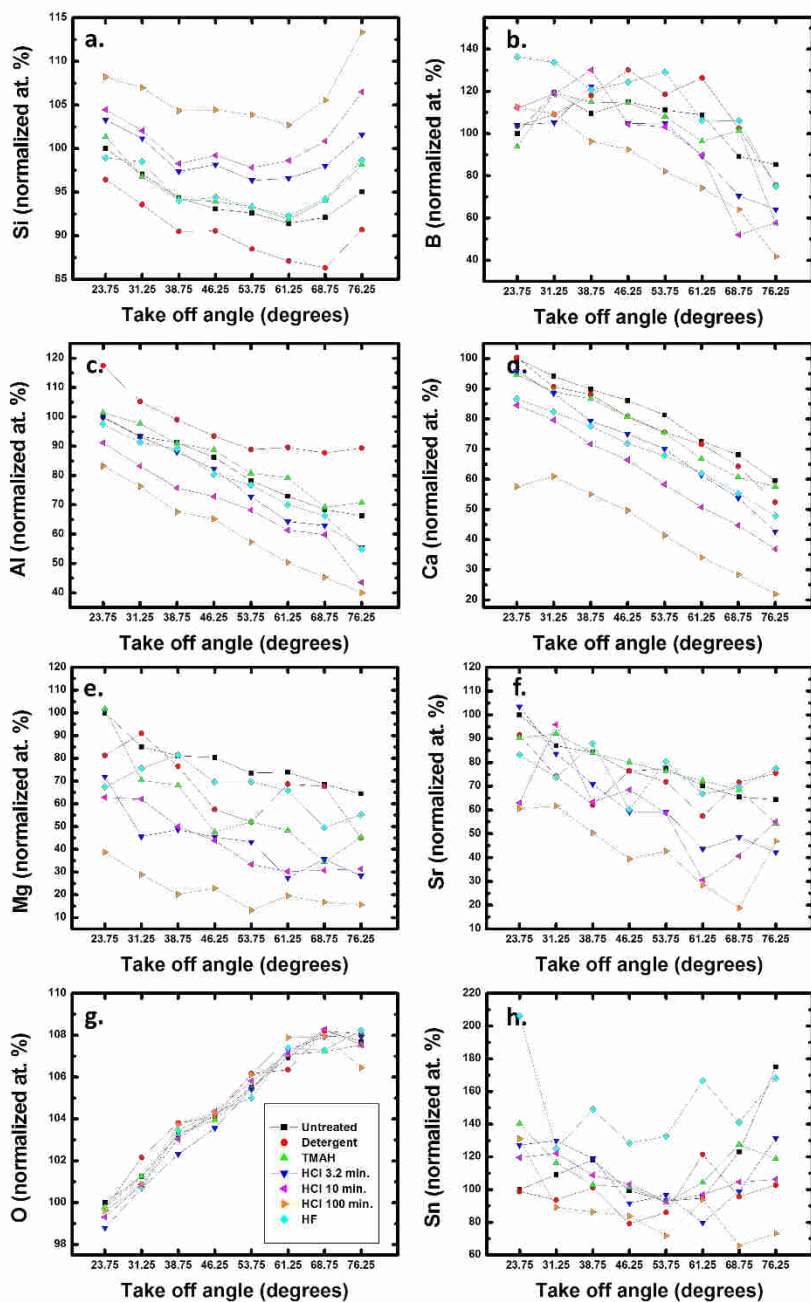
Figure 4.4. AR-XPS results showing relative elemental composition of Eagle XG® samples as a function of take off angle. Concentrations have been normalized to the concentration obtained for the untreated sample at a take off angle of 23.75° to protect confidential compositional information about this material.
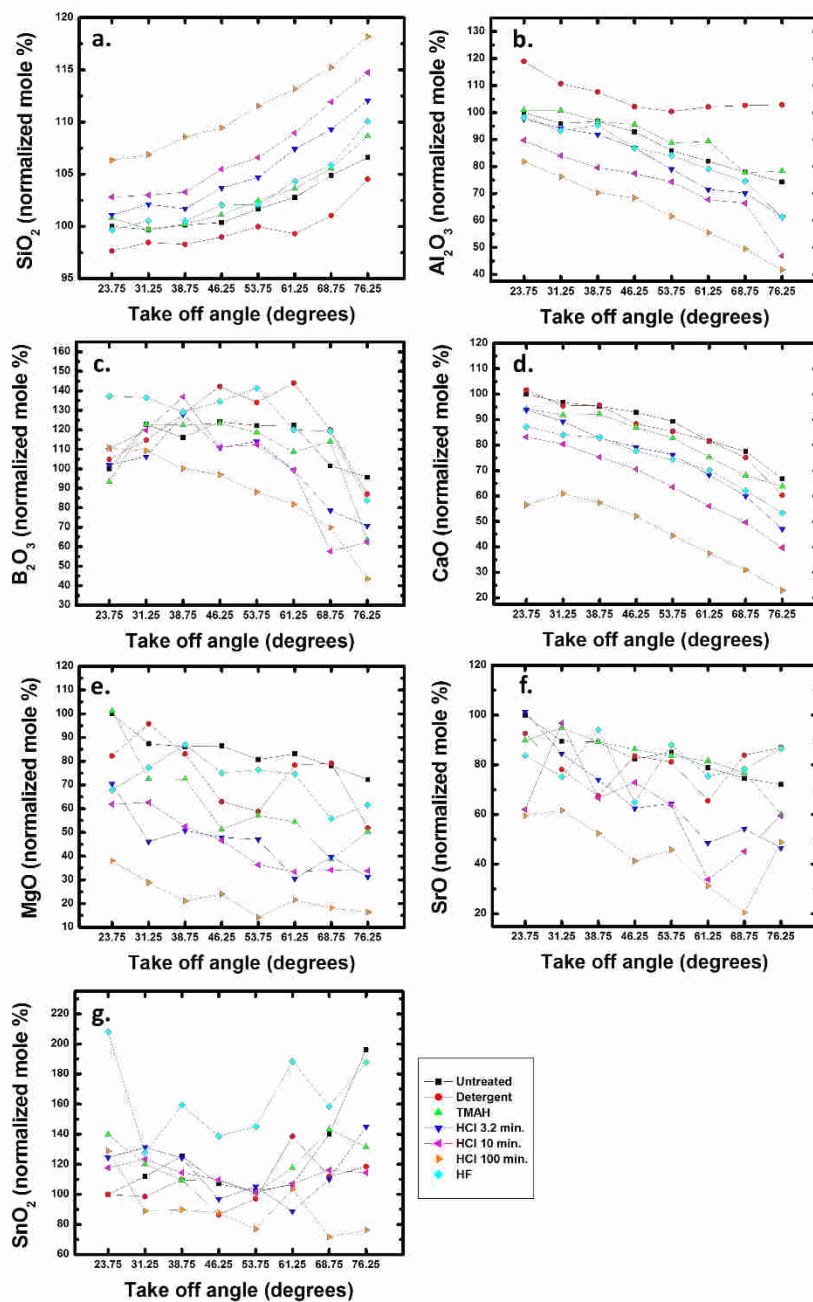
Figure 4.5. Relative molar percent compositions for samples for Eagle XG® samples as a function of take off angle. Concentrations have been normalized to the concentration obtained for the untreated sample at a take off angle of 23.75° to protect confidential compositional information about this material.

177

4.8 References

1.   Paynter, R. An ARXPS primer. *Journal of Electron Spectroscopy and Related Phenomena* **2009,** *169* (1), 1-9.

2.   Brundle, C.; Conti, G.; Graoui, H.; Foad, M.; Hung, S.; Wang, C.; Uritsky, Y.; Mack, P.; Wolstenholme, J. In *Depth-Resolved Composition and Chemistry of Ultra-Thin Films by Angle-Resolved X-Ray Photoelectron Spectroscopy*, AIP Conference Proceedings, AIP: 2005; pp 307-313.

3.   Brundle, C.; Conti, G.; Mack, P. XPS and angle resolved XPS, in the semiconductor industry: Characterization and metrology control of ultra-thin films. *Journal of Electron Spectroscopy and Related Phenomena* **2010,** *178*, 433-448.

4.   Herrera-Gomez, A.; Grant, J.; Cumpson, P.; Jenko, M.; Aguirre-Tostado, F.; Brundle, C.; Conard, T.; Conti, G.; Fadley, C.; Fulghum, J. Report on the 47th IUVSTA Workshop 'Angle-Resolved XPS: the current status and future prospects for angle-resolved XPS of nano and subnano films'. *Surface and Interface Analysis: An International Journal devoted to the development and application of techniques for the analysis of surfaces, interfaces and thin films* **2009,** *41* (11), 840-857.

5.   Kimura, K.; Nakajima, K.; Zhao, M.; Nohira, H.; Hattori, T.; Kobata, M.; Ikenaga, E.; Kim, J. J.; Kobayashi, K.; Conard, T. Combination of high-resolution RBS and angle-resolved XPS: accurate depth profiling of chemical states. *Surface and Interface Analysis: An International Journal devoted to the development and application of techniques for the analysis of surfaces, interfaces and thin films* **2008,** *40* (3-4), 423-426.

6.   AJ, R.; Macak, K.; Takahashi, K. Test of the Consistency of Angle Resolved XPS Data for Depth Profile Reconstruction using the Maximum Entropy Method. *Journal of Surface Analysis* **2009,** *15* (3), 291-294.

7.   Scorciapino, M. A.; Navarra, G.; Elsener, B.; Rossi, A. Nondestructive surface depth profiles from angle-resolved x-ray photoelectron spectroscopy data using the maximum entropy method. I. A new protocol. *The Journal of Physical Chemistry C* **2009,** *113* (51), 21328-21337.

8.   Macak, K. Encoding of stoichiometric constraints in the composition depth profile reconstruction from angle resolved X-ray photoelectron spectroscopy data. *Surface and Interface Analysis* **2011,** *43* (13), 1581-1604.

9.   Doremus, R. H. Interdiffusion of hydrogen and alkali ions in a glass surface. *Journal of Non-Crystalline Solids* **1975,** *19*, 137-144.

10.   Hench, L.; Clark, D. E. Physical chemistry of glass surfaces. *Journal of Non-Crystalline Solids* **1978,** *28* (1), 83-105.

11.   Cushman, C. V.; Brüner, P.; Zakel, J.; Dahlquist, C.; Sturgell, B.; Grehl, T.; Lunt, B. M.; Banerjee, J.; Smith, N. J.; Linford, M. R. Low Energy Ion Scattering (LEIS) of As-Formed and Chemically Modified Display Glass and peak-fitting of the Al/Si LEIS peak envelope. *Applied Surface Science* **2018,** *455*, 18-31.

12.   Cushman, C. V.; Zakel, J.; Sturgell, B. S.; Major, G. I.; Lunt, B. M.; Bruner, P.; Grehl, T.; Smith, N. J.; Linford, M. R. Time-of-flight secondary ion mass spectrometry of wet and dry chemically treated display glass surfaces. *Journal of the American Ceramic Society* **2017,** *100* (10), 4770-4784.

13.   Van der Heide, P., *X-ray photoelectron spectroscopy: an introduction to principles and practices*. John Wiley & Sons: 2011.

14.   Fearn, S.; McPhail, D. S.; Oakley, V. Room temperature corrosion of museum glass: an investigation using low-energy SIMS. *Applied surface science* **2004,** *231*, 510-514.

15.   Mahoney, C. M., *Cluster secondary ion mass spectrometry: principles and applications.* John Wiley & Sons: 2013; Vol. 44.

16.   Stevie, F., *Secondary ion mass spectrometry: Applications for depth profiling and surface characterization.* Momentum Press: 2015.

17.   Suzuki, S.; Yanagihara, K.; Hirokawa, K. XPS study of oxides formed on the surface of high-purity iron exposed to air. *Surface and Interface Analysis: An International Journal devoted to the development and application of techniques for the analysis of surfaces, interfaces and thin films* **2000,** *30* (1), 372-376.

18.   Adolphi, B.; Jähne, E.; Busch, G.; Cai, X. Characterization of the adsorption of ω-(thiophene-3-yl alkyl) phosphonic acid on metal oxides with AR-XPS. *Analytical and bioanalytical chemistry* **2004,** *379* (4), 646-652.

19.   Smith, G. C. Evaluation of a simple correction for the hydrocarbon contamination layer in quantitative surface analysis by XPS. *Journal of electron spectroscopy and related phenomena* **2005,** *148* (1), 21-28.

20.   Banerjee, J.; Bojan, V.; Pantano, C. G.; Kim, S. H. Effect of heat treatment on the surface chemical structure of glass: Oxygen speciation from in situ XPS analysis. *Journal of the American Ceramic Society* **2018,** *101* (2), 644-656.

21.   Banerjee, J.; Kim, S. H.; Pantano, C. G. Elemental areal density calculation and oxygen speciation for flat glass surfaces using x-ray photoelectron spectroscopy. *Journal of Non-Crystalline Solids* **2016,** *450*, 185-193.

Chapter 5: ToF-SIMS Analysis of Surface Hydroxyls on Multicomponent Display Glass Surfaces

Cody V. Cushman, Cameron T. Dahlquist, Scott S. Parker, J. Brigham Clawson, Landon S. Fisher, Andrew Ralph, Jeff Chapman, Albert J. Fahey, Christine M. Mahoney, James Coombs, Barry M. Lunt, Joy Banerjee, Nicholas J. Smith, and Matthew R. Linford.

5.1 Abstract

Surface hydroxyls govern a number of surface-mediated processes on glasses and oxides. Understanding glass surface chemistry at this level is necessary for improving alkali-free display glass substrates—currently the premier substrate for fabricating flat panel displays. Methodologies for measuring surface hydroxylation on low-surface-area multicomponent glass substrates in a planar form factor are needed. This study evaluates in detail time-of-flight secondary ion mass spectrometry (ToF-SIMS) as a method for quantifying surface hydroxyls on multicomponent glasses, examining the impact of instrumental parameters, the influence of adventitious surface contamination, and variability of results, both spot-to-spot (within a sample) and between replicates (sample-to-sample). Results for a common multicomponent display glass surface indicate that as-formed and detergent treated surfaces generally have fewer surface hydroxyls than those treated with acidic treatments including hydrofluoric and hydrochloric acid.

5.2 Introduction

5.2.1 Overview

Flat panel displays (FPDs) are microfabricated devices, where display pixels are typically fabricated using photolithographic processes, thin-film deposition, and etching. These devices are often fabricated on the surface of specially engineered display glass substrates.[1-4] Consequently, display glasses must meet exacting requirements in terms of their macroscale dimensional uniformity, cleanliness, nanoscale roughness, and ability to withstand the processing conditions associated with FPD production.[1] This requires glass compositions that are dimensionally stable with exposure to high temperature and chemically durable with respect to the conditions they will encounter. The glass must also be free from more-mobile elements that can diffuse from the glass substrate into the microelectronics fabricated thereon. As a result, most display glasses have nominally-alkali-free borosilicate compositions.[1]

The surface composition of display glass is fundamentally important for its intended use.[1] Glass surface chemistry influences wetting, thin-film adhesion, particulate adhesion, the rate of organic contamination, and static buildup and discharge on glass surfaces, all of which can potentially influence FPD device yield and performance variability during fabrication and/or over the lifetime of the device.[5-8] Current industry trends are increasing the demands placed on display substrates. On one hand, FPD panel sizes are increasing, driving a need to provide glass substantially free of contamination or defects over large surface areas. On the other hand, increased pixel counts have resulted in more challenging critical dimensions.[9] As a result, particulate adhesion and static discharge have become important modes of FPD device failure during

181

fabrication.[9] The demands placed on display glass surfaces will likely increase with the introduction of curved and flexible display geometries.[9]

Understanding display glass surface chemistry at the nanoscale, as it relates to FPD device fabrication, is a difficult analytical challenge. In its as-formed state, the surface composition of multicomponent glasses can differ significantly from its bulk composition and is further dependent on the method of manufacture by which that surface is created.[10-11] Furthermore, display glass surfaces can be considered somewhat labile, in that their surface elemental compositions at the nanoscale can be altered by brief exposures to typical production-line wet chemical treatments including acids, bases, industrial detergents, and/or etchants employed during glass sheet finishing and display device fabrication.[11-13] Our previous efforts focused on characterizing the elemental surface composition of display glasses exposed to various model process chemistries.[12-13] In this work, we turn our attention to understanding how the surface hydroxylation state of display glass changes with exposure to these treatments.

As surface hydroxyls are among the most polar and reactive sites on an oxide surface, they are considered to play a governing role in several surface-mediated properties and processes of oxide glass materials.[6, 14-21] Therefore, methodologies for quantifying surface hydroxyls are important for improving display substrates and addressing production-line challenges. From a wider perspective, glass surface modifications and coatings are used to add functionality and value to a wide range of products, and a better knowledge of surface hydroxylation is potentially important for all such applications.[22]

5.2.2 Surface Hydroxyl Measurements on Powders and Fibers

Surface hydroxyl measurements have been an important research topic for over fifty years. High-surface area silica, including powders and gels, are the most-studied class of material because (i) they are technologically important in their own right, being used in catalysis, chemical separations, as filler materials in polymers, etc. and (ii) because their high surface area makes it possible to readily detect and characterize surface hydroxylation using techniques such as infrared spectroscopy, gravimetric analysis, and temperature-programmed desorption mass spectrometry.[5, 17-18, 23-28] These studies have been foundational in establishing the hydroxylation properties of oxide surfaces. Infrared spectroscopy studies on powdered synthetic silica, for example, detect multiple types of silanol sites on its surface—so-called vicinal, geminal, and isolated silanols—each of which have different reactivities due to differing hydrogen-bonding states from proximity to neighboring silanols.[17] IR studies have also shown that the reactivity of silanols could be altered significantly with the addition of boron on these surfaces, as is common for many technologically important multicomponent borosilicate glasses.[5, 17] There have also been numerous attempts to quantify the maximum number of silanols per unit surface area on powdered silica, which have reported varying results.[18, 23, 25, 28] A review article summarizes many of these attempts.[18] Silica surface hydroxylation has also been modeled in several computational studies, which have established that three-coordinated Si, strained siloxane bonds, and non-bridging oxygens are important sites for surface hydroxyl formation.[29-32]

More recently, a comprehensive model for the hydroxylation of silica surfaces has been proposed based on a detailed characterization of more than 100 high-surface area amorphous silica powders using a combination of thermogravimetric analysis, temperature-programmed desorption mass spectrometry (TPD-MS), Brunauer–Emmett–Teller (BET) surface area measurements,

infrared spectroscopy, and other techniques.[18] According to this work, a fully-hydroxylated amorphous silica surface has 4.6 OH/nm^2 (least squares average).[18] This value is widely accepted, but has not gone entirely undisputed.[25] At low temperatures, silica surfaces are typically covered in physisorbed water—i.e. adsorbed molecular H_2O—from the atmosphere. Heating *in vacuo* to ca. 200 °C completely removes physisorbed water from the silica surface.[14, 18] At higher temperatures, first vicinal and then geminal silanols condense to form siloxane bonds and liberate water as a desorption product—a process referred to as dehydroxylation. At temperatures between 200 and 400 °C, these changes are mostly reversible upon re-exposure to water vapor (rehydroxylation). Treatments of silica at higher temperatures induces further dehydroxylation but also causes the surface to reconfigure, resulting in long-lasting changes to its hydroxylation state upon subsequent cooling. Surfaces treated at 1000 °C can take years to fully rehydroxylate at room temperature, and the maximal extent of rehydroxylation has been debated.[18] Therefore, silica's hydroxylation state is a strong function of its thermal history.

Studies of surface hydroxyls and other surface functions have also been performed on multicomponent glass surfaces in powdered and fiber formats.[8, 33-34] Multicomponent glasses are more complex than silica because they include non-bridging oxygens, modifier species, and sometimes alternate species incorporated into the network such as aluminum and boron. As a result, multicomponent glass surfaces can have significantly different site speciation and reactivities than silica surfaces.[8, 35] In addition, sub-surface hydrous species can form during the leaching of modifier ions from multicomponent glass surfaces.[33] Previous studies attempted to derivatize hydroxyl functions on glass fibers with fluorosilanes and quantify them using ^{19}F nuclear magnetic resonance (^{19}F-NMR).[34, 36] The lower surface area of glass fibers compared to silica powders required long acquisition times in order to quantify surface hydroxyls. Due to steric

considerations, this technique was estimated to have an upper measurement limit of ca. 3.0 OH/nm^2, with A glass and E glass fibers giving 0.78 and 1.31 OH/nm^2, respectively.[34] Other studies have examined surface adsorptive sites using temperature programmed desorption inverse gas chromatography (TPD-IGC).[35] One study demonstrated that (i) there are weak and strong adsorption sites on multicomponent glass surfaces; (ii) the type of modifier ions used and their concentrations heavily influences the type and number of adsorptive sites; and (iii) boronols (B-OH) are an important adsorption site for some glass compositions, in addition to the more widely-studied silanols.[37]

5.2.3 Surface Hydroxyl Measurements for Planar Substrates

While previous studies on powder surfaces have expanded theoretical understanding of surface hydroxylation, powder surfaces may not be representative of melt-formed planar surfaces.[10-11] This is especially true for multicomponent glasses, where elements can be lost to evaporation or preferentially diffuse to the surface during the glass forming process.[10, 38-39] Also, altered surfaces can result from exposure to aqueous chemistries or atmospheric contaminants.[11, 40] Therefore, understanding the hydroxylation state of planar display glass substrates requires direct measurement of these surfaces. Given the low surface area inherent in planar samples, however, this poses a significant analytical challenge. Techniques such as Fourier transform infrared spectroscopy (FTIR) lack inherent surface sensitivity/specificity and instead access surface information by increasing the ratio of surface-to-bulk within the analytical volume. This strategy is often not available to quantify hydroxyls on planar surfaces, wherein the low surface area provides an exceedingly small number of hydroxyls to measure within a specified analytical

volume. This limits analytical possibilities to methods with a high degree of (surface) sensitivity, as well as possible coupling with strategies to improve surface-specific signals (e.g. chemical tagging).[14]

Over the past three decades, several approaches have been attempted for measuring hydroxyls on planar substrates. Despite its inability to directly detect H, hydroxyl measurements by X-ray photoelectron spectroscopy (XPS) have been attempted in some cases, often by peak fitting of the O 1s envelope to resolve signal contributions from surface hydroxyls versus non-bridging and bridging oxygens.[41-42] While such an approach is possible for some materials, e.g., hydroxyls on tin oxide, it is now generally accepted that there is not an appreciable chemical shift between silanol oxygens and bridging oxygens in fused silica and silicate glasses.[43-44] Any results obtained through this route are based on rather arbitrary peak fitting assumptions, and our own attempts with multicomponent display glasses in question have yielded similarly arbitrary or non-unique fit results.[45] Alternatively, chemical derivatization of surface hydroxyls has also been widely used.[6, 8, 46] This approach uses reactions with surface silanols to "tag" the sites with a more-readily detected heterospecies (or in some cases a fluorophore). Subsequently, the number of reacted groups is quantified using a suitable technique like XPS, FTIR, or fluorimetry. This approach has been used successfully in several studies, but it also has several drawbacks. Steric limitations can prevent all surface hydroxyls from reacting with the derivatizing agent.[47-49] It is also assumed that the reaction efficiency of the tagging species is complete, and that all unreacted derivatizing agent has been removed from the surface prior to quantitation.[14, 45, 49] In addition, some reagents used for this purpose may be selective toward freely-vibrating silanols and have limited reactivity toward H-bonded silanols.[8, 46] Sum frequency generation spectroscopy and

evanescent wave cavity ring down spectroscopy have also been used to study the interaction of surface silanols on amorphous silica surfaces with water and adsorbates.[50-52]

More recently, a calculation-based approach using surface composition obtained from XPS has been used to estimate the number of surface hydroxyls.[43, 53] This approach is based on the fact that surface hydroxyls contribute more oxygen to the surface than bridging oxygens. Therefore, the number of surface hydroxyls can be estimated from excess oxygen quantified within the information depth of XPS at a sample surface. This requires a careful measurement of the glass's elemental composition using appropriate sensitivity factors to estimate the number of bridging and non-bridging oxygens in the network based on stoichiometric assumptions. The samples must also be heated to remove physisorbed water because XPS cannot distinguish between oxygen from physisorbed water and oxygen from the sample surface.[43] Ca. 2.5 OH/nm^2 were measured for unleached soda-lime silicate glass, while 4.6 OH/nm^2 were measured on an acid-leached surface.[43] A key advantage of this approach is its ability to quantify not only surface hydroxyls but also other important surface sites like bridging and non-bridging oxygens. One key disadvantage is that it can only average information over the depth of analysis of XPS, which is typically cited as ca. 10 nm.[45] However, significant gradients in glass composition can occur even over this short length scale.[38]

5.2.4 Secondary Ion Mass Spectrometry for Surface Hydroxylation Measurements on Low-Surface Area Samples

Time-of-flight secondary ion mass spectrometry (ToF-SIMS) offers some advantages compared to other surface analytical approaches for surface hydroxyl measurements. It can directly

detect hydrogen and hydrogen-containing fragments.[54] In contrast, the presence of hydrogen is only inferred in XPS, low energy ion scattering (LEIS), and Auger electron spectroscopy. Also, ToF-SIMS is among the most surface-sensitive analytical techniques. The depth of analysis commonly cited for the Ga^+ beam used in this study is 1-3 atomic layers, though the exact depth of analysis is dependent on many factors, including the beam energy, angle of incidence, and analyte composition.[54-56] This extreme surface sensitivity is well-suited for measuring surface functions at the outermost atomic layer of a sample. SIMS has among the lowest detection limits of all surface analytical techniques, ranging from ppm to ppb for most elemental species.[57] ToF-SIMS detects all ions of a selected polarity.[54] Accordingly, it simultaneously obtains information about a sample's surface composition, its degree of surface contamination, and signals relating to surface hydroxylation. Its surface sensitivity, low detection limits, ability to detect hydrogen, and high information content make ToF-SIMS a promising tool for measuring the surface hydroxylation state of a variety of oxide materials.

Dynamic SIMS is routinely used to measure bulk water concentration in minerals and thin films.[58-66] However, there are comparatively few studies using static SIMS to measure surface hydroxylation.[14-16, 20, 41, 44-45] There are a few possible reasons why this method is not more widely used and accepted. There are still questions about the best experimental protocol for static SIMS measurement of surface hydroxyls. Studies to date have provided little discussion of the influence of instrument parameters and settings on measurements, and few provide statistics on spot-to-spot and sample-to-sample measurement repeatability. An additional challenge is that any SIMS hydroxyl measurements can be affected by redeposition of water or hydrogen from the vacuum chamber.[62] Direct measurement of hydrogen and hydrogen containing fragments is complicated by the presence of background water and hydrogen gas in vacuum systems and can be sensitive to

analysis conditions.[58, 62-67] However, these considerations have largely been discussed in the context of achieving low detection limits for dynamic SIMS measurements of trace amounts of hydrogen or OH^{-} fragments in minerals or oxide materials, and different considerations may apply for the present study. Some studies call for lengthy sample heating *in vacuo* to remove physisorbed water from the sample surface, adding to the time and expense of the measurement.[14-16] Also, adventitious surface contamination can interfere with surface hydroxyl measurements, though the mechanisms and extent of this effect have not been explored in detail. [44-45] Finally, many of the static SIMS surface hydroxylation studies cited here predate the widespread use of modern ToF-SIMS instruments, relying instead on sector or quadrupole instruments.[14-16, 45] While these instrument geometries have unique advantages for some applications, ToF-SIMS is especially well-suited for static SIMS analysis because of its parallel detection and high mass resolution.[54]

Previously, SIMS was used to measure surface hydroxylation of thin films of SnO_2 using a combination of sector and quadrupole SIMS instruments.[44] Both the $SnOH^+$ and OH^- signals showed a positive correlation with the degree of surface hydroxylation, where both signals were normalized to matrix signals for the sake of quantitation. In practice, the $SnOH^+/Sn^+$ ratio was used as a metric for hydroxylation in positive ion mode, and the OH^-/O^- was used in negative ion mode. This study suggested that a thick hydrocarbon overlayer could suppress the $SnOH^+$ signal, and provided some potential mechanisms to explain this phenomenon.[44] Cleaning the surface with water plasma to remove adventitious hydrocarbon enhanced the $SnOH^+$ signal. In addition, physisorbed water at the sample surface enhanced the $SnOH^+$ signal, and had to be removed by heating *in vacuo* to achieve accurate hydroxyl measurements. These SIMS findings agreed with XPS results published in the same study.[44] Note that there is an appreciable chemical shift in the

O 1s peak position between bridging oxygens and surface hydroxyls in SnO_2, while the shift is very minor for SiO_2.[44]

An early static SIMS study analyzed fused silica surfaces as a function of chemical treatment and temperature.[45] Several SIMS peak area ratios correlated with surface hydroxylation, including the $SiOH^+/Si^+$ and OH^-/O^- ratios. The $SiOH^+/Si^+$ ratio was considered less susceptible to influence by background gas levels in the vacuum chamber than the OH^-/O^- ratio.[45] Sputter-etched silica surfaces gradually reacted with residual water vapor in the vacuum system to form hydroxyls, as indicated by an increase in the sample's $SiOH^+/Si^+$ ratio. Significant scatter in the data occurred below 200 °C, which was attributed to the presence of physisorbed water.

Later studies demonstrated that physisorbed water could be removed from silica surfaces by heating the sample *in vacuo* to 200 °C, after which the $SiOH^+/Si^+$ ratio varied linearly with surface hydroxyl concentration.[14-16] Sensitivity factors were established for the SIMS measurements by analyzing powdered silica reference samples using both SIMS and transmission infrared spectroscopy, and reported 4.6 OH/nm^2 for a fully-hydroxylated fused silica fracture surface. This value agrees with results from powdered silica studies.[15, 18] SIMS $SiOH^+/Si^+$ ratios also correlated linearly with complementary measurements from chemical derivatization/XPS measurements.[14]

These studies also explored the dehydroxylation and rehydroxylation behavior of vacuum-fracture fused silica surfaces as a function of temperature.[15-16] The surfaces dehydroxylated reversibly between 200 and 400 °C, with complete rehydroxylation occurring upon exposure to water vapor. Above 400 °C, the rehydroxylation kinetics get appreciably slower and rehydroxylation is potentially incomplete due to remodeling of the fracture surface at higher temperatures.[18] The initial hydroxylation state of fracture surfaces was only weakly correlated with

water vapor partial pressure at the time of fracture.[15] A two-step model for the hydroxylation of fracture surfaces was proposed. In the first step, dangling bonds that formed during the fracture process immediately react with neighboring species to form bridging siloxane bonds. In the second step, water vapor reacts with strained-siloxane bonds at the sample surface. Fused silica fracture surfaces dosed with water vapor in vacuum typically gave ca. 2.5 OH/nm^2.[15]

More recently, studies have used SIMS to measure hydroxylation on sputtered silicon oxide films doped with various metals, as well as other metal-oxide films.[19-20] These studies show a strong correlation between the wetting and contamination behavior of these films as measured by water contact angle goniometry and their hydroxyl coverage, as indicated by SIMS and chemical derivatization/XPS measurements. However, these studies do not mention sample heating to remove physisorbed water prior to SIMS measurement.

We are currently aware of only one published study using static SIMS to analyze hydroxyls on multicomponent glass surfaces.[41] This study was visionary in that it was one of the earliest to propose the use of static SIMS for surface hydroxyl measurements. However, it attempted quantitation by cross-calibration to XPS peak fitting results. It is now generally accepted that such peak fitting results are unreliable. In addition, no effort was made to remove physisorbed water from the samples, which is a likely source of error in the quantitative results.

5.3 Aims

Most SIMS hydroxylation studies to date focus on relatively simple oxide surfaces, and we are aware of only one that applied static SIMS to multicomponent glass surfaces.[41] In addition, most studies focus on surfaces carefully prepared in vacuum by sputtering or fracture, or surfaces

cleaned with UV-generated ozone (UVO). While these studies on model surfaces are valuable, there has been consequently only limited discussion about the influence of adventitious hydrocarbon contamination on the reproducibility and validity of SIMS surface hydroxylation measurements. This type of contamination is expected on any "real-world" glass surface that has been exposed to ambient atmosphere and thus presents a noteworthy analytical challenge for applying the SIMS approach to glass sheet products of technological interest.

The principle aim of our study is to use ToF-SIMS to characterize surface hydroxylation on multicomponent display glass surfaces—both in as-formed (melt surface) conditions, as well as changes therein upon exposure to model wet chemical treatments expected to alter the chemistry of the surface. Treatments include exposure to HCl, HF, tetramethylammonium hydroxide (TMAH), and an industrial detergent, with the long-term goal of understanding how surface hydroxylation affects surface-mediated processes and downstream performance for display substrates. This study will also give needed insight into the applicability of ToF-SIMS measurements of surface hydroxylation for the general class of compositionally-complex oxide materials, given the prevalence of multicomponent oxides and glasses in other technological applications including optical coatings, memory devices, chemical sensors, etc. A secondary goal of this study is to explore the effects of instrument settings and surface contamination on the measurements, and to provide a more detailed statistical analysis of the reproducibility of SIMS surface hydroxylation measurements than in previous studies.

While the focus of this work is on display substrates, this study may have a much wider impact, given that oxide films and materials are technologically important in the fields of catalysis, chemical separation, optics, semiconductors, photonics, sensing, etc. Surface hydroxyls play an important role in many of these applications.

5.4 Experimental

5.4.1 Sample Preparation and Storage

Samples for this study included chemically treated surfaces of fused quartz slides (GE 124, Type-I silica), purchased from Structure Probe Incorporated (SPI supplies, Westchester, PA), and Corning® Eagle XG® display glass. Eagle XG® was sampled directly from the production line immediately after forming and stored in airtight containers lined with UHV foil to preserve the surface until the time of analysis. We have confirmed by XPS that this sample storage protocol limits adventitious hydrocarbon contamination to nominal levels (ca. ~3-4 at.%) over extended periods. Therefore, this starting material represents a reasonable approximation of the melt-formed glass surface in its as-formed state—free of undue adventitious contamination—and allows us to perform a representative study of the surface evolution as it is subsequently exposed to typical production-line chemistries. In addition, we used fracture surfaces formed from bars of re-melted Eagle XG® to establish elemental sensitivity factors for SIMS signals to obtain quantitative information about the surface composition of these samples. We fractured these samples in air and introduced them into the vacuum chamber as rapidly as possible in order to limit contamination by adventitious hydrocarbon. They were typically exposed to air for ca. 3 minutes. This is a single-point calibration approach and assumes a linear response over the compositional range of interest. Complementary analysis by AR-XPS was used to validate this assumption.

We analyzed these surfaces in their as-treated state as well as after exposure to wet-chemical treatments typical of FPD production lines including HCl, HF, TMAH (a base commonly used as an etchant and a common ingredient in some photoresist developers), and industrial

alkaline detergents. We also treated fused quartz surfaces with boiling water because this treatment was used in SIMS surface hydroxyl studies of fused quartz elsewhere.[15] Sample treatment conditions are summarized in Table 5.1. For chemical treatments performed at 60 °C, we preheated the solution by immersing the reaction vessel in a heated water bath for 20 minutes prior to introducing the sample. For reactions performed at room temperature, all reagents were equilibrated to room temperature prior to mixing the solution and introducing the sample. We typically treated ca. 1 x 5 cm^2 glass segments in 50 mL of solution. Immediately after chemical treatment, the solution contents of the vial were exchanged five times with deionized water to quench the reaction, after which the sample was extracted with tweezers, rinsed under a deionized water spray for ca. 1 minute, and finally blown dry with nitrogen. Smaller coupons were cut from these samples using a glass cutter. Prior to chemical treatment, the back side ("B" side) of the Eagle XG® samples was marked with titanium pen to ensure that all analyses were performed on the opposing ("A" side) surfaces that were protected from the environment. All samples were stored in airtight, pre-cleaned glass vials with UHV-foil-lined caps immediately after chemical treatment to preserve their surfaces until they could be analyzed.

To study the effects of surface contamination on our measurements, we dosed fused quartz surfaces with perdeuterated triacontane ($C_{30}D_{62}$). Triacontane is a long-chain aliphatic C_{30} molecule that can be taken as a model for adventitious carbon contamination commonly observed on air-contaminated surfaces, which is often substantially aliphatic in nature. Perdeuterating this molecule replaces all H with deuterium, D—forming $CD_3(CD_2)_{28}CD_3$—and thus allows for signal specificity when probing this molecule on dosed glass surfaces. For the substrate, we used HF-treated fused quartz as the starting material for these studies because HF treatment was shown to remove carbonaceous surface contaminants detected in significant concentrations on the as-

received fused quartz samples. These surfaces were dosed with ca. 20 µL of 500 µg/mL solution of perdeuterated triacontane in methylene chloride (Restek Incorporated, Bellefonte, PA).

Table 5.1. Wet chemical treatment conditions.

Reagent	Grade	Supplier	Conc.	pH	Temp. (°C)	Time (m)
Industrial Detergent	N/R	N/R	1% v/v	12	60	10
HCl	Optima®	Fisher Scientific	0.1 M	1*	60	10
HF	ACS	EMD	0.1 M	2*	20	10†
TMAH	TraceSelect® Ultra	Fluka	0.1 M	11*	60	10

N/R = not reported. *Calculated pH. †HF-treated Fused Quartz 2 was treated for 24 hours.

5.4.2 Instrumental Details

All SIMS measurements were taken using a TOF-SIMS IV instrument (IONTOF, Munster, Germany), using a 25 KeV Ga^+ ion source. An electron flood gun at ca. 5 nA of current and 20 eV of electron energy was used for charge compensation. Prior to recording data, we explored the effects of several instrument parameters, including reflector voltage/acceptance energy, sample

cooling time prior to measurement, chopper width (ion dose per Ga^+ pulse), and beam damage effects.

In a typical experiment, two measurements were taken at room temperature, after which the temperature was rapidly ramped to 200 °C and held for ca. 8 hours. A 200 x 200 μm spot size was used at 128 x 128 pixels and 120 μs cycle time. Measurements were taken every ca. 30 minutes for the first 200 minutes to monitor physisorbed water desorption. After that, measurements were taken every 40 minutes until the end of a day's run (8-10 hours). In order to limit the potential effects of beam damage and also understand spot-to-spot variability, a new spot was used for each spectrum. For some samples, we also acquired several positive ion spectra at arbitrary sample positions in rapid temporal succession to understand whether statistical scatter or drift in our data resulted from temporal variation (e.g. gradually decreasing main chamber pressure over the course of an experiment), spot-to-spot variation in our samples, or some other unidentified source of random variance.

For some experiments, sample temperature was ramped stepwise from 200 °C to 400 °C. For others, we reversed the temperature ramp from 400 °C to 200 °C to understand how much samples rehydroxylated *in vacuo*. Alternatively, some samples were rehydoxylated by removing them from vacuum and exposing them to the water vapor in ambient air. After ca. 12 hours of laboratory air exposure, these (ostensibly) rehydroxylated samples were re-inserted into the vacuum chamber and re-heated from room temperature to 200 °C to evaluate their hydroxylation state.

Typical Ga^+ beam current for measurements was ca. 0.3 pA, though we adjusted beam current as necessary to avoid exceeding one uncorrected count per Ga^+ pulse for important signals in the spectra. For the majority of measurements, 30 second acquisitions were used in both positive

196

and negative ion mode, though longer acquisition times were used to achieve better signal-to-noise ratios for samples treated with perdeuterated triacontane. In all cases, measurements were well below the static limit of 1 x 10^{13} ions/cm^2, which would allow approximately 2000 seconds of analysis at 0.3 pA over 200 x 200 μm^2. Mass resolution (m/Δm) in this study usually ranged from 5000-7500. Typical system pressure immediately after sample introduction was 5 x 10^{-7} mbar, while pressure near the end of a run was typically ca. 1.5 x 10^{-8} mbar. Analyzer acceptance energy, as determined by reflector voltage, had an important influence on instrument response, and an acceptance energy of 90 eV was used throughout the study. This topic is discussed in more detail in the Results and Discussion section.

5.5 Data Analysis

For data analysis, we imported dead-time corrected ToF-SIMS spectra into CasaXPS (Casa Software Ltd. ver. 2.3.20 rev1.1o). Data regions without overlapping peaks were analyzed by applying a zero-type background and selecting peak integration limits, while regions with overlapping signals were fit using LF-type lineshapes, which can be described as asymmetric Gaussian-Lorentzian shapes.[68] We have provided mathematical description of this lineshape elsewhere.[13] Peak fitting was better for deconvoluting overlapping signals than arbitrarily establishing integration limits.[68-69] In addition, peak-fitting is somewhat adaptive to peak width changes due to sample charging, which varied from spot to spot and sample to sample. Signal intensities measured in CasaXPS were used in all further data analysis. In the case of resolving ^{29}SiOH$^+$ and SiOD$^+$ signals, the SiOD$^+$ peak area was obtained by subtracting the ^{29}SiOH$^+$ peak area calculated based on its isotope ratio to ^{28}SiOH$^+$ from the overall ^{29}SiOH$^+$/SiOD$^+$ envelope.

Some outliers were removed from the data. A complete list of outliers is provided in the Supporting Information. Data points were considered outliers if their $SiOH^+/Si^+$ ratios were significantly different than the majority of the data points. They were also considered outliers if their count rates and resolutions were significantly different than all other data points in a data set, which could suggest artifacts due to incorrect instrument settings or sample charging. In most cases, evidence of sample contamination or errors in instrument settings could be found to explain the outlying data.

5.6 Sensitivity Factors for SIMS Quantitation

We attempted to quantify the elemental surface composition of the Eagle XG® samples in this study using static SIMS. SIMS is not often used for quantitation of matrix species, but it is possible, in principle, provided that suitable reference materials are available. We used fracture surfaces of rectangular bars formed from remelted Eagle XG® to derive relative sensitivity factors (RSFs) by assuming that instrument response from the fracture surface corresponded to the known bulk composition of Eagle XG®. These Eagle XG® surfaces were fractured in air and rapidly loaded into the sample chamber. Typical air exposure for these surfaces was *ca.* 3 minutes. These surfaces were incompatible with our heating stage, and were analyzed at room temperature. We note that the experimentally-determined bulk composition of Eagle XG® is proprietary, and have not reported it here, though it was analyzed for the purposes of RSF determination.

We applied equations commonly used for deriving RSFs in XPS analysis to our SIMS data. Three spectra each were obtained from two separate Eagle XG® fracture surfaces for a total of six replicates. Each spectrum was obtained at a new sample location. The relative intensities of the

B^+, Si^+, Al^+, Mg^+, Ca^+, and Sr^+ signals were assumed to vary linearly with the relative concentrations of their respective oxides. A similar assumption is often used in the LEIS analysis of oxide materials.[70-71] The sensitivity factors were calculated according to Equation (5.1),

$$(5.1) \quad RSF_x = \left(\frac{A_x}{Mol\%_{X_{oxide}}}\right) \times \left(\frac{Mol\%_{SiO_2}}{A_{Si^+}}\right),$$

where RSF_x is the relative sensitivity factor for a selected elemental signal, A_x is the elemental peak area for the species of interest, $Mol\%_{X_{oxide}}$ is the molar percentage of the element's corresponding oxide in the reference material, $Mol\%_{SiO_2}$ is the known molar percentage of SiO_2 in the reference material, and A_{Si^+} is the Si^+ peak area. The average RSFs obtained from six replicates were used in subsequent measurements of sample elemental composition for this glass. Uncertainties in RSFs ranged from 6-12%. Reproducibility in measurements from the fracture surface were lower than for planar surfaces, likely due to uneven sample topography, which can have an influence on SIMS quantitative results.[72-73] RSFs in SIMS are matrix dependent, and we have made the assumption that Eagle XG® fracture surfaces are of a sufficiently similar matrix to the melt-formed and chemically-treated surfaces in this study to act as a valid calibration. We have checked this assumption by comparing the SIMS quantitative results to XPS results.

Molar percentages of oxides in the samples of interest are calculated according to Equation (5.2),

$$(5.2) \quad Mol\%_{X_{oxide}} = \frac{A_x/RSF_X}{\sum A_i/RSF_i},$$

where the summation in the denominator includes the areas and sensitivity factors for the B^+, Si^+, Al^+, Mg^+, Ca^+ and Sr^+ signals.

Notably, we did not attempt to derive an RSF for oxygen. We could not assume that oxygen concentration at the fracture surfaces was equivalent to their bulk concentration because (i) we

could not heat the fracture surfaces to remove physisorbed water, which would contribute to the oxygen signal; (ii) adventitious hydrocarbons may also contribute to the oxygen signal; and (iii) surface hydroxyls contribute more oxygens to an oxide surface than bridging oxygens, making it difficult to know the exact oxygen concentration at an air-fracture surface. Also, the O^+ signal had a low intensity in our spectra, which would contribute to its uncertainty. Accordingly, sensitivity factors we derived for the component oxides of the glass based on the Si^+, B^+, Ca^+, Sr^+, Mg^+, and Ca^+ signals are expected to be more robust than elemental sensitivity factors that include and account for the oxygen signal. For calculations below that require an estimate of oxygen concentration, we have inferred oxygen concentration from the stoichiometry of the glass's component oxides, noting this to be only an approximation.

We note that much of the compositional information obtained through this route is considered confidential information for Corning Incorporated, and has been removed from this report.

5.7 XPS Analysis

XPS data in this study was acquired using a ThermoFisher Thetaprobe XPS instrument. This instrument obtains angle-resolved XPS data without the need for tilting the sample. For the purposes of this study, we compared the SIMS results to results obtained at the most surface-sensitive take-off angle—76.25° from surface normal—giving an approximate information depth of ca. 2 nm. A more detailed AR-XPS analysis of these glass surfaces is intended to be the topic of a future publication.

We obtained RSFs for the quantitation of the XPS data using the same protocol as for the SIMS RSFs, assuming that relative areas of the Si 2p, Al 2p, B 1s, Ca 2p, Mg 1s and Sr 3d signals scale with the concentrations of their respective oxides and deriving sensitivity factors by analyzing an Eagle XG® fracture surface. This allows for easy comparison between the SIMS and XPS results. We have also ignored the O 1s signal in the XPS analysis, again noting that adventitious hydrocarbon and physisorbed water may contribute to this signal.

This elemental information is considered proprietary, and much of it has been removed from this report.

5.8 Results and Discussion

5.8.1 Instrumental Factors Influencing Measurement Reproducibility

A major concern in this study was understanding how instrumental parameters affected the repeatability of our measurements. We examined the reflector voltage/acceptance energy, beam damage as a function of ion dose, and beam current per ion shot as governed by the chopper width setting. In addition, the heater could not be switched on during measurements as it resulted in spectral artifacts, so we tested whether allowing the sample to cool briefly between measurements influenced instrument response. Of these factors, we found that ion dose per shot (chopper width) had no influence provided that we avoided saturating the detector (i.e. there was < 1 uncorrected count per Ga^+ shot for a given signal). Allowing the sample to cool from 200 °C for 10 minutes before analyzing it (resulting in a temperature of ca. 100 °C) gave the same response as analyzing it immediately after turning off the heater. To evaluate the effects of beam damage, we repeatedly

recorded spectra from the same spot in 30 second increments for a total of 300 seconds at beam current of 0.3 pA. Figure 5.1 displays the measured $SiOH^+/Si^+$ ratios from this experiment, where there is no appreciable change as a function of cumulative ion dose. Thus, beam damage is a minor concern, provided ion dose is maintained below the static limit of 1×10^{13} ions/cm^2. Mole ratios derived from elemental SIMS signals were also measured. There was no systematic drift in response as a function of cumulative ion dose in these ratios. However, for later spectra we opted to analyze a new spot with each spectral measurement in any case, given that a typical day's worth of measurements required ca. 25 positive ion and 25 negative ion SIMS measurements. Recording measurements at different sample locations also gave us insight into the spot-to-spot variability across a sample.

The measurements shown in Figure 5.1 are also a useful indicator of measurement reproducibility, given that they were taken at identical instrument settings in rapid temporal succession at the same sample location. The relative standard deviation for the $SiOH^+/Si^+$ ratio was 1% for these measurements. Relative standard deviations for molar ratios of the Eagle XG's major oxides, not shown, ranged from 0.01%-2% depending on the relative abundance of the species in question. Thus, the random error from the instrument itself is < 2%. We note, however, that this experiment only accounts for short-term measurement reproducibility, and cannot account for long-term instrument drift.

Reflector voltage, which governs the acceptance energy in a ToF-SIMS instrument, had an important influence on instrument response. Acceptance energy is the maximum initial kinetic energy an ion can have while still reaching the detector. This is represented schematically in Figure 5.2a, where ions with an excessive initial kinetic energy with respect to reflector voltage settings penetrate the reflector entirely, or at minimum, are not focused onto the detector, and thus go

undetected. Elemental and molecular species typically have different initial kinetic energy distributions in SIMS, with elemental species having up to ca. 100 eV, while molecular species have a maximum of ca. 20 eV.[74] Consequently, changing the reflector voltage directly impacts the measured $SiOH^+/Si^+$ ratio. For example, a relatively low acceptance energy may capture practically all of the $SiOH^+$ ions while only capturing a fraction of the Si^+ ions, as shown in Figure 5.2b. Meanwhile, a wider acceptance energy results in a higher total measured Si^+ peak area and a lower overall measured $SiOH^+/Si^+$ ratio, as shown in Figure 5.2c.

Figure 5.3a shows a plot of the $SiOH^+/Si^+$ ratio versus acceptance energy and demonstrates that the measured ratio changes as a function of acceptance energy. Here, we measured acceptance energy starting from the reflector voltage that resulted in essentially no signal at the detector. There is steep downward trend in the $SiOH^+/Si^+$ ratio in Figure 5.3a and an upward trend in overall measured counts in Figure 5.3b for acceptance energies between 0 and ca. 30 eV. Some scatter in overall count rate in Figure 5.3b may also be attributable to fluctuations in primary ion beam current, explaining the higher level of scatter in Figure 5.3b. Above acceptance energies of 50 eV, the trends are relatively flat, suggesting that practically all Si^+ ions and $SiOH^+$ ions are accepted.

Analyzer acceptance is also impacted by sample charging, which influences the initial kinetic energy of ions leaving the surface through electrostatic interaction. Insulating surfaces may charge unpredictably. To account for these sample charging effects, we used a nominal acceptance energy of 90 eV, placing our measurements on the flat region of Figure 5.3a, where unpredictable spot-to-spot variations in secondary ion energy due to sample charging would have a minimal impact on instrument response. This setting also gave optimal mass resolution, as shown in Figure 5.3c. Other studies have recommended or used high acceptance energies to achieve repeatable analysis of insulating materials.[75-76] For example, an interlaboratory study on the reproducibility

of static SIMS used an acceptance energy of 50 eV.[76] A ToF-SIMS depth profiling study on glass samples also used relatively high reflector voltages.[63] Generally, higher acceptance energies offer improved sensitivity at the expense of mass accuracy.[75] However, we have focused primarily on species with m/z <100, where extreme mass accuracy is not needed to identify the species present.

5.8.2 Discussion of Selected Mass Spectra

Figure 5.4 shows positive ToF-SIMS spectra for as-received fused quartz and HF-treated fused quartz. In Figure 5.4a, contaminant peaks for Ca, Na, and various hydrocarbon fragments are prominent on the as-received fused quartz surface. Figure 5.4b illustrates that a brief etch with hydrofluoric acid removes most of these contaminants, suggesting that they were adventitious surface contaminants rather than bulk impurities. Similarly, the other wet-chemical treatments in this study effectively reduced or eliminated contaminants from the fused quartz surface. In contrast, the as-received Eagle XG® (Figure 5.5a) surfaces show relatively small Na^+ and hydrocarbon signals, suggesting that the careful storage protocol used here effectively maintained its cleanliness after shipping from the production line. We note here that both fused quartz and Eagle XG® are nominally alkali-free in their bulk composition. In addition, ToF-SIMS is very sensitive to Na^+, and this species is thus often detected on most SIMS samples to some degree. The mass spectrum for the HF-treated Eagle XG® surface shown in Figure 5.5b has decreased network modifier concentrations (Mg, Ca, and Sr) and hydrocarbon signals compared to the untreated surface. These results agree with our previously published results.[12-13]

5.8.3 SiOH$^+$/Si$^+$ Peak Area Ratios for Samples Held at 200 °C

Most samples in this study were analyzed at a constant temperature of 200 °C. We chose this temperature based on the required temperature to fully remove physisorbed water from a fused silica surface in a previous study.[14] A range of temperatures have been reported for the complete removal of physisorption of water in other studies.[18] Zhuravlev and coworkers found that a temperature of 190 ± 10 °C was sufficient to remove physisorbed water from silica surfaces and micropores for a range of amorphous silica powders without causing significant dehydroxylation of the surface.[18] Therefore, the conditions used in this study are in reasonable agreement with established literature precedent. We have made the assumption that water removal temperature for fused silica can be applied to multicomponent silicate glasses and acknowledge that this may be an imperfect assumption. However, given that there are relatively few studies on water desorption from multicomponent glass surfaces, it is currently the most reasonable assumption we can make.

An annotated plot of the SiOH$^+$/Si$^+$ ratio as a function of heating time for an HF-treated Eagle XG® surface held at a constant temperature of 200 °C is shown Figure 5.6. The first two data points indicated by 5.6a, which were taken at room temperature, show a much higher SiOH$^+$/Si$^+$ ratio than all other points. This is attributable to the formation of SiOH$^+$ ions during bombardment when significant quantities of physisorbed water are still present on the glass surface. As the sample is heated *in vacuo*, a gradual decrease in the measured ratio (Fig. 5.6b) results from the presumptive desorption of physisorbed water from the sample surface. After approximately 190 minutes, the measured SiOH$^+$/Si$^+$ ratios indicated by 5.6c have a near-zero slope. Two data points were taken at adjacent 200 x 200 μm^2 spots across the sample at each time interval, with a new spot used for every acquisition. Noticeable scatter in the data can be observed, even after 190 minutes of heating. We attribute this scatter to spot-to-spot variation in the samples,

given that each data point represents a new sample location, especially in light of the excellent repeatability for repeated analysis of the same spot shown in Figure 5.1a. In order to gain a better understanding of the magnitude of spot-to-spot variation, we began obtaining ca. 10 spectra in rapid succession at arbitrary sample locations at the end of each run, seen here as a cluster of data points near 625 minutes (indicated by 5.6d). Possible explanations for this spot-to-spot variation include variable levels of adventitious surface contamination across the sample surface, variations in electrical field due to sample charging affecting analyzer transmission as a function of sample location, or spot-to-spot variations in the degree of surface hydroxylation. These possibilities are explored in greater detail below.

For samples held at a constant 200 °C, we have assumed that physisorbed water has been completely removed from the sample surface after 190 minutes, and have taken the average $SiOH^+/Si^+$ ratio of all data points obtained thereafter as a measure of the degree of surface hydroxylation, as shown in Figure 5.6c. Figure 5.7 shows these average $SiOH^+/Si^+$ ratios for all samples held at a constant 200 °C. Error bars are given as standard deviations, and samples are labeled according to their chemical treatments. A new sample was prepared for each of the replicates. Relative standard deviations in the $SiOH^+/Si^+$ ratios range from 5% to 12%, and replicates mostly give overlapping error bars. However, for some sample types, some replicates give significantly different mean $SiOH^+/Si^+$ ratios. In particular, HCl-treated Eagle XG®, Detergent-treated Eagle XG®, and fused quartz treated with boiling water all have at least one replicate with a statistically different mean $SiOH^+/Si^+$ than the others. Pooled averages for each sample type are shown in Figure 5.8, where pooled standard deviations are ca. 7-12%.

These $SiOH^+/Si^+$ ratios are only an instrument response, and converting them to an areal density number in terms of $SiOH/nm^2$ requires the use of a suitable reference material with known

hydroxylation behavior to establish a sensitivity factor. However, even without using a reference material, these $SiOH^+/Si^+$ ratios show some interesting trends. The hydroxylation rankings seem reasonable if we only make comparisons between samples prepared from the same substrate. Ranking the Eagle XG® sample treatments from most hydroxylated to least, we have HCl ≈ HF > TMAH > Detergent > Untreated. For the fused quartz surfaces, we have HF ≈ HCl > boiling water > as-received. These rankings agree with other studies that have shown that aqueous treatments with acids and bases, as well as hydrothermal treatment with boiling water, significantly hydroxylate silica surfaces.[15, 18] The trends make less sense if we compare Eagle XG® samples to fused quartz samples. Fused quartz samples in their as-received state had significantly lower $SiOH^+/Si^+$ ratios than all other sample types, giving less than half the ratio of the as-received Eagle XG®. The HF- and HCl-treated Eagle XG® surfaces also gave higher $SiOH^+/Si^+$ ratios than the HF- and HCl-treated fused silica samples. It seems physically unreasonable that an as-received fused quartz surface would have a lower silanol count than an as-received multicomponent glass surface, due to the great degrees of compositional freedom and the lower bulk Si content in the latter. It seems equally implausible that a chemically-treated multicomponent glass surface could have more OH/nm^2 than a comparably treated fused quartz surface. This suggested that there were additional factors at play in our measurements, prompting us to explore the variability in elemental composition between spectra obtained from our samples and to perform experiments on the influence of hydrocarbon contamination on these measurements.

5.8.4 Variability in Elemental Composition of Eagle XG® Surfaces

To better understand the sources of variance in our data, we analyzed the elemental composition of the Eagle XG® samples using the positive ion SIMS spectra. Relative sensitivity factors were derived as described in the experimental section using Eagle XG® fracture surfaces as reference materials. The molar percentages of the oxides were calculated for each positive spectrum recorded from the sample. All of the mole percentages recorded throughout the day (typically *ca.* 25 positive SIMS spectra) were averaged and renormalized to 100 mole% to obtain the average surface composition for the sample. These molar ratios are not shown due to their confidential nature.

SIMS is not often used for quantitative elemental analysis for matrix constituents due to the matrix effect that is often present. Rather, it is most often used to measure concentration of trace constituents.[57] However, some dynamic SIMS studies have attempted to quantify matrix species in glass based on relative sensitivity factors derived from fracture surfaces.[77-80] We have attempted it here based on the assumption that the Eagle XG® fracture surface has a sufficiently similar matrix composition to our samples of interest to act as a valid reference. In order to prove the validity of this approach, we compared SIMS results to results obtained by XPS for similarly treated samples. These XPS data were obtained at take-off angles of 76.25° to surface normal, giving information depths of approximately 2 nm. Sensitivity factors for the XPS data were also derived from Eagle XG® fracture surfaces, and the concentrations were also measured in units of mole % of Eagle XG's component oxides. These data are also not shown due to their confidential nature. We note here that a detailed analysis of angle-resolved XPS data for these samples is intended to be the subject of a future publication.

The SIMS and the XPS data generally agreed well with one another. SIMS is generally more surface sensitive than XPS and has better detection limits. Meanwhile, XPS is generally free from matrix effects, and is typically considered to be more quantitative. Concentrations fall in a similar range for both techniques. Agreement to within 8 mole % between the XPS and SIMS results was obtained for SiO_2, which is the most abundant species in Eagle XG[®]. Agreement to within 2.6 mole % or better for was obtained for Al_2O_3, CaO, and B_2O_3, and agreement to within 0.25 mole % was obtained for MgO, and SrO. The SIMS results generally showed surfaces that are more silica-rich/modifier depleted than XPS. These differences are attributable to the greater surface sensitivity of ToF-SIMS. We additionally note that signal-to-noise was low for a few species by XPS, including boron, strontium, and magnesium, and that signal-to-noise ratios in XPS suffer at more surface-sensitive take-off angles, contributing to measurement uncertainty. Therefore, it is no surprise that there are minor compositional discrepancies between XPS and SIMS for some species. However, the good overall agreement between the XPS and ToF-SIMS results suggests that no significant matrix effect is present in the quantified SIMS elemental results over the compositional ranges considered here.

Spot-to-spot variations in elemental concentration within samples are small, as reflected by low RSDs between concentrations calculated from spectra recorded at different locations within a sample. RSDs in SiO_2 concentration calculated from all spectra recorded from a given sample ranged from 0.1% to 2.5%, with an average value of 0.6%. Variances between replicates are also small. The largest spread in silicon concentration for a group of replicates was 3 mole %, occurring for the HF-treated samples. Accordingly, Si^+ is a suitable normalization to which to compare the $SiOH^+$ peak intensity, given that error bars are small and SiO_2 mole percentages are repeatable for a given sample treatment. This indicates that the relatively wide variations in the measured

$SiOH^+/Si^+$ ratios within a sample group cannot be attributed to variations in the intensity of the Si^+ signal. Rather, the $SiOH^+$ signal is varying. Possible explanations for this variance are: (i) there are legitimate differences in surface hydroxylation; (ii) the $SiOH^+$ signal is enhanced or suppressed by the presence of some other surface species (e.g. physisorbed water); or (iii) instrumental phenomena, e.g., field effects, are influencing the signal.

In addition, the SiO_2 concentration varied significantly depending on sample treatment, with detergent-treated surfaces showing a relatively Al_2O_3 rich/SiO_2 poor surface, and acidic treatments giving surfaces that are relatively rich in SiO_2 and relatively depleted in all other oxides. These results are consistent with those published in a previous SIMS analysis of similarly-prepared Eagle XG® samples.[12] Given that we are using the $SiOH^+/Si^+$ ratio as a metric for surface hydroxylation, it is necessary to account for differences in surface Si concentration between sample types when calculating the number of OH/nm^2 for the multicomponent glass samples.

In relative terms, compositional variations between replicates for B_2O_3, Al_2O_3 and modifiers in Eagle XG® are more dramatic than for SiO_2. The differences in Al_2O_3 and B_2O_3 concentrations are the most pronounced. This is reasonable, given that these components are readily extractable during wet chemical treatments at acidic or basic extremes of pH, and their concentrations may be sensitive to slight variations in the sample treatment conditions. There is a more marked variation in the concentrations of these species between sample treatments. Detergent and TMAH treated surfaces give significantly higher aluminum concentrations than the untreated Eagle XG® surface. B, Al, and network modifiers are depleted from the sample surface after treatment with HCl or HF. In general, these findings are in good agreement with our previously published LEIS and ToF-SIMS studies on similarly treated glass surfaces.[12-13]

To better visualize spot-to-spot variations in elemental composition within a sample, Figure 5.9a plots the percent standard deviations in molar composition obtained from each spectrum from an HF-treated Eagle XG® sample. Here, very low standard deviations can be observed (noting again that a new sample spot was used for each data point). SiO$_2$, the most abundant species in this glass, has < 0.17% standard deviation in concentration as a function of sample location. The less-abundant species give slightly higher values, but all have < 8% standard deviations as a function of sample location. This was generally the norm. Importantly, the measured elemental ratios did not fluctuate when we removed the physisorbed water during the early stages of sample heating.

There were significant spot-to-spot variations in elemental composition for at least one sample, an HF-treated Eagle XG® surface that was ramped to 400 °C. The relative standard deviations in molar composition for this sample are shown in Figure 5.9b, where there were ca. 87% standard deviations in CaO concentrations across sample locations and similarly high deviations in MgO concentration. Error bars for other species in this sample are generally higher than those shown in Figure 5.9a. In a follow-up analysis, we converted several of the spectra from this sample to images, and discovered calcium-rich regions in several of them. These are shown in the Supporting Information. These Ca$^+$-rich regions often correspond to spots with a higher-than-average C$_3$H$_7^+$ signal, suggesting that both may have come from adventitous contamination. We can only speculate as to the source of this calcium enrichment. However, we note that variations in surface composition correlate with high variances in the SiOH$^+$/Si$^+$ ratio. These are shown in Figure 5.18b, and will be discussed further in the context hydroxyl behavior at higher temperatures.

5.8.5 The Influence of Adventitious Hydrocarbon Contamination on Surface Hydroxyl Measurements

The degree of adventitious surface contamination on these samples is a potentially important dimension of variance between samples. It is also possible for 'clean' and 'dirty' regions to exist within a single sample. Figure 5.10 shows the average $C_2H_3^+/Si^+$ ratios for all samples analyzed at 200 °C taken for all data points after 190 minutes of heating. Here, as-received fused quartz has the highest degree of hydrocarbon contamination by a significant margin, as indicated by the $C_2H_3^+/Si^+$ ratio. Figure 5.8 also shows that this sample has the lowest $SiOH^+/Si^+$ ratio of any sample. The same effect may be present to a lesser degree for some fused quartz surfaces treated with boiling deionized water. In contrast, even the "dirtiest" of the Eagle XG® samples had a much lower $C_2H_3^+/Si^+$ ratio than the heavily-contaminated fused quartz surfaces. With the exception of the very-contaminated samples already mentioned, however, there is no correlation between the degree of adventitious hydrocarbon surface contamination and the measured $SiOH^+/Si^+$ ratios. Sometimes the most contaminated sample in a group gives the highest $SiOH^+/Si^+$ ratio, and sometimes it gives the lowest. In some cases, replicates show almost exactly the same level of adventitious hydrocarbon contamination, and yet give noticeably different $SiOH^+/Si^+$ ratios.

From these observations, we hypothesized that high concentrations of hydrocarbon contamination on a surface may suppress the measured $SiOH^+/Si^+$ ratio, while other effects may dominate the measurement when the surface is substantially cleaner and free of this contamination. To test this hypothesis, we dosed HF-treated fused quartz surfaces with perdeuterated triacontane ($C_{30}D_{62}$)—a simple alkane taken to be representative of aliphatic hydrocarbon contamination. The presence of deuterium in the molecule allowed us to observe specific reaction products between

the substrate and the adventitious hydrocarbon overlayer. However, only ions are detected, and so this experiment is insensitive to reaction pathways that result in neutral species.

Triacontane is volatile enough that it can be mostly removed from a sample surface with mild heating *in vacuo.* Figure 5.11a shows a fused quartz surface with a high dose of perdeuterated triacontane analyzed at room temperature. Here, there are peaks from perdeuterated alkane fragments. While there is still a significant Si^+ signal at $m/z = 28$, the $SiOH^+$ signal at 45 is significantly suppressed. Figure 5.11b shows a zoomed-in view of the m/z 45 region from Figure 13a, demonstrating that the $SiOH^+$ signal is still present. The $SiOH^+/Si^+$ ratio for this sample was 0.10, placing it well below the values obtained for a clean HF-treated fused quartz surface. Figure 5.11c shows a spectrum from the same surface after most of the perdeuterated triacontane has been removed by heating the sample to 100 °C. Only a small deuterated signal at m/z 34 remains on the surface, having a comparable magnitude to the non-deuterated CH_3^+ signal resulting from adventitious hydrocarbons at m/z 15. The $SiOH^+$ signal at m/z 45 has a much higher relative intensity in this spectrum. The $SiOH^+/Si^+$ ratio from this spectrum was 0.25, a significant rebound from the quantity measured before contamination removal. *This is strong evidence that a significant carbon overlayer can suppress the $SiOH^+/Si^+$ ratio.* There are two plausible mechanisms for this suppression: (i) suppression through chemical reaction, and (ii), kinetic-energy dependent attenuation of substrate signals by the hydrocarbon overlayer. The chemical route was posited in a previous study on SnO_2 surfaces, where it was hypothesized that H^- ions reacted with $SnOH^+$ ions to form neutral, undetectable recombination products.[44] A similar logic likely applies for reaction of $SiOH^+$ ions with H^- ions. A substrate ion's ability to penetrate a carbon overlayer is also a function of that ion's kinetic energy. One study analyzed polyelectrolyte self-

assembled monolayers (SAMS) on silicon substrates, and found that the SAMS attenuated the $SiOH^+$ signals more strongly than the Si^+ ions, due to the lower kinetic energy of the $SiOH^+$ ions.[81]

Ions formed from reactions between the substrate and the hydrocarbon overlayer may also enhance the $SiOH^+/Si^+$ ratio. Figure 5.11d is a zoomed in view of the *m/z* 46 region of the spectrum shown in 11c, showing that $SiOD^+$ fragments are formed by recombination reactions between the hydrocarbon fragments and the substrate. *This demonstrates that pathways are available through which non-deuterated hydrocarbons can enhance the $SiOH^+$ signal*. It can be seen in Figure 5.11d that there is significant overlap between the $^{29}SiOH^+$ and the $SiOD^+$ signals. For comparison, Figure 5.11d also shows a spectrum from a clean HF-treated fused quartz surface where no $SiOD^+$ peak is present. The blank spectrum has been normalized to have the same peak intensity for $SiOH^+$ at *m/z* 45 as the perdeuterated triacontane-treated sample. Thus normalized, both spectra give the same $^{29}SiOH^+$ intensity at *m/z* 46 as expected based on the expected isotope ratio between $SiOH^+$ and $^{29}SiOH^+$. Clearly, there is sufficient mass resolution to distinguish between $^{29}SiOH^+$ and $SiOD^+$. However, resolving signals that are overlapping to this degree via peak fitting can be challenging without *a priori* knowledge of their shapes, positions, and widths. Instead, we subtracted the area of the $^{29}SiOH^+$ contribution from the envelope based on the known isotope ratio between $SiOH^+$ and $^{29}SiOH^+$. The resulting calculated $SiOD^+$ peak areas are shown in Table 5.2.

A plausible molecular mechanism for formation of $SiOD^+$ is that SiO^+ induces hydrogen atom transfer from a neighboring alkane to produce the even-electron $SiOH^+$ ion, which is consistent with even-electron species that tend to be favored in SIMS.[57] To gain insight into this possibility, we performed gas-phase electronic structure density functional theory (DFT) calculations using the Gaussian 09 software. All calculations used the M06-2X density functional with unrestricted orbitals, which provides accurate structures and energies of organic and main-

group compounds.[82-83] Unrestricted M06-2X/6-31G** structures and energies were confirmed to be stationary points and minima by vibrational frequency analysis.

Figure 5.12a,b shows the energies and shapes of the frontier (HOMO and LUMO) occupied and unoccupied DFT orbitals for the open-shell SiO^+. Because the shape of the α_{HOMO} orbital at -19.5 eV matches the shape of the β_{LUMO} at -12.9 eV, this orbital is half filled and primed to induce hydrogen atom transfer. Using propane as a model alkane, we examined the thermodynamics and possible transition states for hydrogen transfer. The highly reactive SiO^+ initially forms a relatively stabilized van der Waal/charge-transfer complex that is (ΔG) exergonic by 25 kcal/mol. This $[SiO\text{-}C_3H_8]^+$ is reactive, and hydrogen atom transfer to the Si atom center has a very low barrier as shown in Figure 5.12c. More importantly, to achieve the separated propyl radical and $H\text{-}SiO^+$, relative to a pre-complex, requires a thermodynamic change ΔG of 49 kcal/mol. However, $H\text{-}SiO^+$ can isomerize to $SiO\text{-}H^+$ that is exergonic by 46 kcal/mol, but requires an intramolecular isomerization barrier of 28 kcal/mol.

As we have noted, molecular species typically have kinetic energies ranging from 0-20 eV and atomic species typically have kinetic energies ranging from 0-100 eV in the SIMS sputter plume. At these energies, the proposed reactions are easily possible. In Figure 5.12b, it can be seen that SiO^+ can also abstract a hydrogen from water molecules at a slightly higher energy cost than for a reaction with propane. It is generally accepted that physisorbed water can enhance the measured $SiOH^+/Si^+$ ratio, and this effect is evident in Figure 5.6. If reactions are occurring between the substrate and physisorbed water, then it stands to reason that the more energetically favorable reaction must be occurring to some extent between the substrate and physisorbed alkanes.

We analyzed $SiOD^+$ formation in relation to the quantity of deuterated alkane present on the surface. We recorded 14 spectra, 7 each from two different HF-treated fused quartz samples heated between 100 ° and 200 °C. We chose to take these measurements from gently-heated surfaces so that the $C_2D_5^+$ intensity was comparable to the $C_2H_5^+$ intensity, i.e., to obtain conditions more representative of "typical" adventitious hydrocarbon contamination rather than a thick deposited overlayer. The $C_2D_5^+/Si^+$ ratios in Table 5.2 indicate non-uniform perdeuterated triacontane coverage across the sample surface. There was little correlation between sample temperature and the $C_2D_5^+/Si^+$ ratio for this temperature range. This suggests that, after the initial desorption of loosely-bound triacontane from the sample surface, relatively high temperatures are needed to desorb the remainder. The average $SiOD^+/C_2D_5^+$ ratio was 0.35 ± 0.19.

We attempted to use the $SiOD^+/C_2D_5^+$ ratio as a correction factor to account for the influence of adventitious hydrocarbons on our measurements, assuming that the $SiOH^+$ peak area from adventitious hydrocarbon could be approximated by the $C_2H_5^+$ peak area multiplied by 0.35. By this assumption, between 5% and 20% of the total $SiOH^+$ peak area for the samples in Figure 5.7 could be attributed to contributions from adventitious hydrocarbon, with the notable exception of the as-received fused quartz samples which were significantly more contaminated than all other sample types. Ultimately, this correction factor proved ineffective. An effective correction factor should result in lower observed spot-to-spot variation for measurements within a sample and better agreement between mean $SiOH^+/Si^+$ ratios between replicates. However, attempts to apply this correction resulted in increased standard deviations within a sample, and no measurable improvement in reproducibility between replicates. The large error bars on the average $SiOD^+/C_2D_5^+$ ratio suggest a high degree of variability in $SiOD^+$ formation as a function of

perdeuterated triacontane coverage, such that attempts to apply such a correction may introduce more error into our measurements than they remove.

In summary, experiments with perdeuterated triacontane gave insight into the influence of hydrocarbons on surface hydroxylation measurements by SIMS. However, effects due to hydrocarbon contamination cannot fully account for spot-to-spot variation within a sample, nor the differences in measured surface hydroxylation between replicates. Given that reaction pathways are present that can both suppress and enhance the $SiOH^+$ signal, it is difficult to know to what extent each occurs as a function of hydrocarbon coverage. We also note that different types of surface contamination may have different proclivities for suppressing or enhancing the $SiOH^+$ signal. One implication of these results is that SIMS is probably best suited for measuring hydroxyls on clean surfaces prepared in the laboratory and stored carefully, and that it may be difficult to measure surface hydroxylation of "real-world" samples that have had the chance to accumulate significant contamination. Any remedial efforts to remove said contamination—such as through certain cleaning treatments—may in fact alter the underlying hydroxylation state intended to be measured, as indicated by the data in Figure 5.7.

Table 5.2. Selected peak areas and ratios for fused quartz surfaces dosed with perdeuterated triacontane.

Sample	Temp. (°C)	Si^+ (cts)	$C_2H_5^+$ (cts)	$C_2D_5^+$ (cts)	$SiOD^+$ (cts)	$C_2D_5^+/Si^+$	$SiOD^+/C_2D_5^+$
1	100	654478	9124	8843	8481	0.014	0.82
1	100	642062	7695	5587	9297	0.009	0.58
1	100	614998	8635	10790	8765	0.018	0.38
1	100	577767	9324	12086	8123	0.021	0.39
1	200	598306	8557	36380	5789	0.061	0.33
1	200	634733	8649	30144	5976	0.047	0.45
1	200	517746	9476	53595	4853	0.104	0.27
2	115	170959	2278	18517	2235	0.108	0.15
2	115	421603	5067	18227	6382	0.043	0.25
2	165	368223	3999	33752	5028	0.092	0.18
2	165	399051	4497	14976	5930	0.038	0.33
2	180	319560	4930	54092	3439	0.169	0.15
2	180	408526	5057	37231	4904	0.091	0.27
						Average	0.35
						St. Dev.	0.19

5.8.6 Summary of Spot-to-Spot and Sample-to-Sample Variability in $SiOH^+/Si^+$ Ratios

We have identified and explored several possible sources for spot-to-spot and sample-to-sample variability in our data, including variability from hydrocarbon contamination, variability in elemental composition, and instrumental performance. Electrical field effects that affect ion transmission are also possible when analyzing insulating surfaces. Finally, it is also possible that the observed spot-to-spot and sample to sample variability in the $SiOH^+/Si^+$ ratio is due to legitimate variations in surface hydroxylation. This is difficult to experimentally verify or refute, but it may be possible to eliminate some other possible explanations.

We established in Figure 5.1 that the short-term repeatability in the $SiOH^+/Si^+$ for our instrument is better than 1% when the same spot is analyzed repeatedly. In contrast, the $SiOH^+/Si^+$ ratio for samples shown in Figure 5.7 where we analyzed a new spot with every acquisition, the relative standard deviation in $SiOH^+/Si^+$ is typically from 8-12%, which is much larger than can be explained by short-term instrument variability alone. Relative standard deviations for elemental composition within a sample were shown to be low in Figure 5.9a , but in Figure 5.9b we observed at least one case of marked spot-to-spot variability in elemental composition within a sample, which was attributable to the presence of contaminants. Sample-to-sample variation in elemental composition was generally low for SiO_2, but somewhat more pronounced for Al_2O_3, B_2O_3, and modifier species in a multicomponent glass. Therefore, the spot-to-spot variance in the $SiOH^+/Si^+$ ratios is not attributable to spot-to-spot variations in elemental composition, with the notable exception of the sample shown in Figure 5.9b. However, there are small but noticeable differences in elemental composition between replicates, and these may account for some of the sample-to-sample variance in the $SiOH^+/Si^+$ ratios.

Our experiments with perdeuterated triacontane have demonstrated that hydrocarbons have the potential to influence the measured $SiOH^+/Si^+$ ratios. Thick overlayers clearly suppress this ratio, while at low hydrocarbon coverages, there are reaction pathways through which it was shown that perdeuterated hydrocarbons can react to form $SiOD^+$. Implied is a corresponding mechanism for common (non-perdeuterated) hydrocarbons to react to form $SiOH^+$ ions and perturb the measured $SiOH^+/Si^+$ ratios away from those intrinsic to the underlying glass surface. However, as we have already noted, there is not a clear correlation between level of surface contamination shown in Figure 5.10 and the $SiOH^+/Si^+$ ratios in Figure 5.7 for any but the most-contaminated samples.

Electrical fields above insulating surfaces can influence quantitative results because they have a kinetic energy-dependent impact on ion transmission.[72-73] We have not performed any experiments that will allow us to rule out these effects, and acknowledge that they may account for some of the variance in the measured $SiOH^+/Si^+$ ratios. We also acknowledge that we have not completely ruled out long-term drift in instrumental performance.

In summary, the spot-to-spot and sample variances in our data do not appear to be attributable to short-term random instrumental error. With one notable exception, we cannot attribute spot-to-spot variations in the $SiOH^+/Si^+$ ratio to spot-to-spot variations in elemental composition. However, variations in elemental composition may account for some of the variance between replicates. Sample contamination appears to play an important role at high hydrocarbon loadings, but we can find no correlation between contamination levels and the $SiOH^+/Si^+$ for relatively clean samples. While the remainder of the variance in the $SiOH^+/Si^+$ may be due to legitimate spot-to-spot variances in the level of surface hydroxylation, we cannot rule out the possible impact of charging-induced electrical fields on ion transmission as a source of variance.

5.8.7 Surface Hydroxyls per Square Nanometer (OH/nm²)

Having explored the dimensions of variance in our data to the best of our ability, we attempted to calculate the number of hydroxyls per square nanometer for the samples measured here. Based on previous studies, we presumed the HF-treated fused quartz samples to be fully hydroxylated, and that they had 4.6 OH/nm^2 per the widely-accepted literature value.[18] We have used the average SiOH$^+$/Si$^+$ ratio from HF-treated fused quartz as our reference material, given that this treatment has been proven an effective hydroxylating treatment.[84-85] Treatment in boiling water has also been shown to be an excellent hydroxylating treatment for silica surfaces.[15, 18] However, the high levels of carbonaceous contamination on some of the fused quartz samples treated with boiling water seem to have suppressed their measured SiOH$^+$/Si$^+$ ratios, rendering them unsuitable as reference materials. For the Eagle XG® samples, we also included a factor for the fraction of silicon at each sample surface. Equation (5.3) shows this calculation,

$$(5.3) \quad \frac{OH}{nm^2} = \frac{R_{sample}}{R_{reference}} \; x \; 4.6 \frac{OH}{nm^2} \; x \; \frac{At.\%_{Eagle\,XG}}{At.\%_{SiO_2}}$$

where R$_{sample}$ is the average SiOH$^+$/Si$^+$ ratio for the sample being measured, R$_{reference}$ is the measured SiOH$^+$/Si$^+$ for the reference material, At%$_{sample}$ is the atom percentage of silicon in the Eagle XG® sample being measured, and At%$_{SiO2}$ is the atom percentage of silicon in the SiO$_2$ reference material.

The scaling factor based on the atom percentage of silicon in the multicomponent glass samples is necessary because we used the SiOH$^+$/Si$^+$ ratio as a metric of surface hydroxylation, but not all samples have the same atom fraction of Si, resulting in bias in normalization between different sample types. Multiplying by the ratio of Si in Eagle XG® to Si in SiO$_2$ approach is reasonable because, to a first approximation, the sputter yield of a given species in SIMS is

proportional to its concentration.[86] Accurate calculations of the atom percentage of silicon in Eagle XG® require oxygen in the sample to be accounted for. However, as we have noted in the experimental section, we could not find a suitable reference for quantifying oxygen. Accordingly, the fraction of oxygen in the sample was estimated based on the molar ratios of the oxides measured from the Si^+, Al^+ B^+, Mg^+, Ca^+ and Sr^+ signals. This approach likely slightly underestimates oxygen at the sample surface because it does not account for differing oxygen contributions between bridging siloxanes and hydroxyls.[43, 53] However, the errors are expected to be small. In similar fashion, we have assumed that the atom percentage of silicon in SiO_2 is 33.3% in all cases. Again, this assumption likely underestimates the amount of oxygen at the sample surface, but we expect the error to be small. The composition of Eagle XG® is considered proprietary, and we have removed this compositional information from this report.

We calculated areal densities of hydroxyls (OH/nm^2) for the multicomponent glass samples based on Equation (5.3) and the assumptions discussed in the previous paragraph. However, these quantities are considered confidential information of Corning Incorporated. To protect this confidential information while presenting some our results, Figure 5.13 shows the number of hydroxyls on Eagle XG® surfaces by sample type as a percentages of the sample with the most hydroxyls (HF-treated Eagle XG®). Relative error bars for most sample types were ca. 12%, owing in part to the relatively large error bars for the HF-treated SiO_2 samples we have used as our reference material. The detergent washed surface, which had the lowest fraction of silica for this sample group in our previous SIMS study also give the lowest number of surface hydroxyls.[12] Meanwhile, the TMAH-treated surface gives an intermediate value. These results are consistent with previous findings that the number of silanols at glass surfaces scale with their SiO_2 concentrations.[6]

5.8.8 Dehydroxylation at Temperatures up to 400 °C

We now turn our attention to sample behavior at higher temperatures. In Figure 5.14a, a HCl-treated fused quartz sample was heated in vacuum to 400 °C (the upper temperature limit for our instrument), held at that temperature overnight, and then temperature ramp was reversed the following day. Following the reverse temperature ramp, the heater was set to 30 °C, and the sample was held overnight at this temperature. The sample dehydroxylated with each increase in temperature up to 400 °C, with the largest step occurring between 300 °C and 400 °C. These elevated temperatures are known to result in the condensation of vicinal silanols to form siloxane bonds.[18] Very little rehydroxylation in vacuum occurred during the reverse temperature ramp, suggesting that holding the sample at 200 °C is sufficient to prevent readsorption and reaction of water with the sample surface. However, a small degree of rehydroxylation occurred while holding the sample in vacuum overnight at 30 °C. Figure 5.14b shows an HCl-treated fused quartz sample that was heated to 400 °C *in vacuo*, rehydroxylated overnight by exposure to ambient air, and then reheated *in vacuo* to 200 °C the following day to remove physisorbed water and measure the final hydroxylation state. Here, the same stepwise dehydroxylation behavior can be seen during the initial temperature ramp. Following exposure to ambient air, the sample rehydroxylated to a significant extent, though the final $SiOH^+/Si^+$ ratio measured for this sample was lower than for similarly treated samples heated only to 200 °C, suggesting that some non-reversible changes in the sample surface begin to occur by 400 °C.

Figure 5.15a shows the results of ramping an HF-treated Eagle XG® sample to 400 °C. The extent of dehydroxylation is much lower than for that of the fused quartz surface. Significant scatter can be seen for this sample. Nonetheless, a step-wise decrease in the measured $SiOH^+/Si^+$ ratio can be seen with each increase in temperature. This sample was rehydroxylated by exposure

to ambient air overnight and re-analyzed the following day at a constant temperature of 200 °C. The resulting average $SiOH^+/Si^+$ ratio after 190 minutes of heating was ca. 0.18 ± 0.03. Figure 15b shows the $SiOH^+/Si^+$ ratio for a HF-treated surface ramped to 400 °C and held overnight. Again, stepwise decreases in the $SiOH^+/Si^+$ can be seen with each temperature increase. Significant variability in the molar composition of this samples was noted, as shown in Figure 5.9b, which may explain some of the scatter in this data. Figure 5.15c shows the results for a similarly heated untreated Eagle XG® sample, where again, stepwise decreases in the measured $SiOH^+/Si^+$ ratio can be seen with increasing temperature. It is interesting to note that while the $SiOH^+/S^{i+}$ ratio clearly decreases with sample heating for the Eagle XG® samples, the magnitude of the decrease is lower than for the fused quartz samples. This may indicate that a greater fraction of hydroxyls on Eagle XG® surfaces are non-interacting, making it difficult for them to condense with neighboring hydroxyls groups to form siloxane bonds. Alternatively, it may suggest that some fraction of the $SiOH^+$ signal results from subsurface hydrous species, in spite of the excellent surface sensitivity of ToF-SIMS.

5.9 Conclusion

Surface hydroxyls on fused quartz and display glass surfaces exposed to various chemical treatments were analyzed using ToF-SIMS. We have provided some discussion of instrumental factors that may influence instrument response. In particular the analyzer acceptance energy had a strong influence on instrument response, and we chose an acceptance energy that optimized mass resolution and minimized the influence of charging on instrument response. We explored possible explanations for spot-to-spot and sample-to-sample variability in our data, including variability in

sample elemental composition and the influence of adventitious hydrocarbon contamination. Most samples showed low spot-to-spot variability in elemental composition, with one notable exception. We noted small but significant differences in elemental composition between some replicates. At high hydrocarbon coverages, the $SiOH^+/Si^+$ ratio was suppressed compared surfaces not dosed with hydrocarbons. At low hydrocarbon coverages, an $SiOD^+$ peak appeared, suggesting that undeuterated hydrocarbons contribute to the $SiOH^+$ signal via recombination reactions with substrate species. While it may be possible to correct for these effects, additional experiments will need to be performed to understand the extent of the contribution and suppression effects as a function of hydrocarbon concentration.

Our results are in good qualitative agreements with previous studies performed on silica surfaces, showing that acidic treatments such as hydrofluoric or hydrochloric acid are effective in hydroxylating these surfaces. HF- and HCl-treated multicomponent glass surfaces gave the highest degree of surface hydroxylation, industrial detergent treatment gave the lowest degree of surface hydroxylation, and treatment with TMAH resulted in intermediate values. Higher temperature treatment of Eagle XG® and fused quartz resulted in significant dehyroxylation for both surfaces. Interestingly, the Eagle XG® surfaces show much lower degree of dehydroxylation upon heating to 400 °C than do fused quartz surfaces, as indicated by a lower fractional decrease in the $SiOH^+/Si^+$ ratio.

5.10 Acknowledgements

5.11 Figures
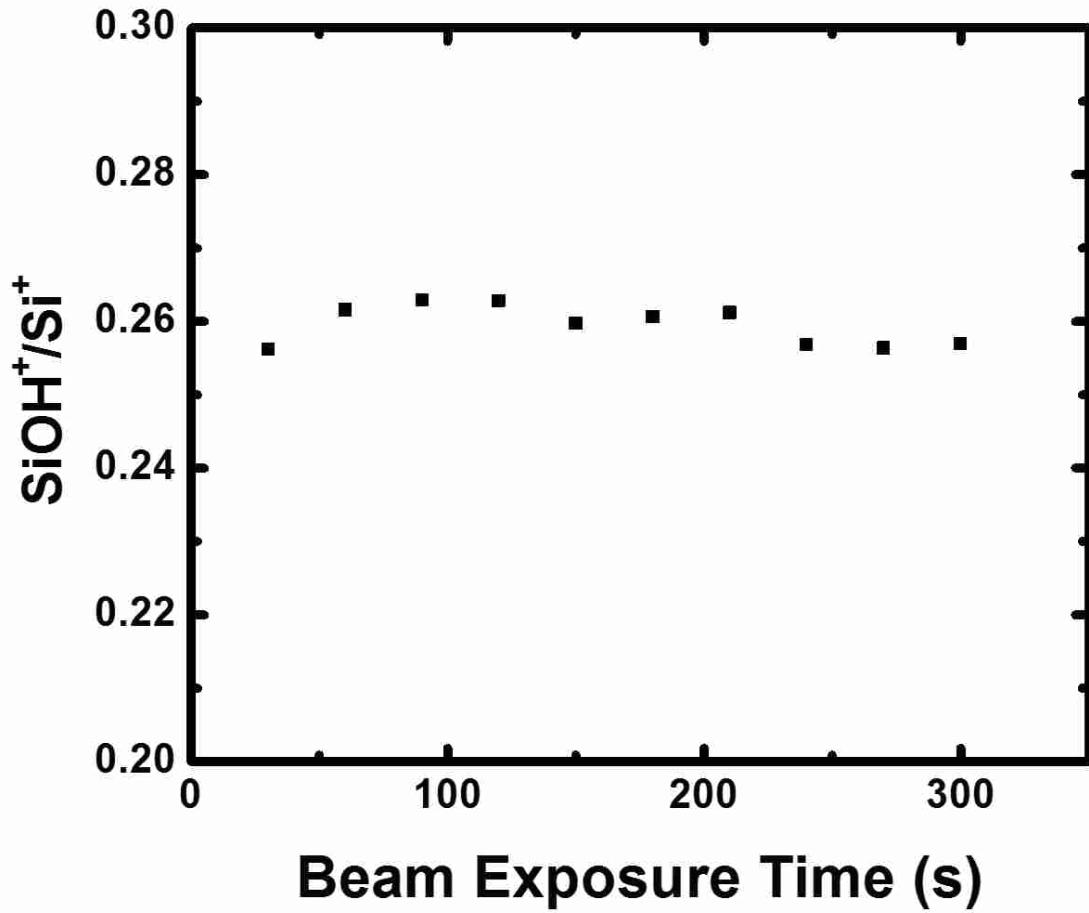
Figure 5.1. SiOH$^+$/Si$^+$ ratio as a function of increasing beam exposure for a series of spectra taken at the same sample location.
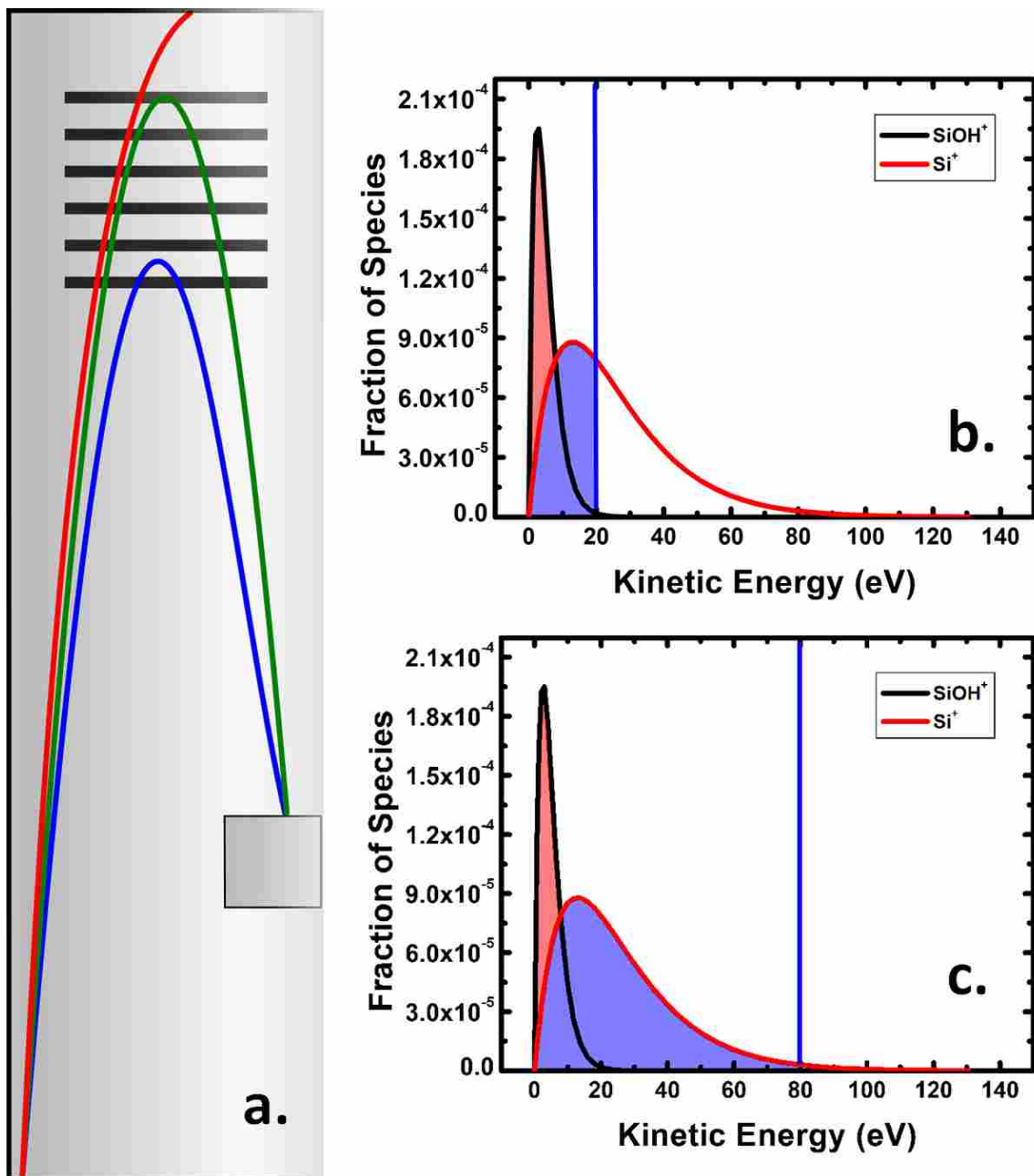
Figure 5.2. Schematic representation of the influence of acceptance energy, governed by reflector voltage, on the measured $SiOH^+/Si^+$ ratio. a) Schematic representation of ToF analyzer with a reflectron. Ions with low kinetic energy (blue) and moderate kinetic energy (green) are focused onto the detector, while ions with too high a kinetic energy (red) do no reach the detector. b and c) hypothetical Boltzmann

distributions for $SiOH^+$ and Si^+ ions, where the blue line indicates acceptance energy, and the shaded regions indicate the fraction of ions accepted by the analyzer for that acceptance energy.
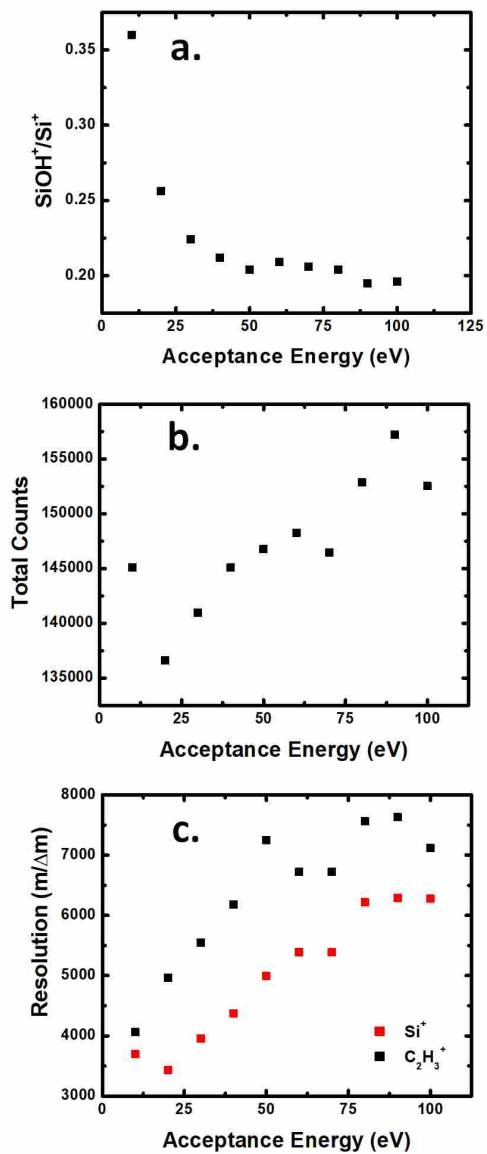
Figure 5.3. The influence of acceptance energy on instrument response. a) SiOH$^+$/Si$^+$ ratio. b) total ion counts in 30 second acquisition. c) Mass resolution for Si$^+$ and C$_2$H$_3$$^+$ peaks.
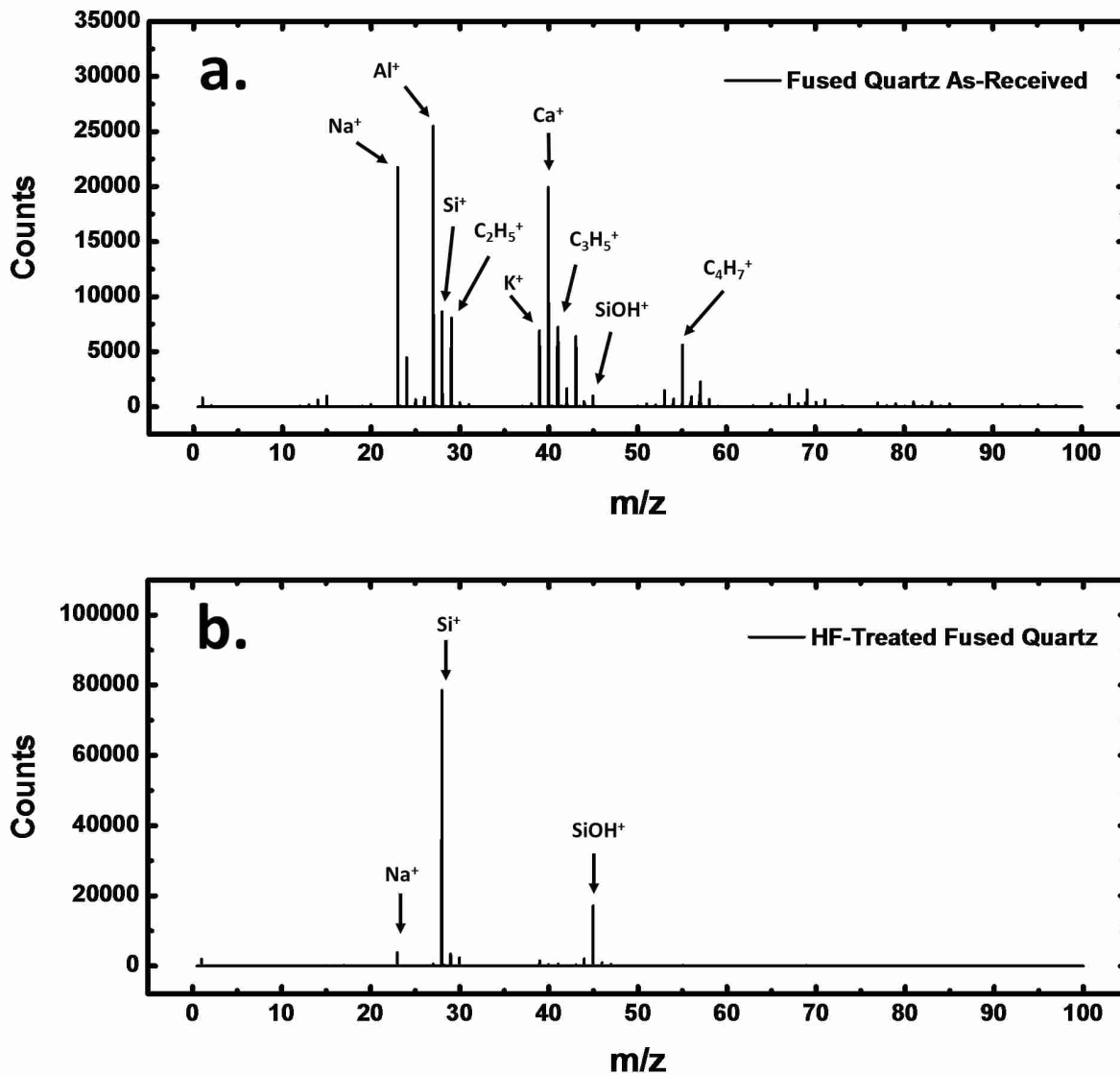
Figure 5.4. Representative spectra for fused quartz samples with selected peaks labeled. a) As-received fused quartz. b) HF-treated fused quartz surface.
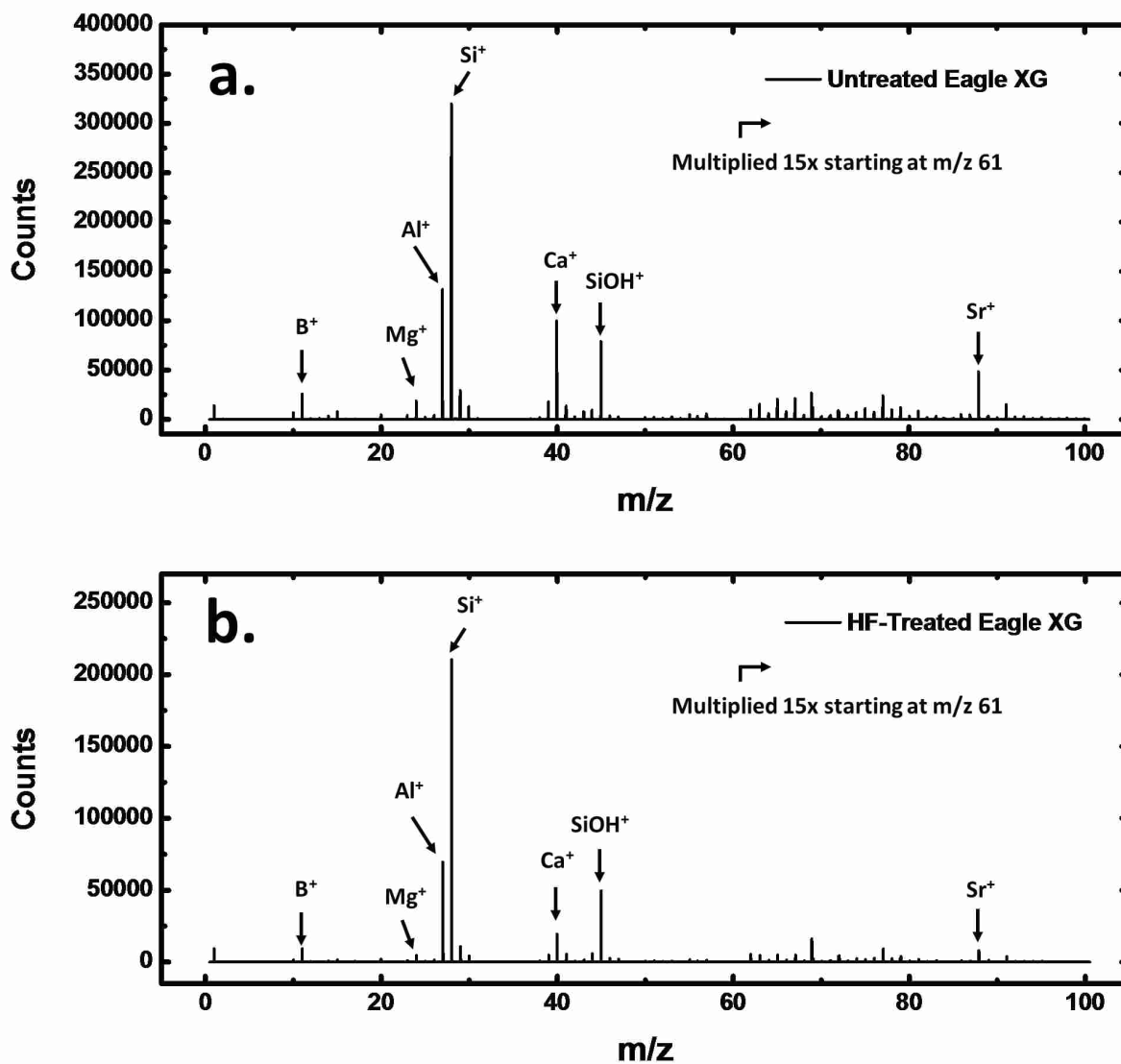
Figure 5.5. Representative ToF-SIMS spectra for Eagle XG® samples. a) As-received Eagle XG®. b) HF-treated Eagle XG®. Both spectra have been multiplied 15x starting at m/z 61 to better show lower intensity signals.
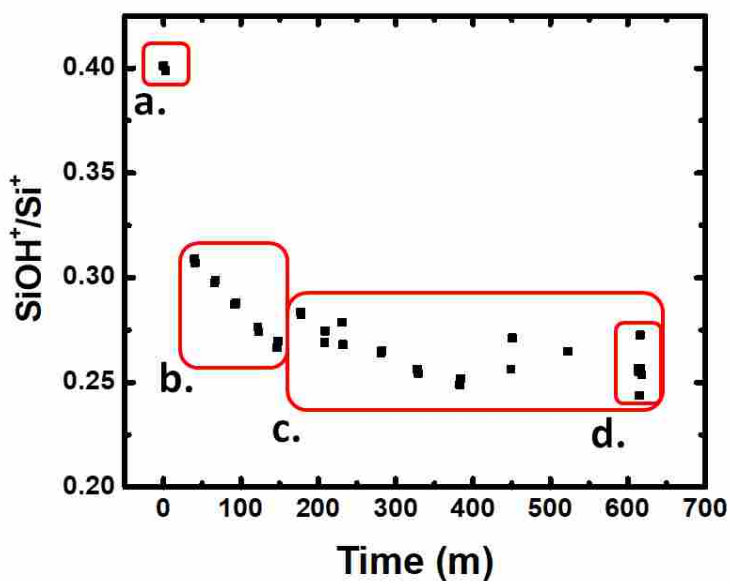
Figure 5.6. Annotated data recorded from an HF-treated Eagle XG® surface held at 200 °C, where each data point is recorded from a new sample position. a) The first two data points are recorded at room temperature. $SiOH^+/Si^+$ ratio is high due to presence of physisorbed water b.) $SiOH^+/Si^+$ ratio declines as physisorbed water is removed from sample. c) $SiOH^+/Si^+$ ratio reaches steady-state after removal of physisorbed water starting at ca. 190 minutes. d) data points recorded in rapid temporal succession at different sample locations to characterize spot-to-spot variation in $SiOH^+/Si^+$ ratio.
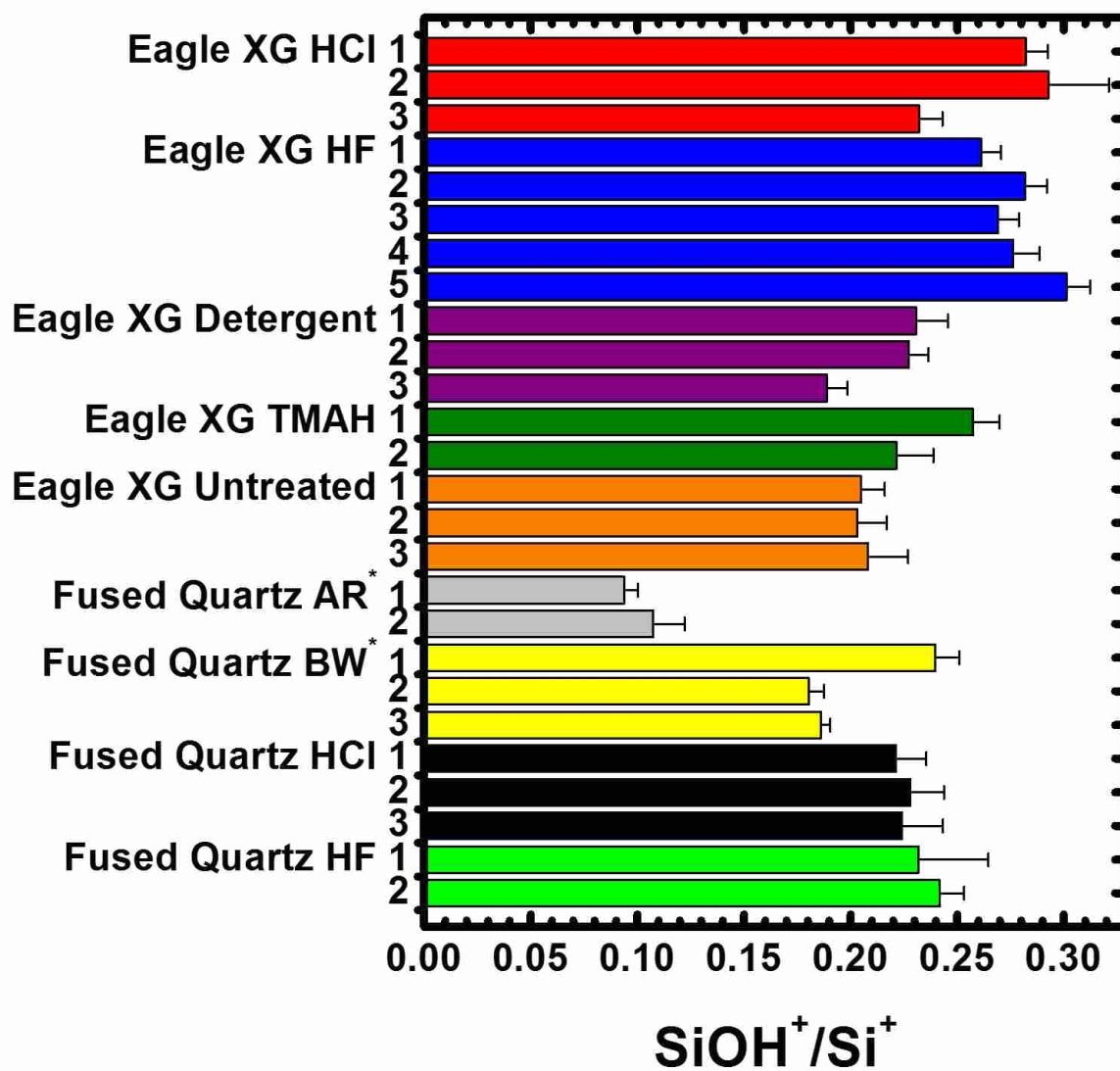
Figure 5.7. Average SiOH⁺/Si⁺ signal ratios for samples analyzed at a constant temperature of 200 °C, where error bars are given as standard deviations. FQ = fused quartz *AR = as-received, BW = boiling deionized water.
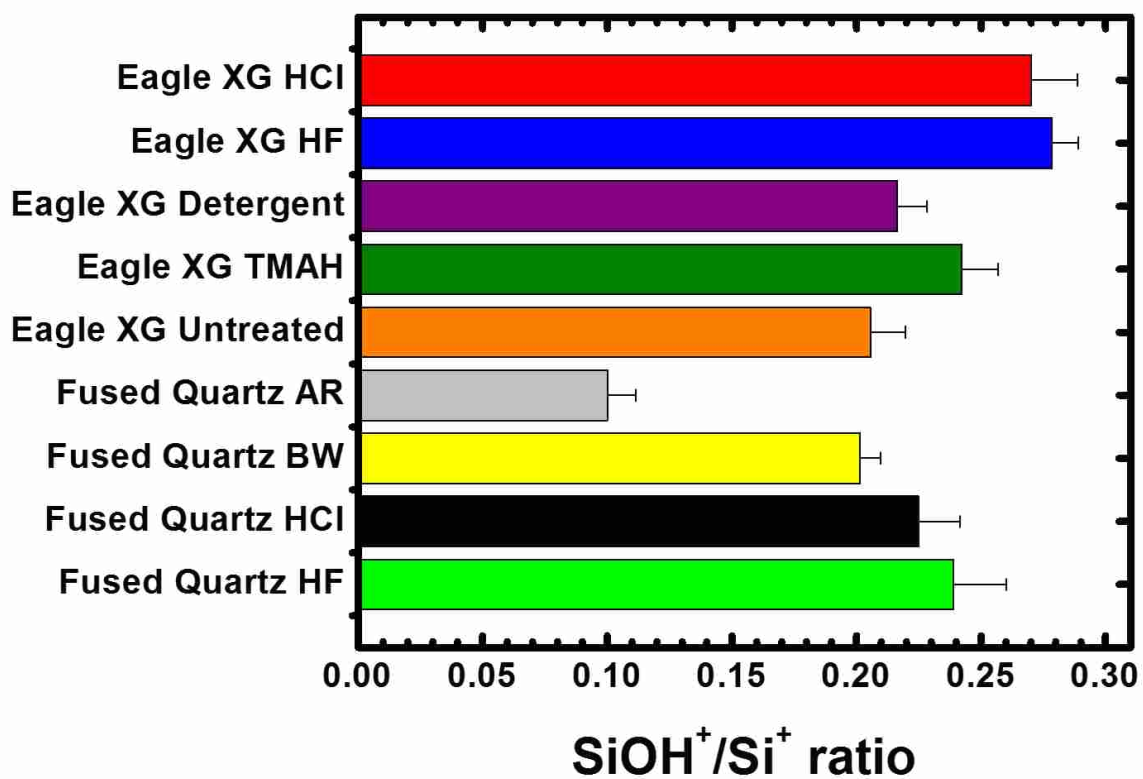
Figure 5.8. Pooled average $SiOH^+/Si^+$ ratios and pooled standard deviations by sample type for samples shown in Figure 5.7. [*]AR = as-received, BW = boiling deionized water.
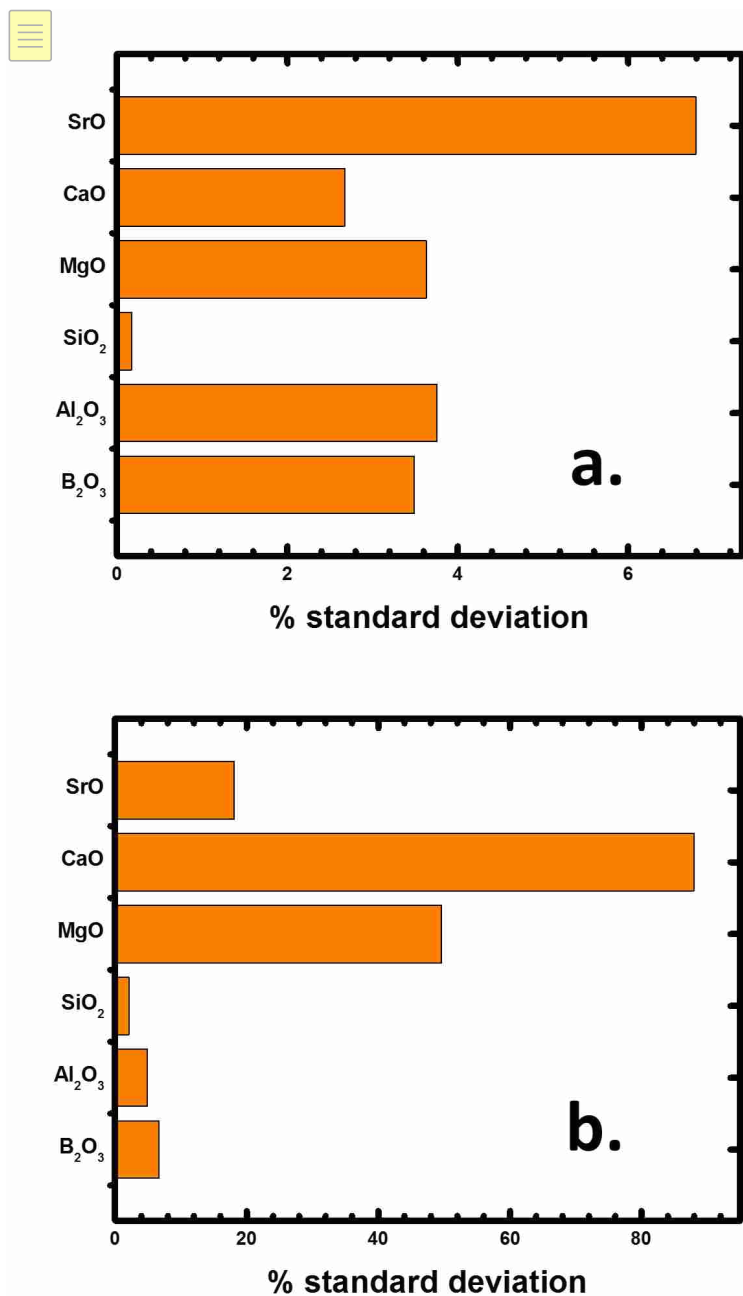
Figure 5.9. Percent standard deviation in molar composition for selected samples as a function of heating time. a) Percent standard deviations in molar composition from an HF-treated Eagle XG® surface analyzed at 200 °C, calculated from 36 spectra recorded at different sample locations. b) Standard deviations in molar composition from an HF-treated Eagle XG® surface ramped to 400 °C, calculated from 56 spectra recorded at different sample locations.
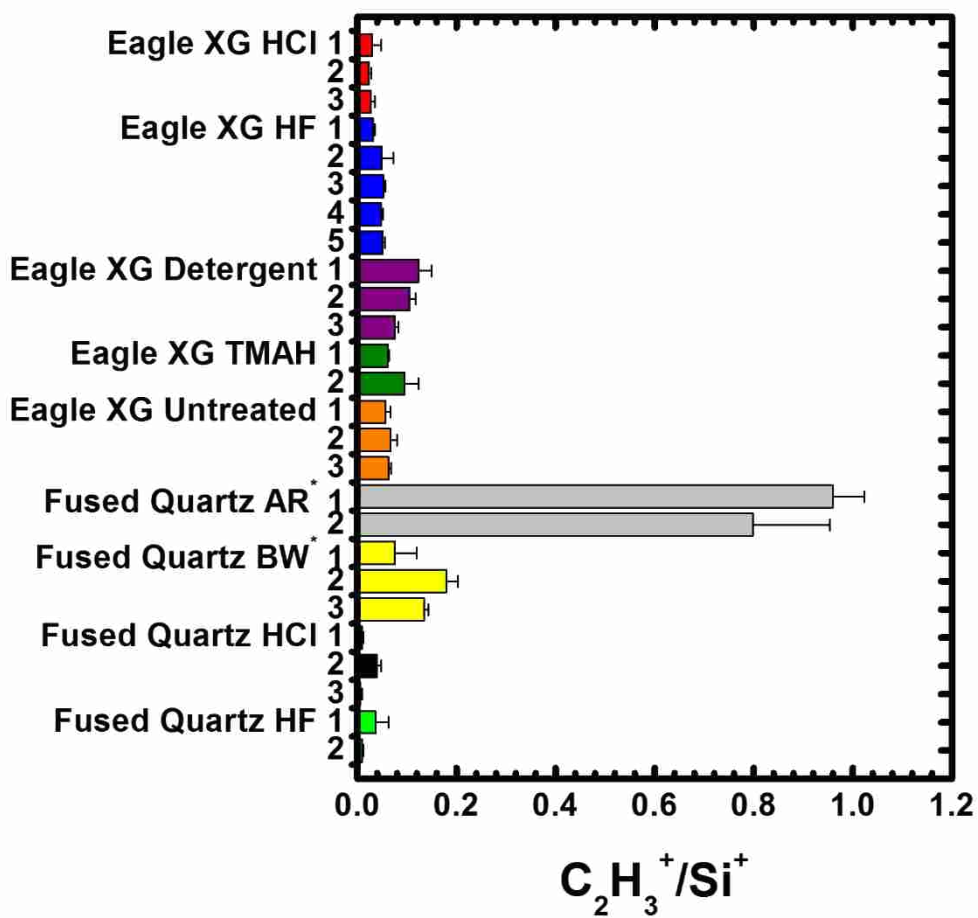
Figure 5.10. $C_2H_3^+/Si^+$ ratio for samples analyzed at a constant temperature of 200 °C. *AR = as-received, BW = boiling deionized water.
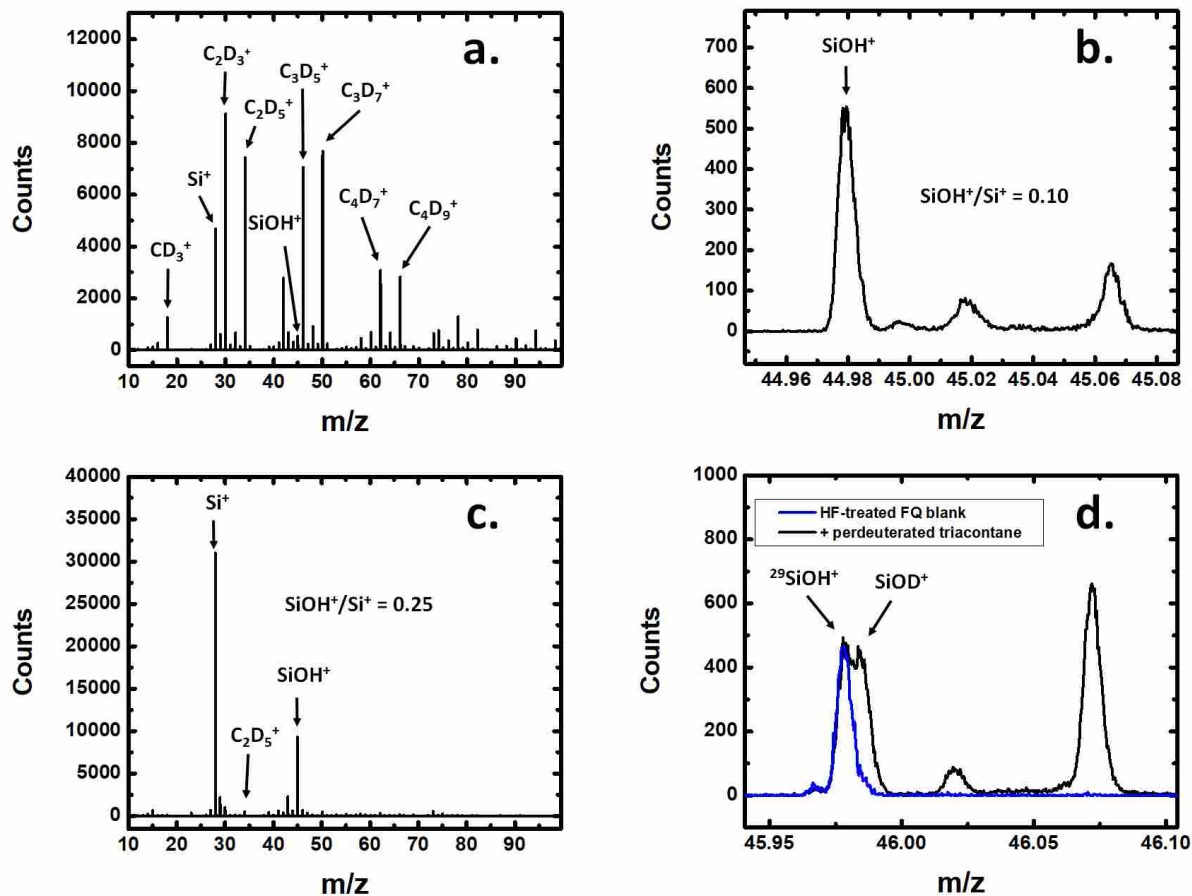
Figure 5.11. a) Spectrum for an HF-treated surface analyzed at room temperature with a high surface loading of perdeuterated triacontane, as evidenced by deuterated hydrocarbon fragments. b) A zoomed in view of the m/z 45 mass region in spectrum a) showing a reduction in the SiOH$^+$ signal at high hydrocarbon coverages. c) Spectrum from the same sample after mild heating to reduce triacontane coverage d) zoomed-in view of the m/z 46 region from the same spectrum as c), plotted with a spectrum from an HF-treated fused quartz blank. The HF-treated fused quartz blank spectrum has been scaled to have same SiOH$^+$ intensity as spectrum c) at m/z 45, such that their ^{29}SiOH$^+$ intensities at m/z 46 are easily compared.
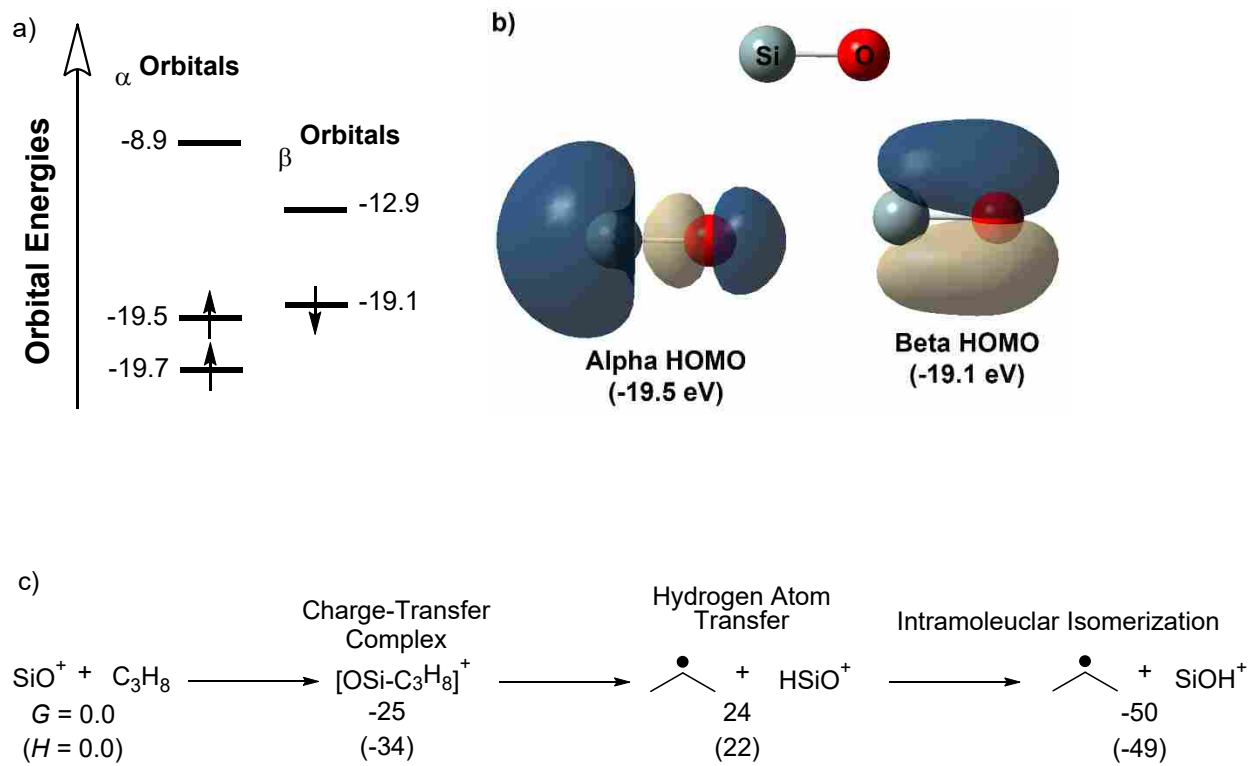
Figure 5.12. a) SiO⁺ unrestricted M06 orbital energies (eV). b) 3D images of SiO⁺ HOMO orbitals. c) Unrestricted M06-2X/6-31G** energies for hydrogen atom transfer between SiO⁺ and propane and intramolecular isomerization.
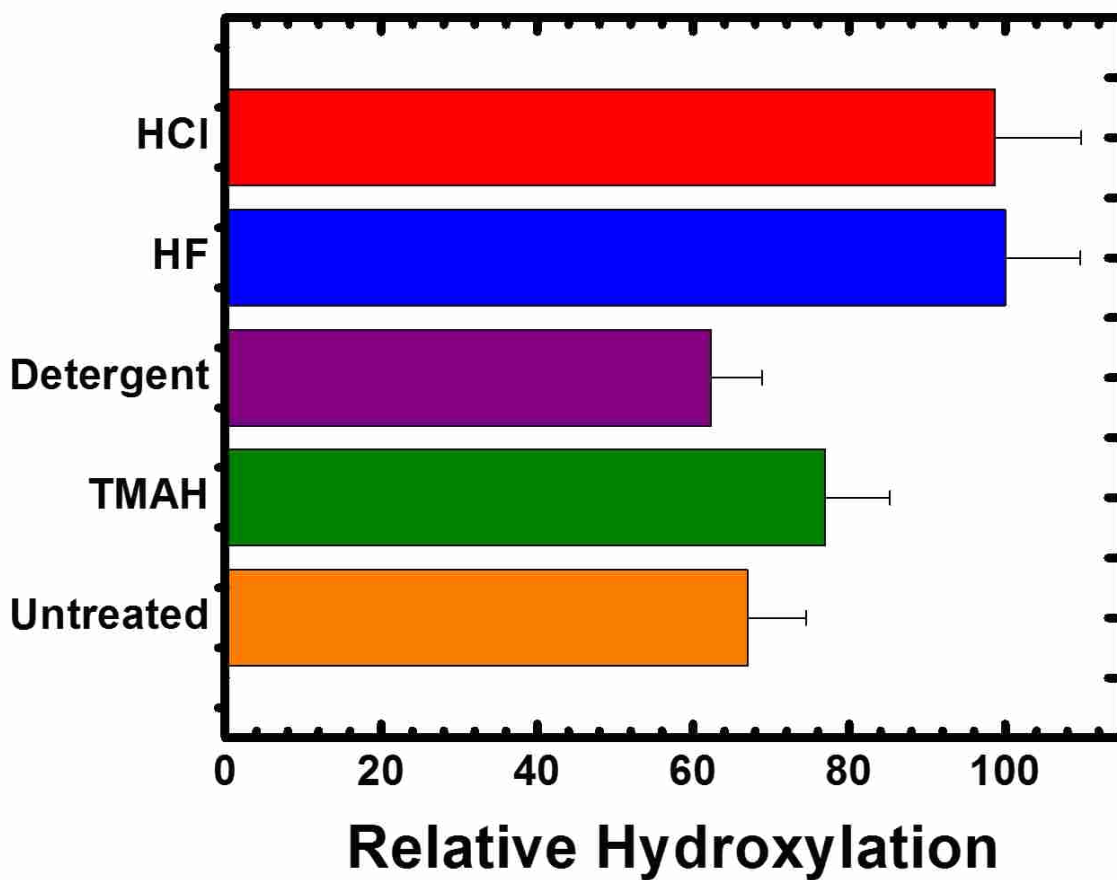
Figure 5.13. Relative hydroxyl coverages by Eagle XG® samples, based on Equation (5.3). To protect confidential information, the number of hydroxyls for all samples have been normalized to HF-treated Eagle XG®, which gave the highest number of hydroxyls per nanometer for the multicomponent glass samples in this study. Accordingly, the data are presented as hydroxylation percentages relative to this sample.
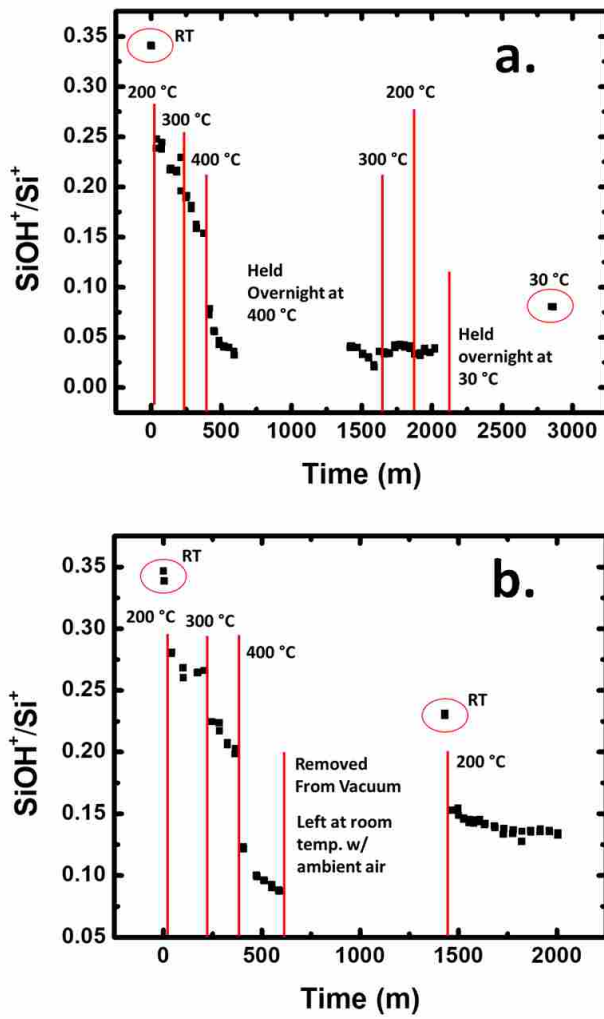
Figure 5.14. SiOH$^+$/Si$^+$ ratios for fused quartz samples ramped to 400 °C. (a.) A sample that was heated and cooled entirely *in vacuo*. (b.) A sample that was exposed to ambient air after ramping *in vacuo* to 400 °C, with follow up analysis *in vacuo* at 200 °C.

241
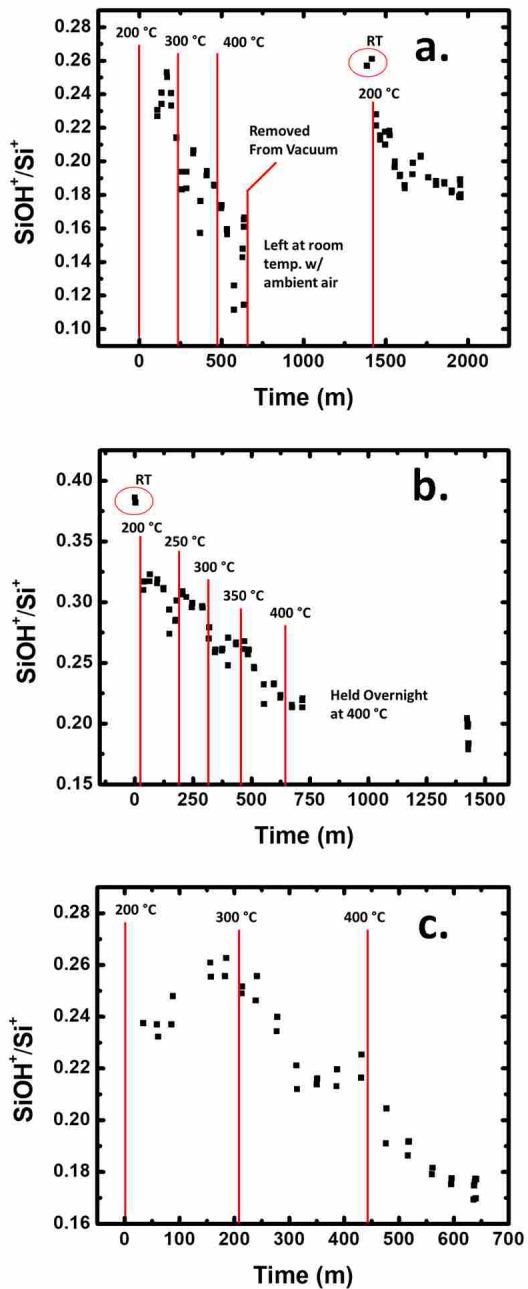
Figure 5.15. SiOH$^+$/Si$^+$ ratios for Eagle XG$^®$ samples ramped to maximum temperature of 400 °C. (a.) HF-treated Eagle XG$^®$ ramped to 400 °C *in vacuo* then exposed to ambient air, with follow-up analysis at 200 °C *in vacuo*. (b.) HF-treated Eagle XG$^®$ ramped to 400 °C and held overnight at this temperature. (c.) Untreated Eagle XG$^®$ ramped to 400 °C.

5.12 References

1. Ellison, A.; Cornejo, I. A. Glass Substrates for Liquid Crystal Displays. *International Journal of Applied Glass Science* **2010,** *1* (1), 87-103.

2. Hamilton, L. L. Display Innovations Through Glass. *Japanese Journal of Applied Physics* **2016,** *55*, 03CA01.

3. Boudreau, R. A.; Bocko, P. L., Glass Substrates for AMLCD, OLED, and Emerging Display Platforms. In *Handbook of Visual Display Technology*, Chen, J.; Cranton, W.; Fihn, M., Eds. Springer International Publishing: Cham, 2016; pp 851-884.

4. Souk, J.; Morozumi, S.; Luo, F.-C.; Bita, I., *Flat Panel Display Manufacturing*. John Wiley & Sons: 2018.

5. Hair, M. L. Hydroxyl groups on silica surface. *Journal of Non-Crystalline Solids* **1975,** *19*, 299-309.

6. Takeda, S.; Yamamoto, K.; Hayasaka, Y.; Matsumoto, K. Surface OH group governing wettability of commercial glasses. *Journal of non-crystalline solids* **1999,** *249* (1), 41-46.

7. Agnello, G.; Hamilton, J.; Manley, R.; Streltsova, E.; LaCourse, W.; Cormack, A. Investigation of Contact-Induced Charging Kinetics on Variably Modified Glass Surfaces. *Applied Surface Science* **2015,** *356*, 1189-1199.

8. Stapleton, J. J.; Suchy, D. L.; Banerjee, J.; Mueller, K. T.; Pantano, C. G. Adsorption reactions of carboxylic acid functional groups on sodium aluminoborosilicate glass fiber surfaces. *ACS applied materials & interfaces* **2010,** *2* (11), 3303-3309.

9. Choi, Y. S.; Yun, J. U.; Park, S. E. Flat Panel Display Glass: Current Status and Future. *Journal of Non-Crystalline Solids* **2016,** *431*, 2-7.

10. Bach, H. Advanced surface analysis of silicate glasses, oxides and other insulating materials: a review. *Journal of non-crystalline solids* **1997,** *209* (1), 1-18.

11. Hench, L.; Clark, D. E. Physical chemistry of glass surfaces. *Journal of Non-Crystalline Solids* **1978,** *28* (1), 83-105.

12. Cushman, C. V.; Zakel, J.; Sturgell, B. S.; Major, G. I.; Lunt, B. M.; Bruner, P.; Grehl, T.; Smith, N. J.; Linford, M. R. Time-of-flight secondary ion mass spectrometry of wet and dry chemically treated display glass surfaces. *Journal of the American Ceramic Society* **2017,** *100* (10), 4770-4784.

13. Cushman, C. V.; Brüner, P.; Zakel, J.; Dahlquist, C.; Sturgell, B.; Grehl, T.; Lunt, B. M.; Banerjee, J.; Smith, N. J.; Linford, M. R. Low Energy Ion Scattering (LEIS) of As-Formed and Chemically Modified Display Glass and peak-fitting of the Al/Si LEIS peak envelope. *Applied Surface Science* **2018,** *455*, 18-31.

14. D'Souza, A. S.; Pantano, C. G.; Kallury, K. M. Determination of the surface silanol concentration of amorphous silica surfaces using static secondary ion mass spectroscopy. *Journal of Vacuum Science & Technology A: Vacuum, Surfaces, and Films* **1997,** *15* (3), 526-531.

15. D'Souza, A. S.; Pantano, C. G. Mechanisms for silanol formation on amorphous silica fracture surfaces. *Journal of the American Ceramic Society* **1999,** *82* (5), 1289-1293.

16. D'Souza, A. S.; Pantano, C. G. Hydroxylation and dehydroxylation behavior of silica glass fracture surfaces. *Journal of the American Ceramic Society* **2002,** *85* (6), 1499-1504.

17. Hair, M. L.; Hertl, W. Adsorption on hydroxylated silica surfaces. *The Journal of Physical Chemistry* **1969,** *73* (12), 4269-4276.

18. Zhuravlev, L. The surface chemistry of amorphous silica. Zhuravlev model. *Colloids and Surfaces A: Physicochemical and Engineering Aspects* **2000,** *173* (1), 1-38.

19.   Takeda, S.; Fukawa, M. Surface OH groups governing surface chemical properties of SiO 2 thin films deposited by RF magnetron sputtering. *Thin Solid Films* **2003**, *444* (1), 153-157.

20.   Takeda, S.; Fukawa, M. Role of surface OH groups in surface chemical properties of metal oxide films. *Materials Science and Engineering: B* **2005**, *119* (3), 265-267.

21.   Schrader, A. M.; Monroe, J. I.; Sheil, R.; Dobbs, H. A.; Keller, T. J.; Li, Y.; Jain, S.; Shell, M. S.; Israelachvili, J. N.; Han, S. Surface chemical heterogeneity modulates silica surface hydration. *Proceedings of the National Academy of Sciences* **2018**, *115* (12), 2890-2895.

22.   Pulker, H.; Pulker, H., *Coatings on glass*. Elsevier: 1999; Vol. 20.

23.   Erkelens, J.; Linsen, B. Quantitative determination of hydroxyl groups and water for silica. *Journal of Colloid and Interface Science* **1969**, *29* (3), 464-468.

24.   Potapov, V.; Zhuravlev, L. Temperature dependence of the concentration of silanol groups in silica precipitated from a hydrothermal solution. *Glass Physics and Chemistry* **2005**, *31* (5), 661-670.

25.   Gallas, J.-P.; Goupil, J.-M.; Vimont, A.; Lavalley, J.-C.; Gil, B.; Gilson, J.-P.; Miserque, O. Quantification of water and silanol species on various silicas by coupling IR spectroscopy and in-situ thermogravimetry. *Langmuir* **2009**, *25* (10), 5825-5834.

26.   McDonald, R. S. Surface functionality of amorphous silica by infrared spectroscopy. *The Journal of Physical Chemistry* **1958**, *62* (10), 1168-1178.

27.   Anderson Jr, J.; Wickersheim, K. Near infrared characterization of water and hydroxyl groups on silica surfaces. *Surface Science* **1964**, *2*, 252-260.

28.   Armistead, C.; Tyler, A.; Hambleton, F.; Mitchell, S.; Hockey, J. A. Surface hydroxylation of silica. *The Journal of Physical Chemistry* **1969**, *73* (11), 3947-3953.

29.   Mahadevan, T. S.; Du, J. Evaluating Water Reactivity at Silica Surfaces Using Reactive Potentials. *The Journal of Physical Chemistry C* **2018**, *122* (18), 9875-9885.

30.   Leed, E. A.; Sofo, J. O.; Pantano, C. G. Electronic structure calculations of physisorption and chemisorption on oxide glass surfaces. *Physical Review B* **2005**, *72* (15), 155427.

31.   Lockwood, G. K.; Garofalini, S. H. Bridging oxygen as a site for proton adsorption on the vitreous silica surface. *The Journal of chemical physics* **2009**, *131* (7), 074703.

32.   Sulpizi, M.; Gaigeot, M.-P.; Sprik, M. The silica–water interface: how the silanols determine the surface acidity and modulate the water properties. *Journal of chemical theory and computation* **2012**, *8* (3), 1037-1047.

33.   Akkopru Akgun, B. ADSORPTION Of WATER ON SILICA and SILICATE GLASSES. **2013**.

34.   Fry, R. A.; Tsomaia, N.; Pantano, C. G.; Mueller, K. T. ^{19}F MAS NMR quantification of accessible hydroxyl sites on fiberglass surfaces. *Journal of the American Chemical Society* **2003**, *125* (9), 2378-2379.

35.   Rivera, L. O.; Bakaev, V. A.; Banerjee, J.; Mueller, K. T.; Pantano, C. G. Characterization and reactivity of sodium aluminoborosilicate glass fiber surfaces. *Applied Surface Science* **2016**, *370*, 328-334.

36.   Fry, R.; Mueller, K.; Pantano, C. Effect of boron oxide on surface hydroxyl coverage of aluminoborosilicate glass fibres: a 19F solid state NMR study. *Physics and Chemistry of Glasses* **2003**, *44* (2), 64-68.

37.   Schaut, R. A. The effect of boron oxide on the composition, structure, and adsorptivity of glass surfaces. **2008**.

38.   Wood, J. G.; Prabakar, S.; Mueller, K. T.; Pantano, C. G. The effects of antimony oxide on the structure of alkaline-earth alumino borosilicate glasses. *Journal of non-crystalline solids* **2004,** *349*, 276-284.

39.   Schaut, R. A.; Lobello, R. A.; Mueller, K. T.; Pantano, C. G. Characterization of boroaluminosilicate glass surface structures by B K-edge NEXAFS. *Journal of Non-Crystalline Solids* **2011,** *357* (19), 3416-3423.

40.   Rodrigues, A.; Fearn, S.; Palomar, T.; Vilarigues, M. Early stages of surface alteration of soda-rich-silicate glasses in the museum environment. *Corrosion Science* **2018,** *143*, 362-375.

41.   Hayashi, Y.; Matsumoto, K. Determination of surface silanol group on silicate glasses using static SIMS. *Journal of the Ceramic Society of Japan* **1992,** *100* (8), 1038-1041.

42.   Sprenger, D.; Bach, H.; Meisel, W.; Gütlich, P. XPS study of leached glass surfaces. *Journal of non-crystalline solids* **1990,** *126* (1-2), 111-129.

43.   Banerjee, J.; Bojan, V.; Pantano, C. G.; Kim, S. H. Effect of heat treatment on the surface chemical structure of glass: Oxygen speciation from in situ XPS analysis. *Journal of the American Ceramic Society* **2018,** *101* (2), 644-656.

44.   Tarlov, M. J.; Evans, J. F.; Newman, J. G. Static SIMS and XPS study of water plasma exposed tin oxide films. *Applied surface science* **1993,** *64* (2), 115-125.

45.   Wood, B.; Lamb, R.; Raston, C. Static SIMS study of hydroxylation of low-surface-area silica. *Surface and interface analysis* **1995,** *23* (10), 680-688.

46.   McCrate, J. M.; Ekerdt, J. G. Titration of free hydroxyl and strained siloxane sites on silicon dioxide with fluorescent probes. *Langmuir* **2013,** *29* (38), 11868-11875.

47.   Xing, Y.; Dementev, N.; Borguet, E. Chemical labeling for quantitative characterization of surface chemistry. *Current Opinion in Solid State and Materials Science* **2007,** *11* (5-6), 86-91.

48.   Van Der Voort, P.; Vercauteren, S.; Peeters, K.; Vansant, E. F., Some precautions when determining the silanol number, using chemical modification with methylchlorosilanes. Elsevier: 1993.

49.   Vansant, E. F.; Van Der Voort, P.; Vrancken, K. C., *Characterization and chemical modification of the silica surface*. Elsevier: 1995; Vol. 93.

50.   Myalitsin, A.; Urashima, S.-h.; Nihonyanagi, S.; Yamaguchi, S.; Tahara, T. Water structure at the buried silica/aqueous interface studied by heterodyne-detected vibrational sum-frequency generation. *The Journal of Physical Chemistry C* **2016,** *120* (17), 9357-9363.

51.   Isaienko, O.; Borguet, E. Hydrophobicity of hydroxylated amorphous fused silica surfaces. *Langmuir* **2013,** *29* (25), 7885-7895.

52.   Fan, H.-F.; Li, F.; Zare, R. N.; Lin, K.-C. Characterization of two types of silanol groups on fused-silica surfaces using evanescent-wave cavity ring-down spectroscopy. *Analytical chemistry* **2007,** *79* (10), 3654-3661.

53.   Banerjee, J.; Kim, S. H.; Pantano, C. G. Elemental areal density calculation and oxygen speciation for flat glass surfaces using x-ray photoelectron spectroscopy. *Journal of Non-Crystalline Solids* **2016,** *450*, 185-193.

54.   Benninghoven, A. Surface analysis by secondary ion mass spectrometry (SIMS). *Surface Science* **1994,** *299*, 246-260.

55.   Benninghoven, A. Some aspects of secondary ion mass spectrometry of organic compounds. *International Journal of Mass Spectrometry and Ion Physics* **1983,** *53*, 85-99.

56.   Delcorte, A.; Leblanc, C.; Poleunis, C.; Hamraoui, K. Computer Simulations of the Sputtering of Metallic, Organic, and Metal–Organic Surfaces with Bi n and C60 Projectiles. *The Journal of Physical Chemistry C* **2013,** *117* (6), 2740-2752.

57.   Stevie, F., *Secondary ion mass spectrometry: Applications for depth profiling and surface characterization*. Momentum Press: 2015.

58.   Mitchell, D.; Graham, M. Quantitative SIMS analysis of hydroxyl ion content in thin oxide films. *Journal of The Electrochemical Society* **1986,** *133* (5), 936-938.

59.   Hauri, E. SIMS analysis of volatiles in silicate glasses, 2: isotopes and abundances in Hawaiian melt inclusions. *Chemical Geology* **2002,** *183* (1), 115-141.

60.   Aubaud, C.; Withers, A. C.; Hirschmann, M. M.; Guan, Y.; Leshin, L. A.; Mackwell, S. J.; Bell, D. R. Intercalibration of FTIR and SIMS for hydrogen measurements in glasses and nominally anhydrous minerals. *American Mineralogist* **2007,** *92* (5-6), 811-828.

61.   Liu, Y.; Guan, Y.; Zhang, Y.; Rossman, G. R.; Eiler, J. M.; Taylor, L. A. Direct measurement of hydroxyl in the lunar regolith and the origin of lunar surface water. *Nature Geoscience* **2012,** *5* (11), 779.

62.   Mitchell, D.; Sproule, G.; Graham, M. Measurement of hydroxyl ions in thin passive oxide films using secondary ion mass spectrometry. *Applications of Surface Science* **1985,** *21* (1-4), 199-209.

63.   Zhu, Z.; Shutthanandan, V.; Engelhard, M. An investigation of hydrogen depth profiling using ToF-SIMS. *Surface and Interface Analysis* **2012,** *44* (2), 232-237.

64.   Magee, C.; Botnick, E. Hydrogen depth profiling using SIMS—Problems and their solutions. *Journal of Vacuum Science and Technology* **1981,** *19* (1), 47-52.

65.   Barnes, J.; Franchi, I.; Anand, M.; Tartèse, R.; Starkey, N.; Koike, M.; Sano, Y.; Russell, S. Accurate and precise measurements of the D/H ratio and hydroxyl content in lunar apatites using NanoSIMS. *Chemical Geology* **2013,** *337*, 48-55.

66.   McCubbin, F. M.; Steele, A.; Nekvasil, H.; Schnieders, A.; Rose, T.; Fries, M.; Carpenter, P. K.; Jolliff, B. L. Detection of structurally bound hydroxyl in fluorapatite from Apollo mare basalt 15058, 128 using TOF-SIMS. *American Mineralogist* **2010,** *95* (8-9), 1141-1150.

67.   Stephan, T. TOF-SIMS in cosmochemistry. *Planetary and Space Science* **2001,** *49* (9), 859-906.

68.   Abel, M.; Shimizu, K.; Holliman, M.; Watts, J. Peak-fitting of high resolution ToF-SIMS spectra: a preliminary study. *Surface and Interface Analysis: An International Journal devoted to the development and application of techniques for the analysis of surfaces, interfaces and thin films* **2009,** *41* (4), 265-268.

69.   Cliff, J. B.; Gaspar, D. J.; Bottomley, P. J.; Myrold, D. D. Peak fitting to resolve CN− isotope ratios in biological and environmental samples using TOF-SIMS. *Applied surface science* **2004,** *231*, 912-916.

70.   Cushman, C. V.; Brüner, P.; Zakel, J.; Major, G. H.; Lunt, B. M.; Smith, N. J.; Grehl, T.; Linford, M. R. Low energy ion scattering (LEIS). A practical introduction to its theory, instrumentation, and applications. *Analytical Methods* **2016,** *8* (17), 3419-3439.

71.   Brongersma, H. H.; Draxler, M.; de Ridder, M.; Bauer, P. Surface composition analysis by low-energy ion scattering. *Surface Science Reports* **2007,** *62* (3), 63-109.

72.   Lee, J.; Gilmore, I.; Seah, M.; Levick, A.; Shard, A. Topography and field effects in secondary ion mass spectrometry Part II: insulating samples. *Surface and Interface Analysis* **2012,** *44* (2), 238-245.

73.   Lee, J. L.; Gilmore, I. S.; Seah, M. P.; Fletcher, I. W. Topography and field effects in secondary ion mass spectrometry–part i: Conducting samples. *Journal of The American Society for Mass Spectrometry* **2011,** *22* (10), 1718.

74. Van der Heide, P., *Secondary ion mass spectrometry: an introduction to principles and practices*. John Wiley & Sons: 2014.

75. Green, F.; Gilmore, I.; Seah, M. TOF-SIMS: Accurate mass scale calibration. *Journal of the American Society for Mass Spectrometry* **2006,** *17* (4), 514-523.

76. Gilmore, I.; Seah, M.; Green, F. Static TOF-SIMS—a VAMAS interlaboratory study. Part I. Repeatability and reproducibility of spectra. *Surface and Interface Analysis: An International Journal devoted to the development and application of techniques for the analysis of surfaces, interfaces and thin films* **2005,** *37* (8), 651-672.

77. Bottazzi, P.; Ottolini, L.; Vannucci, R. SIMS analyses of rare earth elements in natural minerals and glasses: An investigation of structural matrix effects on ion yields. *Scanning* **1992,** *14* (3), 160-168.

78. Smith, D. H.; Christie, W. A comparison of a theoretical model and sensitivity factor calculations for quantification of sims data. *International Journal of Mass Spectrometry and Ion Physics* **1978,** *26* (1), 61-76.

79. Takizawa, K.; Ohno, M.; Saito, H.; Kobayashi, M.; Sagara, H. SIMS Analysis of Borosilicate Glasses using Sensitivity Factor Calculation. *Journal of the Mass Spectrometry Society of Japan* **1980,** *28* (2), 161-168.

80. Bojan, V.; Büyüklimanli, T.; Pantano, C. G. Quantification of SIMS data for multicomponent glasses. *Surface and interface analysis* **1994,** *21* (2), 87-94.

81. Delcorte, A.; Bertrand, P.; Arys, X.; Jonas, A.; Wischerhoff, E.; Mayer, B.; Laschewsky, A. ToF-SIMS study of alternate polyelectrolyte thin films: Chemical surface characterization and molecular secondary ions sampling depth. *Surface Science* **1996,** *366* (1), 149-165.

82. Zhao, Y.; Truhlar, D. G. A new local density functional for main-group thermochemistry, transition metal bonding, thermochemical kinetics, and noncovalent interactions. *The Journal of chemical physics* **2006,** *125* (19), 194101.

83. Zhao, Y.; Truhlar, D. G. The M06 suite of density functionals for main group thermochemistry, thermochemical kinetics, noncovalent interactions, excited states, and transition elements: two new functionals and systematic testing of four M06-class functionals and 12 other functionals. *Theoretical Chemistry Accounts* **2008,** *120* (1-3), 215-241.

84. Kanyal, S. S.; Singh, B.; Cushman, C. V.; Jankowski, D. T.; Linford, M. R. Hydroxylation of the silica in microfabricated thin layer chromatography plates as probed by time-of-flight secondary ion mass spectrometry and diffuse reflectance infrared Fourier transform spectroscopy. *Surface and Interface Analysis* **2015,** *47* (3), 340-344.

85. Köhler, J.; Kirkland, J. Improved silica-based column packings for high-performance liquid chromatography. *Journal of Chromatography A* **1987,** *385*, 125-150.

86. Mahoney, C. M., *Cluster secondary ion mass spectrometry: principles and applications*. John Wiley & Sons: 2013; Vol. 44.

6.1 Key Findings from Each Chapter

Display glass surface composition is important to its end use. In particular, display glass surface composition affects particulate adhesion, thin film adhesion, adsorption of atmospheric contaminants, and thin film adhesion. These processes directly influence display glass's suitability as a microfabrication substrate.[1-4] Understanding these processes in greater detail begins with obtaining a detailed knowledge of display glass surface composition as a function of the environments it is exposed to. In this dissertation, we analyzed display glass surfaces exposed to various wet chemical treatments, addressed data analysis challenges, and proposed a method for measuring surface silanols on multicomponent glass substrates. In the process, we gained detailed surface compositional understanding of Eagle XG® at multiple length scales.

In Chapter 2, we performed a multivariate data analysis of Eagle XG® using SIMS and multivariate curve resolution (MCR). Manual examination of the elemental signals showed that as-formed Eagle XG® is significantly modifier-depleted/silica rich compared to Eagle XG® fracture surfaces. We considered the spectra from a wider perspective by using MCR, which revealed three compositional extremes for the samples we studied. Samples treated with hydrochloric acid were depleted in modifier species, boron, and aluminum, leaving a substantially silica-enriched surface. In contrast, the bulk composition of Eagle XG®, represented by a fracture surface, showed high modifier, aluminum, and boron concentrations. Samples treated with industrial detergents differed from all other samples in their concentrations of sodium and potassium. However, because SIMS is extremely sensitive to these species, the increase it detected

does not necessarily correspond to a dangerously high level of sodium from a device perspective. Treatment with industrial detergents also increased Al concentration at Eagle XG® surfaces compared to the as-formed Eagle XG® surfaces.

The negative ion spectra showed oxide cluster ions extending to high masses. One group of clusters contained both aluminum and silicon, while the other contained only silicon. We verified the identity of these clusters by checking their isotopic ratios. A multivariate curve resolution analysis of these cluster ions showed that the Al-containing clusters increased in intensity with elemental aluminum concentration. Clusters that contained only Si, on the other hand, were dominant in acid-treated Eagle XG® surfaces. Previous work has attempted to derive information about glass network connectivity through larger cluster ions like these.[5] While it is possible that the cluster ions in our samples convey information about their chain length, we need control samples of known compositions and with well-characterized network connectivities to make any such conclusions.

Multivariate curve resolution results for models containing over 200 peaks gave similar results to models containing only elemental signals. This useful finding suggests that elemental signals alone provide useful conclusions about these samples in spite of their spectral complexity. Also, the large negative-ion cluster intensities showed a high degree of correlation with the positive ion elemental signals for Al and Si.

Our efforts focused on the inorganic glass composition and paid little attention to organic contaminants. The chemical treatments we used generally reduced adventitious hydrocarbon contamination compared to the untreated samples, as indicated by a decrease in hydrocarbon signals like $C_2H_3^+$. However, we made no effort to identify organic contaminants introduced by these treatments.

In Chapter 3, we analyzed the elemental composition of the outermost atomic layer of Eagle XG® using low-energy ion scattering. The results were in good general agreement with those presented in Chapter 2, but the modifier depletion appeared much more severe due to LEIS extreme surface sensitivity. The LEIS results suggested that sodium, calcium, and magnesium were completely absent from the outermost atomic layer of Eagle XG® following acid treatment. The results also indicated that as-formed Eagle XG® surfaces had approximately 30-50% the modifier ion concentration of Eagle XG® fracture surfaces. Magnesium was only detected in the fracture surface, though its detection limit was likely impacted by interference from the Si/Al peak envelope, especially for LEIS spectra recorded with 3 keV ^{4}He$^+$. Interestingly, LEIS analysis detected no sodium, even for the detergent-treated samples. This finding suggests sodium contamination is only present at trace levels and is only detected in SIMS analysis due to its extreme sensitivity towards sodium.

Resolving the Al and Si signals in this analysis was a major challenge. We are not the first to attempt resolving these signals, but we are the first to publish instrumental parameters and data analysis protocols for addressing this challenge. Resolving these signals required analysis at 6 keV, giving peak separation of 55% of the Si FWHM compared to only ca. 30% at 3 keV. We attempted peak fitting the 6 keV ^{4}He$^+$ LEIS data under several different sets of fitting constraints. The positions and widths of the Al and Si peaks in the fit were poorly determined in the absence of fitting constraints. Reasonable fitting results were only obtained by constraining the positions and widths of peak fit components to those obtained by reference materials.

We also attempted a linear least squares (LLS) approach using reference spectra from Al_2O_3, SiO_2, and MgO as basis sets. This approach required an additional spectral component to account for LEIS background from the modifier species in Eagle XG®. We derived this

background spectrum through a series of difference spectra between the Eagle XG® fracture surface and reference materials spectra. In general, all three of the fitting approaches gave good agreement, with the LLS approach showing the lowest levels of Al at the samples' surface by a small margin.

This analysis demonstrated that as-formed Eagle XG® surfaces were severely depleted in aluminum. While the fracture surface gave Al_2O_3 coverages of ca. 31%, the as-formed Eagle XG® surfaces had only 1-4% and the HCl treated surfaces had no detectable aluminum at the sample surface. These findings suggest that aluminum is not a major contributor to the surface mediated processes on as-formed and leached Eagle XG®. However, in keeping with the findings from SIMS analysis in chapter 2, the aluminum concentration at the Eagle XG® surface increased significantly compared to the as-formed surface when treated with industrial alkaline detergent. This surface gave ca. 17% Al_2O_3 coverage.

Fitting the Al/Si peak envelope in LEIS remains a significant challenge. While SIMS and XPS analysis corroborate our LEIS peak fitting results, the method could be further validated. Analyzing a series of simple sodium aluminosilicate glass fracture surfaces of known bulk composition with varying aluminum concentrations would determine the limits of uncertainty in the fits, better understand variability in spectral background, and identify artifacts from sample charging.

Chapter 4 briefly discussed the angle-resolved XPS analysis of these glass surfaces. These analyses are vital to the conclusions of this dissertation because they demonstrate that Eagle XG's surface composition varies significantly even over a ca. 6 nm length scale. Results from this study support the SIMS elemental analysis in Chapter 4.

The XPS results show dramatic differences between as-formed Eagle XG® surfaces and all chemically treated surfaces, and are in good agreement with all other elemental analysis presented in this dissertation. The acid-treated surface showed modifier, Al, and B depletion, while the detergent-treated surface showed a marked increase in Al compared to the as-formed surface.

All surfaces showed a compositional gradient. In general, the extent of modifier, Al, and B depletion increased at more surface-sensitive take-off angles. These near-surface compositional gradients cannot be detected through sputter depth profiling. The trend in Al concentration for the detergent-treated sample varied from all other samples. It showed a maximum in relative Al concentration at a take-off angle of 61.25°, rather than a monotonic decrease in Al_2O_3 concentration as observed for all other samples. Further modeling of this data may provide insight into the mechanism of aluminum enrichment for this sample treatment. We also varied the severity of HCl treatment in this study, and longer-duration treatments yielded more modifier, Al, and B depletion.

We only interpreted this data in a qualitative sense. Turning these measurements into true concentration profiles requires mathematical modeling. Given the complexity involved in modeling gradients in AR-XPS data, such a task is not possible without making reasonable assumptions and applying reasonable fitting constraints. Because classical interdiffusion (CID) is the most likely corrosion process for these samples, we could derive reasonable profiles by constraining the fit to solutions consistent with this corrosion model.

In Chapter 5, we developed a ToF-SIMS protocol for measuring surface silanols on multicomponent glass surfaces. This protocol is likely our most significant contribution to glass surface science, as surface hydroxyls are among the most important reactive groups at multicomponent glass surfaces. We explored instrumental parameters that influenced our

instrument response and the impact of adventitious hydrocarbon contamination on measurements. We quantified the elemental composition of the samples using SIMS, explored their dehydroxylation behavior at elevated temperatures, and reported the number of surface hydroxyls per square nanometer (OH/nm^2) on various chemically treated Eagle XG® samples. In the process, we collected a large number of positive SIMS spectra, giving us statistical insight into the variability of this measurement protocol and the sources of variance.

Adventitious hydrocarbon contamination greatly influenced SIMS surface hydroxylation measurements. At high hydrocarbon loadings, the $SiOH^+/Si^+$ ratio was suppressed. There were two possible explanations for this effect. First, chemical reactions between $SiOH^+$ and H^- ions produced neutral, undetectable species.[6] Second, $SiOH^+$ ions with their low kinetic energy may penetrate the hydrocarbon overlayer less effectively than the Si^+ ions.[7] For the relatively clean samples, there was no clear correlation between their contamination levels as indicated by their $C_2H_3^+/Si^+$ ratios and $SiOH^+/Si^+$ ratios. Samples dosed with perdeuterated triacontane showed reactions between the substrate and adventitious hydrocarbons occur during ionization and enhance the $SiOH^+/Si^+$ signal. However, only a weak correlation existed between the degree of surface contamination and the magnitude of this effect. From all these findings we concluded that ToF-SIMS surface hydroxyl measurements required substantially contamination-free samples.

To calculate the samples' degree of surface hydroxylation we measured their elemental compositions. Although SIMS is rarely used for this purpose, we demonstrated good agreement between SIMS and XPS quantitative results when Eagle XG® fracture surfaces were used to derive sensitivity factors for both techniques. This finding was significant because it demonstrated that static SIMS results can be interpreted quantitatively for clean glass surfaces. We have only demonstrated this for one composition, though, and more exploration is required to understand the

type and extent of matrix effects across a broad range of glass compositions. For this reason, studies repeating these results for a range of glass compositions are still needed.

We found that HF- and HCl- Eagle XG® were generally more hydroxylated than as-received surfaces or surfaces treated with alkaline detergents. The HF- and HCl treated surfaces were also the most silica rich, as indicated by SIMS analysis in Chapter 2 and XPS analysis in Chapter 5. These results are in good agreement with previous findings that show surface silanol concentration scales with silica concentration in multicomponent glass surfaces. Because we developed a suitable method for measuring surface hydroxylation, follow-up studies can now focus on understanding how surface-mediated processes vary with hydroxyl concentration.

This study advanced the science of surface hydroxyl measurements but also presented new questions. Is there a way to remove hydrocarbon contamination from glass surfaces so this surface hydroxyl measurement method can be applied to failure analysis of production-line samples? The method is currently best suited for very clean model surfaces, but understanding the link between surface hydroxylation and other surface mediated processes may require analyzing samples with long atmospheric exposures and high-levels of adventitious contamination. Removing hydrocarbon contamination without altering the underlying surface hydroxyls is a challenge. Wet-chemical, plasma, and most sputter cleaning approaches likely alter the surface hydroxyl concentration to some degree.

Is this protocol applicable to a wide range of multicomponent glasses? Our study focused only on Eagle XG®, and though the surface composition of Eagle XG® varies dramatically as a function of chemical treatment, we did not explore other common compositions including soda-lime and sodium-borosilicates.

Can SIMS be used to detect other types of surface hydroxyls, e.g. aluminols and boronols? Although we discovered other hydroxyls in our SIMS analysis, including relatively small signals $CaOH^+$ and $AlOH^+$, it is unclear whether these signals have any quantitative value. Our analysis benefitted from previous studies on silica powder and SIMS studies on amorphous SiO_2. There is little comparable literature for aluminols, boronols, and hydroxyls associated with modifier ions. Understanding the behavior of these signals requires exploring their simple model systems, e.g., their pure oxides where possible, and simple binary and ternary silicate glasses when pure oxides are not possible.

6.2 Overarching Conclusions

Taken together, these results depict Eagle XG's surface composition, which transitions from bulk-like to silica-like at the surface. Modifier, Al, and B depletion are readily apparent in the AR-XPS data in Chapter 5. This depletion appears more severe in the more surface-sensitive SIMS elemental analyses in Chapters 2 and 4. LEIS results in Chapter 3 show absolute modifier and Al depletion at the sample surface. Accordingly, in terms of its reactivity the surface chemistry of Eagle XG® is expected to be similar to surface chemistry of SiO_2. The surface hydroxyl results in Chapter 4 support this conclusion. Leached Eagle XG® surfaces have compositions that are *ca.* 90% SiO_2 by SIMS, and give surface hydroxyl quantities in the range of 4.6 OH/nm^2. These values are similar to the value widely accepted for SiO_2. In spite of the similarity in surface composition, however, Eagle XG® appears to dehydroxylate to a lesser extent than fused silica when heated *in vacuo* to 400 °C. The as-formed Eagle XG® surface is also somewhat modified, with Al and B depleted relative to the bulk composition.

The formation of an Al-rich layer with detergent treatment is a surprise. The detergent solutions in this study had pHs of ca. 12, and should etch the Eagle XG® surface through dissolution of the silicate network.[8] This would normally give a type V surface with a composition similar to the bulk. Detergent-treated surfaces do not give modifier concentrations equivalent to the bulk in any of our analyses, though, suggesting that some degree of ion exchange occurs at the outer few nanometers of the sample. Etching possibly explains the aluminum-rich surface layer. The alkaline solution may etch through the silica-enriched layer that appears on as-formed Eagle XG® to uncover a more bulk-like layer. An alternative possibility is that some alumina precipitates from solution.[8] However, this seems unlikely, given that detergent contains chelating agents to prevent this sort of reprecipitation. A more thorough analysis of the AR-XPS data may conclusively answer this question. A thin alumina-rich layer over an alumina-depleted, silica-rich layer would indicate precipitation, while a gradual increase in aluminum from surface to bulk would imply an etching mechanism.

HF treatment also depletes modifiers from the Eagle XG® surface for the reaction conditions used in this study. This is unexpected, given that HF is an etchant and would normally produce congruent network dissolution and compositions similar to bulk Eagle XG®.[8] This suggests that some finite degree of ion exchange occurs ahead of the network dissolution front. It indicates that the surface composition of etched Eagle XG® is not always equivalent to its bulk composition.

This analysis enhanced our knowledge of display glass surface composition. It demonstrated that a multi-technique approach provides glass elemental composition at length scales ranging from the outermost atomic layer to a depth of 6-10 nm. This information is valuable because this region's composition influences surface mediated processes. In addition, sputter depth

profiles struggle to obtain this information.[9-10] The compositional knowledge we obtained is an important first step to understand surface mediated processes on display glass.

We also demonstrated that the surface sensitivity of the analytical approach is of paramount importance. For example, we would have a very different perception of Eagle XG® surface composition if we had considered only XPS results, which revealed a noticeable fraction of modifiers, Al, and B at the sample surface. In contrast, LEIS revealed that the outermost atomic layer of Eagle XG® surfaces are often entirely depleted of modifiers and Al.

We developed a protocol for measuring surface hydroxyls on multicomponent glass using ToF-SIMS. In the process, we addressed previously ignored issues including how to account for varying elemental compositions between glass samples and the influence of adventitious hydrocarbon contamination on the measurements. We showed the technique's potential, identified several remaining questions about its efficacy, and proposed additional experiments to address these concerns.

Multi-instrument surface analysis is a synergistic approach. Each technique provides different information at different length scales with different detection limits. For example, only SIMS detected some contaminants in this study, and neither XPS nor LEIS detected surface hydroxyls. However, we would have little confidence in SIMS quantitative elemental results without confirmatory data from XPS and LEIS. SIMS and XPS detect and quantify boron, but LEIS has poor detection limits for this element. Of these techniques, only SIMS provides molecular information, which is key to its ability to measure surface hydroxyls on glass surfaces. SIMS also detects large cluster ions from glass surfaces. The level of detail in compositional knowledge we obtained using a multi-instrument approach is valuable in future experiments and computational studies probing surface mediated processes on glass substrates.

6.3 References

1.   Choi, Y. S.; Yun, J. U.; Park, S. E. Flat Panel Display Glass: Current Status and Future. *Journal of Non-Crystalline Solids* **2016,** *431*, 2-7.

2.   Agnello, G.; Hamilton, J.; Manley, R.; Streltsova, E.; LaCourse, W.; Cormack, A. Investigation of Contact-Induced Charging Kinetics on Variably Modified Glass Surfaces. *Applied Surface Science* **2015,** *356*, 1189-1199.

3.   Ellison, A.; Cornejo, I. A. Glass Substrates for Liquid Crystal Displays. *International Journal of Applied Glass Science* **2010,** *1* (1), 87-103.

4.   Hamilton, L. L. Display Innovations Through Glass. *Japanese Journal of Applied Physics* **2016,** *55*, 03CA01.

5.   Crobu, M.; Rossi, A.; Mangolini, F.; Spencer, N. D. Chain-length-identification strategy in zinc polyphosphate glasses by means of XPS and ToF-SIMS. *Analytical and bioanalytical chemistry* **2012,** *403* (5), 1415-1432.

6.   Tarlov, M. J.; Evans, J. F.; Newman, J. G. Static SIMS and XPS study of water plasma exposed tin oxide films. *Applied surface science* **1993,** *64* (2), 115-125.

7.   Delcorte, A.; Bertrand, P.; Arys, X.; Jonas, A.; Wischerhoff, E.; Mayer, B.; Laschewsky, A. ToF-SIMS study of alternate polyelectrolyte thin films: Chemical surface characterization and molecular secondary ions sampling depth. *Surface Science* **1996,** *366* (1), 149-165.

8.   Hench, L.; Clark, D. E. Physical chemistry of glass surfaces. *Journal of Non-Crystalline Solids* **1978,** *28* (1), 83-105.

9.   Mahoney, C. M., *Cluster secondary ion mass spectrometry: principles and applications*. John Wiley & Sons: 2013; Vol. 44.

10.   Van der Heide, P., *Secondary ion mass spectrometry: an introduction to principles and practices*. John Wiley & Sons: 2014.

Appendix 1: Supporting Information for Chapter 2

Table A1.1. Peak masses from the positive and negative ion spectra and proposed assignations.

Positive Species		Negative Species	
Mass	Proposed assignation	Mass	Proposed assignation
1.008	H^+	1.009	H^-
7.016	Li^+	10.014	$^{10}B^-$
10.013	$^{10}B^+$	11.010	B^-
11.009	B^+	15.996	O^-
12.017	BH^+	17.005	OH^-
13.025	BH_2^+	17.999	H_2O^-
15.995	O^+	18.999	F^-
16.019	NH_2^+	19.007	H_3O^-
17.003	OH^+	26.004	CN^-
17.027	NH_3^+	27.004	BO^-
18.010	H_2O^+	27.977	Si^-
19.020	H_3O^+	28.985	SiH^-
22.990	Na^+	29.974	$^{30}Si^-$
23.986	Mg^+	29.984	$^{29}SiH^-$
24.986	$^{25}Mg^+$	29.993	SiH_2^-
24.993	MgH^+	30.982	$^{30}SiH^-$
25.983	$^{26}Mg^+$	31.972	S^-
26.982	Al^+	31.990	O_2^-
27.977	Si^+	32.981	HS^-
28.975	$^{29}Si^+$	32.997	O_2H^-
28.984	$SiH+$	34.970	Cl^-
29.972	$^{30}Si^+$	36.966	$^{37}Cl^-$
29.983	$^{29}SiH^+$	42.002	$^{10}BO_2^-$
29.992	SiH_2^+	42.976	AlO^-
30.981	$^{30}SiH^+$	43.001	BO_2^-
31.001	SiH_3^+	43.972	SiO^-
31.989	$^{30}SiH_2^+$	44.980	$SiHO^-$
32.001	$^{29}SiH_3^+$	45.969	$^{30}SiO^-$
32.998	O_2H^+	45.979	$^{29}SiHO^-$
38.965	K^+	45.994	NO_2^-

38.986	NaO^+	47.967	SO^-
39.963	Ca^+	58.972	AlO_2^-
40.971	CaH^+	58.994	$SiCH_3O^-$
40.986	$MgOH^+$	59.969	SiO_2^-
43.954	$^{44}Ca^+$	60.974	$SiHO_2^-$
43.970	SiO^+	62.971	$^{30}SiHO_2^-$
43.984	$AlOH^+$	63.966	SO^{2-}
44.981	$SiHO^+$	74.991	$SiCH_3O_2^-$
46.977	$^{30}SiHO^+$	75.964	SiO_3^-
46.996	SiH_3O^+	76.972	$SiHO_3^-$
47.951	Ti^+	78.918	Br^-
54.011	$MgBOH_3^+$	78.967	$_{30}SiHO_3^-$
54.987	SiH_3Mg^+	79.968	SO_3^-
55.957	CaO^+	86.948	SiO_2Al^-
56.968	$CaOH^+$	91.957	SiO_4^-
57.973	CaH_2O^+	92.965	HO_4Si^-
59.950	$^{44}CaO^+$	101.970	$AlBO_4^-$
59.965	SiO_2^+	102.943	SiO_3Al^-
59.980	AlO_2H^+	102.967	SiO_4B^-
60.959	$^{44}CaOH^+$	103.941	$Si_2O_3^-$
60.975	$SiHO_2^+$	103.966	$Al_2O_3H_2^-$
60.988	$AlH_2O_2^+$	117.944	$Al_2O_4^-$
61.983	$SiH_2O_2^+$	118.939	SiO_4Al^-
62.992	$SiH_3O_2^+$	119.935	$Si_2O_4^-$
63.945	S_2^+	120.939	$Si_2HO_4^-$
63.962	Mg_2O^+	131.919	$Si_3O_3^-$
63.979	$^{30}SiH_2O_2^+$	132.926	$Si_3HO_3^-$
66.965	TiH_3O^+	135.929	$Si_2O_5^-$
66.988	SiC_2HN^+	136.938	$Si_2HO_5^-$
67.938	$SiCa^+$	158.922	$Si_3O_4B^-$
67.957	$SiOMg^+$	162.908	$Si_2O_5Al^-$
68.965	$SiHOMg^+$	162.935	$Si_2O_6B^-$
70.954	$SiOAl^+$	176.914	$Al_3O_6^-$
71.949	Si_2O^+	177.911	$SiO_6Al_2^-$
72.956	Si_2HO^+	178.906	$Si_2O_6Al^-$
74.933	$CaCl^+$	179.904	$Si_3O_6^-$

77.979	$SiH_2O_3^+$	180.903	$Si_3HO_6^-$
78.987	$SiH_3O_3^+$	195.895	$Si_3O_7^-$
80.966	$Mg_2O_2H^+$	196.903	$Si_3HO_7^-$
82.939	$CaAlO^+$	236.880	$SiO_8Al_3^-$
82.963	$CaBO_2^+$	237.876	$Si_2O_8Al_2^-$
82.983	$MgBO_3^+$	238.872	$Si_3O_8Al^-$
83.055	$BO_4H_8^+$	239.870	$Si_4O_8^-$
83.935	$SiOCa^+$	240.869	$Si_4HO_8^-$
83.955	SiO_2Mg^+	255.861	$Si_4O_9^-$
83.990	$Mg_2O_2H_4^+$	256.868	$Si_4HO_9^-$
84.942	$SiHOCa^+$	294.826	$Si_5O_8Al^-$
84.962	$SiHO_2Mg^+$	296.840	$Si_2Al_3O_{10}^-$
84.999	$Mg_2O_2H_5^+$	297.840	$Si_3Al_2O_{10}^-$
85.908	$^{86}Sr^+$	298.838	$Si_4O_{10}Al^-$
86.975	$^{87}Sr^+$	299.837	$Si_5O_{10}^-$
87.905	Sr^+	300.833	$Si_5HO_{10}^-$
87.944	$Si_2O_2^+$	315.822	$Si_5O_{11}^-$
88.914	SrH^+	316.834	$Si_5HO_{11}^-$
88.952	$Si_2HO_2^+$	354.794	$Si_6O_{10}Al^-$
95.922	Ca_2O^+	357.802	$Si_4Al_2O_{12}^-$
96.929	Ca_2OH^+	358.800	$Si_5AlO_{12}^-$
97.971	$Al_2BO_2H^+$	359.799	$Si_6O_{12}^-$
99.931	SiO_2Ca^+	360.796	$Si_6O_{12}H^-$
100.939	$SiHO_2Ca^+$	376.798	$Si_6O_{13}H^-$
100.957	$SiHO_3Mg^+$	418.766	$Si_6AlO_{14}^-$
101.903	$^{86}SrO^+$		
102.912	$^{86}SrOH^+$		
103.902	SrO^+		
104.910	$SrOH^+$		
104.949	$Si_2HO_3^+$		
110.980	$CaB_2O_3H^+$		
111.915	$Ca_2O_2^+$		
112.924	$Ca_2O_2H^+$		
114.955	$CaBO_4^+$		
115.926	SiO_3Ca^+		
116.935	$SiHO_3Ca^+$		

119.902	Sn^+
136.906	$SnOH^+$
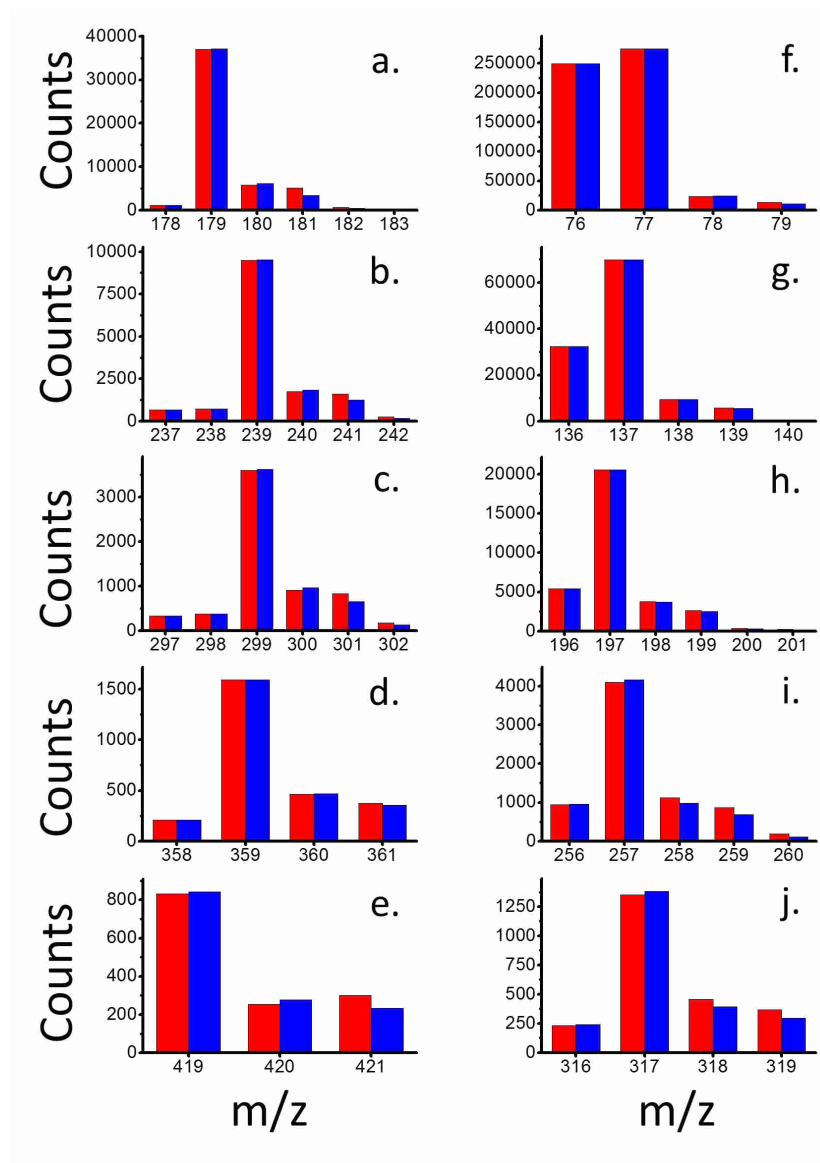
Figure A1.1. Classical least squares fit of isotope ratios (blue) to integrated peak areas from untreated Eagle XG® (red) for selected isotope clusters. (a.) SiO_3H^-, (b) $Si_2O_5H^-$, (c) $Si_3O_7H^-$, (d) $Si_4O_9H^-$, (e) $Si_5O_{11}H^-$, (f) $Si_2AlO_6^-$, (g) $Si_3AlO_8^-$, (h) $Si_4AlO_{10}^-$, (i) $Si_5AlO_{12}^-$, and (j) $Si_6AlO_{14}^-$ (labeled according to the most prominent peak in each cluster).
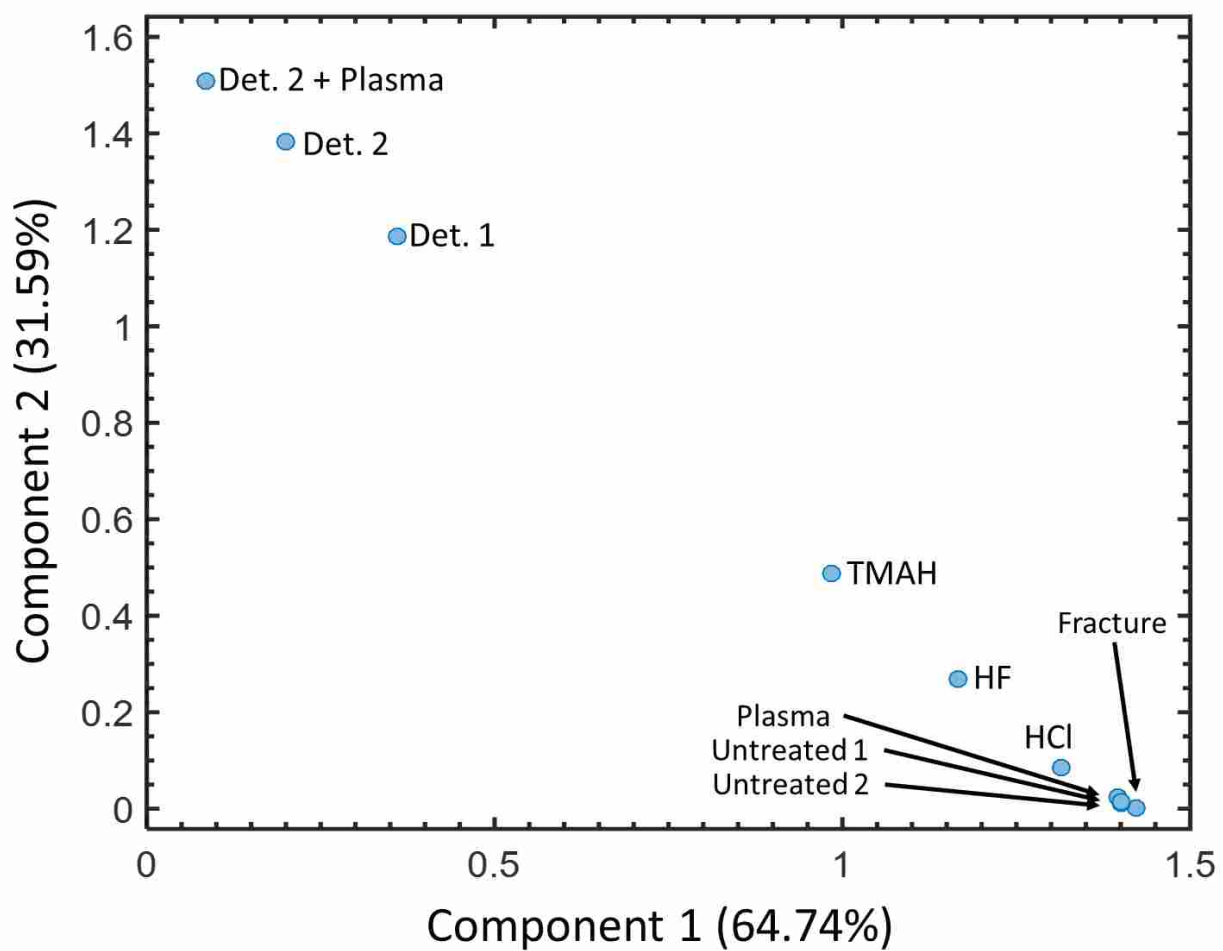
Figure A1.2. Two-component MCR analysis scores plot for elemental species. The loadings for the pure component spectra are shown in Appendix 1, Figure A1.3.
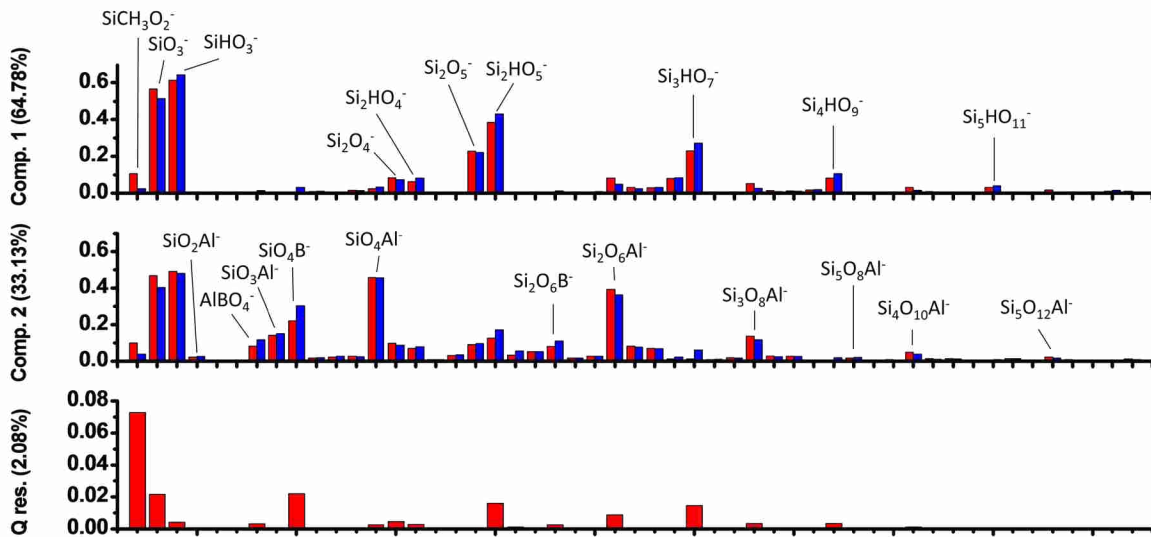
Figure A1.3. Loadings and Q residuals for two-component MCR of negative cluster ions, shown in Figure A1.9. (Top) Component 1 loadings (red) compared to preprocessed data for 'HCl' sample (blue). (Middle) Component 2 loadings (red) compared to preprocessed data for 'Fracture' sample (blue). (Bottom) Q residuals.
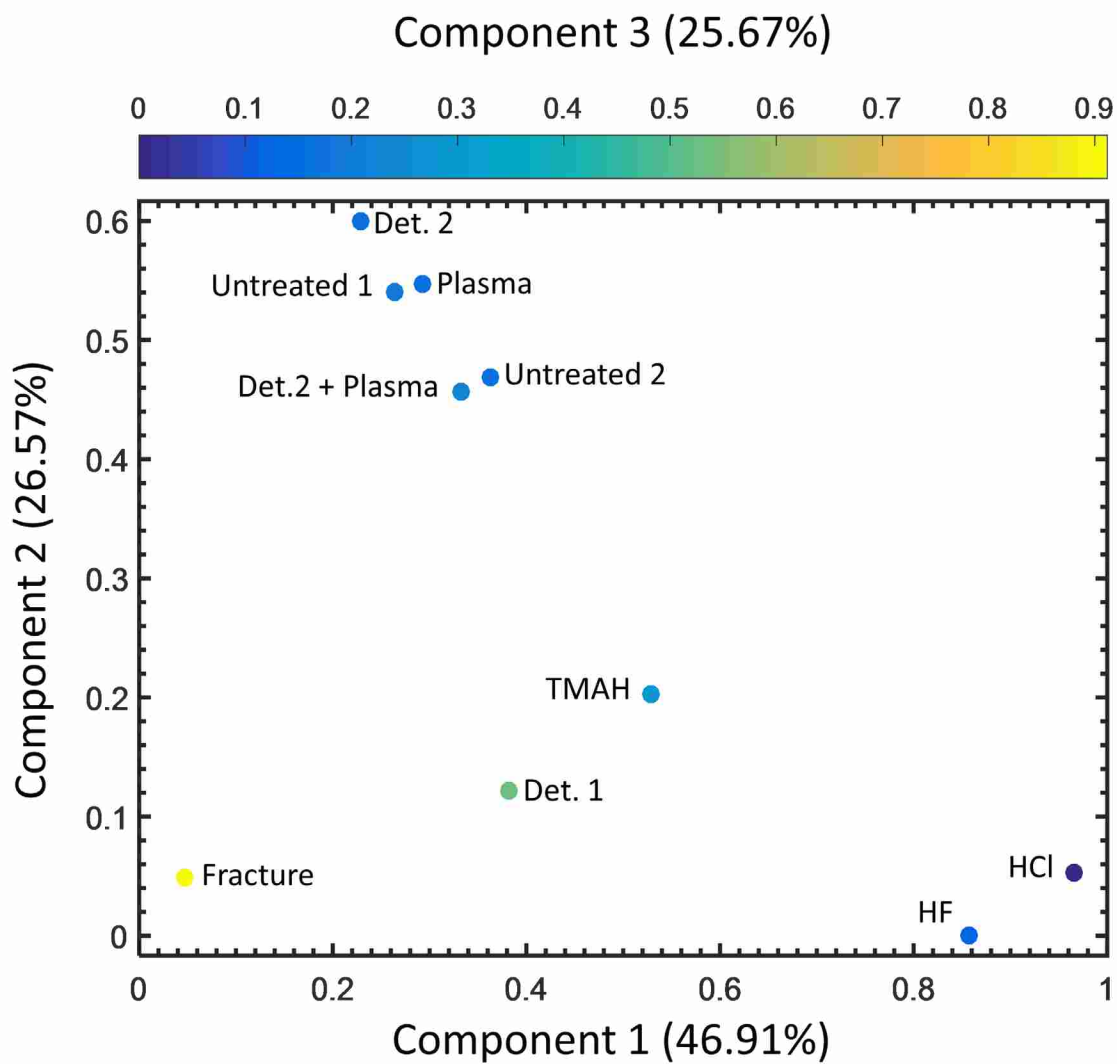
Figure A1.4. Scores for three component MCR of high mass negative cluster ions. The loadings for the pure components are shown in Figure A1.5.
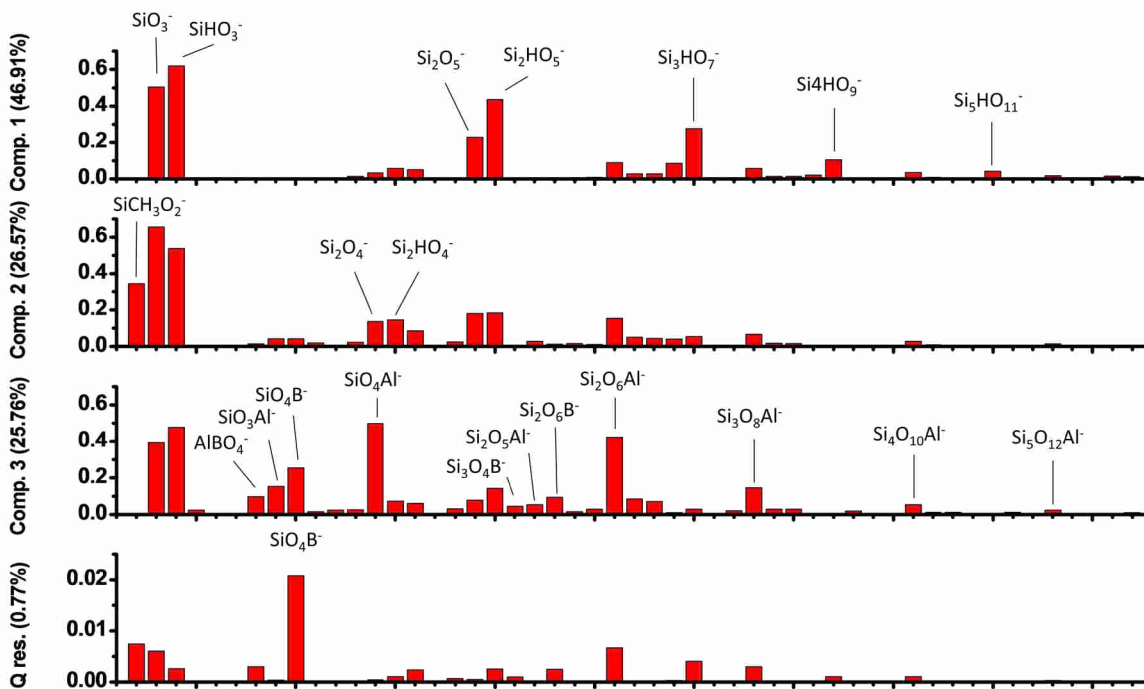
Figure A1.5. Loadings for 3 component MCR of negative cluster ions shown in Figure A1.4, with prominent peaks labeled.
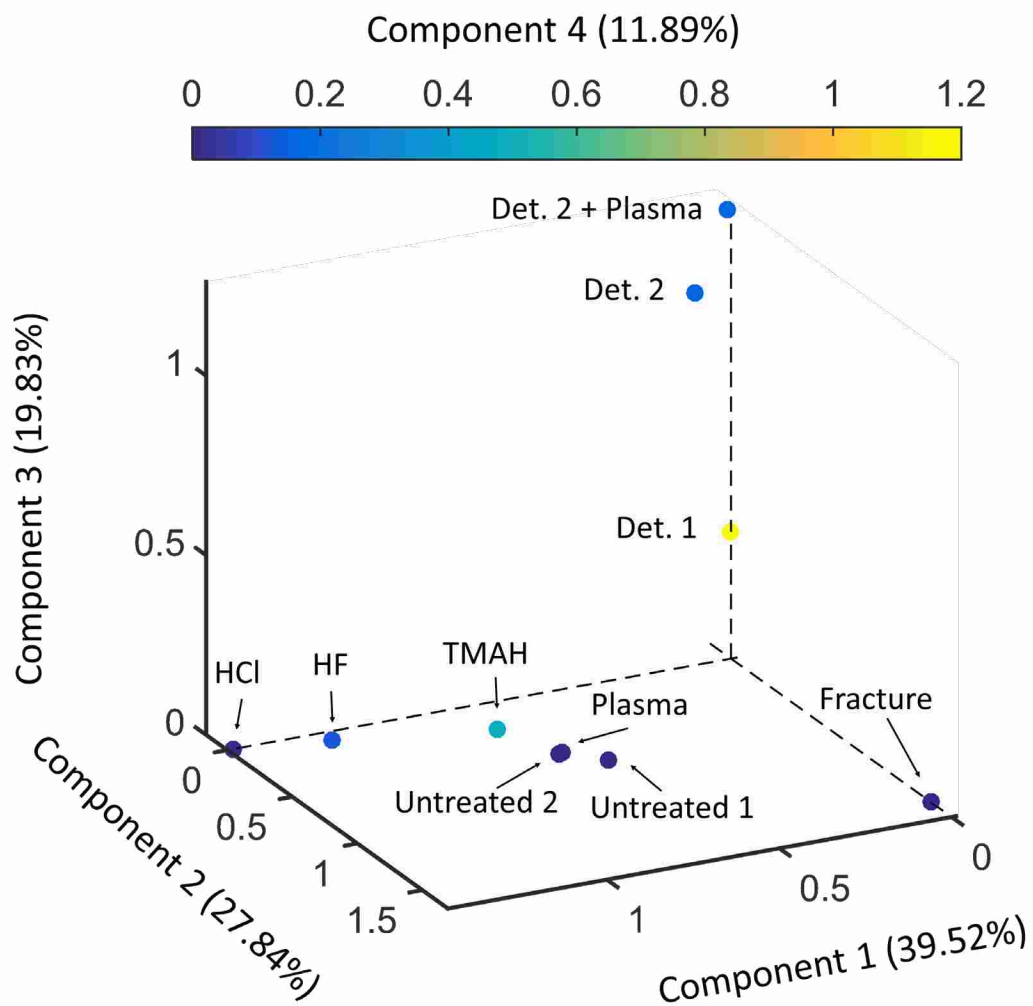
Figure A1.6. Scores for 4 component MCR analysis of all integrated peaks. The loadings for the pure components are shown in Figure A1.7.
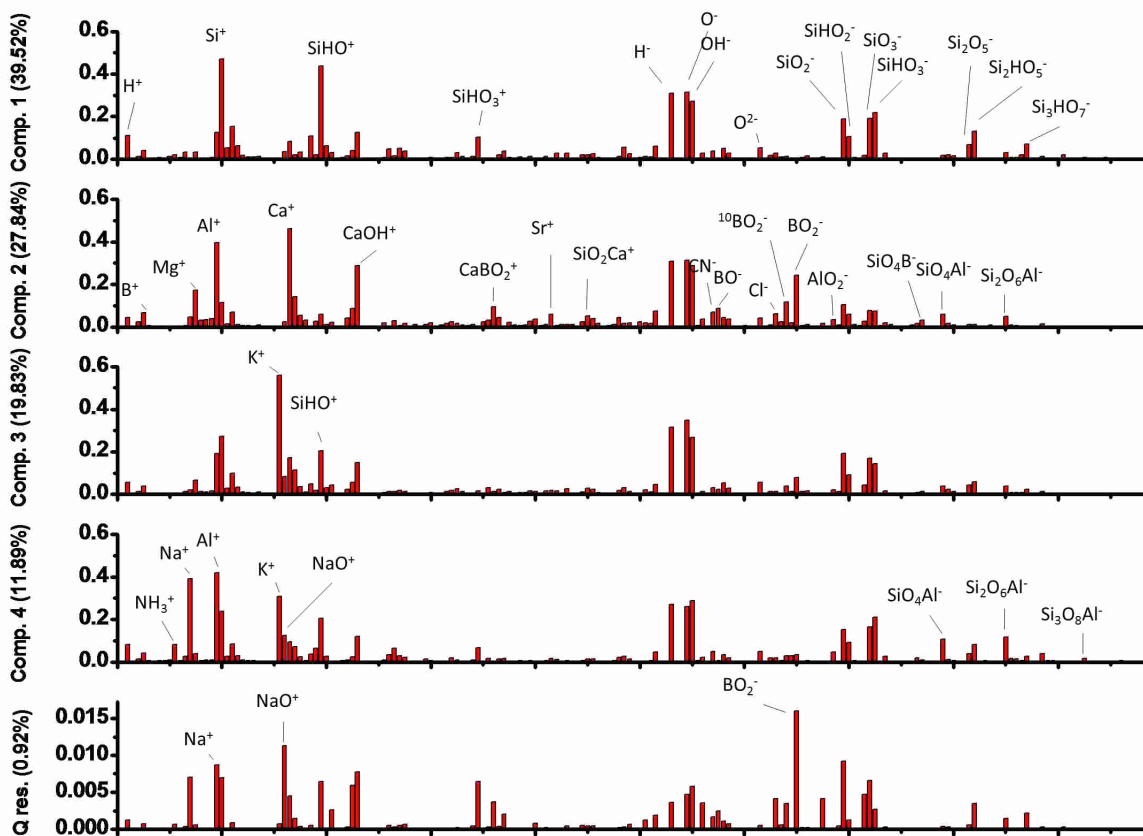
Figure A1.7. Loadings for 4 component MCR analysis of all integrated peaks shown in Figure A1.6. Prominent peaks are labeled.
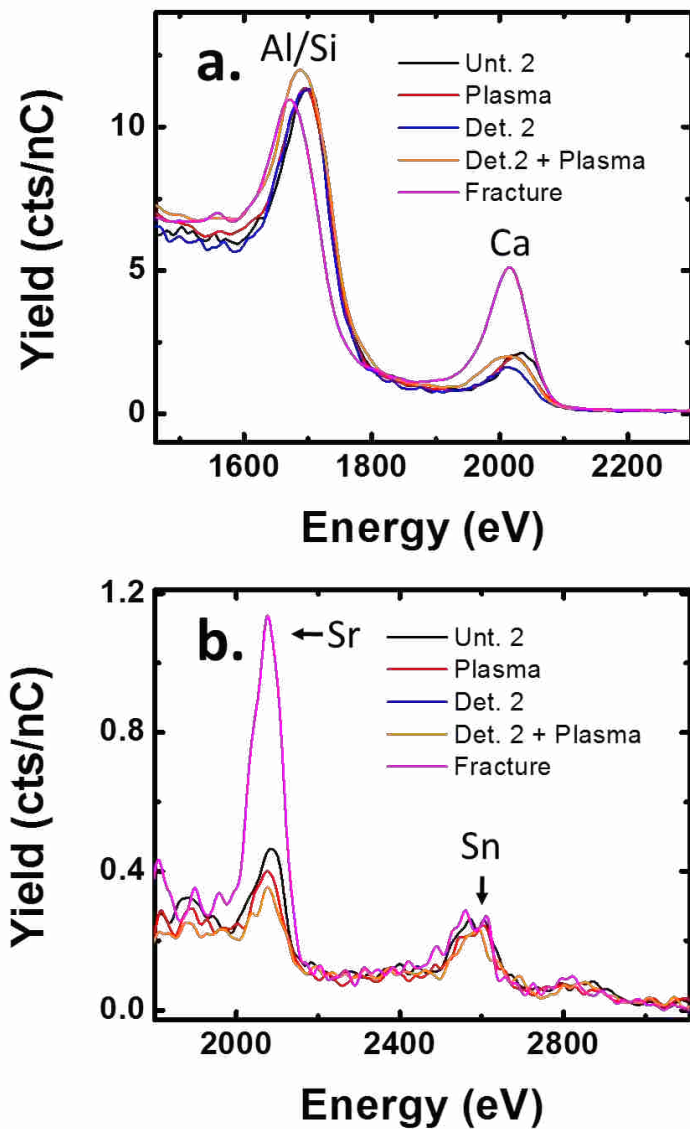
Figure A2.1. (a) 3 keV ^{4}He$^+$ LEIS spectra for samples treated with detergent and/or atmospheric plasma compared to an untreated melt surface and a fracture surface. (b) 5 keV Ne$^+$ LEIS spectra for the same samples.
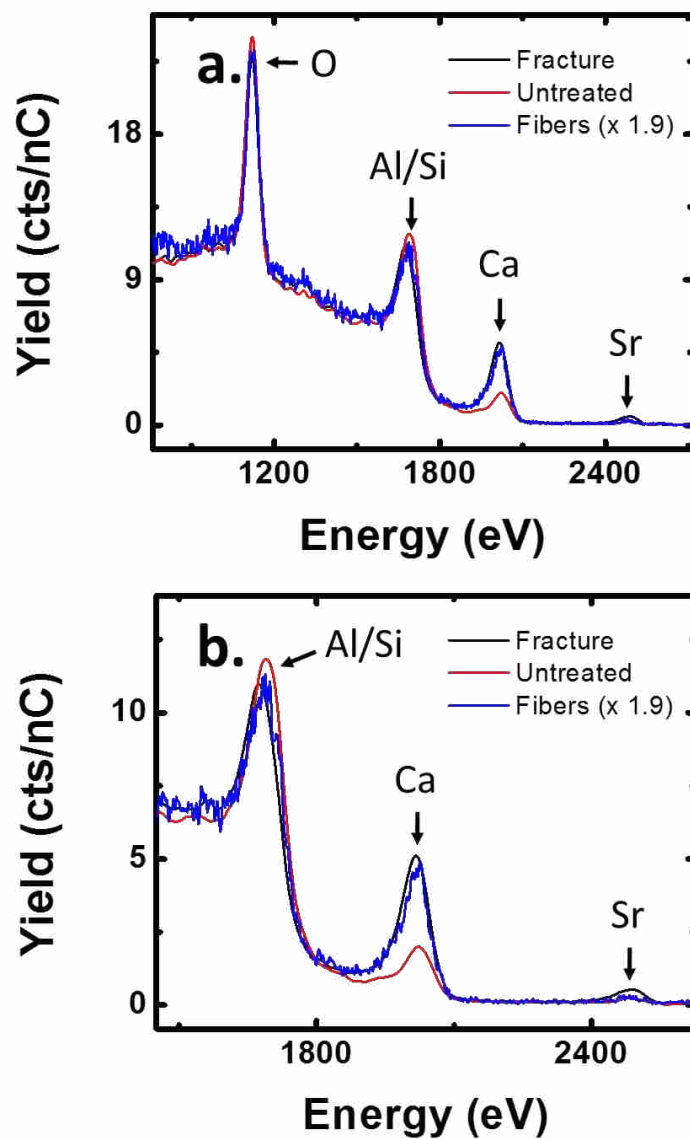
Figure A2.2. (a.)3 keV $^4He^+$ LEIS spectra comparing Fracture, Untreated, and Fiber samples. (b.) A zoomed-in view showing the Al.Si, Ca, and Sr peaks. A geometry factor of 1.9 has been applied to the Fiber spectrum as dicussed in the Experimental section.
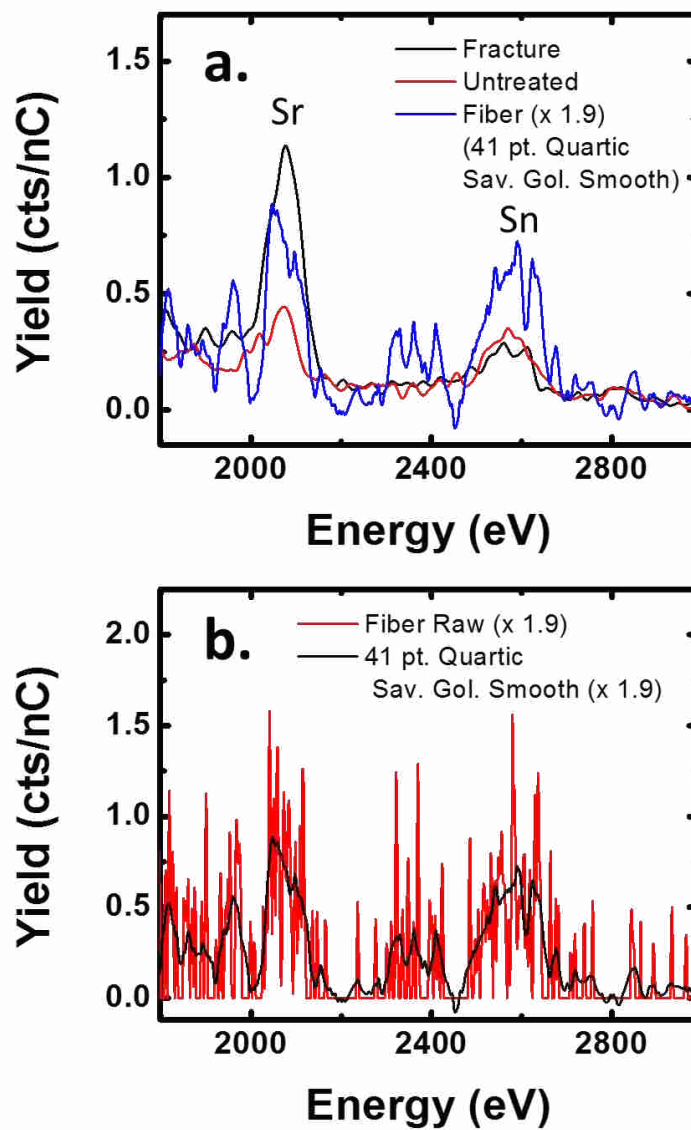
Figure A2.3. (a) 5 keV Ne[+] spectra, comparing Fiber, Fracture, and Untreated Surfaces. (b) Raw 5 keV Ne[+] spectrum for the Fiber surface compared to the Savitsky-Golay-smoothed data.
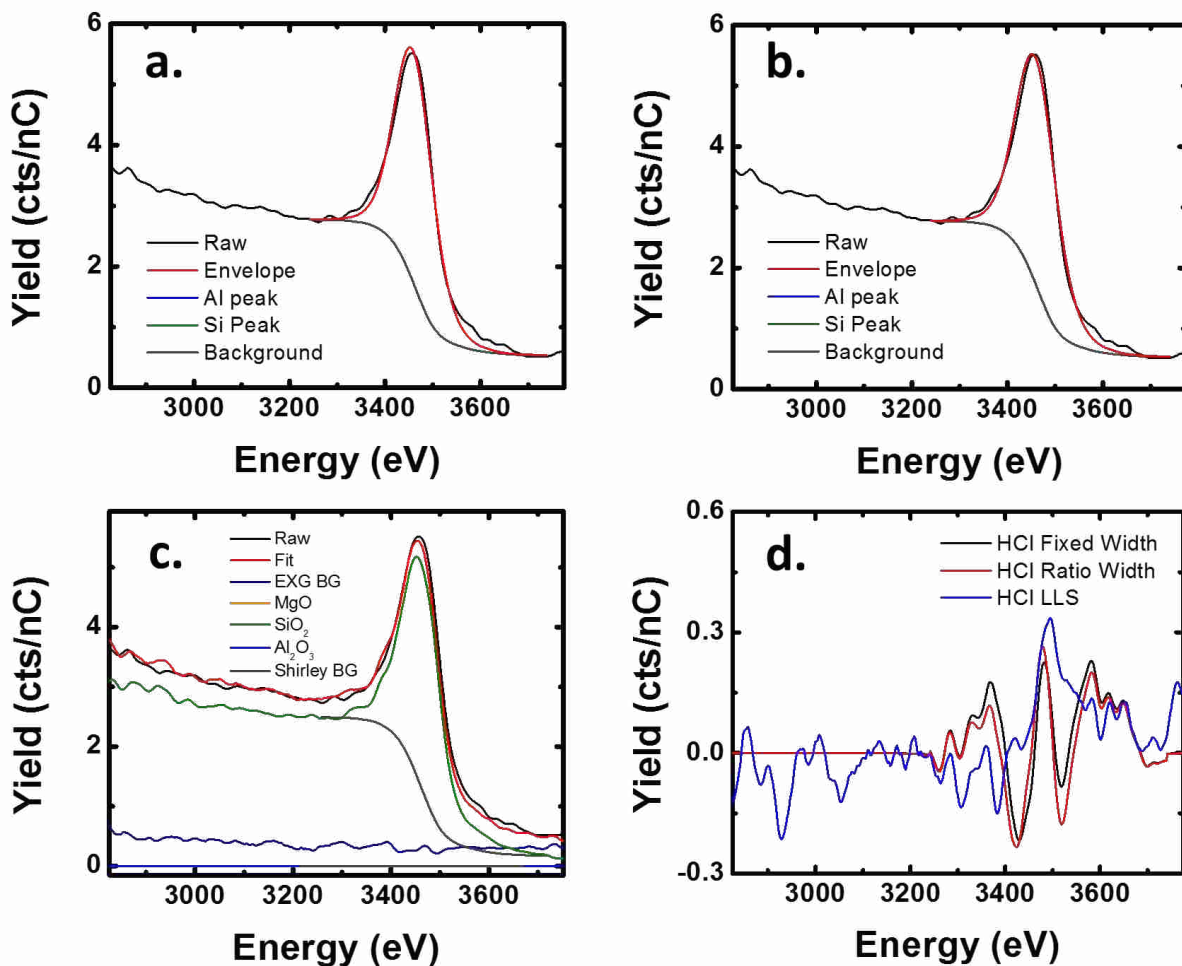
Figure A2.4. Fits for the Al/Si peak for HCl-treated Eagle XG®. (a) Synthetic peak fitting with positions and widths fixed to fits from reference materials. (b) Synthetic peak fitting based on reference materials, with peak widths set to a fixed ratio relative to the oxygen peak. (c) ISMA LLS fits, using the basis spectra shown in Figure A2.10. (d) Residuals for all three methods.
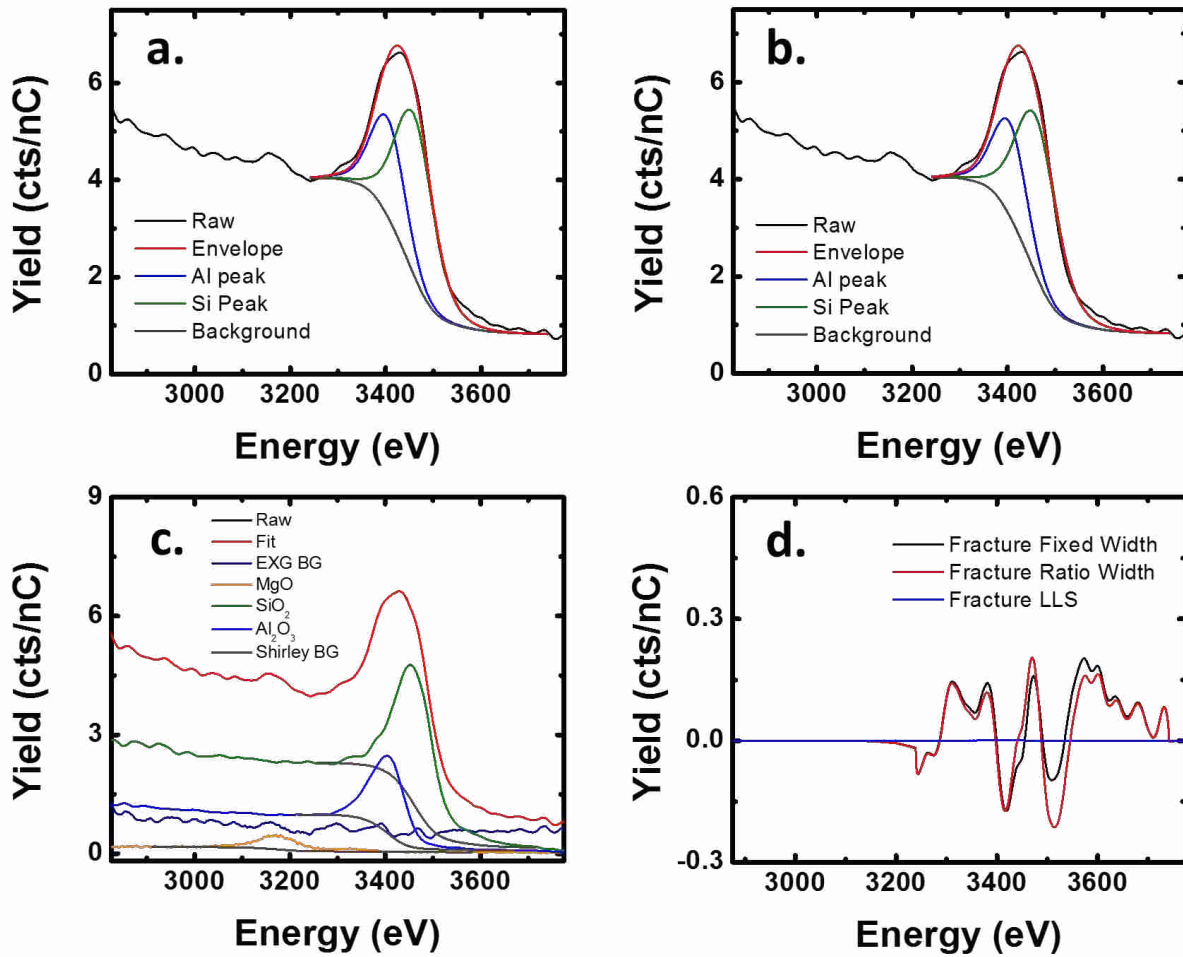
Figure A2.5. Fits for the Al/Si peak forEagle XG® Fracture surface. (a) Synthetic peak fitting with positions and widths fixed to fits from reference materials. (b) Synthetic peak fitting based on reference materials, with peak widths set to a fixed ratio relative to the oxygen peak. (c) ISMA LLS fits, using the basis spectra shown in Figure A2.10. (d) Residuals for all three methods. Here, the residuals for the ISMA LLS fits are null because the Fracture surface was used to derive one of the basis sets.

274

A3.1 Image Analysis for HF-Treated Eagle XG®, Ramped to 400 °C

This sample's elemental composition varied as a function of sample position, as shown in Figure 5.11b of the main document. A correspondingly high variance in the SiOH+/Si+ ratio can be seen in Figure 5.18b.

We converted several of the positive ion spectra from this sample into SIMS images, which are shown in Figures A3.1-A3.6. In selecting samples to display here, we were most interested in samples that displayed Ca^+-rich and Ca^+-poor regions in a single spectrum, such that we were capable of observing boundaries between these regions. Na^+ and $C_3H_7^+$ are also imaged. These species are not native to Eagle XG®, and are most likely from adventitious hydrocarbon. Some of these regions also shown Na^+-rich and hydrocarbon-rich regions can be observed. In some cases, hydrocarbon-rich regions correspond to Ca^+ rich regions, suggesting that some of the Ca we detected may have also come from adventitious sources for this sample.

We have not made an attempt to display images from all spectra. Each figure notes the timestamp at which the spectrum was recorded and the sample coordinates.

These figures also show the Si^+ and Ca^+ spectra reconstructed from Ca^+-rich and Ca^+ poor regions of interest (ROIs). The ROIs used to construct these spectra are shown in the figures. We have normalized these spectra according to their Si^+ peak areas, such that differences in the relative intensities of the Ca^+ signals are easily observed. In some cases, Na^+ peak intensities from ROI spectra are also shown.

We note that these images are the result of a retrospective analysis. Of our data, and that the analysis conditions were optimized to achieve optimal mass resolution rather than optimal lateral resolution. The images were recorded with the primary beam set in high-current bunched mode. This mode affords optimal mass resolution and relatively poor spatial resolution. Beam spot size is estimated at 7μm. Pixel-binning in these images was set at 4 pixels to achieve reasonable signal to noise. The images themselves have nominal dimensions of 200 x 200 μm^2 and a resolution of 128 x 128 pixels. i.e., the spot size is much larger than the pixel size, giving poor overall spatial resolution. In spite of these limitations, Ca^+ rich regions are readily observed, generally corresponded to regions that are also high in $C_3H_7^+$.
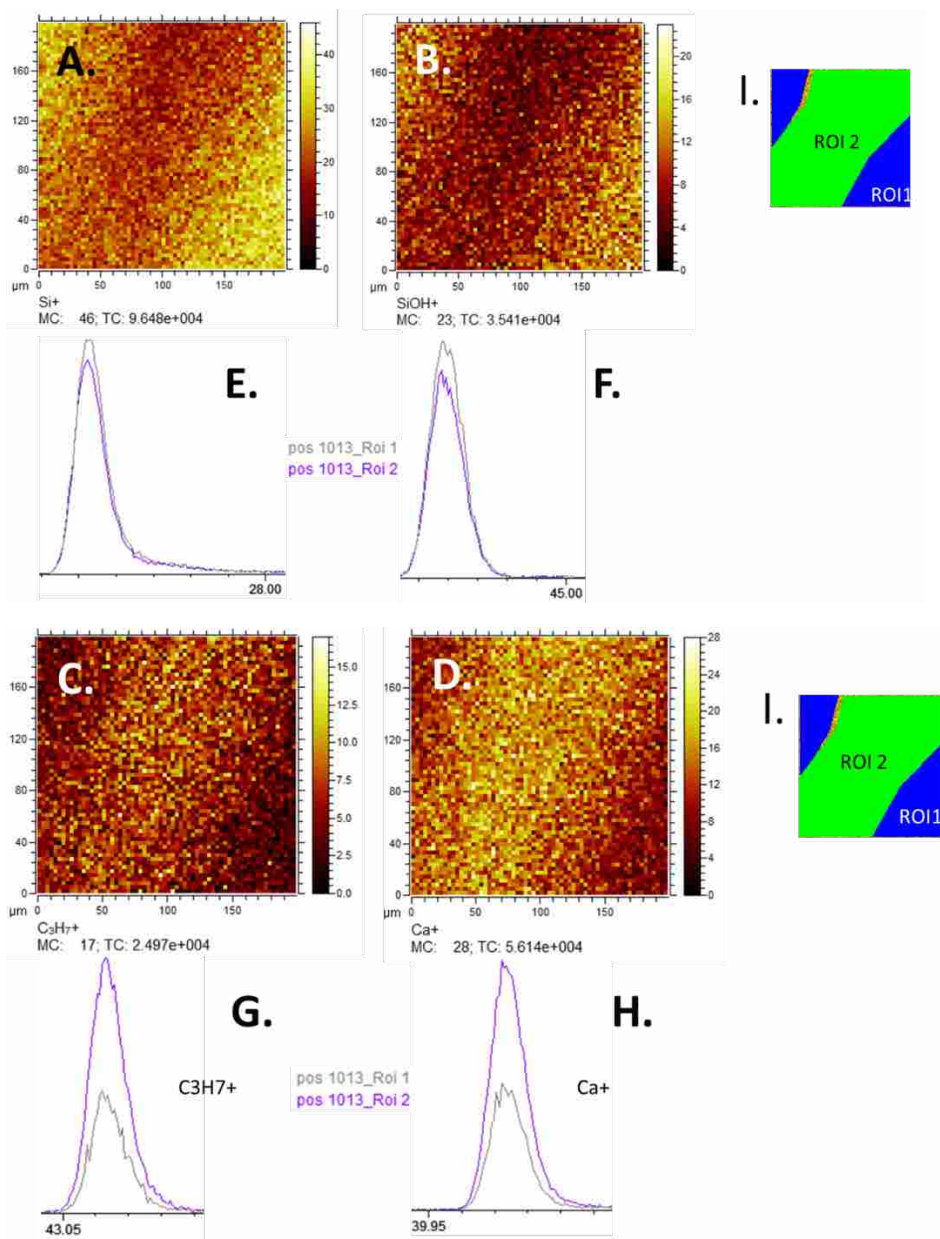
Figure A3.1. Spectrum taken at 10:13 AM at coordinates X: 0.3674mm and Y: 19.9762mm. Spectral images of Si^+(A), $SiOH^+$(B), $C_3H_7^+$(C), and Ca^+(D) are shown. Peaks corresponding to areas of the regions of interest (I) for each species are shown with (E) Si^+, (F) $SiOH^+$, (G) $C_3H_7^+$, (H) Ca^+. ROI 1 is shown as a grey peak, while ROI 2 is shown as a purple peak.
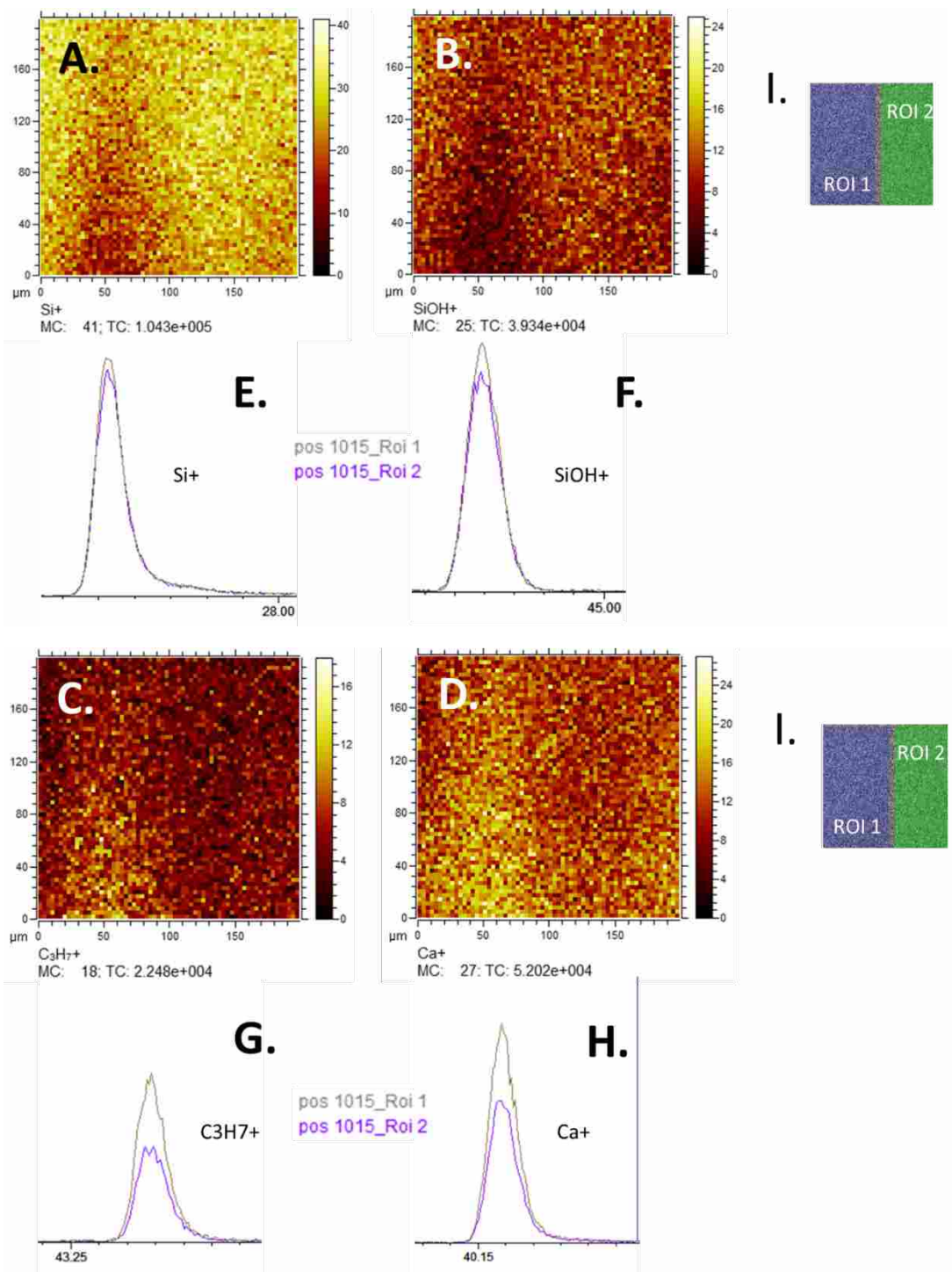
Figure A3.2. Spectrum taken at 10:15 AM at coordinates X: 0.3646mm and Y: 19.7804mm. Spectral images of Si^+(A), $SiOH^+$(B), $C_3H_7^+$(C), and Ca^+(D) are shown. Peaks corresponding to areas of the regions of interest (I) for each species are shown with (E) Si^+, (F) $SiOH^+$, (G) $C_3H_7^+$, (H) Ca^+. ROI 1 is shown as a grey peak, while ROI 2 is shown as a purple peak.
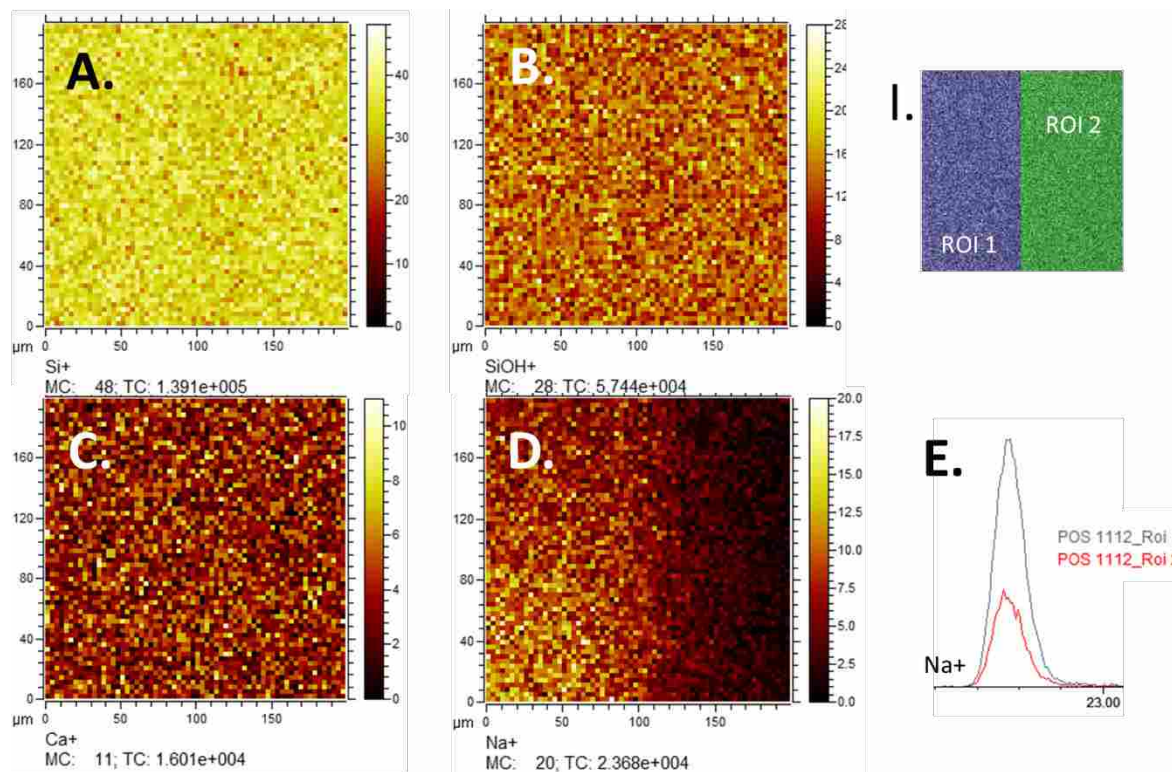
Figure A3.3. Spectrum taken at 11:12 AM at coordinates X: -0.0284mm and Y: 20.3901mm. Spectral images of Si^+(A), $SiOH^+$(B), Ca^+(C), and Na^+(D) are shown. Peaks corresponding to areas of the regions of interest (I) for Sodium are shown (E). ROI 1 is shown as a grey peak, while ROI 2 is shown as a red peak.
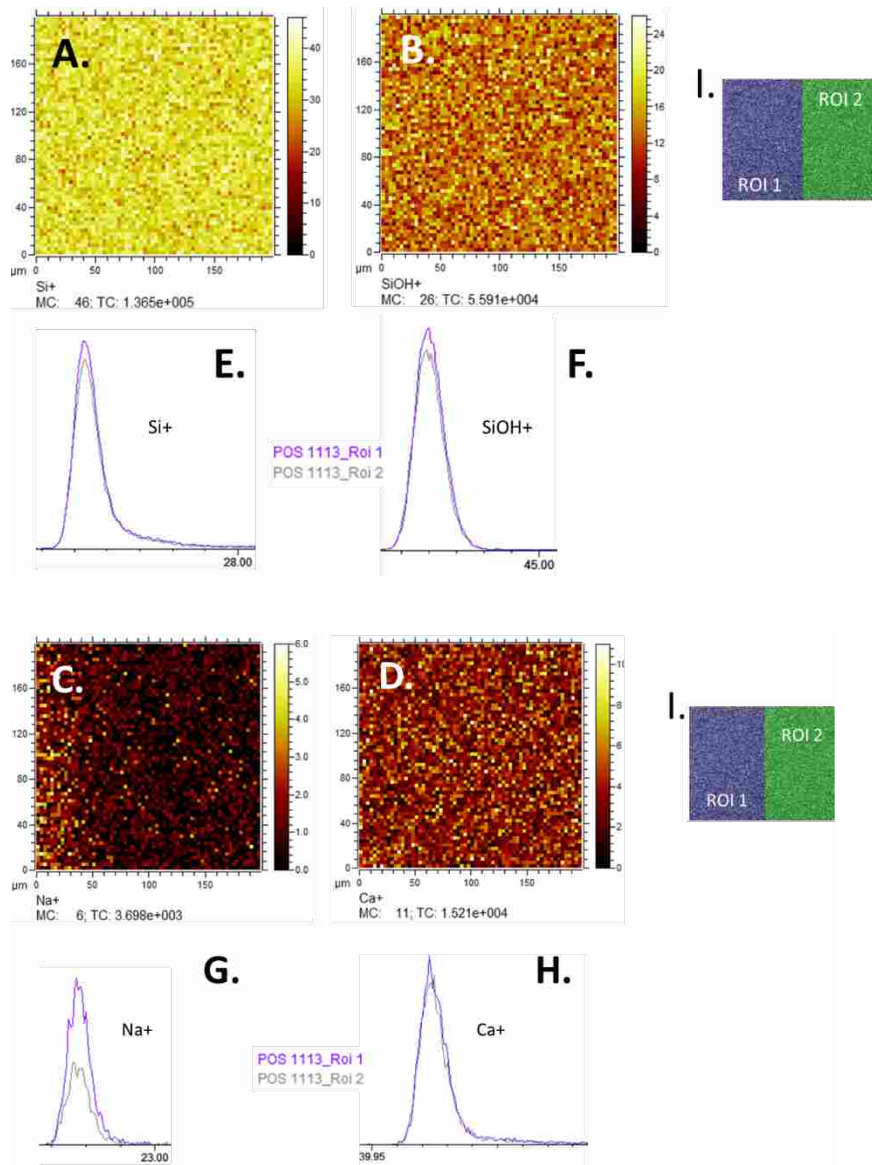
Figure A3.4. Spectrum taken at 11:13 AM at coordinates X: 0.1654mm and Y: 20.3870mm. Spectral images of Si$^+$(A), SiOH$^+$(B), Na$^+$(C), and Ca$^+$(D) are shown. Peaks corresponding to areas of the regions of interest (I) for each species are shown with (E) Si$^+$, (F) SiOH$^+$, (G) Na$^+$, (H) Ca$^+$. ROI 1 is shown as a grey peak, while ROI 2 is shown as a purple peak.
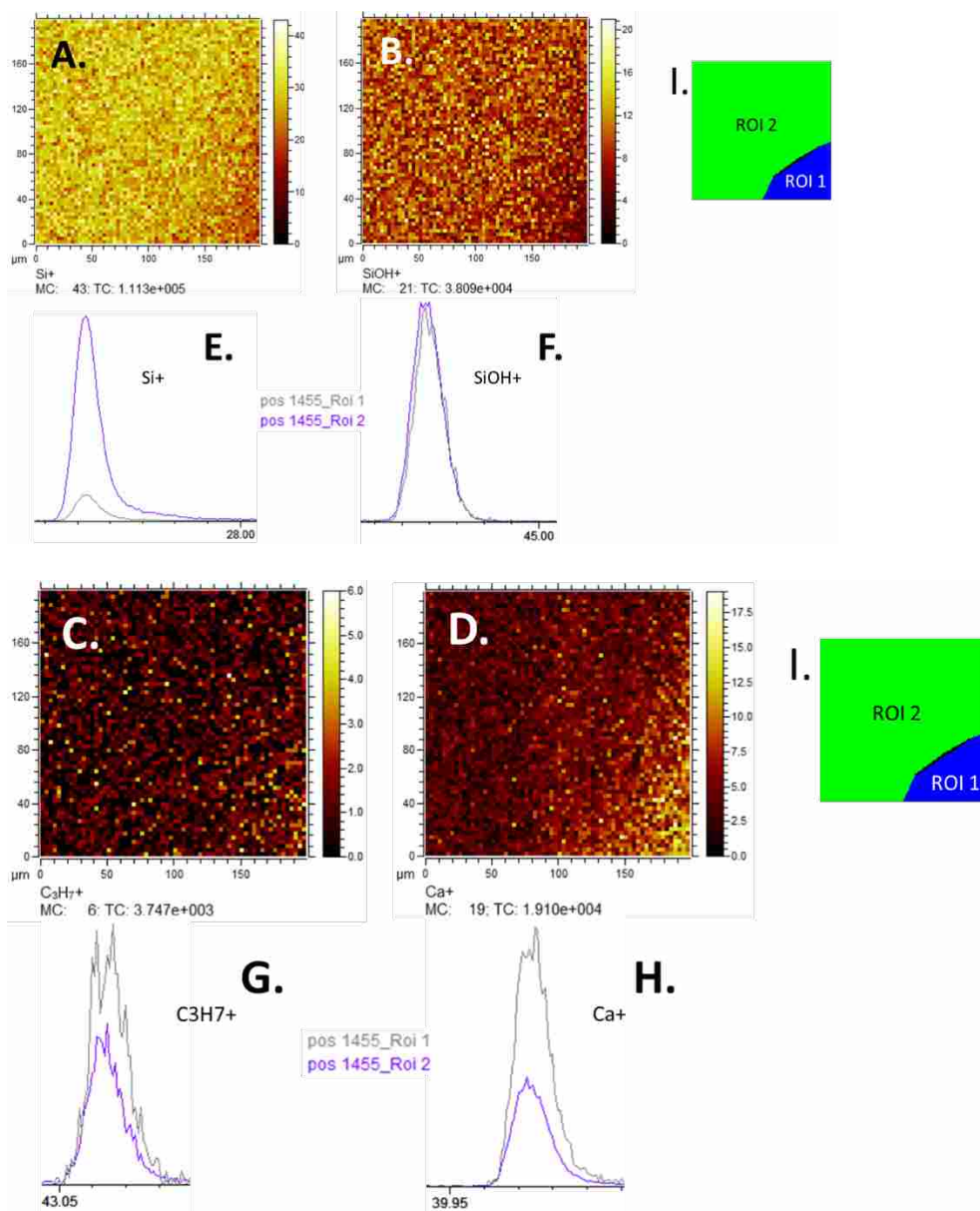
Figure A3.5. Spectrum taken at 2:55 PM at coordinates X: 0.7596mm and Y: 19.589mm. Spectral images of Si^+(A), $SiOH^+$(B), $C_3H_7^+$(C), and Ca^+(D) are shown. Peaks corresponding to areas of the regions of interest (I) for each species are shown with (E) Si^+, (F) $SiOH^+$, (G) $C_3H_7^+$, (H) Ca^+. ROI 1 is shown as a grey peak, while ROI 2 is shown as a purple peak.
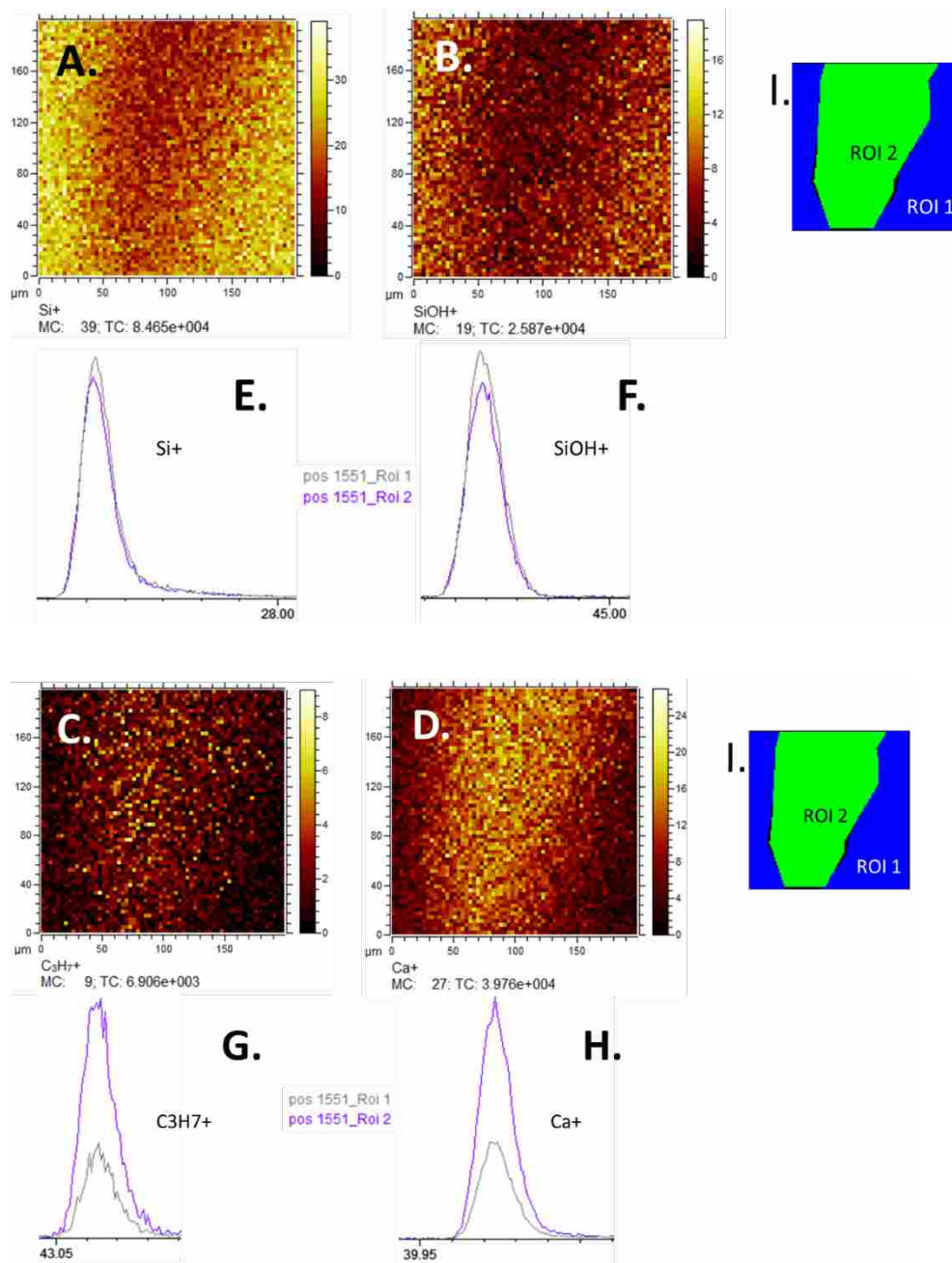
Figure A3.6. Spectrum taken at 3:51 PM at coordinates X: -0.629mm and Y: 19.3744mm. Spectral images of Si^+(A), $SiOH^+$(B), $C_3H_7^+$(C), and Ca^+(D) are shown. Peaks corresponding to areas of the regions of interest (I) for each species are shown with (E) Si^+, (F) $SiOH^+$, (G) $C_3H_7^+$, (H) Ca^+. ROI 1 is shown as a grey peak, while ROI 2 is shown as a purple peak.

A3.2 Acknowledgement of Outliers

Some outliers were removed from the data prior to analysis. Table A3.1 is a list of the datasets from which outliers were removed. We performed follow-up analysis inasmuch as we were able to understand why these data points may have deviated from the rest, and the causes for deviation are listed in the table inasmuch as we could find them.

During data acquisition, we recorded mass resolution, reflector voltage, and instrument count rate as a first-pass indicator that the instrument was performing to specification. The instrument also automatically records important information, including various instrument voltages and sample coordinates, which were helpful in explaining the cause of outlying data points.

Table A3.1. A list of outliers removed from data sets prior to analysis.

Sample	# of outliers	Reason
TR 4	4	Noted severely low count rates, suggesting incorrect instrument settings
FQ HCl 3	2	One sample was taken with the heating element still on. The other had low resolution due to sample charging.
FQ HF 1	1	Spot with intense sodium signal, suggesting contamination
EXG Det 2	4	Spectra taken too close to sample edge
EXG HCl 2	1	Cause unknown. Sample fails Q test.
EXG HCl 3	2	Severely low count rates, suggesting incorrect instrument settings
EXG U 3	2	Lower than average counts, reflector voltage lower than normal

Appendix 4: Eagle XG® Glass: Optical Constants from 196 – 1688 nm (0.735 – 6.32 eV) by Spectroscopic Ellipsometry

A4.1 Statement of Attribution

Surface Science Spectra is a peer-reviewed spectra data base. Accordingly, this document is formatted to present much of the data in tabular format.. We have omitted some information fields from this document to improve its readability in this format. We refer readers to the original document for complete sample and instrument information. We have also presented some information in paragraph format instead of tabular format as in the original publication.

A4.2 Abstract

Corning® Eagle XG® glass is widely used in the manufacture of electronic displays. In a previous submission, we provided its optical constants from 230 – 1690 nm (0.73 – 5.39). This spectral range reflected the fact that for a thickness of 0.5 mm the material had zero transmission below 230 nm. These previously reported optical constants relied on a simple curve fitting approach that consisted of pole-pole (Sellmeier), Tauc-Lorentz (T-L), and Gaussian oscillators. However, while the model agreed well with the experimental data over the selected spectral range, when extrapolated to shorter wavelengths it showed a sharp decrease in absorption, which seemed

physically unreasonable. To improve upon the previous model, we have now obtained transmission data down to 196 nm using thin (100 and 200 μm) samples. Using this data, the optical constants were modeled using a T-L oscillator, 2-3 Gaussian oscillators, and a pole in the infrared. The center energies of the Gaussian oscillators corresponded approximately to previously reported absorptions from iron and tin in silicate glasses, and the band gap of the T-L oscillator was fixed at 5.8 eV, corresponding approximately to previously reported values of the onset of intrinsic absorptions. The resonance energy of the T-L oscillator was initially fixed at 12 eV following published values for fused silica, after which it was allowed to adjust. The optical constants for the 100 and 200 μm samples could be fit simultaneously using the same model, but slight adjustment to the amplitude and broadening of the Gaussian oscillators was required to fit the transmission data of standard 0.5 mm (500 μm) Eagle XG®. We attribute this apparent difference in the optical properties of these nominally identical materials, which were manufactured at different sites, to differences in the concentrations of iron and tin. Iron is a trace impurity in Eagle XG®, while tin is a minor constituent.[2] These have a profound effect on the UV absorption of glass. For the simultaneous fit of the 100 and 200 μm thick samples, our approach gave an unweighted MSE of 1.19, while the model adapted to fit the 0.5 mm sample gave an unweighted MSE of 0.97. These models gave non-zero, but still quite small values of k, at shorter wavelengths. Additionally, in situations where the glass is not analyzed in transmission mode, the refractive index can be reasonably modeled over this entire spectral range using only a Sellmeier model. This model showed an MSE value of 1.09, where, of course, k was null throughout it. This reflection approach may be useful where transmission data is not included in the model.

A4.3 Introduction

Eagle XG® glass is a widely used substrate for manufacturing flat panel displays. SE characterizes materials by their optical properties. It has previously been used to analyze display glass[3], float glasses[4], fused silica[5], silicon nitride[6], aluminum nitride[7], and a variety of related materials that show transparency in the visible region of the electromagnetic spectrum. Several approaches for modeling the optical constants of glasses have been reported, including fitting the data to a Cauchy or Sellmeier dispersion relationship or with a B-spline.[4, 8] Unlike the Cauchy and Sellmeier models, the B-spline can fit the absorption features of a glass.[4, 9] Gaussian oscillators are also well suited for modeling absorption features in amorphous materials like glass,[10-12] and a Bruggeman effective medium approximation (BEMA) roughness layer is often necessary to account for surface roughness to correctly model glasses' optical constants.[13] In addition, Tauc-Lorentz (T-L) oscillators are widely used to model the optical properties of amorphous semiconductors and other materials.[14-15] For example, Synowicki and Tiwald used multiple T-L oscillators to fit absorptions in ZrO_2 in the UV.[16]

The absorbing features in optical glasses have been described as the sum result of intrinsic absorptions from the glass, absorptions from trace impurities/minor constituents (often iron or tin), absorptions from included water, and absorptions from lattice vibrations in the glassy network.[11] In addition, color centers in glass may be induced by exposure to high-energy photons.[11-12] Iron impurities in particular are present at low (ppm) levels in most commercially available silicate glasses, and is derived from low levels of iron in glass batch materials.[11-12] The absorbing features from iron and tin have been characterized by UV-VIS spectroscopy in previous studies.[11-12, 17] One of them showed that iron gave silicate glasses absorbing features throughout the UV, visible, and IR regions of the spectrum, though the specific absorbance features across the visible region are

orders of magnitude weaker than those in the UV and IR regions such that they may not be detected at low concentrations.[11] Another study identified the locations of several absorbing bands from iron and tin species in the UV region of the spectrum, even when these are only present at ppm concentrations.[12] The positions of these absorbing features depend on the oxidation states of the metals and their coordination numbers, which in turn depend on the forming conditions for the glass melt.[12, 17] Glass composition also has a strong influence on the positions of these absorbing bands, with the bands appearing at different positions for fluoride, phosphate, and borosilicate glasses.[12] The optical properties of silicate glass in the UV are also influenced by the onset of intrinsic absorptions from luminescence centers (L-centers) in silicate glasses.[11-12, 18] Glebov and coworkers placed the onset of these absorptions at ca. 5.8 eV.[11] There are relatively few studies on the optical constants of glass at higher energies. Ultra-pure soda-lime silicate glass was analyzed up to photon energies of 22 eV.[19] For this glass, there was a maximum absorption at ca. 12 eV, with additional features near 8 and 10 eV. The position of maximum absorption compares well to reported values for fused silica, which also appear around 12 eV.[20]

In a previous SSS submission, we fit the optical constants of Eagle XG® using a rather simple curve fitting approach.[3] A pre-fit of the optical constants was obtained using a B-spline, and then oscillators were fit to the shape of this curve. In a final step, the fit parameters of the oscillators were allowed to vary to fit the experimental data. We had little physical justification for the positioning of these oscillators except the goodness of fit. This approach worked well over the range where transmission data was available (above 230 nm). However, when extrapolated to shorter wavelengths, these models gave a sharp decrease in the extinction coefficients, k. This seemed unphysical, given the expected increases in absorption for fused silica and silicate glasses (vide supra).

Here, we have expanded the spectral range of our analysis by more than 1 eV, which will be useful for applications of Eagle XG® at shorter wavelengths. Using very thin samples of this glass (100 and 200 μm), we obtained transmission data down to ca. 196 nm (6.4 eV). The optical constants were then modeled from 191-1690 nm using a Tauc-Lorentz oscillator, three Gaussian oscillators, and a pole in the IR region. As in our previous publication, a B-spline fit was the starting point for this approach.[3, 9] Following published values for soda-lime glass and fused silica,[19-20] the position of the T-L oscillator was initially fixed at 12 eV (ca. 100 nm), after which it was allowed to vary. The band-gap energy (E_g) for the T-L oscillator was fixed at 5.8 eV, corresponding approximately to the onset of intrinsic absorptions in the glassy network.[11] Thus, the T-L oscillator fit the Urbach-like absorbing features in the UV and also helped to fit the real portion of the dielectric function (ε_1) over the visible, eliminating the need for the UV-pole employed in the previous approach. The Gaussian oscillators were used to account for absorptions in the UV region, probably resulting from the tin included in this glass and low-level iron impurities. Here, we have reduced the number of oscillators to three, corresponding to the number of distinct features that appear to be present in the transmission spectra of the thinner Eagle XG®. This approach gave an unweighted MSE of 1.19, and provided a good fit to the transmission data when both the 100 and 200 μm samples were fit simultaneously.

Interestingly, the standard 0.5 mm (500 μm) thick sample could not be fit simultaneously with the thinner samples, regardless of whether we used the above-mentioned oscillator model or a B-spline. This suggests that there is a difference in the optical properties between the thicker and thinner samples. However, a good fit for the thicker sample could be obtained by allowing the amplitudes and widths of the Gaussian oscillators to vary while fixing their energies (positions) to the same values used for the thinner samples. We additionally fit the amplitude and resonance

energy of the T-L oscillator and the amplitude of the IR pole in this model. Because transmission was null below 230 nm for this sample, it was relatively insensitive to the third Gaussian oscillator positioned at 5.866 eV. Accordingly, we fixed the amplitude and width of this oscillator at the values obtained for the 100 and 200 μm samples. Thus, while this analysis indicates that there is some variability in the UV optical properties of this glass depending on its provenance, these differences can be accounted for with relatively minor adjustments to our basic model. Accordingly, this modeling approach serves as a general procedure for fitting the absorbing features of Eagle XG® in the UV region.

Finally, we note that under the analytical conditions described herein, reflection ellipsometry essentially provides a single-bounce measurement from the sample surface, and is much less sensitive to absorptions than transmission data. Accordingly, we only report the optical constants for the absorbing features (k and ε_2) over the spectral range where there is non-zero transmission, i.e., from 196 to 1690 nm for the thinner samples, and from 230 to 1690 nm for the 0.5 mm sample. When no transmission data is included in the analysis, the optical constants are well-modeled by assuming k = 0 and using a Sellmeier model. This approach gave an MSE of 1.09. Obviously this model does not account for absorptions in the material and thus would only be appropriate for modeling reflection data.

To account for surface roughness, the models included a Bruggeman effective medium approximation (BEMA) layer with optical constants corresponding to 50% void and 50% bulk glass volume fractions.[4, 13] For the 100 and 200 μm samples, the BEMA layer gave roughnesses (BEMA layer thicknesses) of 0.76 and 0.74 nm, respectively. For the 0.5 mm sample, the BEMA layer in the oscillator and Sellmeier models gave roughnesses of 0.47 and 0.48 nm, respectively. These values are systematically higher than those obtained by atomic force microscopy (AFM) for

the 0.5 mm sample (0.3 nm, R_a or R_q), and may reflect small amounts of surface contamination or a gradient in the near-surface composition in addition to physical roughness.

A4.4 Specimen Description

Eagle XG® is a commercially available boroaluminosilicate display glass, manufactured by Corning Incorporated. This glass is widely used as a substrate for manufacturing flat panel displays. Samples were ca. 1.5 cm x 1.5 cm rectangles of glass with thicknesses of 100, 200, and 500 μm thicknesses. The samples were transparent from 400-1690 nm and lightly to strongly absorbing below 400 nm.

The glass samples were derived from different production lots corresponding to different draw rates to achieve the target thickness with high surface quality. The 100 and 200 μm Eagle XG® samples were shipped to us by Corning Incorporated in a non-airtight container. They were washed prior to packaging and shipping. The 0.5 mm samples were sent to us directly from a Corning production facility in a sealed container that protected one side of the sample from exposure to the environment. This sample was packaged prior to any industrial washing or treatments, and thus represents the glass in its pristine state. We have confirmed by XPS that this packaging method is effective in limiting contamination from adventitious hydrocarbons.

Reflection ellipsometry and transmission data were collected from 191 - 1690 nm. For the 0.1, 0.2, and 0.5 mm samples, transmission was null below ca. 195, 215, and 230 nm, respectively. To collect reflection ellipsometry data from these samples, it was necessary to suppress unwanted reflections from their bottom surfaces. For the 0.5 mm sample, this was accomplished by sandblasting. To avoid contaminating the surface that was to be analyzed by ellipsometry, this

sandblasting was performed while one surface of the sample remained sealed in its original shipping container. Portions of the back of the sample were masked off using painter's grade easy-release masking tape so unroughened glass was available for transmission measurements. The glass was sandblasted using 80 grit glass based media at ca. 20 psi. Prior to opening the shipping container, the outside surface of the glass/shipping container was blown off with compressed air to remove particulates. The masking tape was then removed and the back side of the sample was thoroughly swabbed with methanol to remove any remaining particulates and/or adhesive residue from the tape. Once we were certain we had removed contaminants from the outside of the shipping container, it was opened and the sample was portioned into roughened segments for ellipsometry and unroughened portions for transmission measurements. These samples were plasma cleaned for one minute before analysis.

We similarly attempted to sandblast the thinner samples. At 20 psi, the 100 μm samples were destroyed by the sandblasting. At lower pressures their backsides could be roughened, but the samples then bowed, such that the smooth side of the glass formed a concave surface. We believe that sandblasting erodes a stressed layer of glass from one side of the sample, resulting in unbalanced stresses. With the samples bowed, it was difficult to perform ellipsometry on them. Accordingly we tried an index-matching approach on unroughened glass using both Scotch tape and an index-matching fluid (cedar oil, n = 1.51).[22] Both approaches gave similar results, and we ultimately opted to use the more traditional index matching fluid method. The transmission and reflection ellipsometry measurements on the 100 and 200 μm samples were obtained from the same piece of glass. For these transmission measurements, the samples were removed from their shipping container, plasma cleaned, and analyzed. They were then pressed onto a droplet of cedar oil on the stage of the ellipsometer to obtain reflection ellipsometry measurements.

Transmission measurements were obtained using both a UV-VIS spectrophotometer and the spectroscopic ellipsometer. Both gave similar results, but the ellipsometer in this case produced higher-quality data. Only the ellipsometery data were used in the model, while the UV-VIS confirmed the presence of an artifact near 193 nm in the data obtained with the ellipsometer.

A4.5 Instrument Description

Data were recorded using an m2000DI ellipsometer (J.A. Woollam, Inc., Lincoln, NE), a variable angle spectroscopic ellipsometer equipped with a CCD array detector, a rotating analyzer, and near IR extension to allow data collection out to 1690 nm.

Data were recorded at 52°, 57°, 62°. Transmission data were also obtained at normal incidence to the sample surface with the ellipsometer. For the analyses where transmission data was considered, two replicate transmission measurements were taken for each sample to confirm reproducibility, but only one transmission data set was included in the fit. The raw transmission data showed some transmission at *ca.* 193 nm. We confirmed that this feature was an artifact by obtaining transmission data with a UV-VIS spectrophotometer. We chose to use the data taken with the ellipsometer rather than with the UV-VIS instrument because (i) the ellipsometer had a broader spectral range and (ii) the ellipsometer produced less noisy data.

A4.6 Data Analysis

All modeling was performed with the CompleteEASE® software package from the J.A. Woollam Co. For the analyses in which we modeled the absorbing features of the glass, a B-spline fit acted as a starting point for the models. All models included a BEMA roughness layer consisting

of 50% volume fractions of glass and void, where the optical constants of the glass in the BEMA layer were coupled to the glass in the underlying layer.

The 100 μm and 200 μm samples were fit simultaneously in a multi-sample analysis. We had previously confirmed the thicknesses of the samples using a micrometer (agreement to within 1.6% with the nominal values). The two samples were allowed to have different roughnesses in the model. The same optical constants were used to fit both sets of data. The model consisted of one pole in the IR region (E_{IR} fixed at 0.124 eV), one T-L oscillator, and three Gaussian oscillators. Here, the band-gap energy (E_g) of the T-L oscillator was fixed at 5.8 eV,[11] corresponding approximately to a literature value for the onset of intrinsic absorptions in glass, while the amplitude and broadening captured the effects of absorbing features outside the spectral range (effectively acting as a UV pole).

For the thicker (0.5 mm) sample, we retained (fixed) the fit energies for the Gaussian oscillators obtained in the analysis of the thinner samples, but allowed their widths (B_G) and amplitudes (A_G) vary. Because the transmission data was null below 230 nm, the highest energy Gaussian oscillator was fixed to the values obtained for the thinner sample. The amplitude and energy of the T-L oscillator, as well as the amplitude of the IR pole were also allowed to vary.

For the Sellmeier analysis of the reflection ellipsometry data, the model consisted of two poles. The position and amplitude of the UV pole were fit, as was the amplitude of the IR pole. The position of the IR pole was fixed at the same position as it was in the other models.

For the first fitting approach, The T-L oscillator had three free parameters: the resonance energy (E_R), the broadening (B_{TL}), and the amplitude (A_{TL}). Here, E_R was initially fixed at 12 eV. This starting position was based on a strongly absorbing feature in soda lime silicate glass.[19] It was then allowed to vary after all the other parameters had been initially fit. The Gaussian oscillator

had three parameters: the amplitude (A_G), the peak broadening (B_G), and the center energy (E_C). The IR pole energy was fixed at 0.435 eV following literature values for hydroxyl absorptions in silicate glass.[23] The amplitude of this pole (A_{IR}) was allowed to vary. The thickness of the BEMA roughness layer also varied.

When the optical constants for the 0.5 mm sample were modeled, the positions of the Gaussian oscillators (E_G) obtained from the thinner glass were fixed, as well as the broadening (B_{TL}) and bandgap (E_g) of the T-L oscillator. However, the widths (B_G) and amplitudes (A_G) of the lower-energy Gaussian oscillators were allowed to vary, as well as the energy (E_R) and amplitude (A_{TL}) of the T-L oscillator.

For the second (pole-pole) approach, the free parameters were the UV pole energy, E_{UV}, and amplitude, A_{UV}, and the IR pole amplitude, A_{IR}. We again fixed the IR pole energy at 0.435 eV.

There is excellent agreement between the refractive indices obtained for all the samples between the various modeling approaches described herein (to *ca.* 0.5%, with the worst deviation occurring at photon energy > 5.9 eV).

N.B.: While we have attempted to base our models as much as possible on data available in the technical literature, it is difficult to ascribe too much meaning to the parameters of the T-L and Gaussian oscillators employed herein. For example, while the T-L oscillator includes a fit parameter for bandgap, this is not the physical bandgap of the material. Nevertheless, they have physically relevant shapes, and the fact that they fit our data may indicate that they have some physical meaning in our model. We have primarily used these oscillators as curve fitting tools/shapes for describing the absorption of the material, as has been previously done.[16]

A4.7 Oscillator Equations

The information in this section was derived from a series of technical notes from the J.A. Woollam Company and a paper by Jellison and Modine.[14-15, 24-25] While the equation for the Gaussian oscillator as it appears in this document was taken from a J. A. Woollam technical note, a more detailed discussion of the Gaussian oscillator as it applies to fitting absorbing features in glasses can be found in an article by De Sousa Meneses.[10]

The pole-pole model is given by Equation (A4.1),

$$(A4.1) \quad n^2 = \varepsilon_\infty + \frac{A_{UV}\lambda^2}{\lambda^2 - \lambda_{UV}^2} + \frac{A_{IR}\lambda^2}{\lambda^2 - \lambda_{IR}^2}$$

where n is the refractive index, A_{UV} is the UV amplitude, A_{IR} is the IR amplitude, λ_{uv} is the position of the UV pole, λ_{IR} is the position of the IR pole, and λ is the wavelength for which the refractive index is being calculated. ε_∞ is the low-frequency offset, which should be fixed at an appropriate value – we used the default value for this parameter provided in our software, i.e., unity. We have provided the values for λ_{uv} and λ_{IR} below in terms of energy instead of wavelength. Accordingly, their symbols have been changed to E_{UV} and E_{IR} in the tables below. ε_∞, A_{UV}, and A_{IR} are unitless. In the case of the analyses where absorbing features were fit using transmission data, no UV pole was used, i.e. A_{UV} was fixed at 0.

The Bruggeman effective medium approximation is given by Equation (A4.2),

$$f_a \frac{\varepsilon_a - \varepsilon}{\varepsilon_a + 2\varepsilon} + f_b \frac{\varepsilon_b - \varepsilon}{\varepsilon_b + 2\varepsilon} = 0$$

(A4.2)

where f_a is the volume fraction of material a, f_b is the volume fraction of material b, and ε is the dielectric constant of the composite material derived from the dielectric constants of the component materials ε_a and ε_b. The model materials in this case were the glass substrate and void,

where the optical constants of the glass substrate in the BEMA layer were coupled to the fit optical constants in the underlying layer. This model gave a roughness of *ca.*0.75 nm for the thin samples, and 0.48 nm for the thick samples. This result is probably reflective of a combination of physical roughness, a small amount of surface contamination, and a compositional gradient in the near-surface region of the glass. The surface roughness (R_a or R_q) of our 0.5 mm samples measured by AFM is 0.3 nm. We consider our ellipsometry results to be in good agreement with the AFM measurement, given that previous studies have shown a linear correlation, but not necessarily a 1:1 correspondence, between roughnesses measured by by the two techniques.[26-27]

The equation for a Guassian oscillator is

$$(A4.3)\ \ \varepsilon_2(E) = A_G\left(e^{-\left(\frac{E-E_G}{\sigma}\right)^2} - e^{-\left(\frac{E+E_G}{\sigma}\right)^2}\right),$$

where E is the photon energy in eV, A_G is the unitless oscillator amplitude, and E_G is the center energy in eV. The value for σ is given by Equation (A4.4),

$$(A4.4)\ \ \sigma = \frac{B_G}{2\sqrt{ln(2)}}$$

where B_G is the broadening (FWHM) of the oscillator in eV.

The equation for a T-L oscillator is

$$(A4.5)\ \ \ \varepsilon_2(E) = \frac{A_{TL}E_R B_{TL}(E-E_g)^2}{(E^2-E_R^2)^2+B_{TL}^2E^2}\cdot\frac{1}{E}\ , E > E_g$$

$$\varepsilon_2(E) = 0, E \leq E_g,$$

where A_{TL} is the amplitude of the oscillator, E_R is the resonance energy, B_{TL} is a broadening term, and E_g is the bandgap of the material, all given in terms of photon energy (here in eV).

For both the Gaussian and the T-L oscillators, the real portion of the dielectric function, ε_1, is calculated using the Kramers-Kronig integral, as shown here,

(A4.6) $\varepsilon_1(\omega) = 1 + \frac{2}{\pi} P \int_0^\infty \frac{\omega' \varepsilon_2(\omega')}{\omega'^2 - \omega^2} d\omega'$,

where ω is the frequency of light and P is the principle value of the integral, given by Equation (A4.7),

(A4.7) $P \int_0^\infty d\omega' \equiv \lim_{\delta \to 0} \left(\int_0^{\omega-\delta} d\omega' + \int_{\omega+\delta}^\infty d\omega' \right).$[28]

    The MSE for the fits was calculated using Equation (A4.8),

(A4.8) $MSE = \sqrt{\frac{1}{4n-m} \sum_{i=1}^n \left[\left(\frac{N_{E_i} - N_{G_i}}{0.001} \right)^2 + \left(\frac{C_{E_i} - C_{G_i}}{0.001} \right)^2 + \left(\frac{S_{E_i} - S_{G_i}}{0.001} \right)^2 + \left(6 * \frac{T_{E_i} - T_{G_i}}{0.01} \right)^2 \right.}$,

where $N = \cos(2\Psi)$, $C = \sin(2\Psi)\cos(\Delta)$, $S = \sin(2\Psi)\sin(\Delta)$, and T represents the transmission measurements. Terms subscripted with an E denote the experimentally measured values at data point i, and terms subscripted with a G indicate the data generated by the model. n is the number of wavelengths at which measurements were taken, and m is the number of fit parameters included in the model. Note here that the term for transmission data has been multiplied by a weighting factor of 6 to compensate for the fact that the ellipsometry data is represented by three measured parameters whereas the transmission data is only represented by one, and also because we have three sets of ellipsometry data and only one set of transmission data per sample. This weighting factor was automatically assigned by the instrument software based on the number of ellipsometry and transmission data sets in our model. The normalization factors for each parameter (0.001 for N, C, and S, and 0.01 for T) reflect the typical magnitude of systematic and random error in these values for the M-2000 ellipsometer. Thus normalized, the MSE for a "good" fit is 1. Note that this is an "unweighted" MSE, i.e., the standard deviation of the measurement at each data point has no effect on its weight in the fit, such that noisier data provides a higher MSE. The term in Equation (A4.8) accounting for the transmission data was omitted in the Sellmeier model, which did not include this type of data.

Table A4.1. Fit parameters for the 100 and 200 µm samples.

Parameter	Value	Error
Roughness$_{0.1}$ $_{mm}$ (nm)	0.84	0.009
Roughness$_{0.2}$ $_{mm}$ (nm)	0.86	0.009
A_{TL} (eV)	62.60	0.38
B_{TL} (eV)	3.152	0.014
E_R (eV)	12.863	0.014
A_{IR} (unitless)	1.16×10^{-2}	1.6×10^{-4}
A_{G1} (unitless)	2.3×10^{-4}	3.1×10^{-5}
B_{G1} (eV)	1.39	0.95
E_{G1} (eV)	5.03	0.011
A_{G2} (unitless)	6.5×10^{-4}	8.2×10^{-5}
B_{G2} (eV)	0.70	0.048
E_{G2} (eV)	5.503	0.031
A_{G3} (unitless)	1.32×10^{-3}	8.3×10^{-5}
B_{G3} (eV)	0.38	0.016
E_{G3} (eV)	5.848	5.4×10^{-3}
MSE	1.186	

Table A4.2. Fit parameters for the 0.5 mm sample (with transmission data).

Parameter	Value	Error
Roughness (nm)	0.46	0.007
A_{TL} (eV)	65.7	0.62
E_R (eV)	13.00	0.018
A_{IR} (unitless)	9.7×10^{-3}	2.0×10^{-4}
A_{G1} (unitless)	1.76×10^{-4}	3.0×10^{-6}
B_{G1} (eV)	1.36	0.011
A_{G2} (unitless)	7.0×10^{-4}	2.8×10^{-5}
B_{G2} (eV)	0.69	0.01
MSE	0.973	

Table A4.3. Fit parameters for the 0.5 mm sample (reflection ellipsometry data only, Sellmeier model).

Parameter	Value	Error
Roughness (nm)	0.48	0.008
A_{UV} (unitless)	197.4	0.37
E_{UV} (eV)	12.62	0.011
A_{IR} (unitless)	7.9×10^{-3}	2.0×10^{-4}
MSE	1.094	

Table A4.4. Spectral features of interest for the 100 and 200 μm Eagle XG®. Slightly differing values over a more limited spectral range are available for the 500 μm sample.

Spectrum ID #	Identity	Composition	Feature	Energy (eV)	Wavelength (nm)	n	k	ε_1	ε_2
41-44	Substrate	Eagle XG® Glass	Range minimum	0.734	1688.2	1.49	0	2.22	0
41-44	Substrate	Eagle XG® Glass	Range maximum (k/ε2)	6.27	197.6	1.64	0.0017	2.67	0.0057
41-44	Substrate	Eagle XG® Glass	Shoulder (ε2)	5.89	210.3	1.61	5.9 x 10⁻⁴	2.6	0.0018
41-44	Substrate	Eagle XG® Glass	Shoulder (ε2)	5.26	235.7	1.59	2.1 x 10⁻⁴	2.51	6.8 x 10⁻⁴
41-44	Substrate	Eagle XG® Glass	Band Edge	3.1	399.5	1.52	0	2.32	1 x 10⁻⁶

A4.8 Fit Parameters Fixed in the Model

We fixed the energy of the IR pole at 0.435 eV (2850 nm) based on a reported value for hydroxyl groups in silicate glasses.[23] Provided it is at low enough energy, the position of this pole appears to have little effect on the MSE in our models, i.e. we get very similar results if we fix it at 0.124 eV, following values for fused silica,[20] or if we fix it at the software default of 1×10^{-8} eV, as in our previous submission.[3]

The bandgap energy (E_g) of the T-L oscillator for some of our approaches was fixed at 5.8 eV, following literature values for the onset of intrinsic absorptions for some glasses.[11] Including this fit parameter gave little improvement in the MSE.

Positions and widths of some oscillators for the fit of the 0.5 mm sample were fixed based on the results obtained for the thinner samples. Specifically, the center energies of all the Gaussian oscillators as well as the amplitude and width of the highest-energy Gaussian oscillator were fixed. Additionally, the width and band gap energy of the Tauc-Lorentz oscillator were fixed. Including these parameters in the fit only slightly improved the MSE.

A4.9 Relevant Reference Materials

Data available for materials comparable to Eagle XG®, including soda-lime silicate glass,[11, 18-19, 23] borosilicate glass,[12] and fused silica[20] have been useful in establishing our theoretical approach to modeling this material and for fixing some values within the models.

A4.10 Acknowledgments

A4.11 Figures
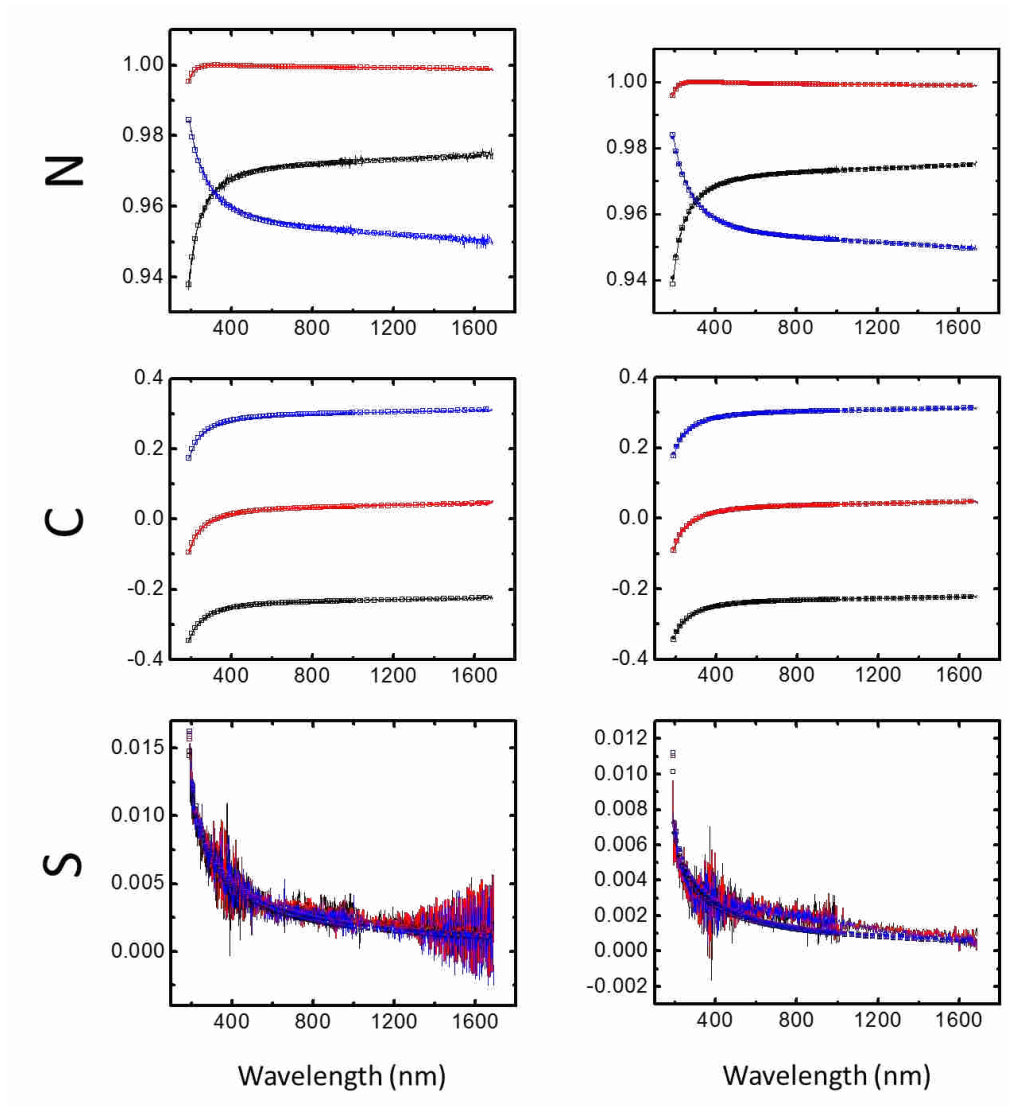
Figure A4.1. Raw (lines) and modeled (symbols) N, C, and S values for 100 and 200 μm samples (left, overlayed), and 500 μm sample (right), obtained at 52° (black), 57° (red) and 62° (blue). For the 500 μm sample, the modeled data from the T-L + Gaussian and Sellmeier approaches are shown in open squares and solid circles, respectively. For the modeled data, every tenth data point is shown to avoid occluding the raw data.
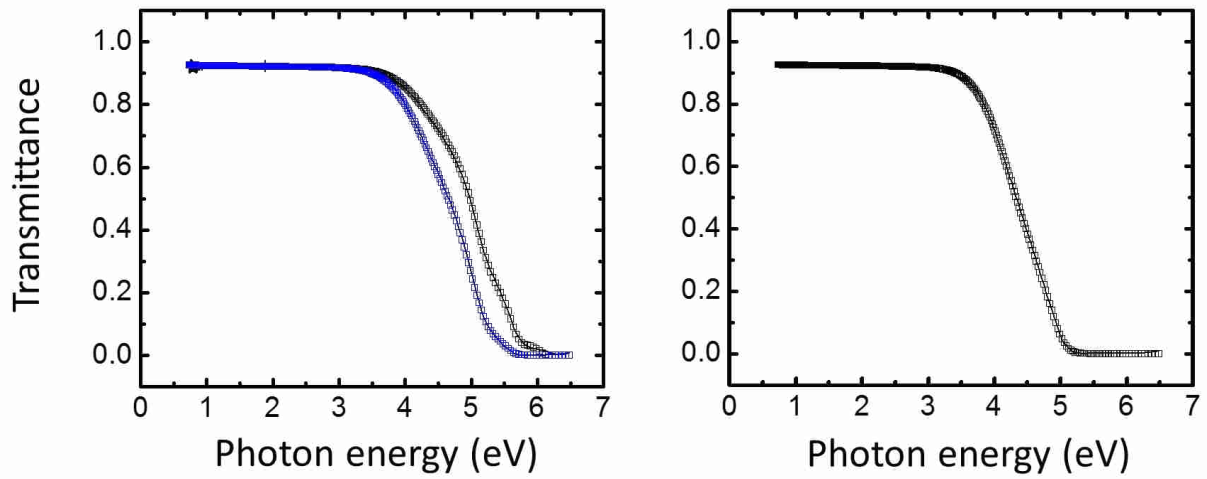
Figure A4.2. Raw (lines) and modeled (open squares) transmission data obtained using a T-L + Gaussian modeling approach. (Left) data for 100 (black) and 200 μm (blue) samples. (Right) 500 μm sample.
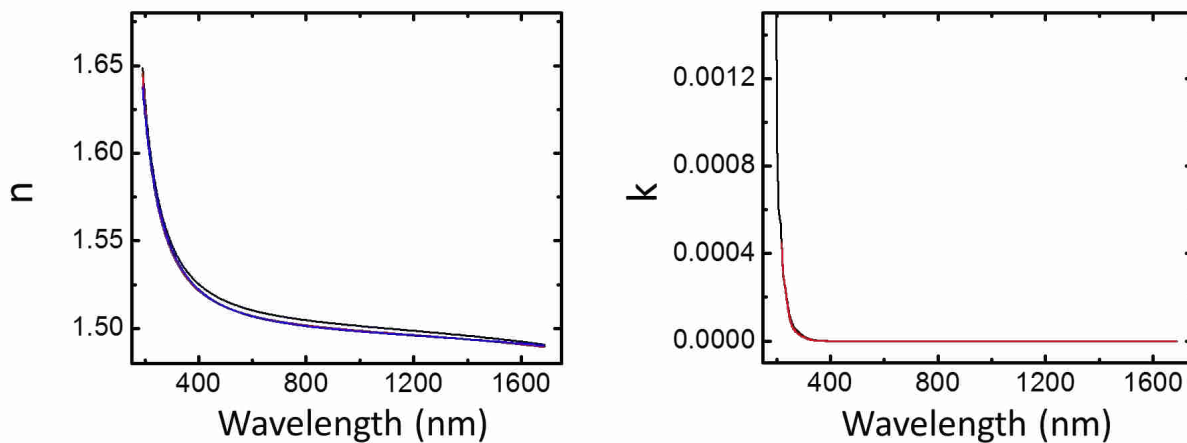
Figure A4.3. Optical constants n and k obtained using the various modeling approaches. (Left) Refractive index for the 100 and 200 μm samples (black), the 500 μm sample modeled using a T-L + Gaussian approach (red), and the 500 μm sample modeled using a Sellmeier approach (blue). The blue and red lower lines are essentially identical. (Right) extinction coefficient for the 100 and 200 μm samples (black), and the 500 μm sample (red). The extinction coefficient is reported only over the range where there is non-zero transmittance for each set of samples.
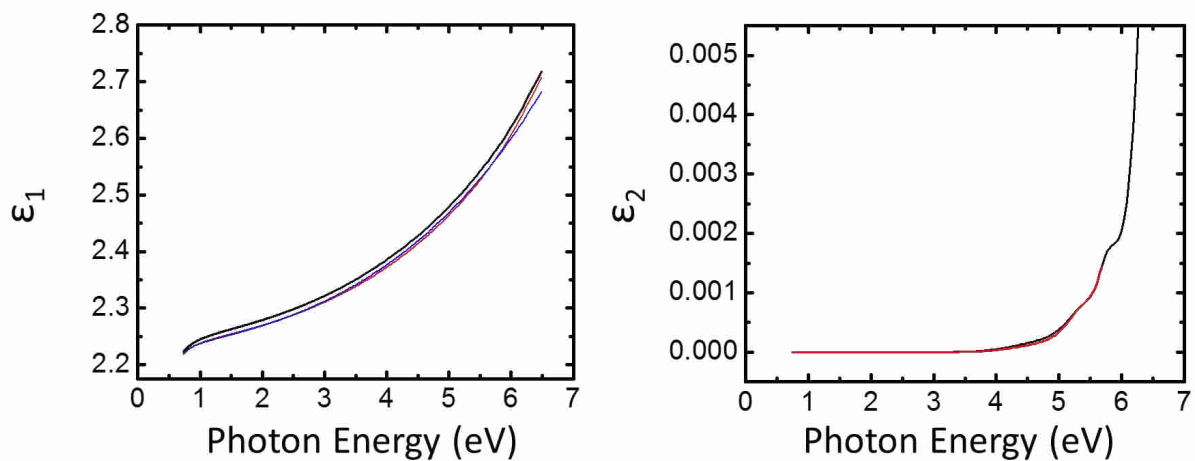
Figure A4.4. Optical constants, ε_1 and ε_2, obtained using various modeling approaches. (Left) ε_1 for the 100 and 200 μm samples (black), the 500 μm sample modeled using a T-L + Gaussian approach (red), and the 500 μm sample modeled using a Sellmeier approach (blue). (Right) The extinction coefficient for the 100 and 200 μm samples (black), and the 500 μm sample (red). The extinction coefficient is reported only over the range where there is non-zero transmittance for each set of samples.

A4.12 References

1.   Cushman, C. V.; Johnson, B. I.; Martin, A.; Lunt, B. M.; Smith, N. J.; Linford, M. R. Eagle XG® glass: Optical constants from 196 to 1688 nm (0.735–6.33 eV) by spectroscopic ellipsometry. *Surface Science Spectra* **2017,** *24* (2), 026001.

2.   Ellison, A.; Cornejo, I. A. Glass Substrates for Liquid Crystal Displays. *International Journal of Applied Glass Science* **2010,** *1* (1), 87-103.

3.   Cushman, C. V.; Sturgell, B. A.; Martin, A. C.; Lunt, B. M.; Smith, N. J.; Linford, M. R. Eagle XG® glass, optical constants from 230 to 1690 nm (0.73-5.39 eV) by spectroscopic ellipsometry. *Surface Science Spectra* **2016,** *23* (1), 55-60.

4.   Synowicki, R. A.; Johs, B. D.; Martin, A. C. Optical properties of soda-lime float glass from spectroscopic ellipsometry. *Thin Solid Films* **2011,** *519* (9), 2907-2913.

5.   Tan, G. L.; Lemon, M. F.; French, R. H. Optical properties and London dispersion forces of amorphous silica determined by vacuum ultraviolet spectroscopy and spectroscopic ellipsometry. *Journal of the American Ceramic Society* **2003,** *86* (11), 1885-1892.

6.   Gautam, L. K.; Ye, L.; Podraza, N. J. LPCVD SiNx thin film on c-Si wafer by spectroscopic ellipsometry. *Surface Science Spectra* **2016,** *23* (1), 51-54.

7.   Jones, D.; French, R.; MuÈllejans, H.; Loughin, S.; Dorneich, A.; Carcia, P. Optical properties of AlN determined by vacuum ultraviolet spectroscopy and spectroscopic ellipsometry data. *Journal of materials research* **1999,** *14* (11), 4337-4344.

8.   Ghosh, G. Sellmeier coefficients and dispersion of thermo-optic coefficients for some optical glasses. *Applied optics* **1997,** *36* (7), 1540-1546.

9.   Johs, B.; Hale, J. S. Dielectric function representation by B-splines. *physica status solidi (a)* **2008,** *205* (4), 715-719.

10.   De Sousa Meneses, D.; Malki, M.; Echegut, P. Structure and lattice dynamics of binary lead silicate glasses investigated by infrared spectroscopy. *Journal of non-crystalline solids* **2006,** *352* (8), 769-776.

11.   Glebov, L. B. In *Optical absorption and ionization of silicate glasses*, Laser-Induced Damage in Optical Materials: 2000, International Society for Optics and Photonics: 2001; pp 343-358.

12.   Ehrt, D. UV-absorption and radiation effects in different glasses doped with iron and tin in the ppm range. *Comptes Rendus Chimie* **2002,** *5* (11), 679-692.

13.   Jellison, G.; Sales, B. Determination of the optical functions of transparent glasses by using spectroscopic ellipsometry. *Applied optics* **1991,** *30* (30), 4310-4315.

14.   Jellison Jr, G.; Modine, F. Parameterization of the optical functions of amorphous materials in the interband region. *Applied Physics Letters* **1996,** *69* (3), 371-373.

15.   Jellison Jr, G.; Modine, F. Erratum: "Parameterization of the optical functions of amorphous materials in the interband region ". *Applied Physics Letters* **1996,** *69* (14), 2137.

16.   Synowicki, R.; Tiwald, T. E. Optical properties of bulk c-ZrO 2, c-MgO and a-As 2 S 3 determined by variable angle spectroscopic ellipsometry. *Thin Solid Films* **2004,** *455*, 248-255.

17.   Uchino, T.; Nakaguchi, K.; Nagashima, Y.; Kondo, T. Prediction of optical properties of commercial soda–lime-silicate glasses containing iron. *Journal of Non-Crystalline Solids* **2000,** *261* (1), 72-78.

18.   Glebov, L.; Boulos, E. Absorption of iron and water in the Na 2 O–CaO–MgO–SiO 2 glasses. II. Selection of intrinsic, ferric, and ferrous spectra in the visible and UV regions. *Journal of non-crystalline solids* **1998,** *242* (1), 49-62.

19.   Bagley, B.; Vogel, E.; French, W. G.; Pasteur, G.; Gan, J.; Tauc, J. The optical properties of a soda-lime-silica glass in the region from 0.006 to 22 eV. *Journal of Non-Crystalline Solids* **1976,** *22* (2), 423-436.

20.   Kitamura, R.; Pilon, L.; Jonasz, M. Optical constants of silica glass from extreme ultraviolet to far infrared at near room temperature. *Applied optics* **2007,** *46* (33), 8118-8133.

21.   Cushman, C. V.; Sturgell, B. A.; Martin, A.; Lunt, B. M.; Smith, N. J.; Linford, M. R. Eagle XG® Glass: Optical Constants from 230 – 1690 nm (0.73-5.39 eV) by Spectroscopic Ellipsometry. *Surface Science Spectra* **2016,** *Submitted*.

22.   Synowicki, R. Suppression of backside reflections from transparent substrates. *physica status solidi (c)* **2008,** *5* (5), 1085-1088.

23.   Boulos, E.; Glebov, L.; Smirnova, T. Absorption of iron and water in the Na 2 O–CaO–MgO–SiO 2 glasses. I. Separation of ferrous and hydroxyl spectra in the near IR region. *Journal of non-crystalline solids* **1997,** *221* (2), 213-221.

24.   Tiwald, T. Sellmeier Dispersion. *J.A. Woollam Co., Inc. Annual Newsletter* **January, 2009,** (10), 8-9.

25.   Tiwald, T. The Gaussian Oscillator. *J.A. Woollam Co., Inc. Annual Newsletter* **January, 2008,** (9), 4-5.

26.   Dahal, L. R.; Sainju, D.; Podraza, N.; Marsillac, S.; Collins, R. Real time spectroscopic ellipsometry of Ag/ZnO and Al/ZnO interfaces for back-reflectors in thin film Si: H photovoltaics. *Thin Solid Films* **2011,** *519* (9), 2682-2687.

27.   Akagawa, M.; Fujiwara, H. Optical characterization of textured SnO2: F layers using spectroscopic ellipsometry. *Journal of Applied Physics* **2012,** *112* (8), 083507.

28.   Fujiwara, H., Data Analysis. In *Spectroscopic Ellipsometry*, John Wiley & Sons, Ltd: 2007; pp 147-207.

Appendix 5: Low Energy Ion Scattering (LEIS). A Practical Introduction to its Theory, Instrumentation, and Applications

A5.1 Statement of Attribution

This document was originally published as Cushman, C. V.; Brüner, P.; Zakel, J.; Major, G. H.; Lunt, B. M.; Smith, N. J.; Grehl, T.; Linford, M. R. Low energy ion scattering (LEIS). A practical introduction to its theory, instrumentation, and applications. *Analytical Methods* **2016,** *8* (17), 3419-3439.[1] Before that, major portions of this article were published in *Vacuum Technology & Coating.*[2-6]

A5.2 Abstract

Low energy ion scattering (LEIS) probes the elemental composition of the outermost atomic layer of a material and provides static depth profiles of the outer *ca.* 10 nm of surfaces. Its extreme surface sensitivity and quantitative nature make it a powerful tool for studying the relationships between surface chemistry and surface related phenomena such as wetting, adhesion, contamination, and thin film growth. The high depth resolution obtained in LEIS in its static and sputter depth profile modes are useful for studying the layer structures of thin films. LEIS instrumentation has improved significantly in recent years, showing dramatic increases in its sensitivity and further expanding its potential applications. In this article, we provide a practical introduction to the technique, including a discussion of the basic theory of LEIS, LEIS spectra,

LEIS instrumentation, and LEIS applications, including catalysts, solid oxide fuel cells (SOFCs), and thin films in integrated circuits.

A5.3 Overview

Atoms at the surface of a material are generally in a different chemical environment than those buried within the bulk. This often results in important compositional and morphological differences between the surface of a material and its interior. For example, surface-bound water molecules experience very different environments than those in bulk water. Surface composition is important because materials interact with their surroundings through their surfaces, and many important phenomena are governed by their surfaces, including wetting, adhesion, contamination, reactivity, corrosion, and catalysis. Because understanding these phenomena is so important, the analysis of surfaces and interfaces has become an important and specialized area of analytical chemistry.

Analyzing surface composition is challenging because, in general, only a relatively small portion of a material is actually at the surface and available for analysis. Depths of analysis in surface studies range from a single atomic layer to a few hundred nm. Surface analysis techniques must be sensitive enough to obtain information from a very small sample volume before damage from the analysis significantly alters the surface. They must also be sufficiently discriminating to differentiate between signals originating from the surface and bulk. The challenge of obtaining information from a surface often increases as the depth of analysis decreases — fewer atoms/molecules become available for analysis, and contamination or damage during the analysis become increasingly important considerations.

In this work, we provide a practical introduction to low energy ion scattering (LEIS). LEIS is an extremely versatile surface analysis technique that is performed under ultra-high vacuum (UHV) conditions. LEIS is specifically sensitive to the elemental composition of the *outermost* atomic layer of a material, and additionally provides depth profile information about its outer *ca.* 10 nm. Information from deeper within the material can be obtained via LEIS sputter depth profiling. Sensitivity to the elemental composition of the outer atomic layer of a material is LEIS's principle asset. Indeed, it is the only technique of which we are aware with its degree of surface sensitivity and specificity. Therefore, LEIS is a powerful tool for understanding the relationship between surface composition and material properties. Here we provide an overview of the basic theory of LEIS, LEIS instrumentation, quantitation in LEIS, LEIS depth profiling, and applications of the technique to catalysts, semiconductor materials, and solid-oxide fuel cells (SOFCs). In particular, we discuss how recent advances in LEIS instrumentation have dramatically improved the limit of detection of the method. This article is not intended to be a comprehensive review on the topic, but rather a practical introduction. A more detailed description of the theory and development of the technique can be found elsewhere,[7-11] particularly in a review by Brongersma and coworkers.[12]

A5.4 Introduction to the Theory of LEIS[13]

LEIS has existed as a technique since the late 1960's, but recent advances in instrumentation have dramatically improved its capabilities and applicability.[7-8, 12, 14] Unlike X-ray photoelectron spectroscopy (XPS) and time-of-flight secondary ion mass spectrometry (ToF-SIMS), which sample the first few nanometers of materials, LEIS is sensitive to their outermost atomic layer.[7-8, 12, 14-15] That is, XPS and ToF-SIMS give incredibly useful information about the

outer few nanometers of materials, where to some degree they average this information, but they struggle to provide definitive information about the final atomic layer of a material.[16] Thus, LEIS occupies an important niche that will likely become more important with time, where LEIS is a powerful tool for understanding the relationship between surface composition and important phenomena such as catalysis, wetting, diffusion, adhesion, and adsorption.[12, 17-20] In this section, we discuss the basic theory of LEIS, which will include an introduction to interpreting LEIS spectra.

Surface instrumentation is often categorized based on the probing species that is directed onto a surface and what leaves it. In XPS, X-rays enter the surface and photoelectrons (energetic electrons) exit. In ToF-SIMS, primary ions bombard the surface and secondary ions are emitted. Scanning electron microscopy has electrons in and electrons out. LEIS probes a surface with noble gas ions, and then detects the same backscattered ions (see Figure A5.1). There is an obvious similarity between LEIS and Rutherford backscattering (RBS), which is also based on the backscattering of atoms.[8, 21] The primary difference between RBS and LEIS is the energy of the incoming ions. LEIS uses a *ca.* 1 to 10 KeV beam of noble gas ions, while RBS uses primary ions with MeV energies. For this reason, RBS is essentially a bulk technique, probing on the order of a micron into materials. The much lower energy primary ions in LEIS are significantly less penetrating. Furthermore, the noble gas ions that are used in LEIS have a high probability of being neutralized when they interact with a material. Since only ions are detected in LEIS, and only ions that scatter off of the outermost atomic layer of a material have short enough interaction times to avoid neutralization, LEIS is uniquely sensitive to the atomic composition of the outermost layer of a material.[8, 15, 22] Indeed, LEIS is so surface sensitive that even a monolayer of contamination, e.g., adventitious carbon, can obscure the signal from a material.

Equation (A5.1) is the governing equation of LEIS. A list of its underlying assumptions can be found in an article by Smith.[7]

$$(A5.1) \ E_S = k \cdot E_P = \left(\frac{\cos \Theta + \sqrt{\left(\frac{M_S}{M_P}\right)^2 - \sin^2 \Theta}}{1 + \frac{M_S}{M_P}} \right)^2 \cdot E_P, \ \frac{M_S}{M_P} \geq 1$$

The variables in this equation are the energy of the primary ion, E_P, the energy it has after scattering, E_S, the mass of the primary ion, M_P, and the mass of the particle it scatters off of, M_S. The other variable in this equation, Θ, is the angle through which the scattering takes place (see Figure A5.1). A condition for Equation (A5.1) is that $M_S/M_P \geq 1$ (the surface atom from which scattering occurs must be heavier than the ion striking it). If this condition is not fulfilled ($M_S/M_P < 1$), e.g., He$^+$ striking a hydrogen atom, no backscattering takes place, only forward scattering. As an analogy, imagine what would happen if the pins in a bowling alley were heavier than the bowling ball. In this case, the bowling ball would recoil upon striking a pin. This would entirely change the game. Bowling, as it stands, is based on forward scattering of the ball, not backscattering. Not to belabor the point, consider what would happen if you used a ping pong ball for bowling, which is obviously much lighter than a bowling pin. Clearly if the much lighter ping pong ball were to strike the bowling pin head on, it would bounce back in the direction from which it came. This metaphor helps us appreciate how scattering depends on the masses of the projectile and the object it strikes. Because in a LEIS experiment E_P, M_P, Θ, and E_S are known or defined by the instrument, M_S can be determined. Equation (A5.1) can be derived entirely from classical physics using the principles of conservation of energy and momentum; the ideal scattering energy in LEIS can be described without quantum mechanics. In practice, however, there are inelastic contributions to the scattering process, which shift the measured scattering energies to slightly

lower energies than those calculated using Equation (A5.1) and give the peaks in LEIS spectra a Gaussian shape.[12]

When one encounters a new equation in physics, it is often a good idea to evaluate it in its limits. Consider the case where M_S is increasingly large compared to M_P, e.g., the case of He$^+$ scattering off of a very heavy atom. First, we multiply Equation (A5.1) by $(M_P/M_S)/(M_P/M_S)$, which yields

$$(A5.2) \quad E_S = \left(\frac{\frac{M_P}{M_S}\cos\Theta + \frac{M_P}{M_S}\sqrt{\left(\frac{M_S}{M_P}\right)^2 - \sin^2\Theta}}{\frac{M_P}{M_S}+1} \right)^2 \cdot E_P.$$

Rearranging the equation, we obtain

$$(A5.3) \quad E_S = \left(\frac{\frac{M_P}{M_S}\cos\Theta + \sqrt{1 - \left(\frac{M_P}{M_S}\right)^2 \sin^2\Theta}}{\frac{M_P}{M_S}+1} \right)^2 \cdot E_P.$$

Now, consider the limit of $M_P/M_S \rightarrow 0$. Of course this is not physically possible, but it becomes a more reasonable approximation as M_S gets large compared to M_P, e.g., ^{4}He$^+$ scattering off of ^{238}U, which gives $M_P/M_S \approx 4/238 \approx 0.02$. In any case, as $M_P/M_S \rightarrow 0$ in Equation (A5.3) becomes

$$(A5.4) \quad E_S = E_P.$$

Thus, for the case of an infinitely heavy M_S atom, the energy of the scattered ion, E_S, is equal to the energy of the primary ion, E_P, i.e., all the energy of the primary ion is in the backscattered ion. Figure A5.2 is a plot of the percentage of the energy backscattered in LEIS as a function of M_S. The previous discussion about Equation (A5.1) in its limit helps us understand why the curve in Figure A5.2 for He$^+$ (the projectile) asymptotically approaches 100% at high M_S. Obviously the other curves in Figure A5.2 are also approaching this limit.

LEIS identifies elements by their masses, and successful identification of an element depends upon optimizing the analysis parameters so that one nuclear mass can be distinguished from another.[12, 14] The most important parameters that the user can control in LEIS are the type and energy of the ions used to probe the surface. The steepness of the curve for He^+ in Figure A5.1 at lower M_S suggests that LEIS with He^+ is very discriminating to the lighter elements. For example, using Equation (A5.1), we calculate an energy difference of 94 eV for 3 KeV He^+ backscattered at 145° from ^{12}C and ^{13}C. Since the widths of these peaks will be around 80 eV, these signals can be resolved.

In contrast to the steep rise in backscattering energy at low values of M_S, the increasing flatness/asymptotic behavior of the curve in Figure A5.1 for He^+ at higher M_S shows that LEIS lacks discrimination/resolution for the heavier elements with this lighter probe. For example, for 3 KeV He^+ at 145° backscattering, the energy difference between ^{58}Ni and ^{59}Co is only 10 eV. LEIS also shows little discrimination between ^{208}Pb and ^{197}Au under these analysis conditions. That is, even though they have a greater mass difference, the higher masses of Pb and Au lead to an energy difference of only 11 eV between their peaks. Thus, LEIS with He^+ nicely resolves the lighter elements while it is less effective at resolving the heavier ones.

A solution to the lack of resolving power of He^+ at higher M_S is to use heavier projectile ions.[12] Figure A5.2 contains plots of the scattering energy for He^+ and three other noble gas ions: Ne^+, Ar^+, and Kr^+ as a function of M_S. These curves were derived directly from Equation (A5.1). It is interesting to note the slopes of these lines. At about $M_S = 40$ u, the curve for Ne^+ has a higher slope than that for He^+, i.e., the resolving power of Ne^+ becomes higher than that of He^+ at this point. Then, a little over 100 u, Ar^+ shows a higher slope than Ne^+, and finally after about 200 u, Kr^+ has the highest slope. Figure A5.3 is a plot of the energy difference per nominal mass vs. M_S,

i.e., it is the plot of the slopes (derivatives) of the curves in Figure A5.2. Note that the plot does indeed show He^+ being the most effective probe up to $M_S \sim 40$ u, followed by Ne^+ up to $M_S \sim 100$ u, etc. Thus, in general, LEIS better resolves heavier atoms with heavier projectiles. This is all consistent with our earlier analogy – imagine how hard it would be to differentiate between 16 lb. and 18 lb. bowling balls by measuring the backscattering energy of ping pong balls bouncing off of them. Equation (A5.1) would apply to this classical problem, and the mass ratio M_S/M_P would be extremely large, essentially giving the same backscattered energy ($E_S = E_P$, Equation A5.4) for the ping pong balls.

Before going on, let's revisit the discussion of LEIS of ^{58}Ni and ^{59}Co. It will illustrate another important concept – consideration of the different isotopes of elements to be analyzed by LEIS. The discussion above on ^{58}Ni and ^{59}Co was true for isotopically pure samples of these elements. However, a real sample of nickel will consist primarily of ^{58}Ni (68.1%) and ^{60}Ni (26.2%). ^{59}Co, in contrast, exists as one stable isotope. It has an odd number of protons (27) so one would expect it to have fewer isotopes than nickel, which has an even number of protons (28). All of this means that a real sample of nickel will produce a broader LEIS signal than the corresponding signal from Co. Accordingly, detecting a small amount of Co in a sample of Ni by LEIS is a difficult proposition – the Co signal lies between the two Ni signals. In contrast, a small amount of Ni in Co can be more readily detected and quantified – the nickel will produce a lower, broader signal that will surround the sharper signal from the Co. We emphasize here that it would be a good idea to perform LEIS in conjunction with other analyses. In this regard, LEIS is the same as any other surface/material analytical method. For example, because of the overlap between the Ni and Co signals, it might be a good idea to perform XPS on any samples that are suspected of containing these two elements. XPS might show, for example, that one of these elements is absent,

which would simplify one's data analysis. Of course, as mentioned above, XPS probes much deeper into materials than LEIS.

We now discuss the energy of the backscattered ion and its impact on signal. We noted above that the slope of the scattering energy in Figure A5.2 changes with increasing M_S. We also noted that the energy difference between He$^+$ backscattered from isotopically pure ^{58}Ni and ^{59}Co was 10 eV for the given conditions. In contrast, the energy differences for 5 KeV Ne$^+$ and 8 KeV Ar$^+$ backscattered at 145° from ^{58}Ni and ^{59}Co are 33.1 and 30.3 eV, respectively. There is little difference between these energies, so one might assume that it does not matter whether one uses 5 KeV Ne$^+$ or 8 KeV Ar$^+$. However, the average backscattering energies (kinetic energies) for these ions are ca. 1363 and 365 eV, respectively. Thus, the Ne$^+$ ion is moving much faster than the Ar$^+$ ion. As a consequence, the Ne$^+$ ion will have a much shorter interaction time with the surface than the Ar$^+$ ion during backscattering. This longer interaction time for Ar$^+$ gives it more time to be neutralized and thus the LEIS signal of Ar$^+$ backscattering off of ^{58}Ni and ^{59}Co is greatly reduced. This shows that, in addition to selecting the projectile ion that maximizes mass resolution, its effect on signal amplitude must be taken into account. Therefore, the energy of the backscattered ion in LEIS is another important factor to consider in optimizing an experiment.[12]

LEIS is primarily considered to be a surface analysis technique, and this is arguably its greatest strength. Nevertheless, scattering from deeper layers occurs and provides additional important information. The information depth for LEIS is 5 – 10 nm. LEIS is unique in its ability to nondestructively provide depth resolved information over this range, yielding much higher depth resolution than RBS.[12, 14] Because this depth profile is obtained without the need for sputtering, it is often called a static depth profile. Of course, sputter depth profiling is performed in both XPS and ToF-SIMS, but the corresponding sputtering process can rapidly scramble the

composition of the outermost layers. Figure A5.4a illustrates the interesting mechanism by which static depth profiling information is obtained in LEIS. For a surface scattering event like the one illustrated in Figure A5.4a to be detected, the incident ion cannot be neutralized when it is scattered. However, when a noble gas ion enters a solid it *is* neutralized and travels through the solid in this uncharged form. As it moves along, it loses energy due to electronic and nuclear stoppage events. At some point, a backscattering event may occur, which reverses the trajectory of the atom and directs it out of the solid. In its neutral state, the projectile will not be detected by the instrument. Fortunately, when neutral noble gas atoms leave a solid, a fraction of them are reionized. But unlike most of the processes considered to this point, which can be explained by classical physics and are independent of chemical bonding or other such complexities, this reionization depends on the surface chemistry of the sample. For example, due to resonance between the core electron levels of He atoms and oxygen atoms, oxygen is particularly effective at reionizing helium atoms as they leave the surface of a sample. Therefore, the magnitude of the depth signal tends to scale with oxygen concentration at the outer surface of a sample.[12] Backscattering from atoms that are below the surface results in the long, relatively flat tails/steps present in Figure A5.4. The depth of an analyte within a material corresponds to the lengths of these tails. More specifically, the lengths of these tails can be converted to physical depths within the sample if the energy loss per depth interval (eV/nm) is known for the energy used. This can either be measured directly from known samples or calculated by use of modeling software for ion implantation such as TRIM/SRIM.[23-25] Software for analyzing RBS data has also been successfully applied to LEIS static depth profiles.[26]

Figure A5.4b shows the theoretical LEIS spectrum for the ZrO_2 film on Si shown in Figure A5.4a. The tall, sharp Zr_{surf} peak at high energy in the spectrum confirms the presence of this

element at the outermost surface of this sample. This sharp signal shows a flat tail, labeled Zr_{depth}, towards lower energy. In accord with the previous discussion, this tail is due to ions that have entered the solid, been neutralized, undergone backscattering (by Zr atoms), and been reionized during their emission from the solid. Their reionization was favored because ZrO_2 is an oxide. Obviously deeper Zr atoms in the film correspond to signal on the tail that is further from the Zr_{surf} peak. Below this tail for Zr is an arrow pointing to where the signal for silicon would appear if silicon atoms terminated the material. They do not, and no signal is observed here. The next lower signal in energy labeled O_{surf} is from surface oxygen atoms. The presence of this peak and the Zr_{surf} peak confirm that this solid is terminated with these atoms. Finally, there is a step labeled Si_{depth}. This signal is due to backscattering from silicon atoms below the ZrO_2 film. Notice that unlike the Zr_{surf} and Zr_{depth} signals that are fused together in Figure A5.4b the hypothetical Si_{surf} and real Si_{depth} signals are separated in energy because of the presence of the ZrO_2 film.

One of the best ways to come to understand a new technique is to study the real data it produces. Accordingly, in Figure A5.5 we show a series of real LEIS spectra from the atomic layer deposition (ALD) of ZrO_2 onto silicon. ALD is a technique for producing highly conformal thin films, and films deposited by ALD are very relevant to semiconductor manufacturing.[27-30] Each ALD cycle here consists of the appropriate two half reactions. These surfaces were cleaned with atomic oxygen prior to analysis, and therefore the outermost layer of the material is expected to be fully oxidized. The spectra in question (see Figure A5.5) were obtained after 10, 20, 30, 40, 50, 70, and 100 ALD deposition cycles. These real spectra correspond to the idealized representation of this system and LEIS spectrum in Figure A5.4. These spectra primarily contain three peaks that are assigned, based on their backscattering energies, to O, Si, and Zr. Qualitatively, the positions of these signals on the energy scale correlate with their mass numbers – Zr is the heaviest atom,

which produces the highest backscattering energy, followed by Si, followed by O. All of this is reasonable. The signal from the Si substrate is initially rather intense, and it has a tail (high background) to lower energy that corresponds to signal from subsurface atoms. The fact that there is *any* signal from the Si substrate is quite interesting. The idealized view of ALD is that it creates perfectly uniform and conformal layers on a substrate, i.e., one might argue that under ideal conditions even a small handful of ALD cycles should completely cover the substrate with ZrO_2. Clearly this is not the case after even 10 deposition cycles. Two possibilities here are (i) that the ALD cycles have led to submonolayer deposition of Zr that is uniformly dispersed across the surface, leaving a significant number of exposed substrate atoms, i.e., not very much material is depositing per cycle, or (ii) that growth of the ZrO_2 is occurring from nucleation sites on this material, which is also leaving a considerable amount of the original surface exposed. Atomic force microscopy or high resolution scanning electron microscopy would help elucidate the actual surface structure. Again, the multi-instrument characterization of materials is often important for these types of problems.[31-33] For now, it is enough to know that LEIS has suggested that some rather interesting complexity is present in this ALD.

The general trends in the peak intensities in Figure A5.5 are consistent with the ALD of ZrO_2. The substrate peak, labeled 'Si', gradually decreases in intensity with increasing number of deposition cycles, which is perfectly consistent with another material gradually covering the substrate. At the same time, the Zr signal is increasing in intensity, i.e., the expected deposition and increasing surface coverage of ZrO_2 is occurring. Interestingly, the oxygen signal stays nearly constant throughout these depositions, suggesting that its surface concentration stays nearly constant. This is reasonable because the samples were all treated with atomic oxygen prior to analysis. This result is also consistent with oxygen in SiO_2 at the surface being replaced with

oxygen in ZrO_2, such that the oxygen concentration at the surface stays roughly constant. As the Zr signal increases in intensity, the tail to its low energy side also increases in intensity. At 100 deposition cycles, this tail is initially flat, suggesting a uniform concentration of Zr to some depth below the surface. The length of the tail corresponds to a thickness of about 2.5 – 3 nm of ZrO_2. The tail then decreases in intensity, which suggests that lower in the film the concentration of Zr has decreased. At 100 deposition cycles, the Si signal is finally gone – all the silicon surface atoms are covered. Quite a few ALD cycles were required to completely cover the substrate. These results are consistent with ZrO_2 growth from nucleation sites, i.e., growth here does not take place as perfectly homogeneous, uniform layers but from select locations. In summary, the real spectra in Figure A5.5 correspond to the rather complex, and interesting, deposition of ZrO_2. It is clear how valuable the remarkable surface sensitivity of LEIS is in this problem.

Finally, we see in Figure A5.5 another analogy between LEIS and RBS. Like LEIS, in RBS incoming projectile ions scatter with greater energy from heavier atoms. Thus, an ideal situation in RBS is the analysis of heavy atoms on a light substrate because the signal from the heavy atoms will be well separated from the substrate signal and most easily analyzed/quantified.[32] These signals often have little or no noise around them. Note that we have this situation for the Zr signal, especially for lower numbers of deposition cycles.

A5.5. LEIS Instrumentation[34]

As noted above, LEIS has been in use since the late 1960's. However, recent developments have dramatically improved its sensitivity and applicability.[7, 12] Here, we discuss some of the basics of LEIS instrumentation, including recent advances in instrument design. The main

components of a LEIS instrument are a noble gas ion source and an energy analyzer/detector for measuring the energies of backscattered particles and for quantifying this signal. Obviously, ion optics are needed to control the incoming ion energy, to focus the probe beam, and to set the pass energy into the kinetic energy analyzer. LEIS analysis takes place under ultra-high vacuum conditions, requiring a vacuum chamber with associated pumps, gauges, and load-locks. Given the extreme surface sensitivity of LEIS, sample preparation is of vital importance. Many LEIS instruments include a sample preparation chamber in which samples are cleaned, cleaved, heated, and/or treated with various gasses to simulate the operating conditions of the materials being analyzed. If the samples cannot be prepared *in situ*, the preferred type of cleaning in LEIS is treatment with atomic hydrogen or oxygen. These species can remove surface contamination without causing sputter damage. In comparison, sputter cleaning and plasma cleaning bombard a surface with high-energy particles, which causes some degree of material removal and surface rearrangement.

The most common type of LEIS instrument is a converted XPS instrument. The electrostatic analyzers (ESA) commonly used in XPS measure the kinetic energies of surface-emitted photoelectrons. To use an ESA for LEIS it is only necessary to reverse its polarity to accommodate particles with positive charges. A hemispherical ESA configured for LEIS analysis is shown in Figure A5.6. Here, the two main components are a set of ion optics that set the pass energy, and a pair of concentric hemispheres with applied voltages. Incoming ions with too little energy collide with the negative hemisphere, while ions with too much energy collide with the positive hemisphere. Only ions with the correct pass energy maintain a stable trajectory through the analyzer and reach the detector.

The advantage of using a converted XPS instrument for LEIS analysis is that for the additional expense of installing a noble gas ion source, a single instrument can serve both functions. However, the geometry of a hemispherical ESA only allows the capture of a small fraction of the total number of backscattered ions. Since the goal in LEIS is almost always to analyze the outermost layer of the material, and the surface can only take a limited ion dose before surface damage from the probe beam influences the analysis, the entrance apertures of the ESA are usually opened to the maximum amount possible to achieve sufficient sensitivity. This results in a spread of several degrees in the accepted backscattered angle, Θ, represented by the dotted lines above the sample in Figure A5.6. As indicated in Equation (A5.1), the energy of backscattered particles depends on Θ, so a spread in Θ results in peak broadening and concomitant loss of mass resolution. For example, using 3 keV He^+ ions at a scattering angle of 145° and a spread in the angle of ± 5°, the peak for ^{65}Cu is broadened by 29 eV. This corresponds to the difference in scattering energy separating Cu and Zn (it is nominally 24 eV), so their identification becomes challenging. As discussed in the previous section, heavy elements are often analyzed with heavier projectile ions. If we tried to resolve Cu and Zn using this same instrumentation, but with 5 KeV Ne^+ ions as the probing beam, the nominal spacing between these signals increases to 88 eV. This is positive. Unfortunately, however, we get an energy spread of 98 eV from the angular spread in Θ. Obviously this difference is large enough that it is again challenging to distinguish these neighboring peaks, especially when other sources of peak broadening are taken into account. For heavier elements, the effect of peak broadening by the wide acceptance angles employed in converted XPS instruments is even more pronounced. Thus, LEIS instruments derived from XPS systems are usually used only with He^+ ions and are not well suited for resolving analytes of high nuclear mass.

Even with a wide acceptance angle, a high ion dose may still be required to achieve a good signal-to-noise (S/N) ratio in a converted XPS instrument, resulting in sample damage. That is, the first ions to backscatter from a region provide information about the pristine surface. However, any ions that strike a sputtered region will provide information about the damaged surface. Therefore, an analysis must be performed within the static limit to obtain information about the pristine sample surface. The static limit, which is also an important consideration in ToF-SIMS, is the ion dose below which there is a low probability of the same spot being struck twice. With converted XPS instruments, the sensitivity of the analyzer may not be sufficient to get a good S/N ratio while maintaining an ion fluence below the static limit. This obstacle can be overcome by analyzing multiple spots on the same sample, but this approach requires a uniform surface.

The first papers on the double toroidal analyzer (DTA) were published in the 1980s.[10-11, 35] This design was refined over the next 20 years,[22] and finally incorporated into a commercial instrument. A schematic representation of a DTA can be seen in Figure A5.7. The DTA is similar in function to the hemispherical ESA used in XPS; in both cases, only an ion of the correct kinetic energy can traverse the space between two charged plates without colliding with one of them. With this geometry, the probe beam strikes the sample vertically, and a nearly 360 degree azimuth of backscattered ions is collected. With this large azimuthal collection angle, it is possible to sample a very narrow range of backscattering angles, Θ, while still collecting a much larger number of ions than with a hemispherical ESA. The typical spread in Θ for an analysis with a DTA-equipped instrument is 1° - 2°, which clearly results in much less peak broadening than with a hemispherical ESA instrument. Accordingly, instruments with DTAs are suited for use with all types of noble gas ions, not just He$^+$, and practically all pairs of elements can be separated.[36] Thus, DTA equipped instruments can achieve much lower detection limits before the static limit of analysis is reached.

ION-TOF has commercialized this technology in their Qtac[100] instrument, which is a dedicated, commercial LEIS instrument. In addition to incorporating a DTA into their design, ION-TOF has introduced other features that further improve the performance of the instrument. The first that bears mentioning is a position sensitive detector. As shown in the Figure A5.7, the DTA can simultaneously pass ions of a range of energies (5 - 10 % of the pass energy). Ions of different energies have different trajectories through the analyzer. Thus, they strike the position sensitive detector plate at different positions, so that their individual energies are determined based on the position at which they strike it. This arrangement has the advantage of accepting a higher scattered ion flux without loss of energy resolution. Similar technology has long been available for use with hemispherical ESAs, but a considerable amount of engineering was required to make a position sensitive detector compatible with the DTA geometry while covering a wide energy range of parallel detection. Another feature included in the instrument is time-of-flight-filtering (ToF-filtering), which allows the backscattered projectile ions to be isolated from sputtered background ions of the same energy. The most abundant background ion in any LEIS analysis is from adsorbed hydrogen that has been sputtered from the sample and ionized in the sputtering event. These secondary hydrogen ions may have the same kinetic energies as backscattered noble gas ions. However, their lower mass gives them a much higher velocity resulting in a much shorter time-of-flight. Therefore, by detecting only ions with the correct flight time for each energy, this background signal can be eliminated. This is especially beneficial in the low-energy region of a LEIS spectrum, where the background signal can be strong enough to obscure the peaks of the light elements.[15] For example, Figure A5.8 shows a LEIS spectrum taken with a conventional XPS-based instrument.[37] The very high background at lower scattering energies is obvious. These

advances in LEIS instrumentation have dramatically improved the sensitivity and applicability of this technique to a variety of samples.

A5.6. A Photographic Tour of the Qtac[100], a Double-Toroidal Analyzer-Equipped LEIS Instrument[38]

Figure A5.9 shows a Qtac[100] LEIS instrument with the locations of a few key components labeled. Clearly, a LEIS instrument will require an ion source (A), a gun for accelerating the ions (B), and an energy analyzer (top of the main chamber, (D)). In addition, instruments can be equipped with sputter guns (C) for depth profiling. In LEIS, ions must travel rather long distances without colliding with other atoms besides those at the sample surface, i.e., have long mean free paths. Thus, LEIS is carried out under ultra-high vacuum (UHV) conditions. Figure A5.9 also shows some of the key components that are necessary for UHV analysis. These include the analysis chamber (D) – these kind of look like divers' helmets, a sample introduction chamber (E, load lock), and a sample manipulator (transfer arm) (F) to move samples from the load lock to the UHV analysis chamber. Almost all UHV analysis systems have this type of two-chamber design – an introductory chamber and an analytical chamber. The purpose of this important design feature is to reduce contamination in the main chamber so that pump down times are not excessively long. The vacuum pumps for the system are housed beneath the analysis chamber (G), which is typical of many UHV surface analytical instruments.

Obviously a LEIS system can be configured with/connected to other analytical instruments. Figure A5.10 shows a combined LEIS/ToF-SIMS instrument. The main chambers of the two

instruments are connected so that samples can be transferred from one instrument to the other without breaking vacuum. Clearly this capability (i) adds noticeably to the cost of the instrument, but (ii) allows sample analysis at a level that is not possible if the material must come in contact with the air prior to or between analyses.

Figure A5.11 shows the sample preparation and loading process for the Qtac^{100}. Because of the extreme surface sensitivity of LEIS, sample cleanliness is very important. Gloves are used for handling samples and the sample holder. We note the irony that gloves are worn in most chemistry laboratories to protect the workers from chemicals, while gloves are worn in most surface analysis labs to protect the samples and instruments from humans! Samples with dimensions of *ca.* 15 mm x 15 mm fit on these sample holders, and depending on the instrument configuration, one or several samples may be loaded at a time. The sample holders connect to a holder pen for easy handling. Because of LEIS' surface sensitivity, adventitious carbon can quickly reduce or eliminate surface signals. The adventitious hydrocarbon typically gives no signal since it is often H-terminated, and LEIS is not sensitive to hydrogen. Accordingly, atomic oxygen or hydrogen cleaning is a common step in sample preparation, where each sample may require a different cleaning time. The samples are typically given increasing doses of atomic oxygen until a stable instrument response is obtained. An optional feature for the Qtac^{100} is an environmental chamber in which samples can be heated, cooled, and/or dosed with various gasses. Single-sample sample holders are practical in LEIS because each sample may need different cleaning times or undergo different treatments in the environmental chamber.

Figure A5.12 shows a close-up view of a Qtac^{100} instrument with some key components labeled. This particular instrument is configured to hold multiple sample holders simultaneously. It also has an optional environmental chamber installed in which the samples may be heated and

dosed with various gases. Identified in this picture are the atomic oxygen generator (A), a sputter gun for sputter depth profiling (B), the analytical (main) chamber (C), the sample introduction chamber (D), the sample preparation chamber (E), and the environmental chamber (F). Three separate transfer arms are visible in this picture – they move samples between the various chambers. Note the small size of the sample introduction chamber on this instrument. Small introduction chambers make for faster pump downs and help minimize contamination of the analytical (main) chamber. Figure A5.13 shows a screenshot of the instrument software. Practically all of the instrument components are controlled through this software, which includes tools for peak fitting spectra.

A5.7 Quantitation in LEIS[39]

We now discuss the quantitative nature of LEIS, why LEIS is inherently quantitative, and how quantitation is accomplished in LEIS. We also mention some of the few cases in which LEIS is not quantitative.

LEIS is inherently quantitative.[12] Thus, unlike ToF-SIMS, there is no matrix effect, with a few exceptions that will be noted below. The governing equation of LEIS (Equation A5.1) is derived entirely from classical principles, where this process (essentially the ricochet of a lighter particle off of a heavier one) occurs independently of the chemical environment of the analyte ion. However, a factor that influences the backscattered intensity is the probability of the ion being neutralized during the scattering event. Recall that the analyzer only detects ions, not backscattered neutrals. Because neutralization effects are dominated by the binary interaction between the ion and the analyte atom, and because of the relatively high energy and short interaction time of the

collision, the chemical environment of the atom and/or the state of the surface as a whole is irrelevant. Because there is no matrix effect, the signal in LEIS is directly proportional to the surface coverage of elements, which makes quantitation straightforward. In contrast, the strong matrix effect in ToF-SIMS causes signals of certain ions to be enhanced or suppressed depending on which other atomic species/compounds are present. In some cases, this can be used advantageously to enhance certain signals, or most of them, as in metal assisted SIMS (MetA-SIMS).[40-42] However, it also means that for most circumstances ToF-SIMS is at best semi-quantitative. While there is no matrix effect in LEIS, each element has its own sensitivity factor. In this regard it is analogous to XPS. Indeed, each element has a unique LEIS backscattering cross-section and also a neutralization cross-section. These vary depending on the projectile ion and projectile energy used. While scattering cross sections can be calculated, there is currently no computational model for predicting neutralization cross sections, and in practice sensitivity factors are established empirically, either by the use of standards or correlation plots.[12] In some sense this is the same as in ToF-SIMS, where the sputtering process is quite well understood and can be modelled by molecular dynamics simulations, while the ionization effects are still not possible to predict.

The data in Figure A5.14A illustrates the absence of a matrix effect in LEIS. This data was collected from tungsten surfaces onto which different amounts of bromine were adsorbed. The signal for tungsten is plotted on they y-axis, and the signal for bromine is plotted on the x-axis. Because LEIS measures atomic surface coverages, as the surface coverage for bromine increases, we should see a decrease in the tungsten signal, and *vice versa*. This is exactly what the data show. When the tungsten signal is high, the bromine signal is low, and *vice versa*. The fact that there is no matrix effect is proved by the linear, anticorrelated relationship shown here. If there were a

matrix effect, we would see a departure from these linear trends. For example, if bromine had a suppressing effect on the tungsten signal, we would see the tungsten signal increase in a non-linear fashion as the bromine concentration decreased. Numerous experiments with other two-component systems have shown similar results. For example, Figure A5.14B shows the steady increase in the LEIS Zr signal in the atomic layer deposition (ALD) of ZrO_2 onto SiO_2 with the expected, concomitant decrease in the Si signal. The linear relationship between these signals further confirms the absence of a matrix effect in LEIS. Besides serving as a proof that there is no matrix effect, the anticorrelation plots in Figure A5.14 are also used to obtain the sensitivity factors for the analytes. When such a plot can be constructed, the signal for 100% surface coverage of each analyte can be obtained by extrapolating to the axes. For the example of W/Br system shown in Figure A5.14A, the signal for the 100% tungsten surface coverage is about 650 arbitrary units, and the signal for 100% bromine surface coverage is at about 175 arbitrary units.

Correlation plots are useful when two (or sometimes three) components in a series of samples vary in coverage.[43] In those cases, the sensitivity factors can be determined without knowledge of any of the sample surface compositions and without pure reference materials. However, samples with many analytes require the use of standards. Pressed oxide powders are the most commonly used reference materials in LEIS. Many samples of interest are oxides, so oxide powders are a natural choice for these applications. Furthermore, samples are often cleaned with atomic oxygen in preparation for LEIS analysis, and samples cleaned in this way will have their outer surfaces oxidized, again making oxide powders a good choice as standards. Most metal oxides are oxygen-terminated, and the metal atoms in the structures are shielded to some degree by oxygen atoms. In these cases, e.g., the samples illustrated in Figure A5.14B, the metal signal is taken to be representative of the metal oxide coverage. For example, if pure zirconium oxide

powder gives a Zr signal of 100 counts for a given set of analysis conditions, then a sample that yields a signal of 50 counts will have a surface coverage of 50% ZrO_2. LEIS is largely insensitive to surface topography, so the inherent roughness of a pressed powder standard poses no problems. One notable advantage that powders have over their bulk counterparts is that they tend to dilute surface contamination. Contaminants often diffuse to the outside of a material to minimize surface energy. Since bulk materials have low specific surface areas (surface area per unit mass), contaminants can become concentrated at their surfaces. For example, a 1 mm thick sample has on the order of 5 x 10^6 atomic planes. If the bulk concentration of a contaminant is 0.2 ppm, there are enough atoms of the contaminant to form a complete layer on the surface, provided all the contaminant atoms are mobile. Powders, with their much higher specific surface areas, tend to dilute these contaminants. Of course, not all samples are oxides. When metals are analyzed, pure metals can be used as standards, although some degree of sputtering may be necessary to remove the native oxide layer. In principle, any material having a known coverage of the element of interest and being reasonably easy to prepare is suited as a reference, e.g., PTFE (Teflon) for fluorine.

There are some circumstances in which LEIS may be subject to a matrix effect. Most often, these occur in situations where the model of a purely binary, inelastic collision interaction between two particles no longer applies. One such example is the difference in sensitivity factor between sp^2 and sp^3 hybridized carbon. The difference in response here is a result of resonant charge exchange between the partially occupied 1s level in the He^+ ion and the filled valence band of graphitic carbon. For sp^3 carbon, this additional source of neutralization does not exist, so the sensitivity factor is significantly different. In some cases, this effect can be turned into something useful. By using this difference and its dependence on the primary energy, graphitic and sp^3 carbon can be distinguished. There may also be tunneling between the partially occupied level of the noble gas

ions and the valence band of the material being analyzed – for materials with low work functions, only a small energy barrier must be tunneled through by an electron to neutralize the ion. Since this no longer is a binary interaction, but rather an interaction between the ion and the whole surface, quantification is difficult. Typically, these cases depend on the nature or energy of the projectile, and these matrix effects can be detected or even overcome by changing the primary ion beam energy or the projectile ion used.

In summary, the principle strength of LEIS is that it provides quantitative information about the outermost atomic layer of a material. In general, LEIS has no matrix effect – it is inherently quantitative; its signals are directly proportional to surface coverage. Quantitation in LEIS can be accomplished either with reference samples or, for simple systems where multiple samples are available, by way of a correlation plot. Standards are often chosen based on the goal of the analysis. If the goal is to quantify the concentration of an oxide, oxide powders are used, while metals are used when metallic samples are probed. With the resulting quantitative information, materials for which performance strongly depends on surface composition can be understood at a deeper level.

A5.8 Comparison of LEIS to Other Surface Analytical Methods[44]

Table A5.1 compares the attributes of LEIS, ToF-SIMS, and XPS. Of course, ToF-SIMS and XPS are two of the most commonly used surface analysis techniques for probing the surface chemistry of materials. Indeed, for years, XPS and ToF-SIMS have been used in tandem for surface analysis because of their powerful complementarity. We have written on XPS and ToF-SIMS a

number of times in recent tutorial articles in Vacuum Technology and Coating,[45-47] and in our papers.[48-52]

As Table A5.1 shows, LEIS is more surface sensitive than the other two techniques, which are already very surface sensitive. LEIS acquires static depth profiles (see below) in a more natural way than XPS, and ToF-SIMS does not have this capability. LEIS can also be used to acquire dynamic depth profiles in the same way as ToF-SIMS and XPS, i.e., in conjunction with a sputter gun. Its analysis time is very fast (minutes), which is generally faster than for XPS and comparable to the acquisition time for ToF-SIMS. Its detection limits are generally poorer than those for ToF-SIMS (extremely low) and XPS (moderately low), especially for lighter elements like boron. However, to be fair to LEIS, XPS averages its signal over 10-20 atomic layers, while LEIS only gets its signal from the outermost layer. Therefore, with regards to the detection limit from the outermost atomic layer, LEIS is more sensitive than XPS. LEIS has essentially no matrix effect – in this regard it is more similar to XPS than ToF-SIMS. Of course, ToF-SIMS shows a significant matrix effect, which is one of its disadvantages. Like XPS, one of LEIS' greatest strengths is that it gives quantitative results. This is in contrast to the limited quantitative information that is usually available from ToF-SIMS. LEIS does not give oxidation state information about elements at surfaces, while XPS provides this information in a direct way,[52] and ToF-SIMS does so indirectly. In addition, LEIS does not provide molecular information about surfaces, while ToF-SIMS does so in a direct way and XPS gives it indirectly. The lateral resolution of ToF-SIMS (micron to submicron) is the highest of the three techniques, and those of LEIS and XPS (ca. 10 μm) are similar. The cost of the instrumentation for all three techniques is quite high. Perhaps a fair concluding statement would be to say that while no surface analytical technique can provide all of the information one might desire about a surface, LEIS, ToF-SIMS, and XPS are clearly

complementary so that they can provide powerful surface and material characterization when used together. A clear advantage of employing all three techniques is that they probe materials at different depths. In summary, it is clear that LEIS has significant capabilities that neither XPS nor ToF-SIMS has. We are confident that in the future we will see more surface analyses that employ all three techniques.

Table A5.1. Comparison of attributes of LEIS, ToF-SIMS, and XPS.

Properties	LEIS	ToF-SIMS	XPS
Surface sensitivity	Outermost atomic layer	a few atomic layers	*ca.* 5 nm
Static depth profiling	Inherent, *ca.* 10 nm	No	If multiple scans taken at multiple angles (angle resolved XPS), *ca.* 10 nm
Dynamic depth profiling	With sputter gun	With sputter gun	With sputter gun
Analysis time per spectrum	Typically minutes	Typically minutes	Somewhat longer
Detection limits	a few % of a monolayer for the lighter elements, up to 0.1 – 1 % for the heavier elements	ppm	0.1 – 1% of a monolayer
Matrix effect	Essentially none	Strong	Essentially none
Quantitative results	Excellent	Relatively poor	Very good
Oxidation state information	None	Somewhat, through molecular fragments	Yes
Molecular information	None	Yes, through molecular fragments	Yes, through chemical shifts
Lateral resolution	ca. 10 microns	Submicron	*ca.* 10 microns
Cost of instrumentation	High, *ca.* $1e6	High, *ca.* $1e6	High, *ca.* $0.5-1e6

A5.9. Static Depth Profiling in LEIS[44]

Obviously, LEIS is not the only technique that can provide depth profile information about the outer ca. 10 nm of a material. Angle resolved XPS (AR-XPS) can also yield this information without the need for sputtering. However, it is generally difficult to obtain quantitative depth information from AR-XPS data. That is, AR-XPS analyses are usually valuable in a qualitative to perhaps semi-quantitative way, but more precise information requires modeling, which can be challenging.[53] Thus, the static depth profile information provided by LEIS, which is obtained in a more direct fashion, is especially useful for very thin films, e.g., in semiconductor devices. It provides better depth resolution than AR-XPS, where the depth resolution in LEIS is high (0.2 – 1 nm, depending on sample composition).[20] The interpretation of LEIS depth signals is probabilistic – it depends on the number of possible paths a particle can take to get to and from a certain depth. Obviously, this number increases with depth. Thus, the uncertainty on the depth resolution in LEIS is less from signals that originate close to the surface, so thinner films are better resolved than thicker ones. LEIS static depth profiles also have clear advantages relative to sputter depth profiles. They avoid the mixing of atomic layers that almost inevitably results when samples are sputtered. This attribute of LEIS static depth profiles has been applied to study diffusion in very thin films.[20, 54]

LEIS is a powerful tool for performing sputter depth profiles. This capability is especially useful for thicker samples (up to about 100 nm). Sputter depth profiles in LEIS provide some unique advantages relative to XPS and ToF-SIMS. The first is that the extreme surface sensitivity of LEIS yields a much higher (finer) depth resolution than can be achieved in XPS or ToF-SIMS, provided the sputtering conditions are chosen to keep the atomic mixing low. Second, the quantitation of LEIS surface signals is straightforward. Third, the static depth profile and the

sputter depth profile in LEIS provide complimentary information. Ter Veen *et al.* demonstrated that the static depth profile information from an Si/SiO$_x$/W/Al$_2$O$_3$ ALD stack provided a useful preview to subsequent sputter depth profiles, making it possible to identify artifacts that result from sputter beam effects.[55] A fourth advantage of combining LEIS and sputter depth profiling is that because many spectra are obtained with varying compositions within the depth profile, sensitivity factors for elements can be obtained without the need for reference materials. This further simplifies the process of using LEIS to obtain quantitative depth profile information. Ter Veen *et al.* explain this method in detail in their article.[55]

A5.10 Application of LEIS to Semiconductors[44]

Critical dimensions in semiconductor devices continue to decrease. Therefore, surface sensitivity is becoming an increasingly important attribute for techniques used to analyze thin films in them. A 2006 study by Stokhof and coworkers takes advantage of the extreme surface sensitivity of LEIS to study the nucleation and growth (to closure) of WN$_X$C$_Y$ films deposited by ALD with the goal of better understanding copper diffusion barrier layers in semiconductor devices.[56] Their article notes that as a consequence of shrinking critical dimensions, copper has replaced aluminum as an interconnect material in semiconductor devices. However, while copper has superior conductivity to aluminum, a barrier layer must be used with it to stop unwanted diffusion into neighboring materials. To stop this diffusion, the barrier must be made from a material with low copper diffusivity, must coat copper conformally, and must form a completely closed coating. This diffusion barrier should also be as thin as possible so that the advantage gained from copper's increased conductivity is not entirely negated by the wasted volume and added resistivity of the

barrier layer. ALD is a coating method that can meet these demands, although sputtered barrier layers remain dominant in the industry.[57]

In Stokhof and coworkers' study, WN_XC_Y was deposited by ALD over two different dielectric layers: SiO_X, deposited by plasma enhanced chemical vapor deposition (PECVD), and Aurora® 2.7, a proprietary low-k dielectric. The thickness of the WN_xC_Y layer was controlled by varying the number of ALD cycles. After the first ALD cycle, a strong W LEIS peak appeared at the surface, indicating that the deposition of the WN_XC_Y film had begun. However, a Si surface signal remained clearly visible. This Si surface signal only disappeared after 40 ALD cycles, indicating film closure. The trends were the same for deposition over the Aurora® 2.7 dielectric material, with film closure again occurring after 40 ALD cycles. For this study, the growth rate was 0.8 Å per ALD cycle, meaning that a film thickness of approximately 3.2 nm was needed to achieve a completely closed film. Here, the surface sensitivity of LEIS permitted an analysis that would have been difficult with XPS or ToF-SIMS because these techniques have probe depths that exceed the thicknesses of most of the WC_XN_Y films examined in this study.

While the closure of an ALD-deposited WC_XN_Y film over dielectric layers is a fairly specific example, it again illustrates an important problem—films in semiconductor devices are becoming thinner than the depth of analysis of the dominant surface analysis techniques. For example, gate oxide thicknesses in semiconductors have been in the sub 10 nm range since the early 1990's.[58] When semiconductor technology reached the 22 nm node in 2011, the gate oxide thickness was down to 0.5-0.8 nm.[58] The target for diffusion barrier layer thickness at the 22 nm node is 3 nm.[27] This downward trend in film thicknesses will probably continue as technology advances to the 10 nm and 7 nm nodes. In short, as films get thinner, surface sensitivity will become increasingly important for understanding film properties in semiconductors.

Diffusion is an important process in the fabrication of microfabricated devices. Sometimes it is wanted, as when a wafer is heated to allow dopants to diffuse through a material. Other times, it is destructive, as when copper from interconnects poisons neighboring materials. Because of its extreme surface and near surface sensitivity, LEIS is a powerful tool for understanding diffusion in thin films. Indeed, LEIS' short analysis times make it suitable for time resolved studies. LEIS systems can be outfitted with heating stages to perform *in situ* diffusion studies.

While various useful conclusions can often be drawn about diffusion in a sample simply by observing the changes in the surface signal when a sample is heated, the static depth profile provides more useful and direct information about diffusion in thin films. One reason for this is that surfaces may have different properties than their underlying layers. In 2009, De Rooij-Lohmann *et al.* studied diffusion non-destructively using LEIS static depth profiling.[20] The total depth of their analysis was 5-10 nm. In particular, the authors studied the diffusion of a Mo/Si system (see Figure A5.15). These materials find use in extreme UV optics. In order to determine the stopping power of silicon, S_{Si}, the authors prepared Mo films covered with Si films of known thickness ($4 - 7$ nm). From this data, they determined that S_{Si} was 36 ± 3 eV/nm. The samples were then analyzed during heating to 500 °C over a period of $40 - 50$ seconds, and the shape of the Mo depth signal was used to extract the diffusion coefficient of Mo in Si for this system. Figure A5.16 shows these 500 °C LEIS results. In a follow up study in 2010,[54] they studied the more complex Mo/B$_4$C/Si system, where B$_4$C acts a diffusion barrier. Using a methodology similar to the one employed in their previous study, they were able to show two distinct diffusion regimes, which corresponded to amorphous and nanocrystaline MoSi$_2$. The results they obtained by LEIS were supported by transmission electron microscopy (TEM) and hard X-ray XPS (HAXPS) analyses.

The extreme surface sensitivity, straightforward quantitation, static depth profile information, and excellent sputter depth profiling capabilities in LEIS make it a potentially powerful tool for studying semiconductor systems. Its utility for studying the closure of very thin films and understanding diffusion has been noted. We anticipate that because of the recent advances in LEIS instrumentation, there will be more LEIS studies on semiconductor materials.

A5.11 LEIS of Solid Oxide Fuel Cells[34]

We now discuss some recent publications in which high-sensitivity LEIS has been used to probe the surfaces of materials used in solid oxide fuel cells (SOFCs).

As is the case with all fuel cells, SOFCs directly oxidize a fuel to produce electricity. This is in contrast to the more common combustion-based electrical generation tools that convert fuels to thermal energy, thermal energy to mechanical motion, and then mechanical motion to electricity. As the name implies, SOFCs use solid oxides as electrolytes. Typically, this electrolyte transports oxygen anions from the cathode to the anode. The solid oxide electrolyte is the defining feature in an SOFC, but the cathode and the anode materials must also be able to sustain high temperatures and transport charge carriers.[59] These cathodes and anodes are usually made of ceramics or ceramic-metal hybrids. SOFCs are being researched for their application to clean, efficient energy generation using a variety of fuels. The major obstacle to the widespread adoption of SOFC technology is their high operating temperature.[59] The materials used in SOFCs must function at between 500 and 1000 °C to conduct oxygen anions. These temperature constraints often require that SOFCs undergo a lengthy pre-heating prior to operation, limit the materials that can be used in their construction, and shorten device life spans. This reduces the applicability and

341

increases the cost of this technology.[59] Therefore, much effort has gone into researching materials that can enable SOFCs with lower operating temperatures. The characterization of SOFC materials been an active area for LEIS.[18-19, 59-62]

Perovskite type materials are being heavily investigated for SOFC applications. These have the general chemical formula ABX_3, where A is a relatively large cation, B is a relatively small cation, and X is an anion that binds to both. There are other more complex variations of this structure that are also of interest. These are explained in more detail below, as well as in a paper by Druce et al.[16] Understanding the surface properties of the materials used as SOFC cathodes is important for improving these devices because oxygen exchange at their surfaces strongly influences device performance – before oxygen ions can be conducted through the electrolyte, O_2 molecules must be split and oxygen incorporated into the material. This is determined by the material's surface properties. With regards to SOFCs, Druce *et al.* noted that "… the exchange of oxygen, at elevated temperatures, between the solid and the ambient gas, mediated by the immediate surface, is a very important process as it determines the oxygen stoichiometry and hence the functional properties".[16] In addition, at elevated temperature, even minor contamination from the bulk of the ceramic can diffuse to the surface, and this can strongly limit its performance. Indeed, only a little bulk contamination is required to form a full monolayer of an alkaline earth oxide, which will significantly compromise the performance of the oxide.[62] Therefore, understanding which cations dominate the surface of the electrolyte is important for understanding oxygen transport through it.

Working towards understanding and improving SOFC cathodes, Burriel *et al.* recently performed a multi-instrument surface analysis of $La_{2-x}Sr_xNiO_{4+\delta}$, which is a promising material for intermediate temperature SOFCs (IT-SOFCs) (they operate from 650 to 800 °C).[19, 59] Prior to this

analysis, the outer surface of this material had only been studied computationally. The computational results indicated that the material would be terminated in nickel-oxide, where Ni is a B-type cation. Computational models of similar perovskite materials predicted that cathodes would be catalytically inactive if terminated in LaO, where lanthanum is an A-type cation. Burriel's characterization utilized crystal truncation rod (CTR) X-ray scattering, angle resolved XPS (AR-XPS), and LEIS to probe the outer few layers of the material. She notes in her paper that analyzing the outermost layer of a material can be challenging. Any exposure to the atmosphere contaminates a surface with adventitious carbon. Furthermore, as noted above, most surface analysis techniques average over several atomic layers and do not provide information specific to the outermost layer. The LEIS analysis was performed using a Qtac[100] instrument. Two single-crystal samples of different orientation were analyzed, both were cleaved and one was heat treated in air at 450 °C for 72 hours. Prior to analysis, all samples were cleaned with atomic oxygen to remove hydrocarbons. Because each element has its own sensitivity factor, high-purity oxide powders were used as standards to establish sensitivity factors and detection limits for each analyte.

A 5 keV ^{22}Ne$^+$ LEIS spectrum from her paper is shown in Figure A5.17. Contrary to the predictions of the computational model, the LEIS spectrum shows signals for the A-type cations, Sr and La, while no Ni is detected at the surface. Both of the samples produced similar results. While neither CTR X-ray scattering nor AR-XPS gave a quantitative analysis of the composition of the outermost layer, both provided information about the near-surface region. CTR-X-ray scattering is a modeling based technique (analogous in some sense to ellipsometry) – data are obtained and fit with either theoretical or empirical models, and conclusions about the material are drawn based on which model gives the best fit. In this case, a model of a La/Sr oxide terminated

343

material provided a good match to the experimental data with some deviations attributed to surface effects, while a model of an NiO_2 terminated material gave a poor fit. This is in good agreement with the LEIS results. Using AR-XPS, the ratio of lanthanum and strontium to nickel ($(La + Sr)/Ni$) ratio was calculated at depths ranging from 0.6 to 7.0 nm. The data were compared to a theoretical ratio based on the stoichiometry of the bulk material, which was calculated to be 2.0. At a depth of analysis of 7.0 nm, the measured ratio was at 2.3, close to the bulk value, while the ratios at depths of 1.8 and 0.6 nm were 8.5 and 5.3, respectively. These results indicate that the near-surface region is enriched in La and Sr, again supporting the La/Sr oxide terminated surface suggested by LEIS. When three established surface analysis techniques support the same conclusion, it is probably true, and of course, it is almost always better to probe a material with multiple analytical techniques than a single one.[32, 63-64]

These results challenged the previous computational models of oxygen transport through this cathode material. With regards to the role LEIS analysis played in this study, the author wrote, "…it is clear that the unique monolayer sensitivity provided by LEIS, complemented by other state-of-the-art surface techniques, can provide a complete picture of the surface and near-surface chemistry of this important class of materials", and that "…the new surface information provided by these techniques will significantly contribute to the understanding of surface processes in mixed conducting materials..."[19]

In another study, Druce et $al.$ used LEIS in conjunction with a sputter beam to depth profile three polycrystaline perovskite-based electroceramics for use in SOFC applications: $La_{0.6}Sr_{0.4}Co_{0.2}Fe_{0.8}O_{0.3-\delta}$ (LSCF-113), $GdBaCo_2O_{5+\delta}$ (GBCO-1125), and $La_2NiO_{4+\delta}$ (LNO-214).[16] LCSF-113 has the single perovskite structure, ABO_3, GBCO-1125 has the ordered double perovskite structure, $AA'B_2O_{5+\delta}$, where A and A' cations alternate in layers of the structure, and

LNO-214 has the Ruddelson-Popper structure, with a formula of $A_2BO_{4+\delta}$, where layers of the perovskite structure are interrupted by layers of AO with the rock salt structure. For this study, the samples were pretreated at high temperature in oxygen to mimic their operating conditions. As in the example above, the samples were cleaned with atomic oxygen prior to LEIS analysis to remove hydrocarbon contaminants. Three spectra at different sputtering depths are shown for each sample in Figure A5.18. Interestingly, spectra taken at different depths show different compositions. The dominant species at the surfaces of these materials are Sr, Ba, and La, for LSCF-113, GBCO-1125, and LNO-214, respectively. This means that for LCSF-113, the A-site cation terminates the surface. For GBCO-1125, which consists of alternating layers of two oxides, the A' site cation terminates the material, and for LNO-214, the A-site cation terminates the material. At its outer surface, LNO-214 additionally shows a Pb peak that is attributed to contamination in the starting materials used for the synthesis. Here, Pb is only detectable at the outermost surface, indicating that it preferentially segregates to the surface. With sputtering of this material, no Pb is observed and LEIS analysis gives concentrations corresponding to the theoretical bulk stoichiometry. Given that the properties of these electrode materials depend so much on their surface compositions, these experiments provide valuable information. They clearly demonstrate that the surfaces of these materials can vary significantly from their bulk compositions. The authors emphasize that while other surface analytical techniques have shown enrichment of certain species near the surface of these materials, LEIS, with its extreme surface sensitivity, was unique in its ability to provide information about the composition of the outermost layer.

While we have only shown two examples here related to the development of better materials for SOFC applications, it is easy to see how information obtained by LEIS would be generally useful for understanding a variety of materials, e.g., gas sensors, catalysts, etc.

In the examples highlighted here, LEIS has revealed how several materials proposed for SOFC applications are terminated. In one case the results were contrary to the predictions of computational models. Both papers highlighted herein noted that while other more conventional surface analytical techniques provide valuable information about the near-surface region of materials, only LEIS provides a quantitative elemental analysis of the outermost atomic layer. This definitive information about surface composition is obviously of value for the characterization and development of SOFCs, where surface composition plays an important role in catalysis and oxygen anion transport.

A5.12 LEIS of Catalysts[65]

The basic purpose of a catalyst is to speed up a chemical reaction by lowering its activation energy. Industrially, heterogeneous catalysts, catalysts that differ in phase from their reactants and products, are preferred because they are easily separable from chemical reagents. That is, they are more easily recovered and will not contaminate the product. In practice, this means that most industrial catalysts are solids.[66] Catalysts have changed our world. For example, the level of agricultural production needed to sustain the world's population would not be possible without the Haber-Bosch process for ammonia production, which depends on a heterogeneous catalyst.[66] Most industrially important building block molecules, such as ammonia, benzene, sulfuric acid, and styrene are synthesized with the help of heterogeneous catalysts.[67] Petroleum refinement also depends heavily on the use of heterogeneous catalysts.[67] Because catalysts are so pervasive, there is an ongoing need to characterize them, both to understand their fundamental science and also to better synthesize them.

Catalysis depends on reactants interacting with the catalyst in a way that favors the desired chemical reaction. In the case of solid catalysts this means that catalysis generally happens at the outermost atomic layer of the material. Accordingly, LEIS, with its extreme surface sensitivity, is especially well suited for analyzing these materials. And many heterogeneous catalysts are complex, multicomponent systems. For example, the catalyst used in the Haber-Bosch process consists of magnetite (Fe_3O_4) with 2.5-4% Al_2O_3, 0.5-1.2% K_2O, 2.0-3.5% CaO and 0.0-1.0% MgO.[66] In such materials, the surface concentration of a species can vary significantly from its bulk concentration. LEIS provides useful information in these situations by directly measuring the surface concentrations of all species. Additionally LEIS static and sputter depth profiles can be used to determine how the surface composition varies from the bulk stoichiometry. Ter Veen et al. published a short article on the application of LEIS to a catalyst.[43] They stated that: "…the availability of a technique that analyzes the chemical composition of this [outermost] layer is of crucial importance in the fundamental study of catalysis as well as in the optimization of industrial catalysts." In contrast, XPS, with its greater depth of analysis provides less information about the outermost atomic layer where catalysis takes place. An article by Celaya Sanfiz et al.[68] states that: "…in cases where conventional surface analytic techniques, such as XPS, do not show correlation with the catalytic activity, the extreme surface sensitivity of LEIS gives a direct relationship between composition and catalysis." To add to the utility of LEIS, LEIS instruments are often equipped with environmental chambers wherein the working environment of a catalyst can be simulated by heating it to a desired temperature and dosing it with gases. Here, a reaction can be rapidly quenched before the sample is transferred to the analytical chamber. This allows a surface to be studied at or near its operating state, giving insight into the surface composition of the catalyst

as it is used. LEIS is relatively insensitive to surface roughness so real industrial catalysts, not just model, planar systems, can be analyzed.

Below, we discuss two examples of LEIS studies of heterogeneous catalysts.

Celaya Sanfiz et al. performed a detailed analysis of an MoVTeNbO$_x$ catalyst, which is used for the selective oxidation of light alkanes, e.g., propane to acrylic acid.[68] Previously, this catalyst had shown enhanced activity after grinding. The authors were interested in studying the (001) plane of the M1 phase of the catalyst. It had previously been suggested that this plane had active and selective sites for partial oxidation reactions. When fractured (ground), M1 phase crystals expose their (001) plane. Accordingly, the authors coated catalyst crystals with silica and then ground them. In theory, the silica should have covered all the planes except for those that were exposed by fracturing during grinding, which, again, would preferentially expose (001) crystal planes. They used uncoated crystallites as a control, and analyzed the catalytic activity of the silica-coated and ground, and untreated crystals. LEIS played an important role in their analysis. First, it was used to determine whether the silica-coated samples had been completely coated. The absence of any surface signals except for Si and O showed that the coating was complete. Based on depth profile information from LEIS, the thickness of this coating was estimated to range from a few atomic layers up to about 20 nm. TEM supported this conclusion. LEIS was also used to determine how much catalyst surface was exposed during grinding. As expected, the percentages of V$_2$O$_5$, Nb$_2$O$_5$, MoO$_3$, and TeO$_3$ were much lower in the coated, ground samples than in the untreated samples. By comparing the signal ratios between the samples, the authors determined that 70% of the ground samples remained coated in silica, while 30% of the surface was freshly exposed. Here, LEIS yielded a much higher percentage of newly exposed surface area than did a shape analysis using SEM images, indicating that in addition to fracturing,

some silica was abraded from the particles during the grinding process. This hypothesis was supported bv TEM images taken post-grinding. To determine if the (001) plane played a special role in determining the selectivity of the catalyst, the authors compared the catalytic activity of the coated, ground sample to the uncoated one. When normalized for exposed catalyst area, the catalytic activity was about the same for both samples. Based on the results, the authors concluded that the selectivity and activity of this catalyst could not be due uniquely to the (001) plane of the material.

LEIS was also used to probe the composition of this catalyst. Given the complexity of this material, a calibration plot could not be used for quantitation, and instead, oxide powders (SiO_2, V_2O_5, NB_2O_5, MoO_3, TeO_2) were used as references. The authors noted that, because these samples were cleaned with atomic oxygen before analysis, they expected all surface species to be in their highest oxidation states, making oxide powders the correct choice for standards. Energy dispersive X-ray analysis (EDX) was used to measure the bulk composition, and the bulk and surface compositions were compared. For the unground material, the surface was enriched in tellurium and deficient in vanadium. For the coated, ground material, the surface was enriched in tellurium and deficient in molybdenum.

Phivilay et al.[69] recently used LEIS in the multi-instrument characterization of a ($Rh_{2-y}Cr_yO_3$)/GaN catalyst, which is used in the UV splitting of water for production of H_2 and O_2. Their goal was to understand the relationship between catalyst structure and photoactivity. While GaN is catalytically inactive in splitting water, the addition of $Rh_{2-y}Cr_yO_3$ nanoparticles to its surface makes it active. Their catalyst system is depicted in Figure A5.19. In addition to probing the surface with LEIS, the authors used high-resolution XPS, Raman spectroscopy, ultraviolet/visible spectroscopy (UV-VIS), and photoluminescence to understand their material. This study is an

excellent example of how bulk techniques (Raman, UV-VIS), and in particular the multi-instrument characterization of materials,[32, 45, 63] play a role in understanding surfaces. Their UV-VIS analysis showed that the addition of ($Rh_{2-y}Cr_yO_3$) nanoparticles to the GaN surface resulted in no change in the bandgap of the bulk GaN, implying that the changes they observed must be occurring at the material's surface. HR-XPS provided information about the chemical states of the species in the system. Based on chemical shifts, the Rh and Cr in the outer 3 nanometers of this material were assigned to their +3 oxidation states. There was no Cr^{6+} or metallic Rh at the surface. LEIS played an important role in this work by providing compositional information for GaN and for the ($Rh_{2-y}Cr_yO_3$)/GaN catalyst. In addition to analyzing the surface region, the near surface region was probed by depth profiling. Interestingly, for the GaN, there was virtually no N signal at the surface. With sputtering, the N signal gradually appeared and the oxygen signal gradually decreased. This indicates that the stoichiometry of the outermost layer is best described as GaO_x, and the subsurface region is best described as GaO_xN_y. The authors noted that this was the first time a surface characterization had revealed this compositional information. The Ne^+ LEIS spectrum for ($Rh_{2-y}Cr_yO_3$)/GaN showed contamination from tin and barium. Again, contaminants often diffuse to the surface of a material and become concentrated there to minimize surface free energy. The authors attributed the contamination they found to the ($Rh_{2-y}Cr_yO_3$) precursors. A depth profile (Figure A5.20) showed that the material became richer in Cr with increasing sputter depth. LEIS measurements indicated that both species were enriched in the near surface region compared to their expected bulk concentrations. The authors used pure metal references to quantify the surface coverage of Cr and Rh because they were interested in the surface coverages of the pure metals rather than their oxides. Using the quantitative information they obtained about the Rh concentration at the surface, they calculated a turnover frequency (TOF) for the material,

350

which is defined as the number of H_2 molecules produced per exposed Rh^{3+} site per second. Obviously, this calculation would not have been possible without a technique capable of quantifying the Rh concentration at the final surface.

In summary, LEIS proved to be very useful in this study. The authors were surprised by the composition of the outer layers of their GaN film, and by the fact that the surface was significantly enriched in Rh and Cr. They were also surprised by the presence of Sn and Ba. Quantitative information about Rh was used to calculate the turnover frequency for hydrogen.

A5.13 Conclusion

LEIS is powerful analytical tool for understanding the outermost atomic layer of a material. The operating principles of LEIS, summarized in Equation (A5.1), can be understood in terms of classical physics. Surface signals in LEIS are Gaussian, while the signal in LEIS static depth profiles appears as a tail on the lower energy side of the surface signal. The components of a typical LEIS system are an ion source, a kinetic energy analyzer, and a detector. All of these are housed in a high vacuum chamber. Advances in detector geometry have significantly improved the sensitivity of the technique. Quantitation in LEIS is generally straightforward, and with very few exceptions, there is no matrix effect in LEIS. For some systems, LEIS can be accomplished without the use of reference samples. For more complex systems, reference powders are used to establish sensitivity factors for each element.

The applications we have shown demonstrate the unique information LEIS can provide. In a study of ALD deposited gate-oxide films, the extreme surface sensitivity of LEIS was valuable for understanding film closure. The static depth profiling capabilities of LEIS are useful in

characterizing the diffusion in thin films for extreme UV optics. In the study of solid-oxide fuel cells, LEIS provided information about the outermost surface that challenged previous conclusions from computational studies about the structure of the material. LEIS is extremely useful for studying catalysts, where the outermost layer plays a determining role in the activity and rate of catalysis.

We again emphasize the importance of multi-instrument surface and material characterization.[32, 63] The fact that LEIS is insensitive to the chemical environments of analytes makes it powerful for quantifying surface compositions. LEIS is complementary to XPS and ToF-SIMS. In general, it is much more surface sensitive than either of these two techniques. However, it only provides information about elemental composition, whereas ToF-SIMS gives molecular information, and XPS is sensitive to chemical environment. We believe that in the future more studies involving all three techniques will be performed, and that this approach will become increasingly necessary for the full characterization of advanced materials.

### A5.14 Acknowledgment

A5.15 Figures
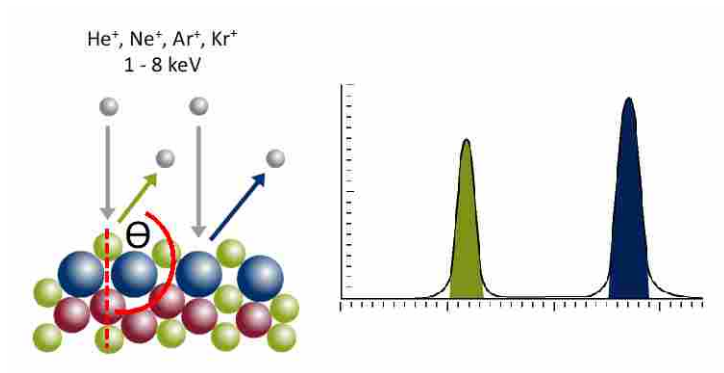
Figure A5.1. (Left) Noble gas ion bombardment of a surface with two types of exposed atoms. (Right) LEIS signal corresponding to the surface on the left. Note that there is no LEIS signal from the 'red' atoms. *Figure used with permission from IONTOF.*
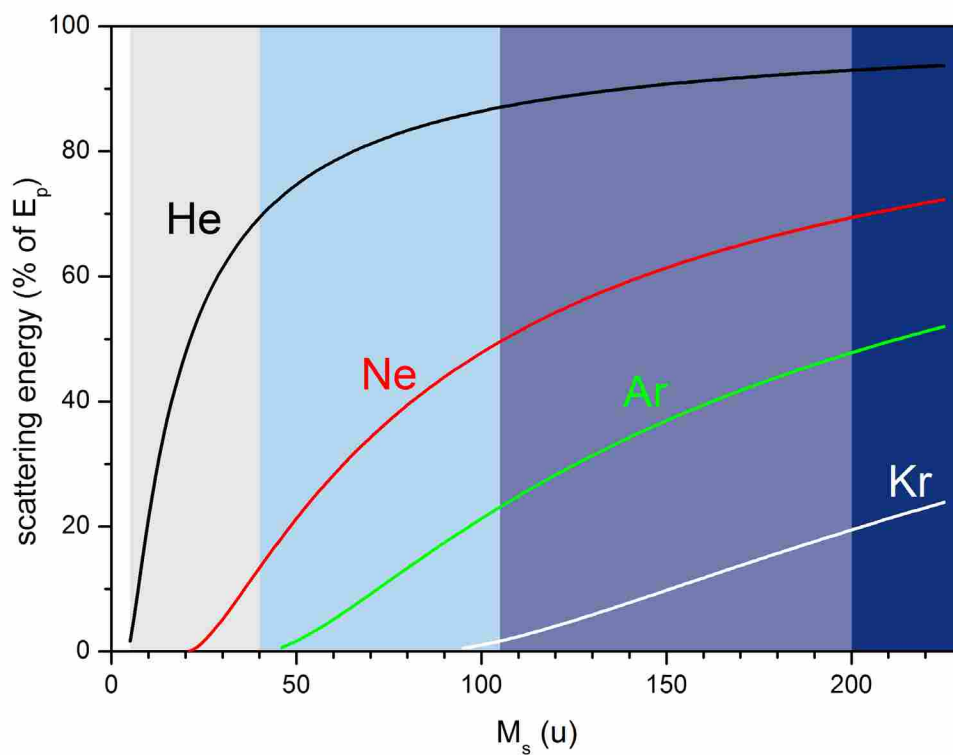
Figure A5.2. Percentage of kinetic energy, obtained through Equation (A5.1), retained by the backscattered projectile ion (E_S/E_P x 100 %) plotted as a function of the mass of the analyte atom, M_S. The colored vertical stripes show which noble gas ion is commonly used to probe elements of the corresponding mass range in LEIS. *Figure used with permission from IONTOF.*
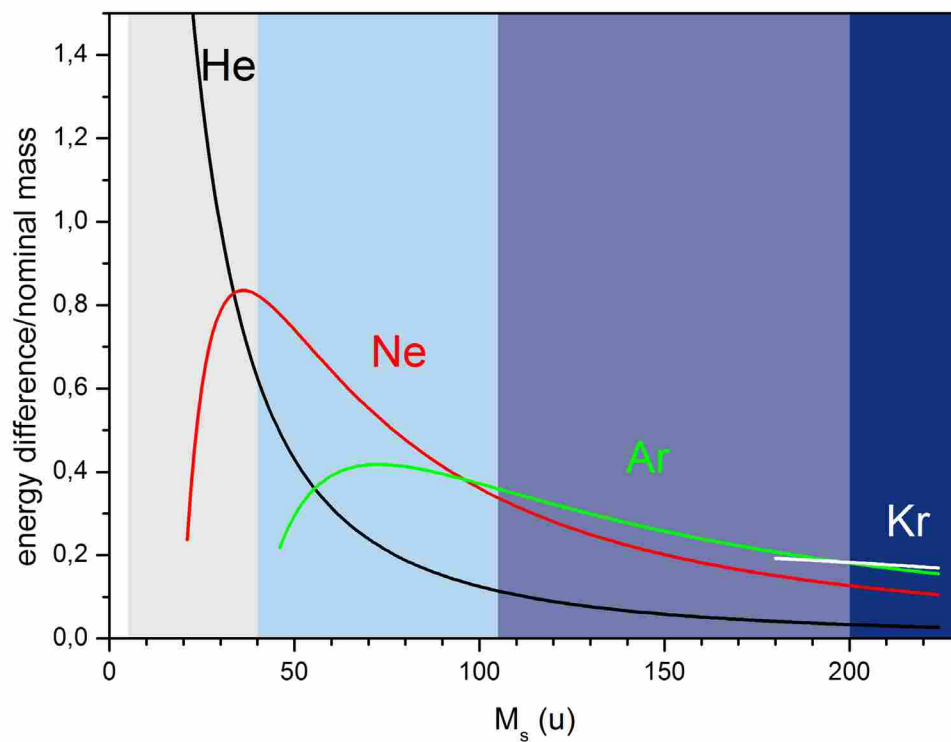
Figure A5.3. Plot of energy difference per unit nominal mass vs. M_s, i.e., the derivative of the curves in Figure A5.2. The colored vertical stripes indicate the noble gas ion that is commonly used to probe elements of the corresponding mass range. The projectile ion that provides the largest energy discrimination per unit mass corresponds to the highest line (curve) at any given M_s in the plot. *Figure used with permission from IONTOF.*
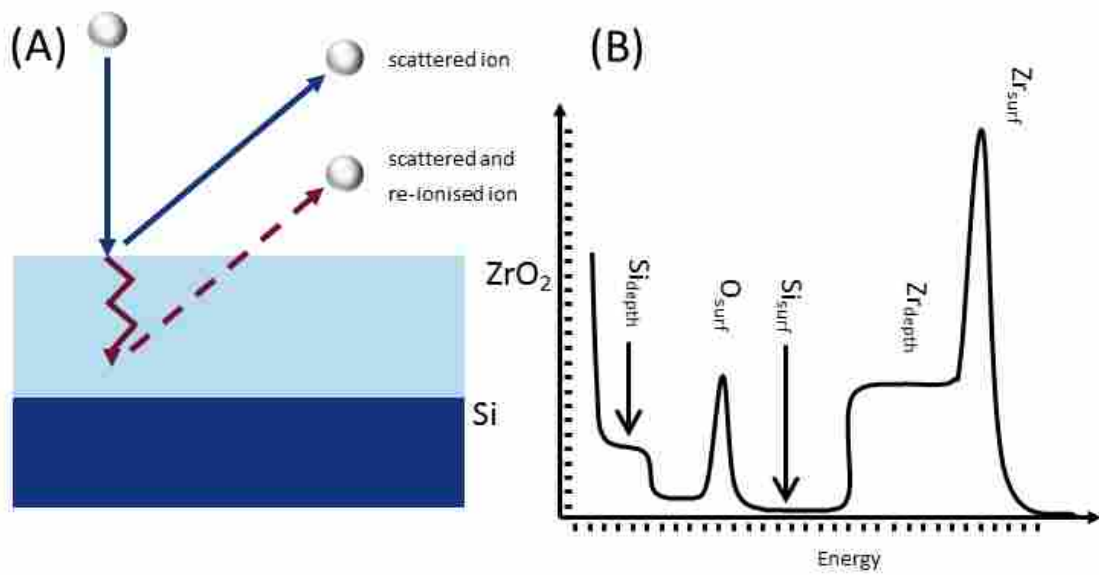
Figure A5.4. (A) Noble gas ion scattering off of a ZrO_2 film on Si. Shown are: (i) ion scattering from the surface, and (ii) particle penetration, neutralization, backscattering, and reionization. (B) Mock LEIS spectrum for the material shown on the left. *Figure used with permission from IONTOF.*
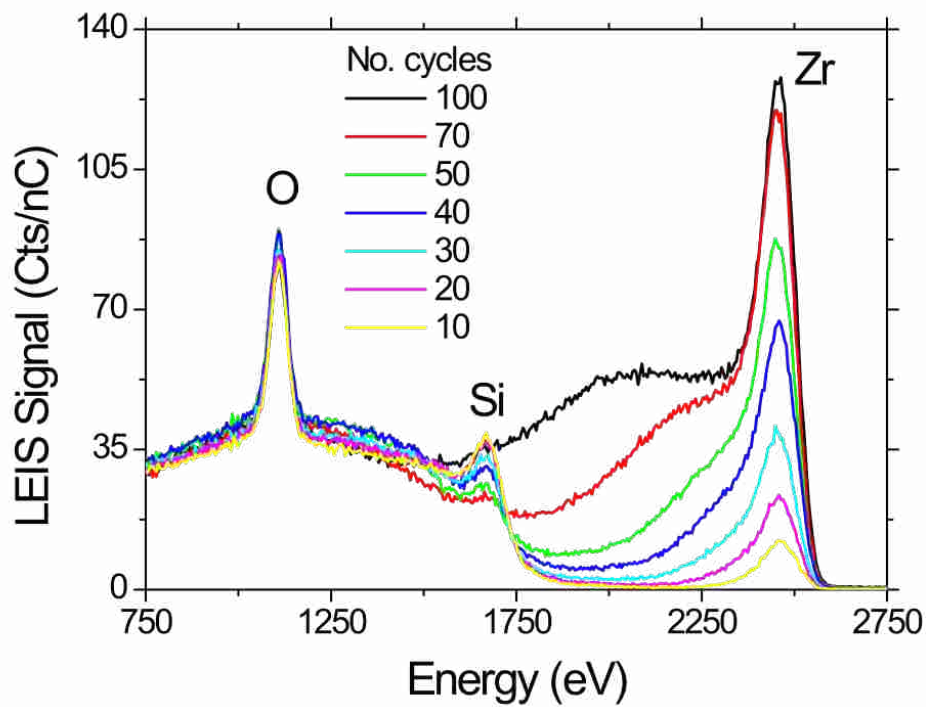
Figure A5.5. LEIS spectra for ALD deposited zirconium oxide on a silicon substrate for 10, 20, 30, 30, 50, 70, and 100 cycles. *Figure used with permission from IONTOF.*
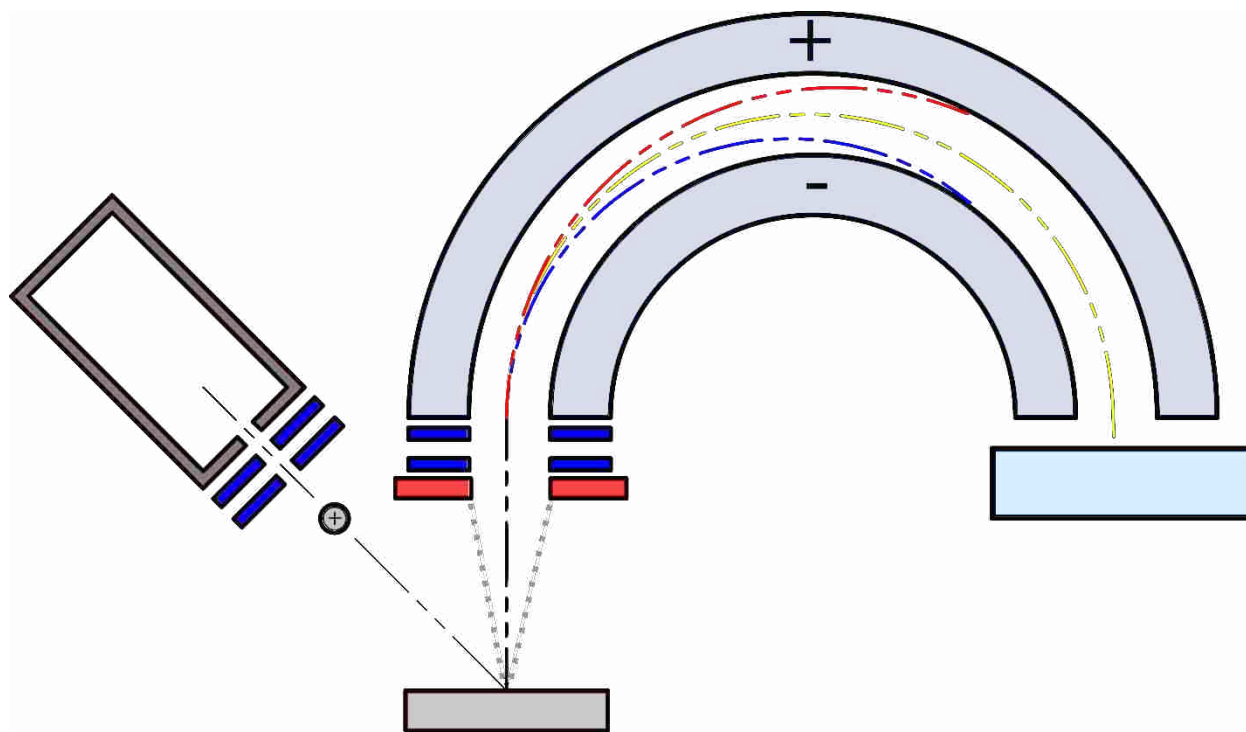
Figure A5.6. Representation of a converted XPS instrument for LEIS analysis. The angle of acceptance permitted by the entrance slits of the hemispherical ESA is represented by a pair of dotted, grey lines. The trajectories of ions with too much energy (red), too little energy (blue), and the correct amount of energy (yellow) are shown.
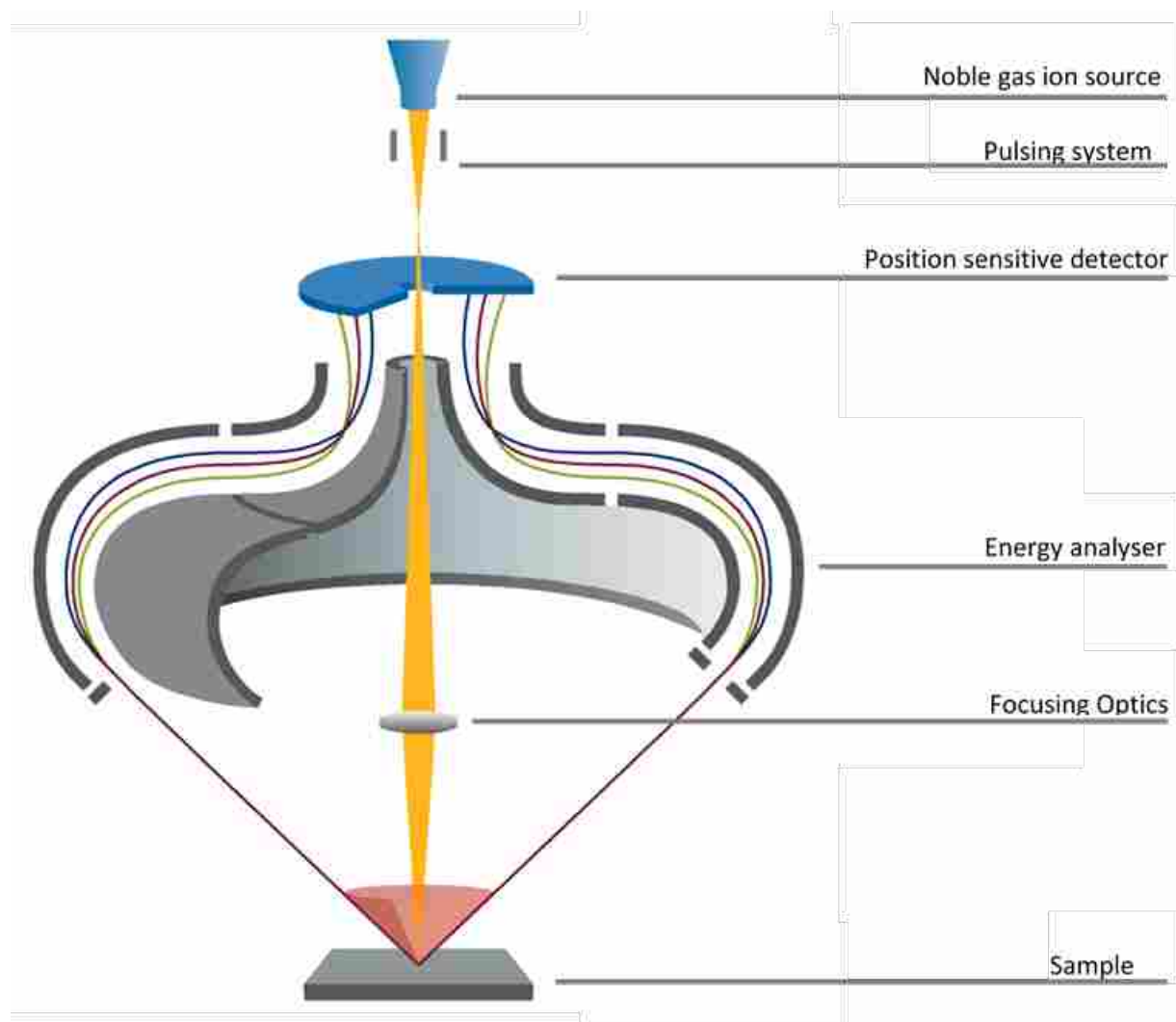
Figure A5.7. Schematic representation of a double-toroidal analyzer, as included in the Qtac[100] instrument by ION-TOF. *Figure used with permission from IONTOF.*
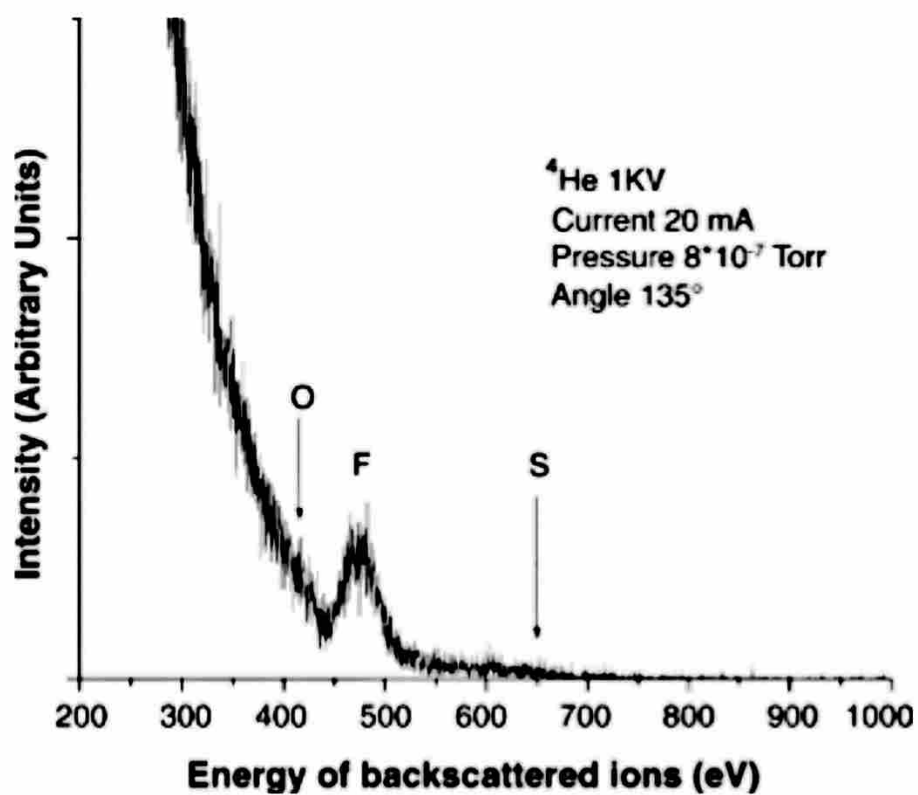
Figure A5.8. LEIS spectrum taken with a conventional XPS instrument using a 1 keV ^{4}He$^+$ ion beam. Reprinted from 'X-ray photoelectron spectroscopy and low energy ion scattering studies on 1-buthyl[sic]-3-methyl-imidazolium bis(trifluoromethane) sulfonamide' by S. Caporali, U. Bardi, and A Lavacchi in Journal of Electron Spectroscopy and Related Phenomena 151 (2006) 4 – 8, Copyright 2005, with permission from Elsevier.

Figure A5.9. LEIS Qtac^{100} instrument with locations of key components labeled. (A) Ion source. (B) Ion gun. (C) Sputter gun for depth profiling. (D) Analysis chamber (the double toroidal analyzer is located at the top of this chamber). (E) Sample introduction chamber (load lock). (F) Sample manipulator (transfer) arm. (G) Vacuum pumps and other hardware are housed below the instrument. *Figure used with permission from IONTOF.*

Figure A5.10. TOF.SIMS 5 and Qtac[100] instruments (left and right, respectively), with their main chambers connected. *Figure used with permission from IONTOF.*
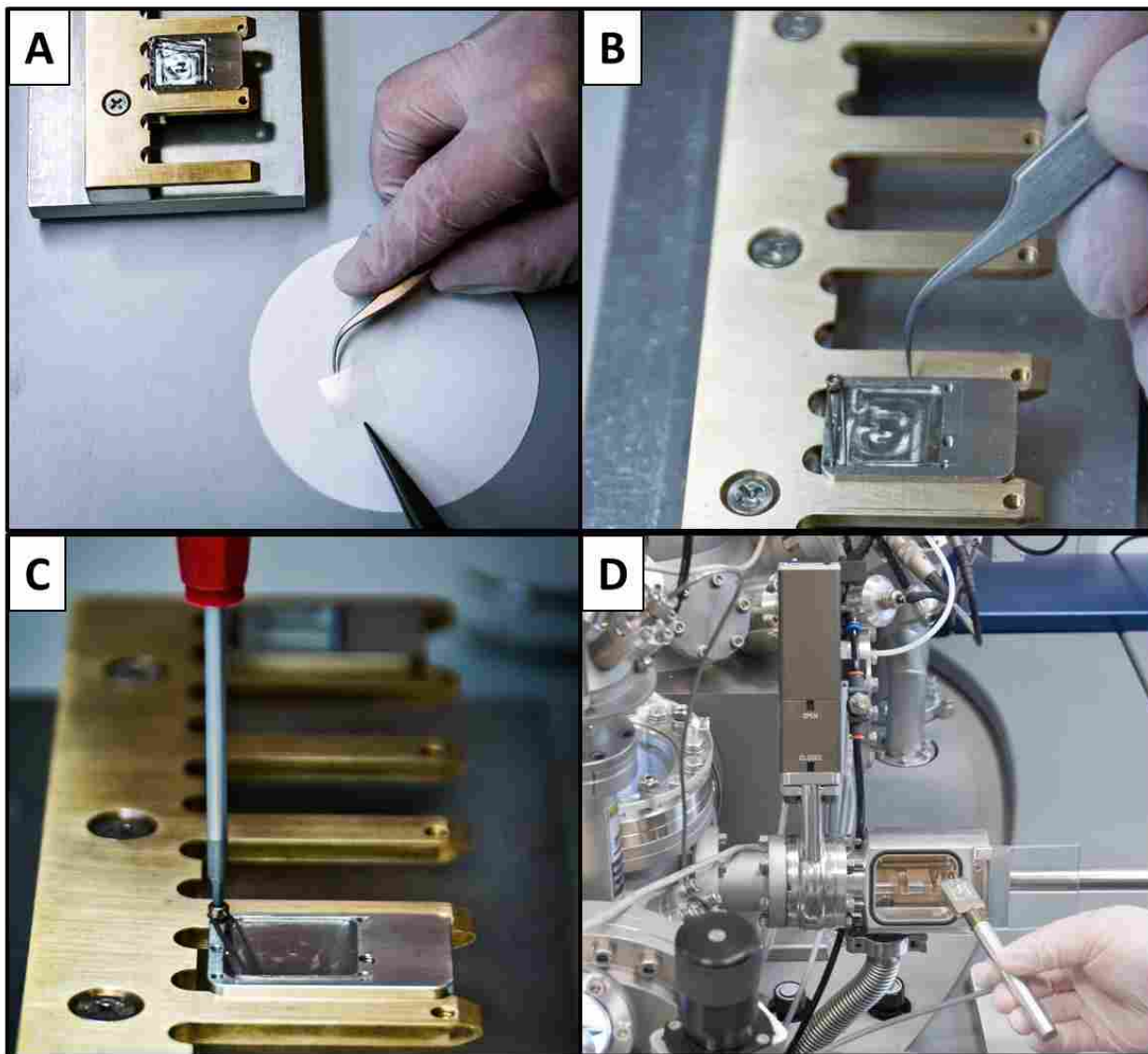
Figure A5.11. Sample loading process for the Qtac^{100}. (A) Glass sample, handled with tweezers and gloves. (B) Placing the sample on the holder (silver colored). (C) Securing the sample to the holder with a spring clip. (D) Sample transfer to the load lock while handling the holder with a special sample-holder pen. *Figure used with permission from IONTOF.*
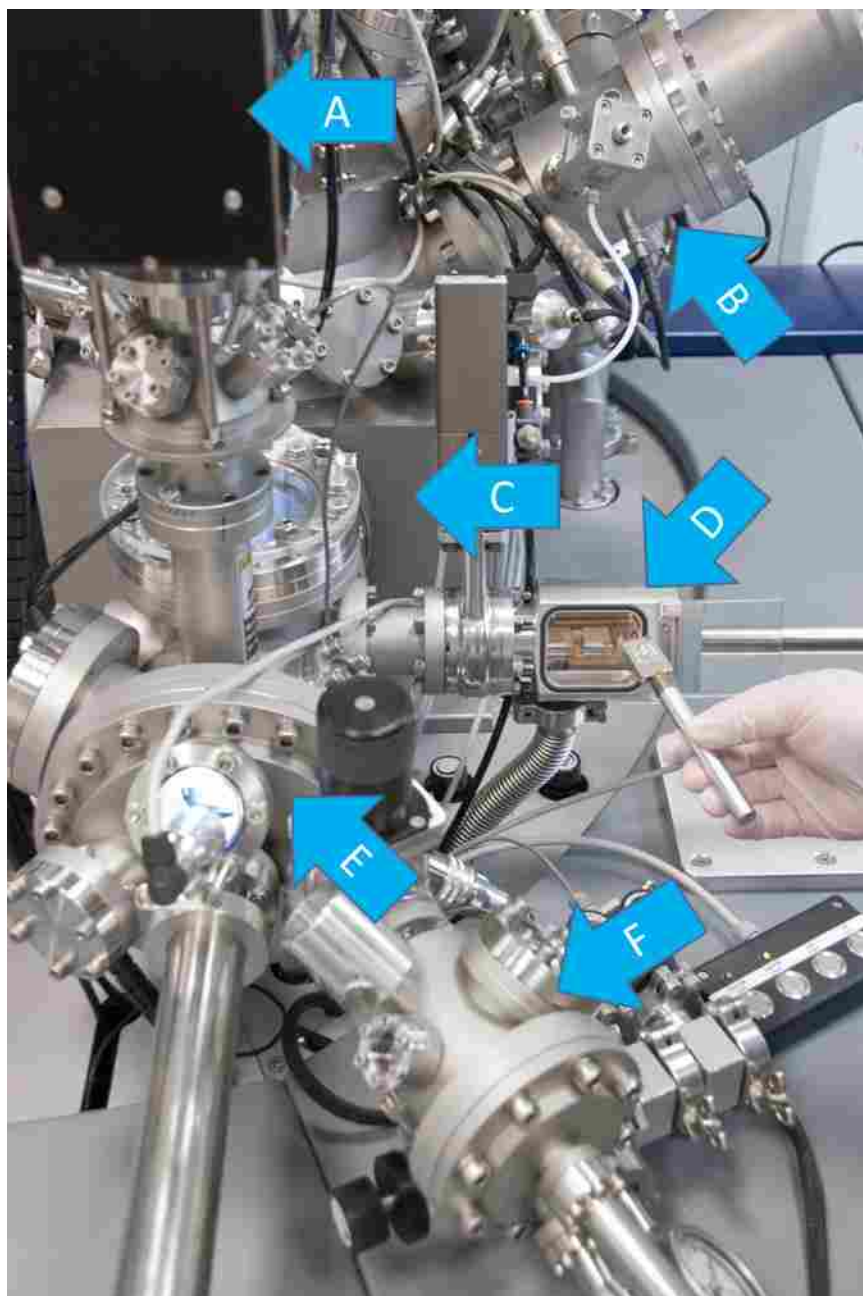
Figure A5.12. Close-up view of the Qtac^{100} instrument at IONTOF with selected components labeled. (A) Atomic oxygen generator. (B) Sputter gun. (C) Analytical (main) chamber (cube). (D) Sample introduction chamber. (E) Sample preparation chamber. (F) Environmental chamber. *Figure used with permission from IONTOF.*
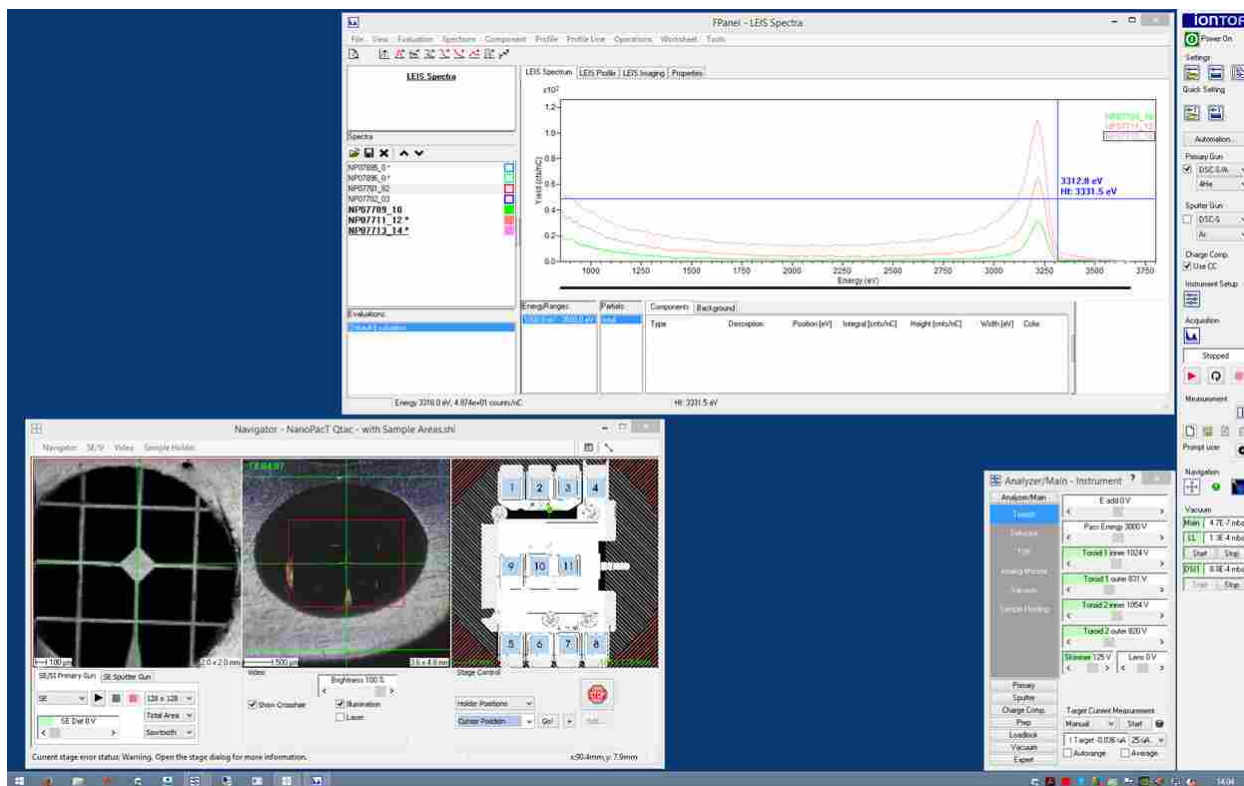
**Figure A5.13.** Screenshot of the Qtac[100] instrument software. Data collection window (Top). Stage control window (Bottom left). Instrument setting window (Bottom right). Instrument controls (Far right). *Figure used with permission from IONTOF.*
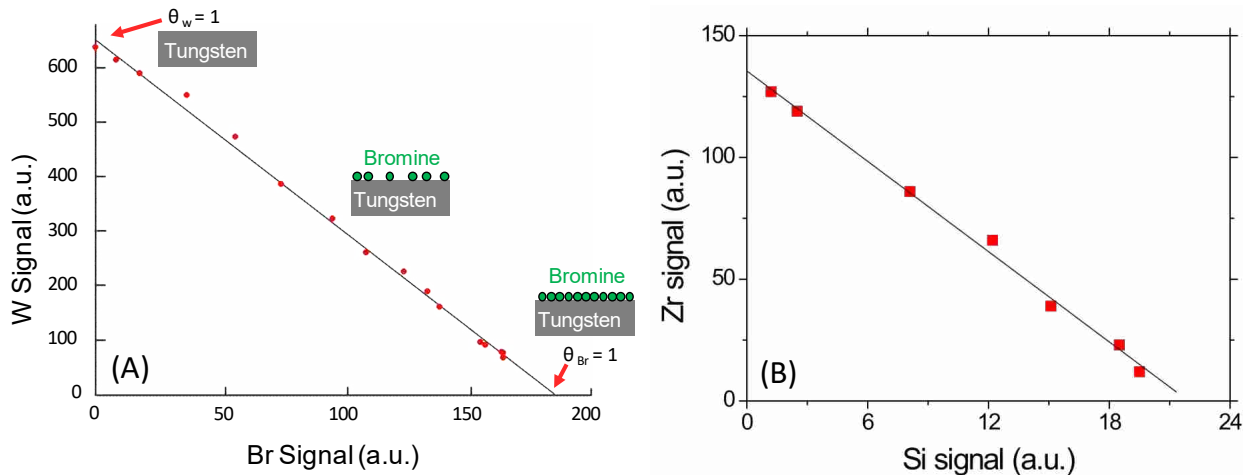
Figure A5.14. (A) Results from a LEIS analysis in which bromine was adsorbed in situ onto a tungsten substrate under different conditions. (B) Results from a LEIS analysis of a series of samples with increasing amounts of ZrO_2 deposited on SiO_2 by atomic layer deposition (ALD). In both cases, the resulting linear relationship between the signals shows that the technique is free of any matrix effect. *Figure used with permission from IONTOF.*
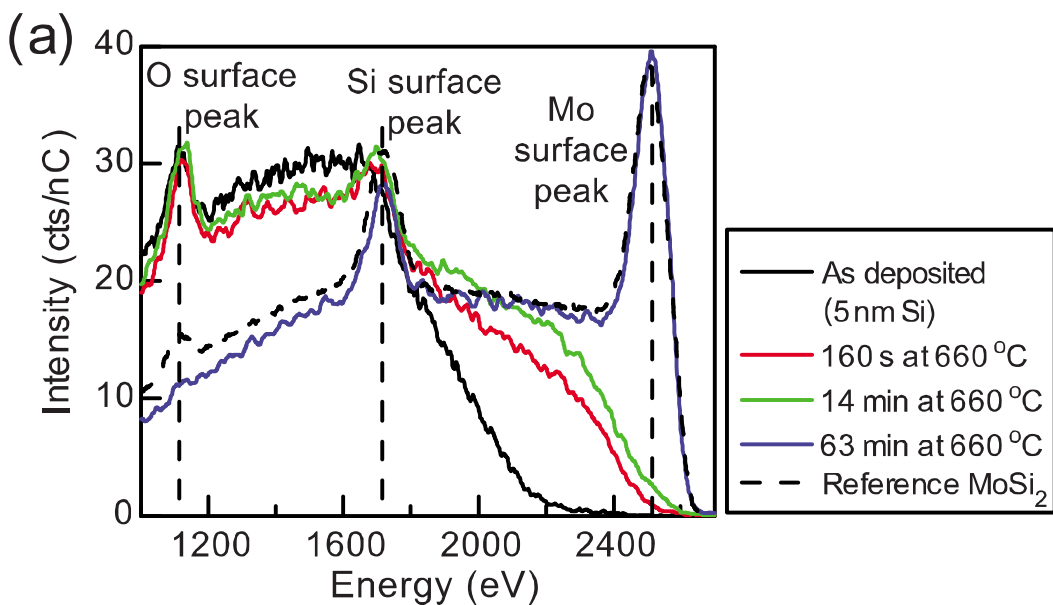
Figure A5.15. The evolution of an Mo/Si system at 660 °C as a function of time as probed by LEIS.

Reprinted with permission from ["Diffusion and interaction studied nondestructively and in real-time with depth-resolved low energy ion spectroscopy" by V.I.T.A. de Rooij-Lohmann, A. W. Kleyn, F. Bijkerk, H. H. Brongersma, and A. E. Yakshin in Appl. Phys. Lett. 94, 063107 (2009); http://dx.doi.org/10.1063/1.3081034]. Copyright [2009], AIP Publishing LLC.
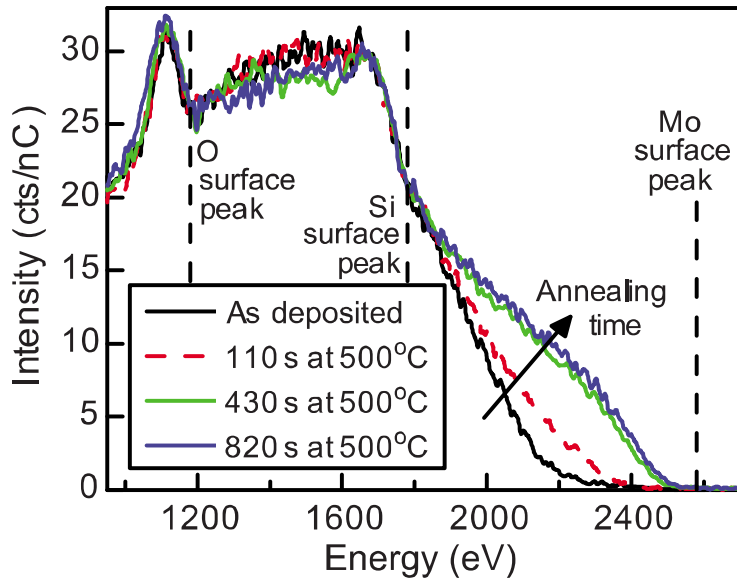
Figure A5.16. The evolution of an Mo/Si system at 500 °C as a function of time as probed by LEIS.

Reprinted with permission from ["Diffusion and interaction studied nondestructively and in real-time with depth-resolved low energy ion spectroscopy" by V.I.T.A. de Rooij-Lohmann, A. W. Kleyn, F. Bijkerk, H. H. Brongersma, and A. E. Yakshin in Appl. Phys. Lett. 94, 063107 (2009); http://dx.doi.org/10.1063/1.3081034]. Copyright [2009], AIP Publishing LLC.
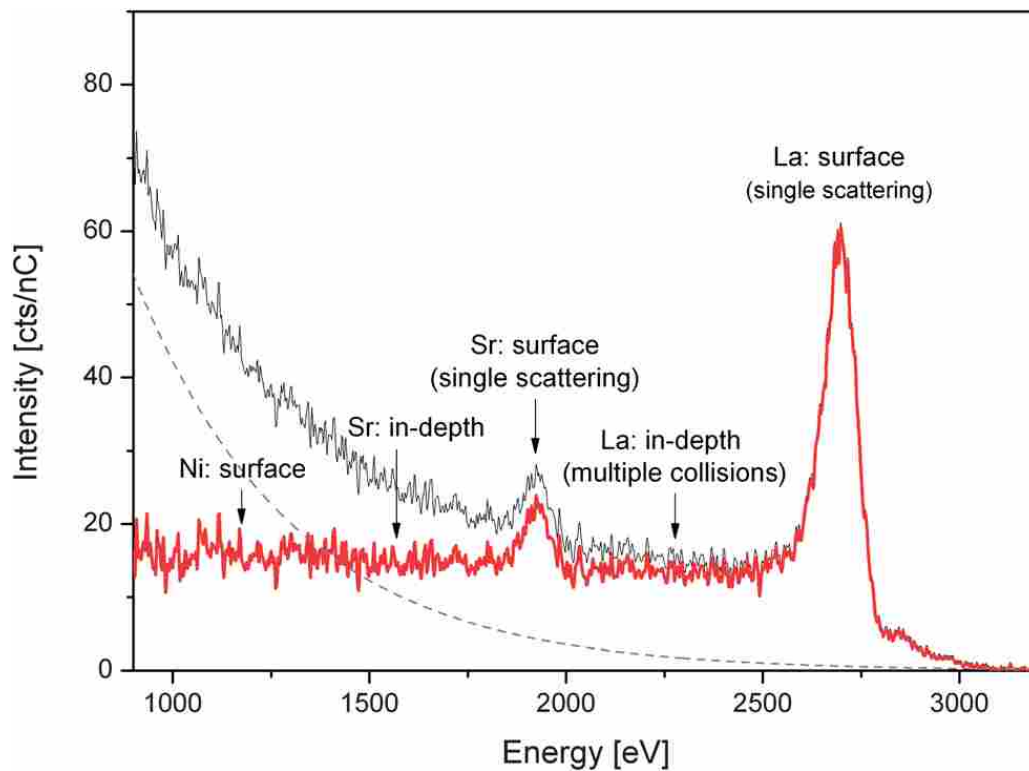
Figure A5.17. LEIS spectrum of $La_{1.67}Sr_{0.33}NiO_{4+\delta}$ shown with and without a background correction. Reproduced from 'Absence of Ni on the outer surface of Sr doped La_2NiO_4 single crystals' by Mónica Burriel, Stuart Wilkins, John P. Hill, Miguel A. Muñoz-Márquez, Hidde H. Brongersma, John A. Kilner, Mary P. Ryan, and Stephen J. Skinner in Energy Environ. Sci., 2014, 7, 311–316, DOI: 10.1039/c3ee41622d with permission of The Royal Society of Chemistry.[19]
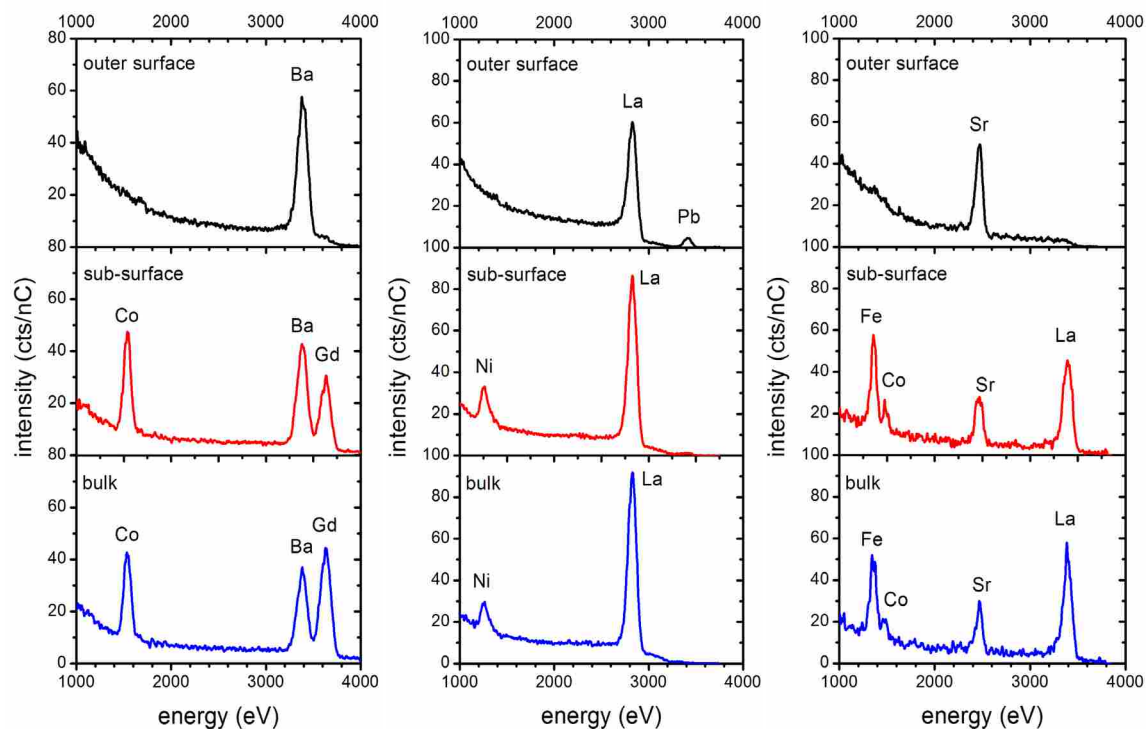
Figure A5.18. LEIS spectra of three SOFC materials: (a) GBCO-1125 (left), (b) LNO 214 (middle), and (c) LSCF-113 (right). Spectra taken at the outer surface (top), the near surface region (middle), and the bulk of the material (bottom). Data were originally plotted in a different format in 'Surface termination and subsurface restructuring of perovskite-based solid oxide electrode materials' by J. Druce, H. T´ellez, M. Burriel, M. D. Sharp, L. J. Fawcett, S. N. Cook, D. S. McPhail, T. Ishihara, H. H. Brongersma, and J. A. Kilner in Energy & Environmental Science, 2014, DOI: 10.1039/c4ee01497a.
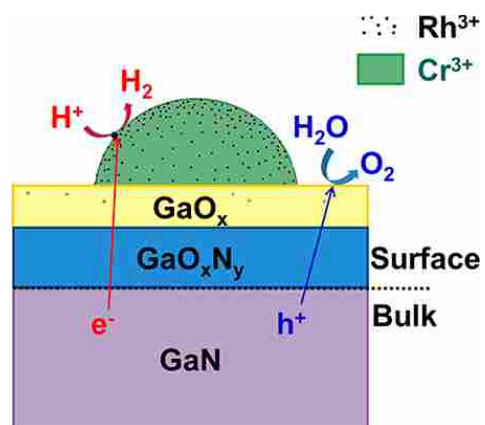
Figure A5.19. Representation of a $(Rh_{2-y}Cr_yO_3)$/GaN catalyst. Reprinted (adapted) with permission from ('Fundamental Bulk/Surface Structure–Photoactivity Relationships of Supported $(Rh2–yCryO3)$/GaN Photocatalysts' by Somphonh P. Phivilay, Charles A. Roberts, Alexander A. Puretzky, Kazunari Domen, and Israel E. Wachs, dx.doi.org/10.1021/jz401884c | J. Phys. Chem. Lett. 2013, 4, 3719−3724).
Copyright (2013) American Chemical Society.
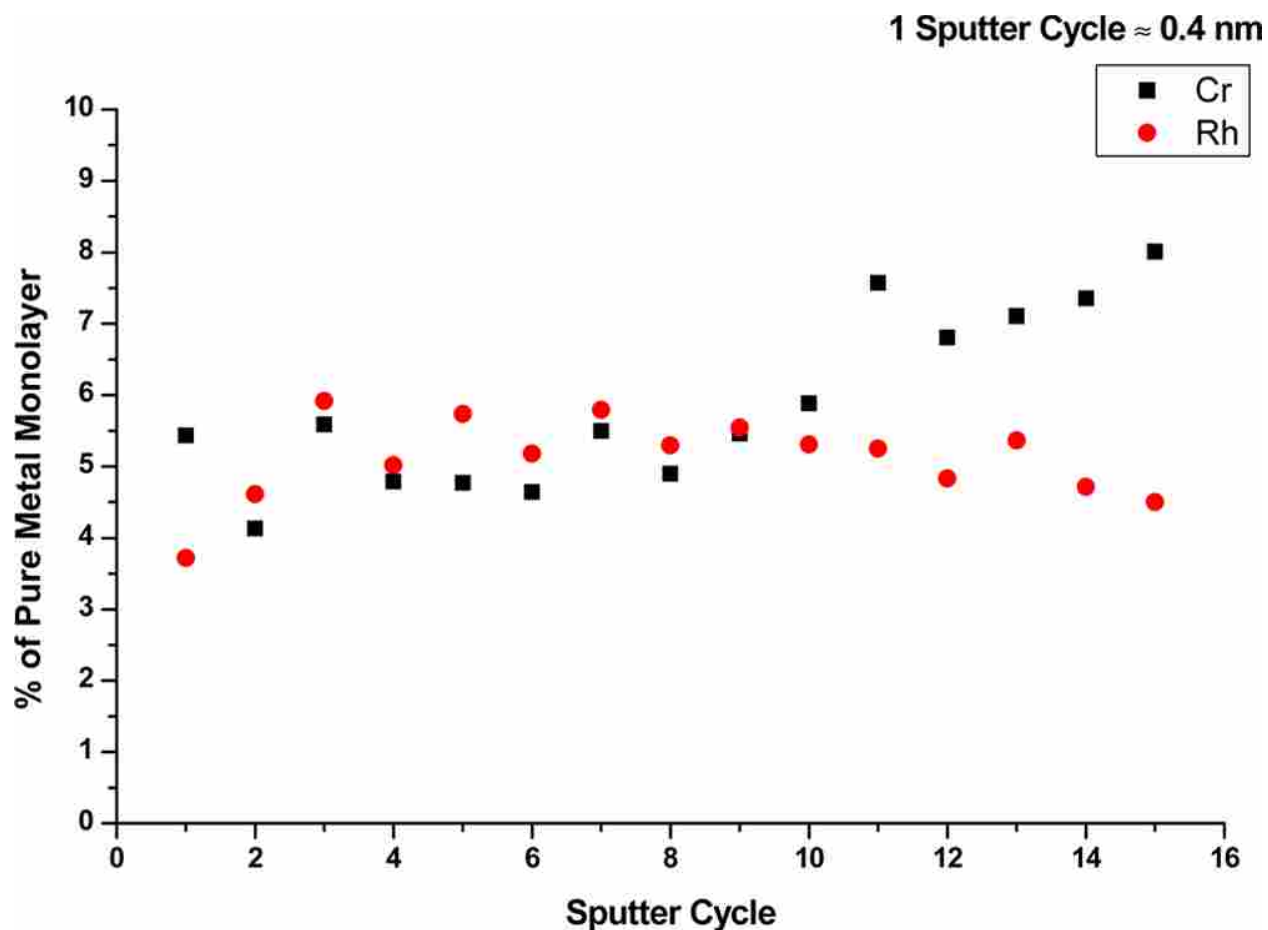
Figure A5.20. Depth profile concentrations of Cr and Rh in a (Rh$_{2-y}$Cr$_y$O$_3$)/GaN catalyst as determined by LEIS. Reprinted (adapted) with permission from ('Fundamental Bulk/Surface Structure–Photoactivity Relationships of Supported (Rh2–yCryO3)/GaN Photocatalysts' by Somphonh P. Phivilay, Charles A. Roberts, Alexander A. Puretzky, Kazunari Domen, and Israel E. Wachs, dx.doi.org/10.1021/jz401884c | J. Phys. Chem. Lett. 2013, 4, 3719−3724). Copyright (2013) American Chemical Society.

A5.16 References

1.	Cushman, C. V.; Brüner, P.; Zakel, J.; Major, G. H.; Lunt, B. M.; Smith, N. J.; Grehl, T.; Linford, M. R. Low energy ion scattering (LEIS). A practical introduction to its theory, instrumentation, and applications. *Analytical Methods* 2016, *8* (17), 3419-3439.
2.	Cushman, C. V.; Grehl, T.; Linford, M. R. Low Energy Ion Scattering (LEIS). I. The fundamentals. *Vacuum Technology & Coating* April, 2015.
3.	Cushman, C. V.; Grehl, T.; Linford, M. R. Low Energy Ion Scattering (LEIS). IV. Applications to Catalysis. *Vacuum Technology & Coating* July, 2015.
4.	Cushman, C. V.; Grehl, T.; Linford, M. R. 'Low Energy Ion Scattering (LEIS). III. Quantitation in LEIS. *Vacuum Technology & Coating* June, 2015.
5.	Cushman, C. V.; Grehl, T.; Linford, M. R. Low Energy Ion Scattering (LEIS). II. Instrumentation and Application to Solid Oxide Fuel Cells. *Vacuum Technology & Coating* May, 2015.
6.	Cushman, C. V.; Grehl, T.; Linford, M. R. Low Energy Ion Scattering (LEIS). V. Static and Sputter Depth Profiling, and Application to Semiconductor Devices. *Vacuum Technology & Coating* November, 2015.
7.	Smith, D. P. Scattering of Low-Energy Noble Gas Ions from Metal Surfaces. *Journal of Applied Physics* 1967, *38* (1), 340-347.
8.	Brongersma, H. H.; Mul, P. M. Analysis of the outermost atomic layer of a surface by low-energy ion scattering. *Surface Science* 1973, *35*, 393-412.
9.	Bronckers, R. P. N.; Wit, A. G. J. d. Reconstruction of the oxygen-covered Cu{110} surface identified with low energy Ne^+ and H_2O^+ ion scattering. *Surface Science* 1981, *112* (1-2), 133-152.
10.	Engelhardt, H.; Bäck, W.; Menzel, D.; Liebl, H. Novel charged particle analyzer for momentum determination in the multichanneling mode: I. Design aspects and electron/ion optical properties. *Review of Scientific Instruments* 1981, *52* (6), 835-839.
11.	Engelhardt, H.; Zartner, A.; Menzel, D. Novel charged particle analyzer for momentum determination in the multichanneling mode. II. Physical realization, performance tests, and sample spectra. *Review of Scientific Instruments* 1981, *52* (8), 1161-1173.
12.	Brongersma, H. H.; Draxler, M.; de Rridder, M.; Bauer, P. Surface composition analysis by low-energy ion scattering. *Surface Science Reports* 2007, *62* (3), 63-109.
13.	Cushman, C. V.; Linford, M. R.; Grehl, T. Low Energy Ion Scattering (LEIS). I. The Fundamentals. *Vacuum Technology & Coating* April, 2015, 26-33.
14.	Brongersma, H. H.; Grehl, T.; van Hal, P. A.; Kuijpers, N. C. W.; Mathijssen, S. G. J.; Schofield, E. R.; Smith, R. A. P.; ter Veen, H. R. J. High-sensitivity and high-resolution low-energy ion scattering. *Vacuum* 2010, *84* (8), 1005-1007.
15.	Brongersma, H. H.; de Ridder, M.; Gildenpfennig, A.; Viitanen, M. M. Insight in the outside: materials science at the atomic level using LEIS. *Journal of the European Ceramic Society* 2003, *23* (15), 2761-2767.
16.	Druce, J.; Téllez, H.; Burriel, M.; Sharp, M. D.; Fawcett, L. J.; Cook, S. N.; McPhail, D. S.; Ishihara, T.; Brongersma, H. H.; Kilner, J. A. Surface termination and subsurface restructuring of perovskite-based solid oxide electrode materials. *Energy Environ. Sci.* 2014, *7* (11), 3593-3599.
17.	Stamenkovic, V. R.; Fowler, B.; Mun, B. S.; Wang, G.; Ross, P. N.; Lucas, C. A.; Marković, N. M. Improved Oxygen Reduction Activity on Pt$_3$Ni(111) via Increased Surface Site Availability. *Science* 2007, *315* (5811), 493-497.

18.   Téllez, H.; Aguadero, A.; Druce, J.; Burriel, M.; Fearn, S.; Ishihara, T.; McPhail, D. S.; Kilner, J. A. New perspectives in the surface analysis of energy materials by combined time-of-flight secondary ion mass spectrometry (ToF-SIMS) and high sensitivity low-energy ion scattering (HS-LEIS). *Journal of Analytical Atomic Spectrometry* 2014, *29* (8), 1361.

19.   Burriel, M.; Wilkins, S.; Hill, J. P.; Muñoz-Márquez, M. A.; Brongersma, H. H.; Kilner, J. A.; Ryan, M. P.; Skinner, S. J. Absence of Ni on the outer surface of Sr doped La_2NiO_4 single crystals. *Energy Environ. Sci.* 2014, *7* (1), 311-316.

20.   de Rooij-Lohmann, V. I. T. A.; Kleyn, A. W.; Bijkerk, F.; Brongersma, H. H.; Yakshin, A. E. Diffusion and interaction studied nondestructively and in real-time with depth-resolved low energy ion spectroscopy. *Applied Physics Letters* 2009, *94* (6), 063107.

21.   Rubin, S. Surface Analysis by Charged Particle Spectrsocopy. *Nuclear Instruments and Methods* 1959, *5*, 177-183.

22.   Brongersma, H. H.; Gildenpfennig, A.; Gon, A. W. D. v. d.; Grampel, R. D. v. d.; Jansen, W. P. A.; Knoester, A.; Laven, J.; Viitanen, M. M. Insight in the outside: New applications of low-energy ion scattering. *New Instruments and Methods in Physics Research B* 2002, *23* (15), 11-18.

23.   Biersack, J. P.; Haggmark, L. G. A Monte Carlo computer program for the transport of energetic ions in amorphous targets. *Nuclear Instruments and Methods* 1980, *174* (1–2), 257-269.

24.   Ziegler, J. F.; Biersack, J. P.; Ziegler, M. D., *SRIM : the stopping and range of ions in matter*. SRIM Co.: Chester, Md., 2012.

25.   Ziegler, J. F.; Ziegler, M. D.; Biersack, J. P. SRIM – The stopping and range of ions in matter (2010). *Nuclear Instruments and Methods in Physics Research Section B: Beam Interactions with Materials and Atoms* 2010, *268* (11-12), 1818-1823.

26.   Brüner, P.; Grehl, T.; Brongersma, H.; Detlefs, B.; Nolot, E.; Grampeix, H.; Steinbauer, E.; Bauer, P. Thin film analysis by low-energy ion scattering by use of TRBS simulations. *Journal of Vacuum Science & Technology A* 2015, *33* (1), 01A122.

27.   Gambino, J., 8 - Process Technology for Copper Interconnects. In *Handbook of Thin Film Deposition (Third Edition)*, Seshan, K., Ed. William Andrew Publishing: Oxford, 2012; pp 221-269.

28.   Ye, G.; Wang, H.; Arulkumaran, S.; Ng, G. I.; Hofstetter, R.; Li, Y.; Anand, M.; Ang, K.; Maung, Y.; Foo, S. C. Atomic layer deposition of ZrO2 as gate dielectrics for AlGaN/GaN metal-insulator-semiconductor high electron mobility transistors on silicon. *Applied Physics Letters* 2013, *103* (14), 142109.

29.   Liu, H.; Ye, P. D. Dual-Gate MOSFET With Atomic-Layer-Deposited as Top-Gate Dielectric. *Electron Device Letters, IEEE* 2012, *33* (4), 546-548.

30.   Suzuki, R.; Taoka, N.; Yokoyama, M.; Lee, S.; Kim, S.; Hoshii, T.; Yasuda, T.; Jevasuwan, W.; Maeda, T.; Ichikawa, O. 1-nm-capacitance-equivalent-thickness HfO2/Al2O3/InGaAs metal-oxide-semiconductor structure with low interface trap density and low gate leakage current density. *Applied Physics Letters* 2012, *100* (13), 132906.

31.   Wang, H.; Madaan, N.; Bagley, J.; Diwan, A.; Liu, Y.; Davis, R. C.; Lunt, B. M.; Smith, S. J.; Linford, M. R. Spectroscopic ellipsometric modeling of a Bi–Te–Se write layer of an optical data storage device as guided by atomic force microscopy, scanning electron microscopy, and X-ray diffraction. *Thin Solid Films* 2014, *569*, 124-130.

32.   Jensen, D. S.; Kanyal, S. S.; Madaan, N.; Hancock, J. M.; Dadson, A. E.; Vail, M. A.; Vanfleet, R.; Shutthanandan, V.; Zhu, Z.; Engelhard, M. H.; Linford, M. R. Multi-instrument characterization of the surfaces and materials in microfabricated, carbon nanotube-templated thin

layer chromatography plates. An analogy to 'The Blind Men and the Elephant'. *Surface and Interface Analysis* 2013, *45* (8), 1273-1282.

33.   Singh, B.; Smith, S. J.; Jensen, D. S.; Jones, H. F.; Dadson, A. E.; Farnsworth, P. B.; Vanfleet, R.; Farrer, J. K.; Linford, M. R. Multi-instrument characterization of five nanodiamond samples: a thorough example of nanomaterial characterization. *Analytical and Bioanalytical Chemistry* 2015, 1-18.

34.   Cushman, C. V.; Grehl, T.; Linford, M. R. Low Energy Ion Scattering (LEIS). II. Instrumentation and Application to Solid Oxide Fuel Cells. *Vacuum Technology & Coating* May, 2015, 28-34.

35.   Ackermans, P. A. J.; Van Der Meulen, P. F. H. M.; Ottevanger, H.; Van Straten, F. E.; Brongersma, H. H. Simultaneous energy and angle resolved ion scattering spectroscopy. *Nuclear Instruments and Methods in Physics Research Section B: Beam Interactions with Materials and Atoms* 1988, *35* (3–4), 541-543.

36.   Brongersma, H. H.; Grehl, T.; Schofield, E. R.; Smith, R. A. P.; ter Veen, H. R. J. Analysis of the Outer Surface of Platinum-Gold Catalysts by Low-Energy Ion Scattering. *Platinum Metals Review* 2010, *54* (2), 81-87.

37.   Caporali, S.; Bardi, U.; Lavacchi, A. X-ray photoelectron spectroscopy and low energy ion scattering studies on 1-buthyl-3-methyl-imidazolium bis (trifluoromethane) sulfonimide. *Journal of Electron Spectroscopy and Related Phenomena* 2006, *151* (1), 4-8.

38.   Cushman, C. V.; Brüner, P.; Zakel, J.; Major, G.; Lunt, B. M.; Grehl, T.; Smith, N. J.; Linford, M. R. A Pictorial View of LEIS and ToF-SIMS Instrumentation. *Vacuum Technology & Coating* February, 2016.

39.   Cushman, C. V.; Linford, M. R.; Grehl, T. Low Energy Ion Scattering (LEIS). III. Quantitation in LEIS. *Vacuum Technology & Coating* June, 2015, 32-35.

40.   Adriaensen, L.; Vangaever, F.; Gijbels, R. Metal-Assisted Secondary Ion Mass Spectrometry: Influences of Ag and Au Deposition on Molecular Ion Yields. *Analytical Chemistry* 2004, *76*, 6777-6785.

41.   Delcorte, A.; Bertrand, P. Interest of silver and gold metallization for molecular SIMS and SIMS imaging. *Applied Surface Science* 2004, *231-232*, 250-255.

42.   Delcorte, A.; Médard, N.; Bertrand, P. Organic Secondary Ion Mass Spectrometry: Sensitivity Enhancement by Gold Deposition. *Analytical Chemistry* 2002, *74* (19), 4955-4968.

43.   ter Veen, H. R. J.; Kim, T.; Wachs, I. E.; Brongersma, H. H. Applications of High Sensitivity-Low Energy Ion Scattering (HS-LEIS) in heterogeneous catalysis. *Catalysis Today* 2009, *140* (3-4), 197-201.

44.   Cushman, C. V.; Grehl, T.; Linford, M. R. Low Energy Ion Scattering (LEIS). V. Static and Sputter Depth Profiling and Application to Semiconductor Devices. *Vacuum Technology & Coating* November, 2015, 28-33.

45.   Linford, M. R. Introduction to Surface and Material Analysis and to Various Analytical Techniques. *Vacuum Technology & Coating* February, 2014, 27-32.

46.   Linford, M. R. The Guassian-Lorentzian Sum, Product, and Convolution (Voigt) Functions Used in Peak Fitting XPS Narrow Scans, and an Introduction to the Impulse Function. *Vacuum Technology & Coating* July, 2014, 27-34.

47.   Linford, M. R. An Introduction to Time-of-Flight Secondary Ion Mass Spectrometry (ToF-SIMS). *Vacuum Technology & Coating* April, 2014, 30-35.

48.   Singh, B.; Velázquez, D.; Terry, J.; Linford, M. R. Comparison of the equivalent width, the autocorrelation width, and the variance as figures of merit for XPS narrow scans. *Journal of Electron Spectroscopy and Related Phenomena* 2014, *197*, 112-117.

49.   Singh, B.; Velázquez, D.; Terry, J.; Linford, M. R. The equivalent width as a figure of merit for XPS narrow scans. *Journal of Electron Spectroscopy and Related Phenomena* 2014, *197*, 56-63.

50.   Yang, L.; Lua, Y.-Y.; Jiang, G.; Tyler, B. J.; Linford, M. R. Multivariate analysis of TOF-SIMS spectra of monolayers on scribed silicon. *Analytical chemistry* 2005, *77* (14), 4654-4661.

51.   Yang, L.; Shirahata, N.; Saini, G.; Zhang, F.; Pei, L.; Asplund, M. C.; Kurth, D. G.; Ariga, K.; Sautter, K.; Nakanishi, T. Effect of surface free energy on PDMS transfer in microcontact printing and its application to ToF-SIMS to probe surface energies. *Langmuir* 2009, *25* (10), 5674-5683.

52.   Gupta, V.; Ganegoda, H.; Engelhard, M. H.; Terry, J.; Linford, M. R. Assigning Oxidation States to Organic Compounds via Predictions from X-ray Photoelectron Spectroscopy: A Discussion of Approaches and Recommended Improvements. *Journal of Chemical Education* 2014, *91* (2), 232-238.

53.   Hofmann, S., Auger- and X-ray Photoelectron Spectroscopy in Materials Science. Springer: Berlin, 2013; pp 297-408.

54.   de Rooij-Lohmann, V. I. T. A.; Yakshin, A. E.; van de Kruijs, R. W. E.; Zoethout, E.; Kleyn, A. W.; Keim, E. G.; Gorgoi, M.; Schäfers, F.; Brongersma, H. H.; Bijkerk, F. Enhanced diffusion upon amorphous-to-nanocrystalline phase transition in Mo/B4C/Si layered systems. *Journal of Applied Physics* 2010, *108* (1), 014314.

55.   ter Veen, R.; Fartmann, M.; Kersting, R.; Hagenhoff, B. Combining dynamic and static depth profiling in low energy ion scattering. *Journal of Vacuum Science & Technology A* 2013, *31* (1), 01A113.

56.   Stokhof, M. S. H.; Li, W.-M.; Ridder, M. d.; Sprey, H.; Haukka, S.; Brongersma, H. LEIS Study of ALD WN_XC_Y Growth on Dielectric Layers. *ECS Transactions* 2006, *1* (10), 71-77.

57.   Jousseaume, V.; Haumesser, P.-H.; Pernel, C.; Butterbaugh, J.; Maîtrejean, S.; Louis, D., Chemistry in Interconnects. In *Chemistry in Microelectronics*, John Wiley & Sons, Inc.: 2013; pp 81-186.

58.   Seshan, K., 2 - Scaling and Its Implications for the Integration and Design of Thin Film and Processes. In *Handbook of Thin Film Deposition (Third Edition)*, Seshan, K., Ed. William Andrew Publishing: Oxford, 2012; pp 19-40.

59.   Wachsman, E. D.; Lee, K. T. Lowering the Temperature of Solid Oxide Fuel Cells. *Science* 2011, *334* (6058), 935-939.

60.   Druce, J.; Téllez, H.; Simrick, N.; Ishihara, T.; Kilner, J. Surface composition of solid oxide electrode structures by laterally resolved low energy ion scattering (LEIS). *International Journal of Hydrogen Energy* 2014, *39* (35), 20850-20855.

61.   Druce, J.; Ishihara, T.; Kilner, J. Surface composition of perovskite-type materials studied by Low Energy Ion Scattering (LEIS). *Solid State Ionics* 2014, *262*, 893-896.

62.   de Ridder, M.; van Welzenis, R. G.; Brongersma, H. H.; Wulff, S.; Chu, W. F.; Weppner, W. Discovery of the rate limiting step in solid oxide fuel cells by LEIS. *Nuclear Instruments and Methods in Physics Research Section B: Beam Interactions with Materials and Atoms* 2002, *190* (1–4), 732-735.

63.   Jiang, G.; Rivera, F.; Kanyal, S. S.; Davis, R. C.; Vanfleet, R.; Lunt, B. M.; Shutthanandan, V.; Linford, M. R. Characterization of the plastic substrates, the reflective layers, the adhesives,

and the grooves of today's archival-grade recordable DVDs. *OPTICE* 2011, *50* (1), 015201-015201-10.

64.   Linford, M. R. The Blind Men and the Elephant as a Metaphor for the Multi-Instrument Analysis of Surfaces and Materials. Analysis of the Surfaces and Materials in Microfabricated Thin Layer Chromatography Plates. *Vacuum Technology & Coating* September, 2014.

65.   Cushman, C. V.; Grehl, T.; Linford, M. R. Low Energy Ion Scattering (LEIS). IV. Applications to Catalysis. *Vacuum Technology & Coating* July, 2015, 34-37.

66.   Ross, J. R. H., Chapter 1 - Heterogeneous Catalysis – Chemistry in Two Dimensions. In *Heterogeneous Catalysis*, Ross, J. R. H., Ed. Elsevier: Amsterdam, 2012; pp 1-15.

67.   Kolasinski, K. W., Heterogeneous Catalysis. In *Surface Science*, John Wiley & Sons, Ltd: 2012; pp 267-303.

68.   Celaya Sanfiz, A.; Hansen, T. W.; Sakthivel, A.; Trunschke, A.; Schlögl, R.; Knoester, A.; Brongersma, H. H.; Looi, M. H.; Hamid, S. B. A. How important is the (001) plane of M1 for selective oxidation of propane to acrylic acid? *Journal of Catalysis* 2008, *258* (1), 35-43.

69.   Phivilay, S. P.; Roberts, C. A.; Puretzky, A. A.; Domen, K.; Wachs, I. E. Fundamental Bulk/Surface Structure–Photoactivity Relationships of Supported (Rh2–yCryO3)/GaN Photocatalysts. *The Journal of Physical Chemistry Letters* 2013, *4* (21), 3719-3724.

70.   Linford, M. R. 'A Discussion of Aspects of a Paper by Caporali, Bardi, and Lavacchi on LEIS and XPS. *Vacuum Technology & Coating* May, 2014.